

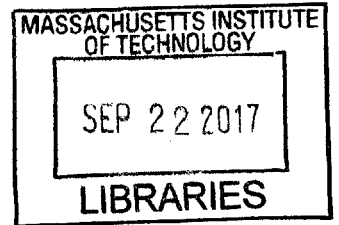
Nonlinear Dynamics of Complex Fluids in Fragmentation and Fracture

by

Bavand Keshavarz

M.A.Sc., University of British Columbia (2011)

B.S., Sharif University of Technology (2008)



ARCHIVES

Submitted to the Department of Mechanical Engineering
in partial fulfillment of the requirements for the degree of

Doctor of Philosophy

at the

MASSACHUSETTS INSTITUTE OF TECHNOLOGY

September 2017

© Bavand Keshavarz, MMXVII. All rights reserved.

The author hereby grants to MIT permission to reproduce and to
distribute publicly paper and electronic copies of this thesis
document in whole or in part in any medium now known or
hereafter created.

Author..... **Signature redacted**

Department of Mechanical Engineering

August 25, 2017

Certified by **Signature redacted**

Gareth H. McKinley

Professor, Mechanical Engineering

Thesis Supervisor

Accepted by **Signature redacted**

Rohan Abeyaratne

Chairman, Department Committee on Graduate Theses

Nonlinear Dynamics of Complex Fluids in Fragmentation and Fracture

by

Bavand Keshavarz

Submitted to the Department of Mechanical Engineering
on August 25, 2017, in partial fulfillment of the
requirements for the degree of
Doctor of Philosophy

Abstract

The fragmentation and breakup of complex fluids are fundamental elements of many industrial and biological processes. The fracture of food gels, atomization of paints, combustion of fuels containing anti-misting agents and application of pharmaceutical and agricultural sprays, as well as involuntary physiological processes such as sneezing, are common examples in which the atomized/fractured material contains synthetic or biological macromolecules that result in viscoelastic fluid characteristics. For many of these processes the effects of varying the rheological properties on the dynamics of fragmentation or fracture are still poorly understood. In this thesis, we investigate some of the underlying complexities associated with varying the rheology of such materials in both shear and elongation. The complex nonlinear rheology of these complex fluids under representative conditions of large strain and deformation rate is difficult to quantify experimentally and is a known challenge for existing constitutive models. The contribution of this thesis is therefore to develop and exploit several new experimental tools that enable precise rheological measurements under appropriate test conditions. A better experimental understanding of the dynamics of fragmentation/fracture in complex fluids will also help guide the development of new theoretical models that can quantitatively predict the mechanical response of complex fluids in such flows. Two distinct classes of model fluids/gels are studied in this thesis. First, a series of model viscoelastic solutions composed of a flexible homopolymer, poly(ethylene oxide) or PEO, dissolved in a water/glycerol mixture. These dilute solutions are known to behave very similarly to their Newtonian solvent in shearing deformations but exhibit markedly different extensional rheological properties due to the onset of a coil-stretch transition in the solvated microstructure at high elongation rates. Secondly we also consider a family of biopolymer networks: acid-induced casein gels. These canonical protein gels display a multiscale microstructure that is responsible for their gel-like viscoelastic properties. Upon external deformation, these soft viscoelastic solids exhibit a generic power-law rheological response followed by pronounced stress- or strain-stiffening prior to irreversible damage and failure, most often through macroscopic fractures. We study the dynamics of fragmentation for the dilute PEO solutions in different canonical flows: air-assisted atomization, drop impact on a small target, jet impact atomization and rotary spraying. We also study the fracture of the casein protein gels un-

der conditions of both constant applied stress and constant applied shear rate. Through quantitative study of these high strain and high deformation rate phenomena, we reach several conclusions about how the rheological properties of these materials can affect their mechanical behavior in fragmentation/fracture. First, for dilute viscoelastic solutions, the breakup and atomization of these fluids is markedly different than the analogous processes in a simple Newtonian fluid. The average droplet diameter shows a monotonic increase with added viscoelasticity, which is precisely monitored by accurate measurements of elongational relaxation times through a novel characterization method we have developed; Rayleigh Ohnesorge Jet Elongational Rheometry (ROJER). Based on our measurements of the material relaxation time scale a new theoretical model for the evolution in the average droplet diameter is developed for viscoelastic sprays. Second, the size distributions measured in each viscoelastic fragmentation process show a systematic broadening from the Newtonian solvent. In each case the droplet sizes are well described by Gamma distributions that correspond to an underlying fragmentation/coalescence scenario. We show that this broadening results from the pronounced change in the corrugated shape of viscoelastic ligaments as they separate from the liquid core. These corrugations saturate in amplitude and the measured distributions for viscoelastic liquids in each process are given by a universal probability density function, corresponding to a Gamma distribution with $n_{min} = 4$. The breadth of this size distribution for viscoelastic filaments is shown to be constrained by a geometrical limit, which can not be exceeded in ligament-mediated fragmentation phenomena. Third, in the fracture of the model acid-induced protein gels, we show that the fractal network of the underlying microstructure leads to a very broad power-law behavior in their linear viscoelastic response that can be precisely modeled by a simple model based on fractional calculus. We show that specific geometric properties of the microstructure set the value of the parameters that are used in the fractional model. The nonlinear viscoelastic properties of the gel can be described in terms of a 'damping function' that enables quantitative prediction of the gel mechanical response up to the onset of macroscopic failure. Using a nonlinear integral constitutive equation – built upon the experimentally-measured damping function in conjunction with power-law linear viscoelastic response – we derive the form of the stress growth in the gel following the start up of steady shear. We also couple the shear stress response with Bailey's durability criteria for brittle solids in order to predict the critical values of the stress and strain for failure of the gel, and show how they scale with the applied shear rate. This provides a generalized failure criterion for biopolymer gels across a range of different deformation histories. Results from this work are of relevance to many processes that involve breakup and rupture of complex fluids such as failure of viscoelastic gels, emulsification, spray painting and even biological processes such as pathogen transfer resulting from violent expiration. By investigating the linear and nonlinear behavior of two distinct classes of soft matter that lie on two ends of the viscoelasticity spectrum, one close to Newtonian liquids and one close to elastic solids, we provide key physical insights that can be generalized to broad classes of different complex fluids that undergo fracture and fragmentation processes.

Thesis Supervisor: Gareth H. McKinley
Title: Professor, Mechanical Engineering

Acknowledgments

This thesis would have not been possible without the help of many people. I will do my best to express my heartfelt gratitude to a number of them. Firstly, I wish to thank my adviser Gareth McKinley. I do not have enough words even in Persian vocabulary to thank Gareth enough, let alone in English. This work would have not been possible without his continuous support and encouragement through years. Every interaction between us has been a great source of joy for me and it has been an absolute pleasure and honor for me to work with him. Our brainstorming sessions on different ideas and challenging each other for more creative and physical thoughts have taught me a great deal about science and the process of creative thinking. Gareth also taught me a great deal about teaching and being next to him several times in the graduate fluid mechanics course (2.25) has been a continuous pleasure for me. The news that I can join his group made me the happiest person on the UBC campus few year ago on a rainy night in Vancouver. I still have the same joy and enthusiasm whenever a chance comes to work and collaborate together. Also it is needless to say that our friendship and humorous casual chats have been priceless for me and have helped me to see also the human side of our work and not get lost only in the burden of daily tasks. Me Lord, it has been a great pleasure for me to be your Baldrick !!!.

I would also like to thank Professors John Bush, Peko Hosoi and Lydia Bourouiba for being in my PhD committee. I have enjoyed every moment of the two fluid classes that John offers at MIT and our collaboration on two papers with Jean Comtet and Michela Geri have been fantastic for me. John's enthusiasm and passion for fluid mechanics is admirable and I have always been inspired by his work. Peko's continuous support and help has been incredible for me. I particularly have enjoyed our collaboration on sport physics project. Lydia's support and time is much appreciated. I also thank Professor Bob Cohen for his interest in my thesis. I am also incredibly thankful to Dr. Micheal Koerner for attending my thesis defense and more importantly for generating this great opportunity for us to collab-

orate with DuPont and later Axalta. My visit to Axalta's lab in Mt. Clemens and Michael's hospitality will be always remembered. I also express my deepest thanks to Eric Houze and John Moore from Axalta for being a great part of our industrial collaboration. Their help and insight has been incredible and in so many occasions vital for this project. I have great memories of all my trips to Wilmington or Mt. Clemens thanks to their help and hospitality. Eric, being a chemist by education, not only helped me immensely in understanding certain complex aspects of paint chemistry but also put a great deal of interest and time in understanding the fluid mechanics from our side and often surprised us by his original ideas. I also have great memories working and doing experiments with John in my visit to Mt. Clemens. It was a pleasure and an honor to work with him and I greatly cherish our friendship and can not thank him enough for the generous support that he and his wife, Maelynn, have always offered to me. Help and support from our other collaborators in both Dupont and Axalta is greatly appreciated. Specific thanks go to Patricia Cotts, Manish Mittal, Christiaan Engels, Koenraad Vandeneede, Paul Bruylants, Vicki Cheng and Florian Nettesheim for all the attention and patience during our numerous teleconferences. Every good experimentalist knows how priceless it is, to have a great technician and assistant during a one-week lab visit. William Bowman and Gary Dasin both helped me extensively during my visits to Axalta in Wilmington and Mt. Clements. I would also thank Axalta and DuPont for their financial support of my project during my PhD.

I was very lucky to work in a field like fragmentation that has attracted a giant such as Emmanuel Villermaux. I have learned a lot from his papers and have enjoyed every moment of the few discussions that we have had together about science and art. Reading his papers and understanding his original ideas have been a blessing for me that I always look forward to. In every APS-DFD meeting I know I will learn something original and new if I see his name in the abstracts.

I also truly cherish my friendship and collaboration with Christophe Clanet during his visit to MIT. His sport physics lectures were some of the best lectures I have ever sat in and our collaboration on elastic effects in walking and running has been

full of joy and excitement. Christophe's frankness and original ideas has been admirable for me and I am looking forward to continuing my collaborations with him. His great French sense of humor is also what I often miss after his MIT visit ended.

A great thank you to all my previous mentors and advisors. Professor Sheldon Green at UBC has been a fantastic adviser for me and his learned advice is always great for me. I was very lucky in undergrad to have the support of two great professors in my department. Professors Reza Soltani and Keveh Ghorbanian trusted me and let me do experiments in their lab which was a rare chance specially in Iran where so many undergrads are only allowed to become the clicking robot in front of a simulation package. My early exposure to experimental fluid mechanics had a great impact on me and my academic trajectory and various helps from Dr. Mehran Masdari is much appreciated. My humble talents in mathematics and specially geometry, which I now often use in my research, owe a lot to my middle-school math teacher, Mr. Said Adeli. Facing every geometry problem, I vividly remember him and his lectures. I learned a lot from lectures offered by Professors Akylas, Hung Cheng, Bora Mikic, Jörn Dunkel, Tomasz Wierzbicki and Pierre Lermusiaux at MIT. I also learned quite a bit from classes offered by Professors Jimmy Feng, Nima Atabaki, Kevin Oldknow, Dan Gelbart, Hesarakı and Rahimitabar at UBC and Sharif University of Technology. Special thanks to my old teachers Mrs. Gorgini and Mr. Eslaminia for their patience in tolerating my occasionally unleashed sense of humor in the class. Mark Belanger and Jim Bales from the Edgerton center were great sources of help in teaching me different machining and imaging skills. Jim Serdy has been always a generous friend in letting me use equipments and electronics; his help is much appreciated. I also would like to thank Yair Kipman from JetXpert for his support and help with the JetXpert camera. During my time at MIT, I have been fortunate to get involved in multiple collaborations with some brilliant researchers all around the world. I truly enjoyed sharing ideas and thoughts with Professors Sébastien Manneville, Emanuela Del Gado, Pat Doyle, Christian Clasen, Dan Curtis, Miguel Nobrega and Kenneth Shull. It was

also a great chance to work and collaborate on different projects with Thibaut Divoux, Mehdi Bouzid, Burak Eral, Philippe Bourrienne, Caroline Cohen, Mathieu Meerts, Michael Kessler, Erica Lai, Abigail Halim, Qiaochu Li, Jean Comtet, Simon Haward, Brice Saint-Michel, Nicole Sharp and Ken Park. I also like to thank Dr. Jessica Erdmann-Sager from Brigham and Women's Hospital for our collaboration on many interesting and exciting applications of rheology.

Many interesting discussions and conversations in conferences and meetings have inspired me and I owe a great thank you to many for sharing with me their time and their insightful thoughts: Professors Ravi Jagadeeshan, Oliver Harlen, Laurent Limat, Jose Bico, Constantino Creton, Henri Lhuissier, Randy Ewoldt, Jeffrey Giacomini, Prabhakar Ranganathan, Rob Poole, Sarah Hormozi, Jimmy Feng and Simon Rogers.

Past five or six years of my life at MIT have been enriched with great friends and no matter how many pages I write I can not thank all of them. From our lab, I would like to thank Chris and Angie, Aditya, Simon and Iraida, Thomas (or Tober), Laura and Marc for their great support and help when I joined NNF. All the fun nights in "People's Republik" and many other places are always in my memory. You helped me a lot to blend in the lab and I could not have asked for better lab-mates. All the chats about my meaningless abbreviation such as EF, WM, ChEF, BP and occasional cultural transactions of Adi and I learning/teaching Farsi and Tamil to each other still make me laugh and miss those days. Also many thanks to Murat, Ahmed, Kaijai, Flore, Emilie, Vivek, Jonn-Ross, and Ken who were great lab-mates for me. I would also like to express my most sincere thanks to Chirag Kalelkar for a great friendship through years. Chirag is one of the most knowledgeable people I have ever met in my life and every email, poem, painting, fluid movie and comment that he has shared with me has been deep and full of thoughtful meanings. As you would say it Chirag, I will "leave it" here since I can write pages about your brilliant originality in life.

After I joined the lab, over years many great friends and visitors joined the lab. My most sincere thanks goes to Divya, Vaibhav, Justin, Siddarth, Philippe, Alex,

Mekala, Shabnam, Salah, Crystal, Jai, Dayong, Amir, Lucien, Naveen Reddy, Joachim, Gustave, Yonatan, Michelle, Anoop, Allison, Jarvis, Professor Gondal, Miguel, Vera, Luis, and Talal. I can not even count how many great memories we have made together. Divya's hair dance and "glassophobia", Justin and Alex storage room story, Sid's books and his excellent scientific knowledge and blunt and sharp wisdom, Alex and Mekala's wonderful wedding, Talal's generosity and pure brilliant creativity, Jai's shaft, Miguel's touch in the jacuzzi, Lucien's love affair with peanut butter and so many others are just few I now remember. You guys were like a family for me and I have learned so much from all of you.

I also thank many friends from HML for their friendship over years: Pawel, Thanasi, Mark, Andrew, Ippolyti, Baudouin, Jai, Qing, Louis, Leopold, Nadia, Terri, Jose and Lisa. Same goes to my other friends at MIT: Siddarth, Aparna, Mayank, Vikram, Poetro, Sin Cheng, Alonso, Benji boy, Allison, Aaron, Ben and Connie, Rathi, Nikhil, Alex, Aly Eltayeb, Zsigi and Luca.

Special thanks to my dear friends at MIT who became like a family for me: Anurag, Ambika, Sergio and Pupy. I have loved all the moments we spent together and you are all dear to me. Many dear friends in the "French gang": Joel, Philippe, PT, Martin, Virginie, Baptiste and his roommate: Kevin the fire-worker, Emanuel and his dear wife and finally Dan and his dear family. Fialense nights with you guys were always great and I have a feeling that without you Caipi will never taste the same, Merci for everything. I also promise Monsieur Bourriane that we will celebrate the exit of France from world cup 2018 very soon, it will be another 2010 for Les Bleus. My dear teammates in the ChemE soccer team: David, Dan, Steve, Xiao, Carlos, Leia, Jen, Kosi, Danny and Professor Love. Thanks for your trust in me as your goalkeeper. That also explains our empty shelf of championship cups. Dear friends from UBC: Mona, Sepideh, Sarah, Saman, Farzaneh, Mehdi Einian, Hamid, Mohammad Mohammadnia, Kousha, Shervin, Andrew Tetzl, Purushotam, Hamed, Payam, Ali Rasekh, Layla, Darya, Mahmoud Ebadian, Ehsan Zaman, Arash Jamali, and Vincente. I miss all of you and I hope to see you again some time soon.

My dearest friends from undergrad: Hamed, Ehsan, Yaser, Majid, Parsa, Mojtaba, Emad, Ramin, Farhad, Farhang, Hossein, Saeid, Salman, Saman, Soheil, and Soheil Kianipur. I have tears in my eyes every time I remember our old memories. Hamed, Ehsan, Soheil and Yaser you are like brothers for me and I owe a lot to you. I have been very lucky to visit Hamed and his dear fiancée Atefeh in North Carolina and I truly hope that I can see you again some time in the near future. Ehsan, I wish we were together when Germany beat Brazil 7-1. I miss you all. Friends from high school and math Olympiads camp: Ehsan, Ehsan, Naser, Hadi and Davoud.

During my PhD, I have been fortunate to be involved in teaching responsibilities for few courses. I would like to again thank Gareth for encouraging me in following my passion for teaching and thank Leslie, Professors John Brisson, Cullen Buie, Rohit Karnik, Irmgard Bischofberger and Betar Gallant for providing me chances to TA for 2.25, 2.005 and 2.006. It was a great pleasure for me to teach and I cherished every moment of my interactions with students. Also many thanks to Ken, Shabnam, Mohammad, Sami, Eunnie and the rest of 2.006 teaching staff. A huge thank you to every student I have been TA for. Every time I TAed for a class I learned a lot thanks to curious questions from the class and it has always been a mutual learning process.

Many warm thanks to Sean, our lab assistant, for always making things happen and being so patient and caring with us. I also like to thank Leslie and Sucharita from the MechE department and also Sylvia from ISO for their boundless care and help in every aspect. Leslie I do now know how the department could survive without you. Every time I am in a conference and I meet an old MechE alumni they just ask me about you. You are an amazing source of help and guidance for all of us. I also would like to thank Doreen Morris from the provost office for her continuous delivery of high quality leftover free food to our lab from faculty meetings. Seeing you with a tray of sandwiches on every other Wednesday does magic to our lab's spirit and while I am at it, please have more faculty meetings !!! I also thank Julie, Gareth's dear wife, for hosting us in their place every few months and

being so kind and caring to all of us.

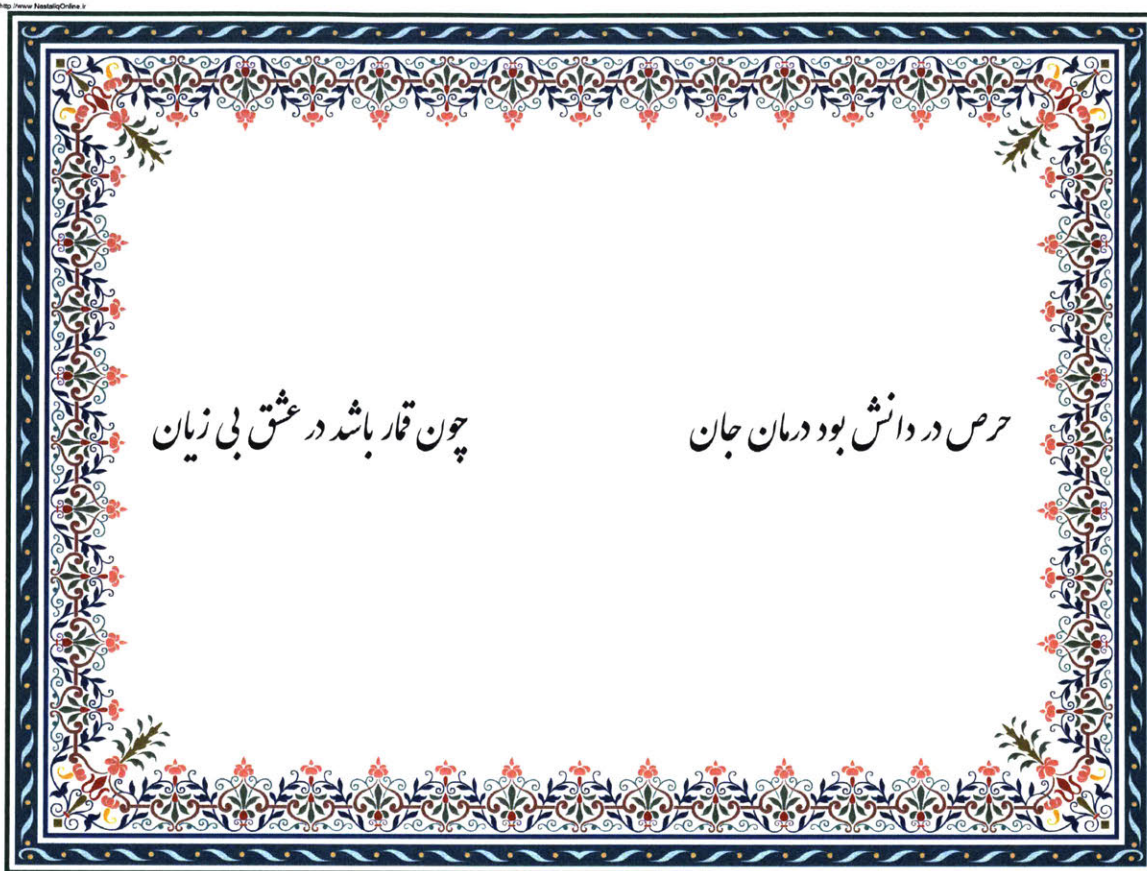
After finishing my PhD, I am joining Niels Holten-Andersen lab in DMSE for my postdoc. Niels, I have been admiring your work for years and it is a great pleasure for me to join your lab. I am very thankful to you and your lab members for making me feel welcome even before officially joining your lab. I hope I can learn a lot more chemistry from you and give my best back to you and your group.

They are certain inspiring figures in science, literature and arts that have always inspired me and given me hope and great ideas in some of the toughest moments of my life. Here are my twelve Olympians: Prandtl, Lord Rayleigh, and G. I. Taylor in science, Ernst Lubitsch, Billy Wilder, Stanley Kubrick and Ingrid Bergman in movies, Alberto Moravia and Anton Chekhov in literature, Friedrich Nietzsche, Erich Fromm and Khayyam in everything. I have cherished their art and science in many aspects of my life and can not imagine doing my PhD without enjoying a sip of wine from their tavern of thoughts.

I like to pay great deal of gratitude to my better half, Michela. Michela, your care, love and passion for me and my work is boundless. Your generosity and kindness is one of a kind. You have been with me in every aspect of life, whether it has been correcting my mistakes in writing, discussing scalings together, having creative ideas for experiments or just the simple joy of a good slice of flatbread pizza, a walk around Charles river, a laughter to my imitation of French accent...in all these moments you have been dearest to me and I love you. I am also grateful to your parents Carlo and Oletta for their endless love. Also thanks to all your dear relatives in Italy for their support and kindness. Garzie a tutti.

I thank all my relatives back in Iran. Special thanks to my aunt Fatemeh and Narges and my cousins Ahmad, Mohammad and Hamid for their love and care. Finally I want to express my deepest gratitude to my family. I owe all my life to them. They are my soul and my mind. They have sacrificed everything for me and have been an infinite source of support and care for me. Words can not describe how much I owe them and I am eternally in their debt. From childhood, I have always been blessed with their care and felt encouraged to follow my curiosity.

My beloved sister has been there for me in every moment of life and has dedicated so much to me. My parents gave the best to me and my sister. From the start, they prepared us for challenges in life and taught us critical thinking. They showed us that the joy of kindness and sacrifice is more lasting and fulfilling than any other joy. They sharpened our senses and gave us an everlasting crave for learning and knowledge. They embraced us with their love and propelled us with their pragmatic mind and fighting spirit. A spirit that never gives up and soars into the sky to avoid the scavengers of the lower heights.



"Greed for knowledge is the soul's wine

As gambling in love has no malign"

Poem by Saleh Keshavarz. Translated poorly by his son.

This thesis is dedicated to:

my mother, Soghra

my beloved sister, Monavar

and to the memory of my dad, Saleh

who always encouraged me in my pursuit of science and knowledge.

You are missed in every moment...

Contents

- 1 Introduction 57**
 - 1.1 Outline of the thesis 57
 - 1.1.1 Publications from this study 61
 - 1.1.2 Related publications from the author 62
 - 1.2 Literature Review 63
 - 1.2.1 Fragmentation of Newtonian liquids 67
 - 1.2.2 Fragmentation of Viscoelastic Liquids 71
 - 1.2.3 Extensional Rheology of Dilute Viscoelastic Solutions 74
 - 1.2.4 Effects of extensional properties on fragmentation 84
 - 1.2.5 Other complex fluids/gels in nonlinear deformations 88
 - 1.2.6 Fracture of soft gels 94

- 2 Instruments, Test Fluids and Experimental Procedures and Challenges 101**
 - 2.1 Scope 101
 - 2.2 Introduction 102
 - 2.3 Test Fluids 103
 - 2.3.1 PEO Solutions 104
 - 2.3.2 Casein Gels 107
 - 2.4 Shear Rheology Measurements 107
 - 2.5 Elongational Rheology Measurements 111
 - 2.5.1 Capillary Breakup Extensional Rheometry (CaBER) 111
 - 2.5.2 Rayleigh-Ohnesorge Jetting Extensional Rheometry (ROJER) 118
 - 2.5.3 EVROC 139

2.5.4	Comparison Between Different Instruments (EVROC and RO- JER)	149
2.6	Operating Limits of the EVROC Device	160
2.6.1	Limits of ROJER	162
2.6.2	Operating Nomogram for Microfluidic Extensional Rheometry	167
2.6.3	Nomogram for Measuring Extensional Viscosity	169
3	Effect of elongational properties on the average diameter of the fragments observed in the atomization	171
3.1	Scope	171
3.2	Introduction	172
3.3	Test liquids	177
3.4	Experimental Setup	178
3.5	Shear and elongational rheology of the spray fluids	180
3.6	Effect of elongational properties on atomization	181
3.7	Toy model	183
3.8	Conclusions	191
4	Droplet Size Distributions in Fragmentation of Viscoelastic Liquids	195
4.1	Scope	195
4.2	Introduction	196
4.3	Test Fluids	198
4.4	Size Distributions in Air-Assisted Atomization	200
4.5	Sudden Stretch Test	207
4.6	Proof for Minimum Value of Smoothness Parameter	208
4.7	Other Ligament-Mediated Fragmentation Flows	211
4.8	Size Distribution of Ligaments	216
4.9	Discussion	219
5	Rotary atomization of Newtonian and viscoelastic liquids	221
5.1	Scope	221

5.2	Introduction	222
5.3	Setup	224
5.4	Test Fluids	227
5.5	Dimensionless Operational Map	229
5.6	Rotary Atomization of Newtonian Liquids	233
5.6.1	Average Droplet Sizes	233
5.6.2	Parameter Study	234
5.6.3	Formation of Ligaments	235
5.6.4	Geometry of a Single Ligament	238
5.6.5	Kinematics of the Flow	240
5.6.6	Model for Predicting the Average Droplet Size	247
5.7	Droplet Size Distributions for Newtonian Liquids	250
5.8	Rotary Atomization of Viscoelastic Liquids	258
5.8.1	Average Droplet Size	258
5.8.2	Droplet Size Distributions for Viscoelastic Solutions	262
5.9	Model for Predicting the Size of Satellite Droplets	265
5.10	Conclusions	267
6	Linear rheology and physical structure of casein gels	269
6.1	Scope	269
6.2	Linear rheology of simple resins	270
6.3	Linear rheology of gel-like colloidal resins	272
6.4	Food gels and soft solids	273
6.4.1	Structure	274
6.4.2	Linear rheology	275
6.5	conclusions	282
7	Nonlinear viscoelasticity and generalized failure criterion for biopolymer gels	283
7.1	scope	283
7.2	Introduction	284

7.3	Experiments and gels	285
7.4	Damping function	287
7.5	K-BKZ description of shear start-up	290
7.6	Failure criteria and discussion	295
7.7	Conclusion	298
8	Conclusions	301
8.1	Conclusions from this study	301
A	Details of ROJER Analysis	305
A.1	Deriving the Strobe Factor	305
A.2	Details of the Linear Stability Analysis	306

List of Figures

1-1	(color online). A graphic introduction to this thesis.	58
1-2	(a) Breakup of a $175\mu m$ diameter Newtonian jet. Similar phenomena is used in continuous inkjetting or CIJ. (b) Air-assisted atomization of a viscoelastic solution (PEO-300K-0.01% wt. in a water-glycerol solvent). (c) A snapshot of a human subject urinating [1]. (d) A snapshot of a human subject sneezing [2]. Image courtesy of Lydia Bourouiba.	64
1-3	(color online). Examples of rotary atomization in (a) metallurgy: a molten metal jet is discharged onto a rotating disc and the centripetal forces atomize the melt into a set of relatively mono-disperse beads [3]. (b) Kanja the tiger shaking off water and drool from its fur. Image courtesy: Kanja Shaking Poster – Tim Flach Wildlife Poster. (c) Rotary/bell atomization cup, installed on a 6 degree of freedom robot arm, spinning at high rotation speeds ($\sim 70,000$ RPM) and delivering a fine mist of paint droplets to the automobile surface. (d) A wet dog shaking water off its fur. The spiral shape of water filaments on the right side of the image is a particularly interesting aspect of rotary fragmentation. Image courtesy: Carli Davidson [4].	65

1-4	(color online). Fragmentation of liquids in the advertisement industry: (a) A female model posing for a calendar entry with a “milk” dress made out of multiple events of milk fragmentation. Image courtesy: Jaroslav Wiczorkiewicz. http://aurumlight.com/ . (b) Splash of viscoelastic paint on the body of a male model. Image courtesy: DieDruckerei.de - Splash 3D (Theatrical Version) https://vimeo.com/22934779	66
1-5	(color online). (a) Wilson Bentley (1865-1931) studying the shape of ice crystals [5]. (b) Size distributions of raindrops gathered by Marschall and Palmer [6]. Inset: Image of flour beads formed after impact of raindrops on a bed of flour spread on a screen made of silk tights. This creative method was used by Bentley [7] years before the advent of high speed photography.	68
1-6	(color online). Great scientists studying different aspects of fluid fragmentation through history [8, 9, 10, 11].	69
1-7	(color online). Different droplet size distributions from studies on liquid sheets by Bremond and Villermaux [12] fitted by different models. (a) A narrow size distribution fitted by lognormal, Gamma and Poisson distributions. The order for the Gamma distribution is $n = 17$. (b) A wider size distribution fitted by lognormal, Gamma and Poisson distributions. The order for the Gamma distribution is $n = 4$. Images are taken from [13].	70
1-8	(color online). (a) Snapshot of a high Reynolds number viscoelastic liquid jet at breakup (200 ppm PEO dissolved in water). Image taken from [14]. The original experiments were performed by Hoyt and Taylor [15]. (b) Cover image of the Society of Rheology Bulletin [16]. Images by Keshavarz and McKinley demonstrate the difference between a viscoelastic liquid and its corresponding Newtonian solvent in air-assisted atomization.	72

1-9 (color online). A “rheological” map for different paints and resins used in the coating industry. Image taken from [17].	73
1-10 (color online). Different daily examples in which the extensional properties (stickiness) of synthetic and biological materials plays an important role: (a) extension of a chewing gum. (b) elongated filaments of a viscoelastic liquid stretching out of the wet strip on a shaving blade holder. (c) large resistance of adhesives in elongational deformations. (d) a saliva drop hold up against gravity by an elongating filament. (e) Hagfish slime is used as a defensive mechanism due to its sticky nature.	74
1-11 (color online). (a) The idea of materials being “slimy” corresponds to their response in shear deformations. (b) “Stickiness” is on the other hand a material property that should be probed in an elongational flowfield.	75
1-12 (color online). Original (and first) set of measured data for extensional rheology of pitch. The test was performed by Trouton in 1906. [18].	77
1-13 (color online). Different methods used in the literature for measuring extensional properties of dilute viscoelastic solutions: (a) tubeless siphon method used by Peng and Landel [19]. Image taken from [20]. (b) Opposed nozzle device used by Dontula et al. [21]. (c) Microfluidic hyperbolic channels used as an extensional rheometer [22].	78
1-14 (color online). Measurements of extensional rheology for a model fluid (M1) performed by different research groups and labs [23]. This plot is some times referred to as the so-called “M1” muddle.	79

1-15 (color online). CaBER device: (a) A liquid sample (Bavand’s saliva in this specific figure) sitting between two stationary plates. (b) A filament is formed after the plates are separated from each other. (c) A look into the dynamics of polymer chains in the solvent as they go through elongation. Multiple scales are involved and to get a macroscopic model, from the microscopic properties, several levels of course graining are required. (d) The final stages of breakup can lead to an iterative instability that involves capillarity, elasticity and inertia giving rise to rather beautiful structures (beads-on-a-string). (e) Magnified image showing the thin filament connecting multiple liquid beads. Surface tension is dominant in the bead region while the elasticity is the major force in the thin elongated filaments. . . .	80
1-16 (color online). (a) An example of CaBER failing to capture the elasto-capillary balance for a dilute viscoelastic solution (PEO-300K-0.01% wt. in the solvent). The filament breaks during the plate separation stage. (b) An approximate map of operation for the CaBER device based on the corresponding dimensionless numbers. Red region corresponds to solutions that are so dilute and non-viscous for proper testing in CaBER [24].	81
1-17 (color online). Jet breakup for different Newtonian and viscoelastic liquids. Image taken from [14].	82
1-18 (color online). Data from a jet breakup elongational rheometer [25]. The device was originally designed by Schümmer and Tebel [25]. . .	83
1-19 (color online). Performance of normal fuel in combustion (a) and atomization (c) compared to the fuel with anti-misting agents ((b) and (d) respectively). Images taken from [26].	85
1-20 (color online). Measurements of relative mass mean diameter (MMD) for viscoelastic sprays performed by Ferguson et al. [27] for a series of PEO solutions.	86

1-21 (color online). (a) Harold (Doc) Edgerton (1903-1990) performing high speed imaging tests in his lab at MIT. (b) High speed visualization of drop pinch off used by Edgerton et al. [28] to quantify the drop-weight method that is used in liquid surface tension measurements. (c) A bombardier beetle discharging a hot spray as a defensive mechanism. Image taken from MIT museum collection of Edgerton's work <http://video.mit.edu/watch/bombardier-beetles-3185/>. 87

1-22 (color online). (a) TEM images of waterborne Polyurethane Dispersions at different waiting times. (b) Linear rheology of the same liquids/gels demonstrating a power law behaviour over a wide range of frequencies. Images taken from [29]. 89

1-23 (color online). (a) TEM image of a typical resin provided by Axalta Coating Systems. (b) Size distribution of gel-like beads shown in part (a). (c) A physical image of the structure of this specific resin. . . 90

1-24 (color online). (a) Fragmentation and fracture of a spoonful of yogurt upon the impact of a strawberry. (b) SEM image of yogurt made from unheated skim milk. Casein micelles aggregate in the form of coarse clusters. Image taken from [30]. (c) and (d) ESEM images of a casein acid-induced polymer gel. The thick fibrous strands of this biopolymer gel provide the elastic response of this material in different deformations. 91

1-25 (color online). Stress relaxation of milk curd after a step in strain. Data were measured by Scott Blair (1902-1987) [31]. The idea of a *fractional* mechanical element that can generate a power law relaxation response with two model parameters \mathbb{V} and α . As α varies from 0 to 1 one can recover a spectrum of material responses ranging from Hookean solids to Newtonian liquids. 93

1-26 (color online). Dimensionless map of fragmentation and fracture for viscoelastic liquids and soft network gels. The $\{\sqrt{We}, Ec, Ca\}$ coordinate system represents dimensionless forms for the inertia, elasticity, and the viscosity of the material. For example in the atomization of non-viscous Newtonian liquids (inset with the blue border), inertia overcomes the capillary forces and the atomization process will be governed by the inertia-capillary balance in the thinning filaments. At the same time, for viscous Newtonian liquids the buckling of a viscous thread which is compressed at a constant velocity V (inset with green borders) is a good example in which viscous stresses can overcome the capillary resistance (at high enough Ca numbers). This results in the buckling of the liquid thread very similar to the buckling of an elastic column under compression. Image is taken from [32]. For viscoelastic liquids/gels, a non-zero relaxation time τ_E leads to high values of elastocapillary number at small length scales. For viscoelastic liquids which do not have a temporary/permanent network this leads to elongated filaments that show enhanced extensional viscosity and inhibit the atomization process (inset image with red borders). However, if the liquid/gel has a temporary/permanent network it is possible that the induced stresses (from either capillary effects, inertia, or external forces) become larger than a critical value that is set by the surface energy of the temporary/permanent network within the material. This can lead to a solid-like fracture of the fluid/gel (inset image with brown borders) [33]. 95

1-27 (color online). (a) Casein gels under a, constant stress, creep experiment. At a certain failure time macroscopic cracks start to appear in the material. (b) Silicone gel implant rupturing under a tensile test. Image taken from [34]. (c) A polymeric liquid fractures under tension by forming a propagating crack. Image taken from [35]. . . . 98

1-28 (color online). "Fracture toughness" of different metallic materials plotted by Basquin [36]. This is usually referred to as Basquin's law of fatigue [37]. 99

1-29 (color online). Strength of different glass samples at the fracture point while they experience an increasing load with a constant stress rate. Results from these tests were first analyzed by James Bailey (1890-1962) [38]. His analysis is now referred to as the Bailey criterion [39]. 100

2-1 (a) and (b): Rheological data for Casein gels were obtained with an ARES-LS strain-controlled rheometer (TA Instrument) using a machined Couette cell made of an outer polished Plexiglas cup of height $H = 20.32$ mm and radius $r_o = 25$ mm which is rotating around a fixed inner bob of radius $r_i = 22.65$ mm made of Delrin, leading to a shear flow in a gap of 2.35 mm. (c) The casein gel formed in the Couette cell on the ARES rheometer. 109

2-2 Mechanical response of the casein gel (4%casein-1%GDL) during the gelation process monitored by the ARES rheometer. The outer cylinder oscillation creates a linear shear flowfield in the gap that oscillates at a fixed frequency. The torque/stress ($M(t)$ or $\sigma(t)$) response of the gel is monitored vis the fixed inner bob. In and out of phase responses are converted to elastic (red dots) G' and loss modulus (blue dots) G'' respectively. 110

- 2-3 CaBER (Capillary Breakup Extensional Rheometry) for a semi-dilute Poly(ethylene oxide) solution (molecular weight $M_w = 5 \times 10^6 \text{ g/mol}$ and 0.15 wt.% concentration, $c/c^* = 1.5$), $Oh = 0.005$, $De = 1.72$. The blue dots are the oversampled data from the laser micrometer while the green circles are the bin-averaged smoothed data. The visualized images of the actual filament thinning with time are at the top. The filament goes through three significant regimes: the initial region (shaded yellow) is still affected by fluid inertia; as the liquid thread thins down under the action of capillary pressure the elastic stresses become increasingly important and an elasto-capillary region emerges. The solid black line indicates an exponential decay with time described by Equation (2.5) (the theoretical prediction for elasto-capillary regime). Finally when the polymer chains in the filament approach their maximum extensibility the diameter approaches zero in a linear manner (shaded orange region). 115
- 2-4 CaBER (Capillary Breakup Extensional Rheometry) for a dilute poly ethylene oxide solution ($M_w = 2 \times 10^6 \text{ g/mol}$ and 0.01 wt.% concentration $c/c^* = 0.1$), $Oh = 0.01$, $De = 0.1$. The blue squares show the data from the laser micrometer; the normalized filament diameter is plotted versus time normalized by the capillary time-scale ($\tau_R \equiv \sqrt{\rho R_{(t=0)}^3 / \sigma} = 6 \text{ ms}$). The solid line is a fit from the expected predictions for inertia-capillary regime (Equation (2.2) in the text). The visualized images of the actual filament thinning with time are shown above. The beads-on-a-string structure that appears in the final stages (picture on the right) makes the measurements of relaxation time almost impossible as the midplane diameter rises and falls with time. 117
- 2-5 (a) The ROJER (Rayleigh-Ohnesorge Jetting Extensional Rheometer) setup. The liquid jet is perturbed by a piezo-electric actuator and then its motion is slowed down and captured using the stroboscope imaging setup. 119

2-6 Rayleigh-Ohnesorge Jetting Extensional Rheometry (ROJER) analysis for the 300K-PEO solution ($c/c^* = 0.036$); $We_j = 16.9, kR_0 = 0.8, Oh = 0.075, De = 0.72$; (a) Visualized images of the jet going through Rayleigh-Plateau instability; both the linear stage of the instability (left) and the nonlinear stage (right) were imaged using the strobe camera. (b) The measured values for the filament neck diameter plotted against time (blue squares). The dashed line is the fit from the linear stability analysis ($D_p/D_0 = 1 - \delta \exp(\alpha(We, Oh, De)t)$ with $\delta = 0.01$). The solid black line indicates exponential decay with time described by Equation (2.5) as the theoretical prediction for elasto-capillary regime. From fitting the exponential thinning region, the value of the relaxation time is found to be equal to $\tau_E = 60\mu s$. (c) Strain rate in the filament neck ($\dot{\epsilon}_p \equiv (-2/D_p(t)) dD_p(t)/dt$) versus time. The calculated values show a plateau at a critical strain rate equal to $2/3\tau_E$ (solid black line). The initial evolution in the strain rate is described well by the predictions from the linear stability analysis (the dashed line). The deviation at very early times ($t \leq 0.3ms$) arises from the effects of the nozzle exit on the jet diameter and velocity profile. 124

2-7 Values of dimensionless growth rate ($\alpha\tau_R$ in which $\tau_R = \sqrt{\rho R_0^3/\sigma}$ is the Rayleigh timescale) for the instability measured from experiments at different dimensionless wave-numbers (kR_0) for the viscoelastic jet (PEO 300K) with $Oh = 0.075$, $We = 16.9$, $De = 0.72$, (blue squares) compared with the theoretical dispersion curve for the Rayleigh-Plateau instability: the dashed line shows the dispersion curve for a Newtonian jet ($Oh = 0.075$, $We = 16.9$) and the solid line is for the viscoelastic jet ($Oh = 0.075$, $We = 16.9$, $De = 0.72$). Theoretical results are evaluated from the linear instability analysis of Brenn et al.[40]. Also shown is a montage of images from the final stages of breakup for two different wavenumbers: the left image for $kR_0 = 0.43$ is below the most unstable wavenumber ($kR_0 < (kR_0)_{max}$) and clearly shows the growth of higher wavenumber modes leading to the appearance of a large satellite droplet which later merges into the leading drop, the right image shows a wavenumber of $kR_0 = 0.80$ that is larger than the most unstable mode and for which the satellite droplets do not appear resulting in a smooth beads-on-a-string structure. 129

2-8 (a) Montage of images obtained at different times from the jet breakup experiment ($We_j = 16.9, kR_0 = 0.8, Oh = 0.075, De = 0.72$) following a fixed Lagrangian fluid element (i.e. the section of the jet shown in the red box) which moves with constant velocity ($V_j = 2.6ms^{-1}$). (b) Sitting in a moving frame translating with constant velocity (V_j) the Lagrangian element becomes stationary and the filament thins down as a results of capillarity in a way that is reminiscent of the dynamics of the filament in CaBER. (c) The normalized diameter versus time for PEO-300K-0.01 wt.%($Oh = 0.075, De = 0.7$) at three different jet velocities: red circles ($V_j = 3.9ms^{-1}, We = 39.6, kR_0 = 0.66$), magenta triangles ($V_j = 4.7ms^{-1}, We = 54.5, kR_0 = 0.80$), blue squares ($V_j = 2.6ms^{-1}, We = 16.9, kR_0 = 0.80$). The dashed lines are the corresponding fits from the linear instability analysis ($D/D_0 = 1 - \epsilon exp(\alpha(We, Oh, De)t)$) and the solid lines each show an exponential decay ($D/D_0 \sim exp(-t/3\tau_E)$) with $\tau_E = 60\mu s$ for each line. The measured relaxation times from ROJER analysis are thus independent of jet velocity. 133

2-9 (a) Montage of images from ROJER test for two different molecular weight polymer solutions (left images are for PEO-300K-0.1 wt.% and the right images are for PEO-1000K-0.05 wt.% $We_j = 8.5, kR_0 = 0.77, Oh = 0.075$) at different times following a Lagrangian fluid element (the section of jet in the green and red boxes respectively) which moves with constant velocity ($V_j = 0.87ms^{-1}$). (b) The normalized diameter versus time for PEO-300K-0.1 wt.% (green squares) and for PEO-1000K-0.05 wt.% (red triangles). The solid lines show exponential decays fitted to Equation (2.5) with $\tau_E = 360\mu s$ for PEO-300K-0.1 wt.% and $\tau_E = 2800\mu s$ for PEO-1000K-0.05wt.%. 136

2-10 (a) The ROJER measurements of the thinning filament diameter as a function of time for both the viscoelastic liquid (PEO-300K-0.01 wt.%-red filled circles) and the corresponding Newtonian solvent (water and glycerol ,60-40 wt.%-blue open circles). Solid line shows the exponential fit for the elasto-capillary regime (Equation (2.5)) and the dashed line is the linear fit for the visco-capillary regime for filament thinning ($D(t) = 0.072(\sigma/\eta_s)(t_b - t)$). (b) Shear (triangle) and extensional rheology (circle) for both the Newtonian solvent (blue open symbols) and the viscoelastic solution (PEO-300K-0.01 wt.%)(red filled symbols). The solid and dashed lines show respectively the FENE-P predictions using model parameters in Table 1 for the extensional and shear viscosities. The transient elongational viscosity data are extracted from the jet thinning dynamics shown in Figure 10(a). 139

2-11 (color online). (a) SEM image of the hyperbolic contraction and the dimensions of the entire geometry. Taken from Ober et al. [41] with permission (Reproduced with permission from Rheologica Acta 52, 6 (2013). Copyright 2013 Springer.). (b) Pressure measurements, for the PEO-4000K-0.05% wt. solution. Four flush-mounted pressure transducers are located along the channel axis. The magnitude of the pressure drop across the contraction/expansion between sensors 2 and 3 (ΔP_c) is an indication of elongational effects. 142

2-12 (color online). (a) Shear viscosity measurements plotted for three different test fluids: the Newtonian solvent (\circ and \blacktriangle), 4M-PEO-0.0025%wt. (magenta open circles \circ and magenta filled triangles \blacktriangle) and 4M-PEO-1%wt. (\circ and \blacktriangle). Open circles are data measured in a double-wall Couette geometry and the filled triangles are shear viscosity measurements from the EVROC device calculated from the measured pressure difference upstream between sensors 1 and 2. (b) Pressure difference across the hyperbolic contraction ΔP_c measured at different flow rates and plotted in a dimensionless form ($\Delta P_c / \mu \dot{\epsilon}_a$) vs. Reynolds number Re for different Newtonian liquids: S60 calibration oil (\square) and water-glycerol solvent (60-40 wt.%) (\circ). . . 146

2-13 (a) Pressure drop across the hyperbolic contraction in EVROC tests measured at different flow rates and plotted in a dimensionless form, $\Delta P_c / \mu \dot{\epsilon}_a$ versus Re , for different fluids: the Newtonian solvent (\circ), 300K-PEO-0.01%wt. (\square), 1000K-PEO-0.01%wt. (\triangle), 4000K-PEO-0.0025%wt. (magenta inverted triangles ∇), 4000K-PEO-0.05%wt. (\diamond), 4000K-PEO-1%wt. (\star). (b) Snapshots of the jet breakup process for the 300K-PEO-0.01%wt. solution in the ROJER setup: (i) An image of the entire process showing the jet exiting the nozzle and breaking up into individual droplets. (ii) A time sequence of enlarged snapshots showing the emergence of a cylindrical filament that can be followed by the Lagrangian box (in green) that is moving downstream with the jet velocity. (iii) Time evolution of the filament in the Lagrangian box shows elasto-capillary thinning. (c) Snapshots demonstrating the elasto-capillary thinning regime in the CaBER device for the 4000K-PEO-1%wt. solution. (d) Time evolution of the filament neck diameter $D_p(t)$ is plotted for different fluids tested in the ROJER setup: the Newtonian solvent(\circ), 300K-PEO-0.01%wt. (\square), 1000K-PEO-0.01%wt. (\triangle), 4000K-PEO-0.0025%wt. (magenta inverted triangles ∇), 4000K-PEO-0.05%wt. (\diamond). (e) Results from CaBER test for the 4000K-PEO-1%wt. solution (\circ). Solid lines in both (d) and (e) show fits of the exponential decay expected from theory (Equation 2.5). Raw measurements of $D_p(t)$ for the 300K-PEO-0.01%wt. solution (\blacksquare) are also plotted, to provide an indication of typical fluctuations in the diameter measurements. 150

2-14 (color online). (a) Circles show the apparent extensional viscosities measured from ROJER experiments for the Newtonian solvent (\circ), 300K-PEO-0.01%wt. (green circles \circ), 1000K-PEO-0.01%wt. (blue circles \circ), 4000K-PEO-0.0025%wt. (magenta circles \circ), and the 4000K-PEO-0.05%wt. (red circles \circ) solutions. Open triangles show the EVROC measurements for the 4000K-PEO-0.05%wt. solution (red triangles Δ). The solid lines are predictions of FENE-P theory plotted for each liquid with the corresponding parameters from Table 1. (b) Same data shown in (a) but plotted in dimensionless form: Trouton ratio $Tr \equiv \eta_E^+(\epsilon, t)/\eta_0$ versus the Weissenberg number $Wi \equiv \tau_E \dot{\epsilon}$. . 156

2-15 (color online). (a) Measurement nomogram in 3-dimensional space for different liquids with coordinate axis x, y, z constructed from $\{\sqrt{We}, Re, Wi\}$ combination. Lines of constant elasticity El , Ohnesorge Oh and Deborah De numbers are shown by blue dashed arrows. The black arc arrows show the direction at which El, Oh and De increase in their corresponding $Re - Wi$, $Re - \sqrt{We}$, and $\sqrt{We} - Wi$ planes. One eighth of a unit sphere is plotted in the corner of the coordinates. Every material location in the x, y, z parameter space can be radially projected onto the surface of this sphere. Shaded colors show regions in which EVROC and the ROJER instrument can/cannot perform. (b) Measurement nomogram based on the key intrinsic properties of the fluid plotted in a 2D representation. The angular orientation of every point in the 3D parameter space sketched in (a) can be uniquely mapped onto this 2D representation ($De - Oh$). The solid and dashed lines are lines of constant elasticity number El and elasto-capillary number Ec respectively. The green area indicates where both ROJER and EVROC are possible ($Ec \geq O(l_{resolution}/R)$ and $El \geq O(1)$). The magenta area is where ROJER is possible and EVROC is impossible ($Ec \geq O(l_{resolution}/R)$ and $El < O(1)$). The blue area is where ROJER is impossible and EVROC is possible ($Ec < O(l_{resolution}/R)$ and $El \geq O(1)$). The red area is where both ROJER and EVROC are not possible ($Ec < O(l_{resolution}/R)$ and $El < 1$). 166

2-16 (color online). Extensional rheometry nomogram based on the key intrinsic properties of the fluid plotted in a 2D representation. The green area indicates where both ROJER and EVROC are possible ($El \geq O(1)$ and $Ec \geq O(l_{resolution}/R)$ using $l_{resolution} \simeq 2\mu m$ and $R_0 \simeq 90\mu m$). The magenta area is where ROJER is possible and EVROC is impossible ($Ec \geq O(l_{resolution}/R)$ and $El < O(1)$ respectively). The blue area is where ROJER is impossible and EVROC is possible ($Ec < O(l_{resolution}/R)$ and $El \geq O(1)$). The red area is where both ROJER and EVROC are not possible ($El < 1$ and $Ec < O(l_{resolution}/R)$). The locus of each test fluids is located on the nomogram based on the corresponding values of Deborah and Ohnesorge numbers (calculated in Table 1 in the main article). For three of the dilute polymer liquids (300K-PEO-0.01%wt., 1000K-PEO-0.01%wt., and 4000K-PEO-0.0025%wt.) measurements were possible using the ROJER instrument while the EVROC data could not be analyzed due to dominant inertial effects (Δ). One dilute solution, 4000K-PEO-0.05%wt.(\circ), and a semi-dilute entangled solution, 4000K-PEO-1%wt.(\bullet) are located in the green region and both EVROC and ROJER measurements give meaningful values for the apparent extensional viscosity of these liquids. 170

3-1 (a) Spray visualization images for the Newtonian solvent close to the nozzle. (b) Spray visualization images for the viscoelastic solution (PEO-300K-0.01 wt.% in the solvent) close to the nozzle. (c) Spray visualization images for the Newtonian solvent far from the nozzle. (d) Spray visualization images for the viscoelastic solution (PEO-300K-0.01 wt.% in the solvent) 5mm away from the nozzle. 174

3-2 (a) Schematic of the industrial spray nozzle used in the experiments with $D_L = 1.5mm$, $b_a = 1.5mm$. A low momentum liquid jet (red color) is surrounded by a coaxial high momentum jet of air (blue color). The oblique air jets are low momentum and only help confine the primary jet in a narrow plane. (b) Spray visualization of water; three different successive instabilities make the liquid jet unstable and finally atomize it into a fine mist of droplets. 176

3-3 The LaVision spray visualization setup. A $1.5mm \times 1.5mm$ frame is illuminated using laser back-lighting and a Flowmaster camera captures individual snapshots from the droplets in the spray fan. . . 179

3-4 (a) Visualization of viscoelastic droplets (PEO-300K-0.01 wt.%) undergoing fragmentation in opposed jet atomization ($Re = 620, We = 300$). (b) Visualization of Newtonian solvent droplets (water and glycerol 60-40 wt.%, $Re = 620, We = 300$) during fragmentation in opposed jet atomization. 181

3-5 (a) Spray visualization image for the viscoelastic polymer solution (PEO-300K-0.01 wt.% in solvent) close to the nozzle. A ligament can be seen in the blue box which is elongated by the air stream (b) Schematic of the suggested model by Marmottant and Villermaux [42] for analyzing the dynamics of the ligament, (reproduced with permission). (c) Montage of images from sudden step-extension test for the viscoelastic solution (PEO-300K-0.01 wt.% in the solvent) in a CaBER instrument. As soon as the flow in the neck region reaches the elasto-capillary balance ($t \geq 20.0ms$) subsequent deformation is localized in the neck while the main ligament stops stretching ($dL_{CaBER}/dt \simeq 0$) and a capillary wave propagates along the filament. 183

- 3-6 (a) Montage of images from the sudden stretch experiment for PEO-300K-0.01 wt.%. (b) Blue squares are average sizes for the viscoelastic solutions normalized by the average diameter for solvent drops as a function of the Deborah (De) number in the ligament ($De \equiv \tau_E / \sqrt{\rho d_l^3 / 8\sigma}$ in which d_l is the characteristic ligament size and is estimated from the average diameter, $\langle d \rangle_N$). The solid black line shows the predictions from the model described in the text (Eq. (3.9)). 185
- 4-1 (color online). Snapshot of the liquid jet in the air-assisted atomization for (a) the Newtonian solvent and (b) the viscoelastic solution (PEO-300K-0.01% wt. in the solvent). 198
- 4-2 (color online).(a) Images from the fragmentation process for a Newtonian ligament. The coalescence of the neighboring blobs in the ligament at $t = 0$ (magenta circles on the left image) results in the final distribution of droplet sizes at $t = 25$ ms. 200
- 4-3 (color online). (a) Droplet size distributions for all tested liquids in the air-assisted atomization process. For each fluid we specify the values of Ohnesorge and Deborah number, $\{Oh, De\}$: $(\square)\{Oh = 0.04, De = 0\}$, $(\triangle)\{0.04, 0.2\}$, $(\triangle)\{0.04, 1.3\}$, $(\bullet)\{0.04, 3.6\}$, $(\bullet)\{0.04, 10.0\}$. Solid lines are Gamma distributions for $n = 6$ (black) and $n = 4$ (red). 201
- 4-4 (color online). Droplet size distributions for different liquids examined in the air-assisted atomization process: (a) Newtonian solvent $(\square)\{Oh = 0.04, De = 0\}$ compared with PEO-1000K-0.01% $(\bullet)\{Oh = 0.04, De = 3.6\}$ and PEO-1000K-0.05% $(\bullet)\{Oh = 0.04, De = 10.0\}$ Solid lines are Gamma distributions for $n = 6$ (black) and $n = 4$ (red). (b) Newtonian solvent $(\square)\{Oh = 0.04, De = 0\}$ compared with PEO-300K-0.1% $(\triangle)\{Oh = 0.04, De = 1.3\}$ and PEO-1000K-0.05% $(\bullet)\{0.04, 10.0\}$ Solid lines are Gamma distributions for $n = 6$ (black) and $n = 4$ (red). 203

- 4-5 (color online). Droplet size distributions for different liquids tested in the air-assisted atomization process: Newtonian solvent (\square) $\{Oh = 0.04, De = 0\}$ compared with PEO-1000K-0.01% (\bullet) $\{Oh = 0.04, De = 3.6\}$ and PEO-1000K-0.05% (\bullet) $\{0.04, 10.0\}$ Solid lines are Gamma distributions for $n = 6$ (black) and $n = 4$ (red). (a) The dashed red line is the best fit to a log-normal distribution. (b) The solid green line is a Gamma distribution with $n = 2$ and is shown solely for comparative purposes. 204
- 4-6 (color online). (a) Computed error in fitting different types of PDF to measured droplet size distributions of four different viscoelastic liquids. The red circles correspond to a Gamma distribution with $n = 4$, red triangles show the log mean square error for the best fit to a log-normal distribution and the black circles are for a Gamma distribution with $n = 6$. (b) Computed error in fitting PDF from Gamma distribution at different values of n for all four viscoelastic liquids. For all liquids the error is minimized for a Gamma distribution with $n = 4$ 206
- 4-7 (color online). (a) Sudden stretch experiment for a viscoelastic solution at high strain rates ($\bar{\epsilon} \simeq 120s^{-1}$). (b) Schematics of a cylindrical ligament with initial radius r_0 corrugated by perturbations with similar wavelengths but varying amplitude ξ . (c) Ligament profiles for the Newtonian solvent (blue curve) compared with the viscoelastic solution (red curve) at the breaking point from the liquid hemispherical reservoirs ($t = 0$). The dashed circles indicate the local proto-blobs inside each ligament. 208

- 4-8 (color online). (a) An undisturbed axi-symmetric ligament with a total volume of V_0 consisting of 9 proto-blobs with equal radius ($r_i = r_0$ for $i = 1 - 9$) leading to a value of $n = \infty$. The red area shows the liquid volume within the proto-blobs and the blue area represents the additional volume in the liquid borders between neighboring spheres. (b) A corrugated ligament with a total volume V_0 identical to the undisturbed ligament in (a) and a corrugation amplitude set $\{\xi_i/r_0\}_{i=1-9} = \{-0.2, 0.1, -0.3, 0.5, -0.5, -0.2, 0.4, 0.3, -0.1\}$. The growth of disturbances have rearranged some of the additional volume (blue in (a)) into the new set of proto-blobs. The resulting ligament has a value of $n = 9.6$ 211
- 4-9 (color online). (a) Schematics of the jet impact atomization test. The two identical nozzles face each other with an intersection angle $\theta \sim 80^\circ$. (b) and (c) Original hand drawings for a similar setup used for studying the atomization of Newtonian jets by G. Magnus [10] at different angles ($\theta \sim 60^\circ$ and $\theta \sim 90^\circ$ respectively). (d), (e) and (f) Visualization of the jet impact test for the Newtonian solvent $Oh = 0.02$ at different jet velocities corresponding to $We \equiv \rho V_j^2 D / \sigma = 1.5, 12.5$ and 150 respectively. The jets impact and form morphologies which resemble a "bay leaf", and a "fish-bone" at lower speeds and finally result in atomization forming filaments and droplets at higher speeds as shown in Fig. 4-9(f). 213
- 4-10 (color online). (a) Fragmentation after drop impact on a small target. Montage of images for (i) the Newtonian solvent and (ii) a polymer solution (PEO 300K). (b) Snapshots of the droplets captured after fragmentation by jet impact atomization for (i) the Newtonian solvent and (ii) viscoelastic solution. (c) Summary of the measured values of the dispersity $SMD/\langle d \rangle$ in three different fragmentation processes for both the Newtonian solvent (blue) and the viscoelastic solutions (red) compared with the theoretical prediction (solid line). 215

4-11 (color online). (a) Ligament size distributions in air-assisted atomization for the Newtonian solvent $\{Oh = 0.04, De = 0\}$ (\square) and the PEO-300K-0.1%wt. solution $\{Oh = 0.04, De = 1.3\}$ (\square). The solid black line shows the fit of a very narrow Gamma distribution with $n = 300$. (b) Ligament size distributions in drop-impact fragmentation (\triangle, \triangle) and the jet impact atomization tests (\diamond, \diamond) for the Newtonian solvent $\{De = 0\}$ (\triangle, \diamond) and the PEO-300K-0.1%wt. solution $\{De = 1.3\}$ (\triangle, \diamond). The black solid line shows a narrow Gamma distribution with $n = 600$. (c) Droplet size distributions in individual ligaments in the sudden stretch test (stretched ligaments in Fig. 4-7(c)) for the Newtonian solvent $\{Oh = 0.04, De = 0\}$ (\square) and the PEO-1000K-0.05%wt. solution $\{Oh = 0.04, De = 10.0\}$ (\circ). The solid blue and red lines are Gamma distributions with $n = 30$ and $n = 4$ respectively. The red cross symbols show the numerical calculation of the convolution integral between the fits for the droplet size distribution in a ligament (red solid line) and the fit for the measured ligament size distribution in the spray (black solid line in (a)). 218

5-1 (color online). Examples of rotary atomizers in the literature: (a) The "atomizer disc" or the "centripetal atomizer" which was studied by Peter Bär [43]. (b) The rotary atomizer used by Fraser *et al.* [44]. (c) Snapshot of the evenly-spaced ligaments that are formed around the rotating cup by Hinze and Milborn [45]. (d) Ligaments formation and breakup into a relatively mono-disperse cloud of droplets, captured by Fraser *et al.* [46] 223

5-2 (color online). Schematics of the visualization setup. A cup with diameter $D = 2R = 3.18$ cm, rotating at an angular speed ω , is supplied with liquid at a volumetric flow rate Q . Due to the centrifugal forces, the liquid is pushed to the rim of the cup and then disintegrates into smaller fragments. A high-speed camera (Phantom-Miro) is used to visualize the fragmentation event. 224

5-3 (color online). (a) and (b) Solidworks CAD drawings of the initial design for the rotary atomizer. (c) The final prototype. (d) The atomizer is fixed on a set of stands inside a transparent glass box that minimizes the spread of the generated mist but allows optical access for imaging purposes. 225

5-4 (color online). Silicone oil ($\nu = 100$ cSt) flows into the the rotating cup ($\omega = 62.8$ rad.s⁻¹) at a constant volumetric flow rate ($Q = 60$ ml/min). The liquid forms a thin torus-like film on the rim of the spinning cup which then, due to the centripetal acceleration, becomes unstable and forms a series of evenly-spaced continuously elongating ligaments. All ligaments form a similar spiral-like pattern. Capillary forces then make the individual Ligaments unstable and consequently break them into small droplets. 227

5-5 (color online). A visual guide showing the formation of single drops (a) ligaments (b) and fluid film (c) for silicone oil ($\nu = 50$ cSt) as the flow rate increases from (a) to (c). The cup is rotating at the same rate for the three images and the corresponding dimensionless groups $\Pi_1 \equiv \omega D \sqrt{\rho D / \sigma}$ and $\Pi_2 \equiv (Q/D) \sqrt{\rho / (\sigma D)} (\mu / \sqrt{\rho \sigma D})^{1/6}$ are: (a) $\{\Pi_1 = 1.95 \times 10^2, \Pi_2 = 1.64 \times 10^{-3}\}$, (b) $\{\Pi_1 = 1.95 \times 10^2, \Pi_2 = 1.64 \times 10^{-2}\}$ and (c) $\{\Pi_1 = 1.95 \times 10^2, \Pi_2 = 9.83 \times 10^{-2}\}$ 231

5-6 (color online). (a) The proposed dimensionless map of rotary atomization by Hinze and Milbourn [45]. Different lines outline the corresponding criteria that differentiate possible morphologies such as drop, ligament and film generation from each other. 232

- 5-7 (color online). Dependency of the average droplet size on different properties. The table, taken from Dombrowski and Liloyd [47], provides a summary of the empirical power law exponents that are suggested in the literature. Results from Hege [48], Oyama *et al.* [49], Kamiya and Kayano [50], Ryley [51] and Dombrowski and Liloyd [47] show approximate values for the corresponding exponents. 233
- 5-8 (color online). Measured values of the average droplet diameter for the ethanol-water (90%-10% wt.) mixture. Dependency of the average droplet diameter $\langle d \rangle$ on: (a) the rotation rate of the cup ω at a fixed value of volumetric flow rate $Q = 60\text{ml/min}$ and (b) the volumetric flow rate Q at a fixed rotation rate $\omega = 172.7\text{rad/s}$ 234
- 5-9 (color online). Silicone oil ($\nu = 100\text{ cSt}$) is delivered to the cup at a constant flow rate ($Q = 60\text{ml/min}$). Three snapshots show the number of formed ligaments at three different values of rotation rate: (a) $\omega = 62.8\text{ rad/s}$, $We \equiv \rho R^2 \omega^2 / \sigma = 100$, (b) $\omega = 94.2\text{ rad/s}$, $We \equiv \rho R^2 \omega^2 / \sigma = 225$ and (c) $\omega = 157\text{ rad/s}$, $We \equiv \rho R^2 \omega^2 / \sigma = 625$ 236
- 5-10 (color online). Number of ligaments N vs. the rotational Weber number $We \equiv \rho R^3 \omega^2 / \sigma$ plotted for three different silicone oils: (\square) $\{\nu = 7\text{ cSt}, Oh_R = 0.01\}$, (\circ) $\{\nu = 100\text{ cSt}, Oh_R = 0.14\}$, (\triangle) $\{\nu = 1000\text{ cSt}, Oh_R = 1.4\}$. The solid black line shows the predictions of the Rayleigh-Taylor instability analysis $N = (1/\sqrt{3})\sqrt{We}$ 237

- 5-11 (color online). A simple schematics for the geometry of the ligaments formed in rotary atomization. The black line shows the rotating cup. Individual fluid elements (\star) leave the rim of the cup, at different times, with a constant $V_0 = R\omega$ speed tangent to the cup and each follow a straight path-line (dashed gray lines) that is tangent to the circle at the corresponding point of departure. However, at the current time, the instantaneous positions of all different fluid elements (\circ) form a continuous spiral pattern (solid red line) that is known as the "*involute of a circle*". 239
- 5-12 (color online). A comparison between the theoretical prediction for the involute of a circle based on Equation (5.6) (blue circles) and the experimental profile of a single ligament observed in the rotary atomization of an industrially used viscous resin (Resin B). The cup rotation rate is $\omega = 125.6$ rad/s and the Resin B with a zero shear rate viscosity of $\eta_0 = 100$ mPa.s is pumped into the cup by a volumetric rate of $Q = 60$ ml/min. 240
- 5-13 (color online). (a) Schematics of the kinematics of a single fluid element. The constant velocity vector of the fluid element with magnitude $R\omega$ is projected on the radial and tangential directions and at every moment, based on the radial position r , the corresponding velocity components V_r and V_θ can be calculated. 241
- 5-14 (color online). Illustration of the continuous elongation of fluid elements as they distance from the cup and move to larger radial positions. The profile of each ligament is the involute of a circle and fluid elements, on the involute, continue to stretch along the local symmetry axis of the ligament. In order to conserve the volume of liquid in the element, the axial stretch leads to the gradual thinning of the ligament. Thus, the local thickness of each ligament decreases with r/R 242

- 5-15 (color online). Dimensionless plot of the radial (red) and tangential (green) components of the velocity as a function of r/R 243
- 5-16 (color online). Illustration of the idea of the *virtual cup* (dashed circle). Fluid elements with non-zero radial velocity ($V_r(r = R) = eR\omega$) at the rim of the real cup (a cup with radius R and rotation rate ω), shown by the solid circle, follow a trajectory that is identical to the elements leaving a virtual cup with modified radius $R' = R/\sqrt{1 + e^2}$ and modified rotation rate $\omega' = \omega(1 + e^2)$, shown by the dashed circle. 244
- 5-17 (color online). Theoretical predictions of the kinematics of the flow: (a) Dimensionless plot of the velocity components (red for V_r and green for V_θ) in the case of zero (solid lines for $e = V_r(0)/V_\theta(0) = 0$) and non-zero (dashed lines for $e = V_r(0)/V_\theta(0) = 0.3$) initial radial velocity. The profile for the tangential velocity is independent of e but the radial velocity is modified and with $0 < e$ the singularity of $\partial V_r/\partial r \rightarrow \infty$ is avoided. (b) Dimensionless profile of stretch rates for different values of e . The maximum stretch rate $\dot{\epsilon}_{max} = \omega/e$ occurs at the rim of the cup $r/R = 1$ 245
- 5-18 (color online). (a) Measured values of the ligament thickness at different radial positions (blue squares). The solid black line shows the prediction of the analytical model (Equation (5.11)). (b) The thickness profile for individual ligaments is measured from the snapshots that are taken by the high-speed camera. 247
- 5-19 (color online). Measured average diameters for all the Newtonian test liquids normalized by the cup diameter $\langle d \rangle/2R$ is plotted versus the suggested relevant dimensionless group $\Pi = \left(\frac{Q/R^2}{R\omega} \right) \left(\frac{\sigma/R}{\rho R^2 \omega^2} \right)$. The solid black line corresponds to the analytical prediction from Equation (5.14). 248

5-20 (color online). Rotary atomization for the Newtonian solvent (ethanol-water 90%-10% wt. mixture, $\eta = 1$ mPa.s, $Oh_R \equiv \eta/\sqrt{\rho R \sigma} = 1.45 \times 10^{-3}$) with the cup spinning at two different values of rotation rate: (a) Ligament formation regime at $\omega = 219.8$ rad/s, $We \equiv \rho R^3 \omega^2 / \sigma = 6442.8$. The image shows an overlay of two consecutive frames each $\Delta t = 0.4$ ms apart from each other. (b) Drop formation regime at $\omega = 78.5$ rad/s, $We \equiv \rho R^3 \omega^2 / \sigma = 821.8$. The image shows an overlay of sixteen consecutive frames each $\Delta t = 1$ ms apart from each other. (c) Corresponding droplet size distributions are plotted in magenta filled circles (\bullet) for the ligament formation regime (shown in (a)) and in open gray circles (\circ) for the drop formation regime (shown in (b)). 251

5-21 (color online). Droplet size distributions for the Newtonian solvents in rotary atomization (green filled circles \bullet) and the corresponding distribution in air-assisted atomization (blue open squared \square). The liquid atomized in the rotary test is the ethanol-water (90%-10% wt.) mixture ($Oh_R = 1.45 \times 10^{-3}$, $We = 13148.6$). The tested liquid in the air-assisted atomization is a water-glycerol (60%-40% wt.) mixture ($Oh_R = 4 \times 10^{-3}$, $We = \rho_{air} V_{air}^2 R / \sigma = 277$). 253

5-22 (color online). Formation of satellite droplets in the final stage of ligament breakup. The tested liquid is silicone oil ($\nu = 50$ cSt, $Oh_R = 7.3 \times 10^{-2}$) and it is delivered with a rate of $Q = 60$ ml/min into the cup that is rotating at $\omega = 125.6$ rad/s, $We = 2103.7$. (a) and (b): Two consecutive snapshots of the fragmentation with $\Delta t = 0.2$ ms between them. The viscous filament in the yellow box is clearly stretched before final pinch-off (see (a)) and after the pinch-off event the volume of the fluid in the filament retracts and forms one or two satellite droplets (see (b)). (c) An overlay of five consecutive frames, with $\Delta t = 0.2$ ms. It is clear to see that while the fragmentation process leads to a relatively mono-disperse group of *main* droplets, there also exists a considerable group of smaller *satellite* droplets. (c) Measured droplet size distributions for this case (blue bullets •) shows the appearance of two separate peaks which correspond to the size of the main and the satellite droplets in the fragmentation event. The black solid line is the sum of two separate Gamma distributions, Equation (5.15) with $a_s = 0.39$, $\langle d \rangle_s = 0.09$ mm, $n_s \simeq 17$, (the red line) and $a_m = 0.61$, $\langle d \rangle_m = 0.24$ mm, $n_m \simeq 33$ (the green line). . . . 254

5-23 (color online). Droplet size distributions for the rotary atomization of Newtonian test liquids: (a) Ethanol-water (90%-10%wt., $Oh_R = 1.45 \times 10^{-3}$) mixture; measured size distributions at four different rotation rates $\{We = 6442.8\}$ (▲), $\{We = 8415.1\}$ (▲), $\{We = 10650.3\}$ (▲) and $\{We = 13148.6\}$ (▲). (b) Silicone oil ($\nu = 7$ cSt, $Oh_R = 1.02 \times 10^{-2}$); measured size distributions at six different rotation rates $\{We = 3287.1\}$ (▶), $\{We = 4735.5\}$ (▶), $\{We = 6442.8\}$ (▶), $\{We = 8415.1\}$ (▶), $\{We = 10650.3\}$ (▶) and $\{We = 13148.6\}$ (▶). (c) Silicone oil ($\nu = 20$ cSt, $Oh_R = 2.90 \times 10^{-2}$); measured size distributions at five different rotation rates $\{We = 2103.8\}$ (■), $\{We = 4735.5\}$ (■), $\{We = 6442.8\}$ (■), $\{We = 8415.1\}$ (■) and $\{We = 10650.3\}$ (■). (d) Silicone oil ($\nu = 50$ cSt, $Oh_R = 7.25 \times 10^{-2}$); measured size distributions at seven different rotation rates $\{We = 1183.4\}$ (●), $\{We = 3287.1\}$ (●), $\{We = 4735.5\}$ (●), $\{We = 6442.8\}$ (●), $\{We = 8415.1\}$ (●), $\{We = 10650.3\}$ (●) and $\{We = 13148.6\}$ (●). For each Newtonian liquid, we can see that normalizing the droplet sizes with the size of the main droplet $\langle d \rangle_m$ shifts all the distributions to a single curve. Black solid lines are the corresponding fits, each of which is a summation of two Gamma distributions. Each distribution is a superposition of a Gamma fit around the satellite droplet size $\langle d \rangle_s$ (-.-) and another fit around the main droplet size $\langle d \rangle_m$ (- -). Fitting Equation (5.15) to the data, the following fit parameters are extracted: $\{\langle d \rangle_s / \langle d \rangle_m, a_s, n_s, a_m, n_m\} =$ (a) $\{0.76, 0.13, 12, 0.87, 18\}$, (b) $\{0.72, 0.06, 7, 0.94, 29\}$, (c) $\{0.58, 0.30, 15, 0.70, 60\}$ and (d) $\{0.38, 0.39, 17, 0.61, 33\}$ 257

5-24 (color online). Visualization of the fragmentation process with the cup rotating at $\omega = 251.2$ rad/s and the test liquids delivered at a rate of $Q = 60$ ml/min. Images show the rotary atomization for (a) the viscoelastic fluid (PEO 1M M_w , 0.01% wt. in the ethanol-water solvent) and (b) The ethanol-water solvent (90%-10% wt.). After the drops are formed on the ligaments, the connecting Newtonian filaments between the solvent drops breakup very fast. However, due to the enhanced elongational viscosity, the viscoelastic filaments stretch continuously and resist the pinch-off, leading to the formation of thinner stringy filaments. 259

5-25 (color online). Measured average diameters for the Newtonian solvent (■) and all the viscoelastic test liquids: PEO 300K M_w 0.01% wt. (○), PEO 300K M_w 0.05% wt. (◦) and PEO 1M M_w 0.01% wt. (▷). Results are normalized by the cup diameter $\langle d \rangle / 2R$ and plotted versus the suggested relevant dimensionless group $\Pi = \left(\frac{Q/R^2}{R\omega} \right) \left(\frac{\sigma/R}{\rho R^2 \omega^2} \right)$. The solid black line corresponds to the analytical prediction from Equation (5.14). 260

5-26 (color online). Dynamics of the viscoelastic filaments during the fragmentation process for the PEO 1M M_w 0.01% wt. solution ($Oh_R = 1.45 \times 10^{-3}$, $De_R = 5.0 \times 10^{-3}$). (a), (b) and (c) are taken with $\Delta t = 1$ ms spacing in time. As shown by the yellow box, two typical droplets are connected to each other by an elongated filament that resists the pinch off and finally transforms to a very thin cylindrical volume of fluid. (d) After the filament pinches off from the connecting drops, it forms few very small satellite droplets. (e) The corresponding size distribution are shown by red filled circles (\bullet) and are compared to the corresponding size distributions for the Newtonian solvent (\square). The solid lines are the fits of Gamma distributions. Each fit is a superposition of two Gamma distributions, one for the smaller sizes that are scattered around the satellite diameter $\langle d \rangle_s$ (-.-) and another for the larger sizes around the main droplet diameter $\langle d \rangle_m$ (- -), Equation (5.15). Parameters extracted from the fits are the following: $a_s = 0.13$, $\langle d \rangle_s = 0.21$ mm, $n_s \simeq 12$, $a_m = 0.87$, $\langle d \rangle_m = 0.27$ mm, $n_m \simeq 18$ for the Newtonian solvent and $a_s = 0.49$, $\langle d \rangle_s = 0.09$ mm, $n_s \simeq 4$, $a_m = 0.51$, $\langle d \rangle_m = 0.27$ mm, $n_m \simeq 40$ for the viscoelastic solution. 261

5-27 (color online). Droplet size distributions for the rotary atomization of viscoelastic liquids: (a) PEO 300K M_w 0.01% wt. solution ($Oh_R = 1.45 \times 10^{-3}$, $De_R = 0.4 \times 10^{-3}$); measured size distributions at four different rotation rates $\{We = 6442.8\}$ (\blacktriangledown), $\{We = 8415.1\}$ (\blacktriangledown), $\{We = 10650.3\}$ (\blacktriangledown) and $\{We = 13148.6\}$ (\blacktriangledown). (b) PEO 300K M_w 0.05% wt. solution ($Oh_R = 1.45 \times 10^{-3}$, $De_R = 0.6 \times 10^{-3}$); measured size distributions at five different rotation rates $\{We = 3977.4\}$ (\blacktriangleleft), $\{We = 4735.5\}$ (\blacktriangleleft), $\{We = 6442.8\}$ (\blacktriangleleft), $\{We = 8415.1\}$ (\blacktriangleleft), and $\{We = 10650.3\}$ (\blacktriangleleft). (c) PEO 1M M_w 0.01% wt. solution ($Oh_R = 1.45 \times 10^{-3}$, $De_R = 5.0 \times 10^{-3}$); measured size distributions at five different rotation rates $\{We = 7396.1\}$ (\bullet), $\{We = 8415.1\}$ (\bullet), $\{We = 9499.9\}$ (\bullet), $\{We = 11866.6\}$ (\bullet) and $\{We = 13148.6\}$ (\bullet). Black solid lines are the corresponding fits, each of which is a summation of two Gamma distributions. Each distribution is a superposition of a Gamma fit around the satellite droplet size $\langle d \rangle_s$ (- -) and another fit around the main droplet size $\langle d \rangle_m$ (- -). Fitting Equation (5.15) to the data, the following fit parameters are extracted: $\{\langle d \rangle_s / \langle d \rangle_m, a_s, n_s, a_m, n_m\} =$ (a) $\{0.70, 0.13, 12, 0.87, 18\}$, (b) $\{0.67, 0.39, 11, 0.61, 42\}$ and (c) $\{0.34, 0.49, 4, 0.51, 40\}$. (d) A comparison between the size distributions of different viscoelastic liquids atomized at a fixed rotation rate $\{We = 8415.1\}$: PEO 300K M_w 0.01% wt. (\blacktriangledown), PEO 300K M_w 0.05% wt. (\blacktriangleleft) and PEO 1M M_w 0.01% wt. (\bullet). The solid black line is the fit for the size distributions of the Newtonian solvent (Figure 5-22(a)). 264

5-28 (color online). Size ratio of the main droplet to the satellite droplet: the x-axis shows the local Ohnesorge number of the filament $Oh_\xi = \eta / \sqrt{\rho \xi_c \sigma}$ for different Newtonian test liquids (\square) and the local Deborah number $De_\xi = \tau_E / 3 \sqrt{\rho \xi_c^3 / \sigma}$ for three viscoelastic fluids (\bullet). The value of ξ is chosen based on the measured values of average droplet diameters ($\xi_c \simeq 66 \mu\text{m}$). The solid black line is the prediction of the model, described in Equation (5.17). 266

6-1 (color online). Oscillatory shear and elongational rheology of Resin A. (a) Small amplitude oscillatory shear (SAOS) rheology. Solid lines are fits of the Oldroyd-B model (Equation 6.1). (b) Diameter evolution in time in several CaBER test. (c) A mechanical representation of the Oldroyd-B model. (d) High-speed visualization of the filament breaking up in the CaBER device. 271

6-2 (color online). (a) Small amplitude oscillatory shear (SAOS) rheology for Resin B. Solid lines are fits of the single mode Maxwell model. (b) and (c) Cryo-TEM images of Resin B. 273

6-3 (color online). Structure of casein gel. Environmental SEM image of the 4%-1% casein-GDL gel. 275

6-4 (color online). Linear rheology of the 4%-1% casein-GDL gel: (a) Small amplitude oscillatory shear (SAOS) rheology. (b) Stress relaxation after a linear step strain test. Solid lines are fits from the fractional model (Equation (6.4)). 276

6-5 (color online). Linear rheology for three different casein gels: SAOS for (a) The 4%-1% casein-GDL gel. (b) The 8%-2% casein-GDL gel. (c) The 12%-3% casein-GDL gel. (d) Stress relaxation for all three gels after applying a linear step in strain. 278

6-6 (color online). Dependency of (a) the power law exponent α and (b) the quasi-property \mathbb{V} on the weight concentration of casein protein (at a fixed 4-1 casein to GDL concentration ratio). 279

6-7 (color online). Linear rheology for four different casein gels: SAOS for (a) The 4%-1% casein-GDL gel. (b) The 4%-2.5% casein-GDL gel. (c) The 4%-3% casein-GDL gel. (d) The 4%-4% casein-GDL gel. 281

6-8 (color online). Dependency of (a) the power law exponent α and (b) the quasi-property \mathbb{V} on the weight concentration of the acidifying agent GDL (at a fixed 4% wt. casein concentration). 281

7-1 (color online) Linear viscoelastic moduli G' (upper, filled symbols) and G'' (lower, hollow symbols) as a function of pulsation ω for a strain amplitude of $\gamma = 0.01$. The symbols \bullet and \blacktriangle respectively correspond to the 4% wt. and 8% wt. casein gels. Dashed and continuous lines correspond to the best fit of the data with the spring-pot model. 286

7-2 (color online) Nonlinear relaxation function $G(\gamma_0, t) = \sigma(t)/\gamma_0$ vs time t determined by step strain tests, each one performed on a freshly prepared 4% wt. casein gel. Colors from blue to red represent strain values ranging from $\gamma_0 = 0.002$ to $\gamma_0 = 5$. The black line is the best power-law fit of the data in the linear region ($\gamma_0 \leq 0.01$). Inset: Stress relaxation exponent α extracted from the power-law fit of the data shown in the main graph with the same color code. The horizontal line is the average exponent $\alpha = 0.18 \pm 0.01$ 287

7-3 (color online) Strain damping function $h(\gamma_0)$ of a 4% wt. casein gel as defined in the text. Same color code as in Fig. 7-2. The solid black line is the best fit function by power series in γ_0^2 as proposed in [52] which captures the stiffening behavior, but does not account for the softening part of the gel response at strains larger than 50%. The red continuous line is the best fit function $\tilde{h}(\gamma)$ of the data (see text). Inset: same data plotted in semilogarithmic scales. 288

- 7-4 (color online) (a) Stress response σ vs time t (lower axis) and vs strain $\gamma = \dot{\gamma}_0 t$ (upper axis) of a 4% wt. casein gel to a constant shear rate $\dot{\gamma}_0 = 10^{-3} \text{ s}^{-1}$ initiated at $t = 0$. The gray dashed line corresponds to linear viscoelastic response [Eq. (7.2)]. The black line corresponds to the K-BKZ equation constructed using only the strain-hardening part of the damping function, $h^*(\gamma_0)$ and reported as the solid black line in Fig. 7-3. The continuous red line corresponds to the K-BKZ equation built upon \tilde{h} , which includes both the hardening and the softening component of the damping function. Lower inset: same data on semilogarithmic scales. Upper inset: sketch and images of the side view of Couette cell at different strains recorded simultaneously to the experiment reported in the main graph. 291
- 7-5 (color online) (b) Stress responses to individual constant shear rate experiments ranging from 10^{-3} s^{-1} to 0.6 s^{-1} . Dashed lines indicate the linear response [Eq. (7.2)], and the continuous lines correspond to the K-BKZ predictions using \tilde{h} [Eq. (7.3)]. (c) Normalized stress responses $(1 - \alpha)\Gamma(1 - \alpha)\sigma(t)/\mathbb{V}\dot{\gamma}_0^\alpha$ vs strain γ for all constant shear rate experiments. 292
- 7-6 (color online) Normalized stress responses $(1 - \alpha)\Gamma(1 - \alpha)\sigma(t)/\mathbb{V}\dot{\gamma}_0^\alpha$ vs strain $\gamma = \dot{\gamma}_0 t$ in the start up of steady shear flow experiments for shear rates ranging from 0.006 s^{-1} to 3 s^{-1} for a 8% wt. casein gel. The dashed gray line corresponds to the linear response (Eqn. 2 in the main text) while the red solid line stands for the K-BKZ prediction constructed from the power-law linear viscoelastic response plus the nonlinear damping function \tilde{h} determined independently from step strain experiment (see main text). Inset: non-normalized stress responses for a subset of shear start-up experiments shown in the main graph. 294

7-7 (color online) Critical stress σ_c vs applied shear rate $\dot{\gamma}_0$ for both a 4% (o) and a 8% (□) casein gel. In both graphs, the dashed and continuous lines stand for the prediction issued from the combination of the Bailey criterion and the stress response computed either from just the linear response (dashed lines) or the full K-BKZ equation built upon h^* (solid lines). 295

7-8 (color online) Critical strain γ_c vs applied shear rate $\dot{\gamma}_0$ for both a 4% (o) and a 8% (□) casein gel. In both graphs, the dashed and continuous lines stand for the prediction issued from the combination of the Bailey criterion and the stress response computed either from just the linear response (dashed lines) or the full K-BKZ equation built upon h^* (solid lines). 296

7-9 (color online) Failure time τ_f as a function of the constant stress σ_0 applied during creep experiments. The solid line is the best power-law fit $\tau_f = A\sigma^{-\beta}$, with $A = (5.0 \pm 0.1) \times 10^{18} \text{ s.Pa}^\beta$ and $\beta = 6.4 \pm 0.1$ for the 8% wt. gel. 297

List of Tables

- 2.1 Properties of the viscoelastic test fluids. Different concentrations of poly (ethylene Oxide) (PEO) at three different molecular weights were dissolved in the Newtonian solvent (60-40% wt. Water+Glycerol $\eta_s = 3.0mPa.s$). Definitions of the Deborah number (De), Ohnesorge number (Oh), Elasticity number (El) and Elasto-capillary number (Ec) that can be spanned by the fluids are described in the text. . . . 105
- 2.2 Rheological properties of the viscoelastic spray test fluids. Two different concentrations of Poly(ethylene oxide) (PEO) at two different molecular weights were dissolved in the Newtonian solvent (Water+Glycerol 60-40 wt.%) which has a viscosity $\eta_s = 3.2mPa.s$. The dimensionless parameters Oh and De are defined in the text (see Eqs. (8) and (9)) and are evaluated using $\rho = 1103kg/m^3$ and $R_l = 85\mu m$. All the measurements were performed at $25^\circ C$ 106
- 2.3 Rheological properties of the viscoelastic fluids tested in Figures 2-3 and 2-4. Two different concentrations of Poly(ethylene oxide) (PEO) at two different molecular weights were dissolved in the Newtonian solvents (water for the 5000K PEO solution and Water+Glycerol 60-40 wt.% for the 2000K solution). The dimensionless parameters Oh and De are defined in the text (see Eqs. (8) and (9)) and are evaluated using $\rho = 1103kg/m^3$ and $R_0 = 3mm$. All the measurements were performed at $25^\circ C$ 106

3.1	Rheological properties of the viscoelastic spray test fluids. Two different concentrations of Poly(ethylene oxide) (PEO) at two different molecular weights were dissolved in the Newtonian solvent (Water+Glycerol 60-40 wt.%) which has a viscosity $\eta_s = 3.2\text{mPa}\cdot\text{s}$. The dimensionless parameters Oh and De are defined in chapter 2 and are evaluated using $\rho = 1103\text{kg}/\text{m}^3$ and $R_l = 85\mu\text{m}$. All the measurements were performed at 25°C	178
4.1	Properties of the viscoelastic test fluids. Two different concentrations of poly (ethylene oxide), (PEO) at two different molecular weights were dissolved in the Newtonian solvent (Water+Glycerol 60-40% wt.)	199
5.1	Properties of the Newtonian test fluids. Five different silicone oils (S.O.) with different viscosities ($\nu = 7, 20, 50, 100$ and 1000 cSt) were used in our tests. An ethanol-water mixture (90-10% wt. $\eta_s = 1.0$ mPa.s) was also prepared to be used as a Newtonian solvent. Definitions of the Ohnesorge number (Oh_R) is described in the text.	228
5.2	Properties of the viscoelastic test fluids. Three different dilute polymer solutions were then prepared by dissolving small amounts of PEO (Poly(ethylene oxide)) in the Newtonian solvent (ethanol-water mixture). Definitions of the Deborah number (De_R), and Ohnesorge number (Oh_R), are described in the text.	229

Chapter 1

Introduction

“The snake which cannot cast its skin has to die. As well the minds which are prevented from changing their opinions; they cease to be mind.”

Friedrich Nietzsche

1.1 Outline of the thesis

The fragmentation of viscoelastic liquids and fracture of soft solids is of great importance for many crucial daily application. The question to address for many of these processes is what affects the failure/disintegration of soft gels and viscoelastic liquids. To answer this question, in this thesis, we study the linear and nonlinear rheology of two classes of complex fluids. The rheological behavior of both dilute viscoelastic solutions and soft gels are studied in linear and nonlinear deformations leading to either fracture or fragmentation. Figure 1-1 shows a graphic overview of the work in the current thesis. The dimensionless ratio of the fracture energy divided by the surface energy varies from very small values for the Newtonian liquids to high values for elastic solids. Fracture energy is the energy required to break primary/chemical bonds within the material. The surface energy on the other hand is a measure of the strength for the secondary bonds (hydrogen bonds or van der Waals forces). Most of the old and recent literature have focused on the two end of this spectrum (fragmentation of Newtonian liquids or fracture

of Hookean elastic solids). The paucity of knowledge about the materials that lie in the space between these two limits is the motivation behind our study. Dilute viscoelastic liquids can go to high deformations, but when deformed at high shear rates the inertia of the liquid can overcome the capillary forces and fragmentation can happen. On the other hand soft gels can exhibit brittle like fracture at finite strains. To explore these processes we require to understand the linear and nonlinear rheology of these materials.

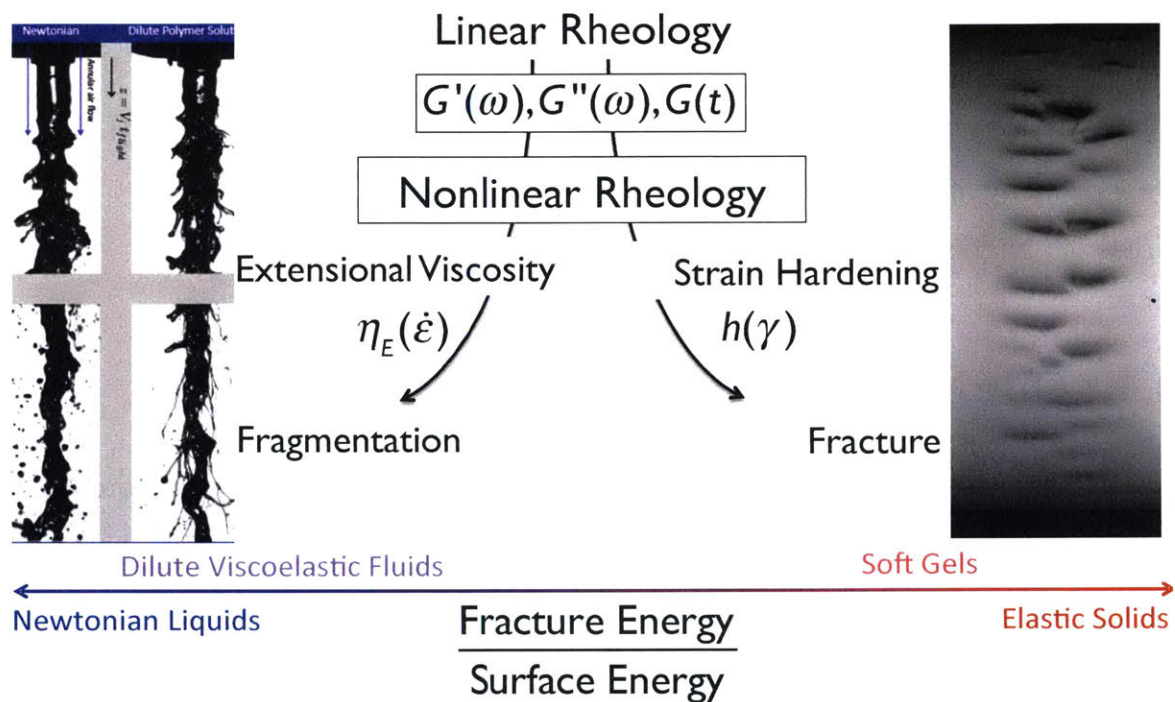


Figure 1-1: (color online). A graphic introduction to this thesis.

Applying any deformation $\gamma(t)$ to any material leads to a mechanical response which can be described as a stress $\Sigma(t)$. In order to understand the characteristics of the materials in the linear region of deformations ($\gamma(t) \leq \gamma_{linear}$), we can transfer their mechanical response $\sigma(t)$ from the time domain into the frequency domain and find about the elastic $G'(\omega) = \bar{\Sigma}(\omega)/\bar{\gamma}(\omega)$ and viscous nature of the material. This, very similar to other examples of system identification for linear systems, is equivalent to finding the elastic response of the material in the time

domain ($G(t) = \Sigma(t)/\gamma_0$) after a step function in strain $\gamma(t) = H(t)\gamma_0$, where $H(t)$ is a Heaviside step function.

Despite being very useful, characterization of materials in linear region of deformations is not enough to understand their response in extreme nonlinear deformations. Massachusetts Institute of Technology has a long history of interest in the topic of nonlinear system/material identification thanks to the great efforts of figures such as Norbert Wiener in the mathematic department [53]. We try to focus in our thesis on the experimental challenges faced in the nonlinear rheology of different soft/viscoelastic solids/liquids. Behavior of soft solid in the nonlinear region of deformation, captured by the damping/stiffening function $h(\gamma)$, or the dilute viscoelastic solutions in the region of high deformation rates, characterized by their extensional viscosity $\eta_E(\dot{\epsilon})$, can be markedly different from their corresponding trends in Hookean elastic solids and Newtonian fluids respectively. We attempt to understand these concepts, address the experimental challenges in measuring the mentioned properties and show their important effect on processes such as fragmentations or fracture. Here we provide a brief outline for different chapters of this thesis:

Chapter 1 provides an introduction to the phenomena of fragmentation and fracture for complex liquids and soft gels. A brief literature review on the subject and related topics is presented in this chapter.

Chapter 2 covers all the details related to different instruments and materials that are used in our experiments. Moreover, we provide a detailed introduction to our extensional viscosity measurements by comparing the rheological measurements from two different classes of instruments. We also compare our measurements with established models and theories in the field. A dimensionless nomogram is offered as a practical guide for comparison between the performance of different instruments.

Chapter 3 focuses on the study of air-assisted atomization for dilute viscoelastic solutions. We provide a simple toy model to understand the dynamics of ligament

formation in this process. Our analysis leads to a theoretical prediction for the dependence of the average droplet sizes on the measured fluid relaxation times. We then compare our model predictions with the experimental measurements on a series of model dilute polymer solutions.

In Chapter 4, we look at the size distributions for fragmentation of viscoelastic liquids. We study three different atomization geometries and look at the final droplet size distributions in all these canonical examples of ligament mediated fragmentation. Our results show an interesting universal behavior in size distributions for viscoelastic drops. We show that the *fragmentation/coalescence* scenario, that has already been introduced in the literature for Newtonian liquids, is also the right framework for studying the fragmentation of dilute viscoelastic solutions. All the measured size distributions for the viscoelastic fluids follow Gamma distributions with an index $n = 4$. We also provide a mathematical proof to show that this limit is triggered by the elongational resistance of viscoelastic fluids and is a geometrical limit for ligament-mediated fragmentation.

Chapter 5 studies the fragmentation of Newtonian and viscoelastic liquids in rotary atomization. In this process, at the rim of a spinning cup, the centripetal acceleration destabilizes the liquid torus that forms due to the Rayleigh-Taylor instability. The resulting ligaments leave the liquid torus with a remarkably repeatable spacing that scales linearly with the inverse of the rotation rate. Filaments then follow a well-defined geometrical path-line that is described by the involute of the circle. A theoretical form is derived for the spatial variation of the filament deformation rate. We couple these derivations with the known properties of Newtonian and viscoelastic liquids to provide a physical analysis for this fragmentation process that is compared in detail with our experiments.

Chapter 6 provides a brief introduction to the linear rheology of casein gels. These soft gels are selected as a family of model soft solids and we show that their linear rheological response follows a power law dependence with time or frequency. We show that this soft glassy behavior can be modeled by a simple *fractional* viscoelastic model and we connect the model parameters to the physical structure of these

protein gels.

In Chapter 7, we show that upon external deformation, these soft viscoelastic gels exhibit a generic nonlinear mechanical response characterized by pronounced stress- or strain-stiffening prior to irreversible damage and failure, most often through macroscopic fractures. Here we show that the nonlinear viscoelastic properties of the gel can be described in terms of a *damping function* which in conjunction with the linear viscoelastic relaxation kernel predicts the gel mechanical response quantitatively up to the onset of macroscopic failure. Using a nonlinear integral constitutive equation built upon the experimentally-measured damping function in conjunction with power-law linear viscoelastic response, we derive the form of the stress growth in the gel following the start up of steady shear. We also couple the shear stress response with Bailey's durability criteria for brittle solids in order to predict the critical values of the stress σ_c and strain γ_c for failure of the gel, and how they scale with the applied shear rate. This provides a generalized failure criterion for biopolymer gels that is applicable for a range of different deformation histories.

Chapter 8 covers a brief description of the general conclusions from this study.

1.1.1 Publications from this study

[1] Keshavarz, B., Houze, E.C., Moore, J. R., Koerner, M. R., McKinley, G.H. Ligament-Mediated Fragmentation of Viscoelastic Liquids, Phys Rev. Lett. accepted, in press 2016.

[2] Keshavarz, B., Sharma, V., Houze, E.C., Koerner, M.R., Moore, J.R., Cotts, P.M., Threlfall-Holmes, P. and McKinley, G.H., 2015. Studying the effects of elongational properties on atomization of weakly viscoelastic solutions using Rayleigh Ohnesorge Jetting Extensional Rheometry (ROJER). Journal of Non-Newtonian Fluid Mechanics, 222, pp.171-189.

[3] Keshavarz, B. and McKinley, G.H., 2016. Micro-scale extensional rheometry using hyperbolic converging/diverging channels and jet breakup. *Biomicrofluidics*, 10(4), p.043502.

[4] Keshavarz, Bavand, et al. "Nonlinear viscoelasticity and generalized failure criterion for polymer gels." *ACS Macro Letters* 6.7 (2017): 663-667.

[5] B. Keshavarz, T. Divoux, S. Manneville, and G. H. Mckinley, "Connecting linear fractional rheology to the structure properties of the gel network for a class of biopolymer gels" in preparation for *Nature Materials*, 2016.

[6] Keshavarz, B., Houze, E.C., Moore, J. R., Koerner, M. R., McKinley, G.H. Fragmentation of Newtonian and viscoelastic liquids in rotary atomization , in preparation for *Phys. Rev. Fluid*. 2016.

1.1.2 Related publications from the author

[7] Eral, H. B*, Safai, E. R*, Keshavarz, B*, Kim, J. J., Lee, J., and Doyle, P. S. (2016). Governing principles of alginate microparticle synthesis with centrifugal forces. *Langmuir*, 32(28), 7198-7209. (*: shared first authorship).

[8] Comtet, J., Keshavarz, B., and Bush, J. W. (2016). Drop impact and capture on a thin flexible fiber. *Soft Matter*, 12(1), 149-156.

[9] Sharma, V., Haward, S.J., Serdy, J., Keshavarz, B., Soderlund, A., Threlfall-Holmes, P. and McKinley, G.H., 2015. The rheology of aqueous solutions of ethyl hydroxy-ethyl cellulose (EHEC) and its hydrophobically modified analogue (hmEHEC): extensional flow response in capillary break-up, jetting (ROJER) and in a cross-slot extensional rheometer. *Soft Matter*, 11(16), pp.3251-3270.

[10] Geri, M., Keshavarz, B., McKinley, G. and Bush J., 2017. Thermal delay of drop coalescence. Submitted to Journal of Fluid Mechanics.

1.2 Literature Review

Fragmentation/disintegration of liquids/solids is an important aspect of many industrial and biological processes [13]. Liquids in particular are atomized/disintegrated into fragments in a variety of different phenomena. Some typical examples are shown in Figure 1-2. The breakup of a single jet into droplets as a result of capillary action can happen in either a jet of a human urine [1] or a jet of ink emerging from an inkjet nozzle. In some other examples such as human sneeze [2] or air-assisted atomization [54] the inertia of a surrounding stream of air destabilizes the liquid and leads to its fragmentation. In many of these examples the liquid of interest can contain suspended materials such as polymers or particles that can affect the disintegration process by increasing the extensional resistance of the liquid in elongational flows. Mucin proteins in human saliva, industrial thickeners in inks or paints and anti-misting polymer agents in fuels are among many synthetic or biological macromolecules that can act as an elastic structure within their corresponding Newtonian solvents, that resists against elongation. One topic of great interest for understanding and quantifying the fragmentation of all of these fluids is studying the final droplet sizes and their corresponding distribution. Specifically, it is crucial to understand how the underlying material properties for different liquids such as viscosity, surface tension, or fluid viscoelasticity can affect the final size distributions. From a scientific point of view the connection between the underlying properties and the resulting fragmentation performance has been a source of both amusement and curiosity for great scientists [13] such as Lavoisier [55] and Born [56]. At the same time, in terms of applications, benefiting from the acquired knowledge, can help us devise creative and novel methods of fragmentation [57].

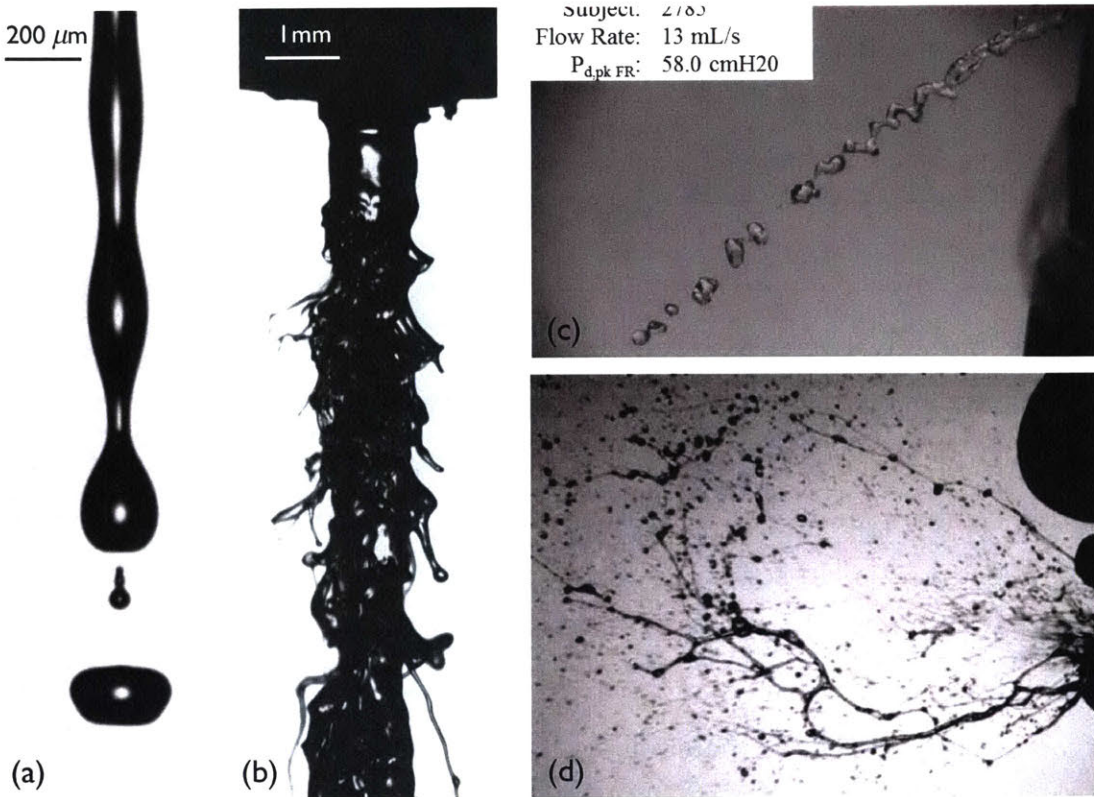


Figure 1-2: (a) Breakup of a $175\mu\text{m}$ diameter Newtonian jet. Similar phenomena is used in continuous inkjetting or CIJ. (b) Air-assisted atomization of a viscoelastic solution (PEO-300K-0.01% wt. in a water-glycerol solvent). (c) A snapshot of a human subject urinating [1]. (d) A snapshot of a human subject sneezing [2]. Image courtesy of Lydia Bourouiba.

Another important example of fragmentation, found in both industrial and natural phenomena, is rotary atomization. Figure 1-3 shows examples in industries such as metallurgy and automobile paint coating in which the liquid is discharged into a spinning cup and finally atomized into a set of tiny droplets as a result of centripetal acceleration. The same mechanism is used in nature by mammals such as tigers and dogs when they “shake” their wet fur and atomize the liquid into a fine mist of droplets that fly away on spiral-like trajectories. A close look at the image in Figures 1-3 (a) and 1-3 (b) shows that the water atomizes relatively well into a fine mist of droplets but the saliva (which contains dissolved mucins) of the animal forms a long elongated filament and shows a significantly different perfor-

mance in this type of atomization.

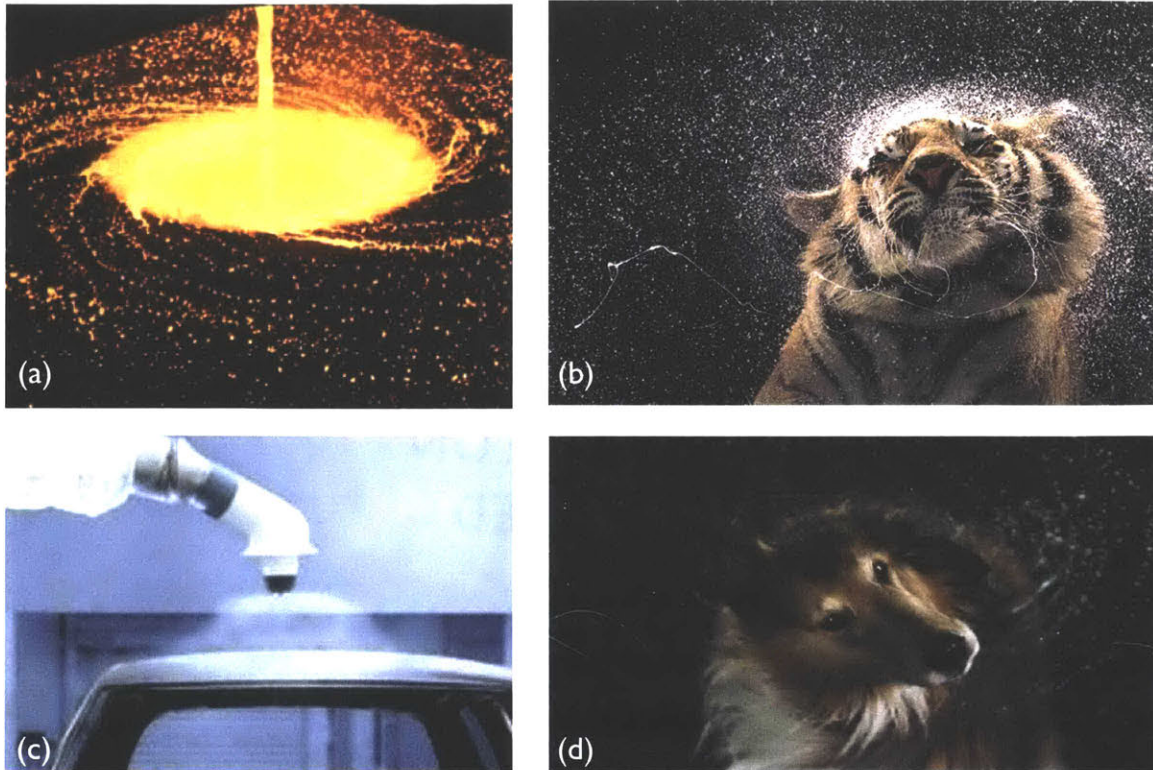


Figure 1-3: (color online). Examples of rotary atomization in (a) metallurgy: a molten metal jet is discharged onto a rotating disc and the centripetal forces atomize the melt into a set of relatively mono-disperse beads [3]. (b) Kanja the tiger shaking off water and drool from its fur. Image courtesy: Kanja Shaking Poster – Tim Flach Wildlife Poster. (c) Rotary/bell atomization cup, installed on a 6 degree of freedom robot arm, spinning at high rotation speeds ($\sim 70,000\text{RPM}$) and delivering a fine mist of paint droplets to the automobile surface. (d) A wet dog shaking water off its fur. The spiral shape of water filaments on the right side of the image is a particularly interesting aspect of rotary fragmentation. Image courtesy: Carli Davidson [4].

The polymeric microstructural constituents in biological fluids such as saliva or mucus can dramatically inhibit atomization. This is also a known challenge in many industrial coating applications in which synthetic polymers are added as thickeners. The paint and inkjet industries in particular face many challenges in atomization or breakup of these structured fluids [58, 59]. While these dissolved polymers help the material stick better to the substrate, they can also inhibit the fragmentation process. Even in the advertisement industry, artists are qualitatively

aware of this phenomena. Figure 1-4 shows snapshots of milk and paint splashed on models' bodies. A close look at the milk droplets and comparing them to the elongated and corrugated paint ligaments is enough to show the enhanced resistance of polymeric fluids, such as paints, in the fragmentation process. Also it is clear from the profile of the filaments, that in these liquids ligaments have a more extended/corrugated geometry compared to the Newtonian case. [60].

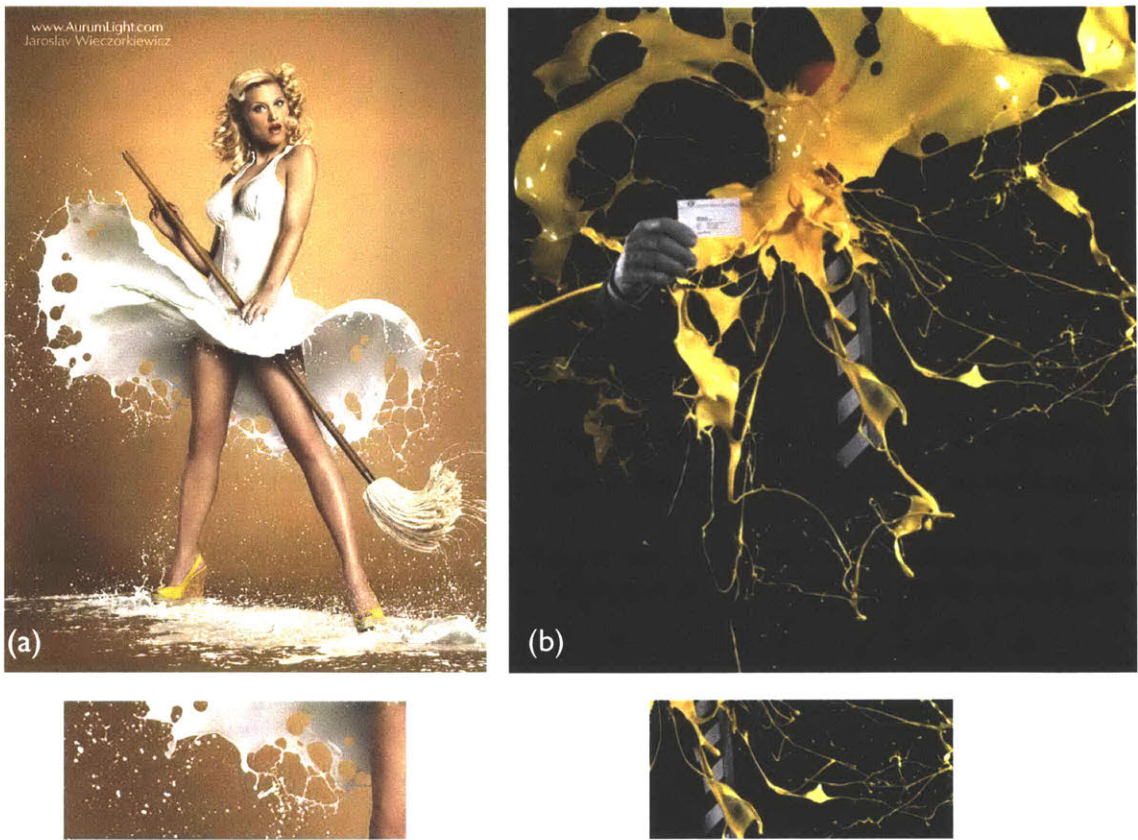


Figure 1-4: (color online). Fragmentation of liquids in the advertisement industry: (a) A female model posing for a calendar entry with a "milk" dress made out of multiple events of milk fragmentation. Image courtesy: Jaroslav Wiczorkiewicz. <http://aurumlight.com/>. (b) Splash of viscoelastic paint on the body of a male model. Image courtesy: DieDruckerei.de - Splash 3D (Theatrical Version) <https://vimeo.com/22934779>

In this thesis we aim to understand the origins and consequences of this behavior for a family of model viscoelastic liquids. We quantitatively measure the elongational properties of these liquids through a set of precise experimental mea-

surements that are performed by an affabrous jet breakup rheometer. We also connect the measured liquid properties to important parameters in the fragmentation process such as the average droplet size and the breadth of the measured size distributions.

1.2.1 Fragmentation of Newtonian liquids

Fragmentation of liquids in natural phenomena has been a source of scientific curiosity from ancient [61] to modern times [13, 62, 63]. However, precise quantitative measurements of the resulting droplet size distributions has been a missing element. Wilson Bentley (1865-1931) was a self taught scientist/farmer from Jericho in Vermont USA who is known for his seminal photography work on ice crystals in snow flakes. He also devised a rather ingenious setup for determining droplet size measurement during rainfall which consisted of flour and a screen made of silk tights ! [64].

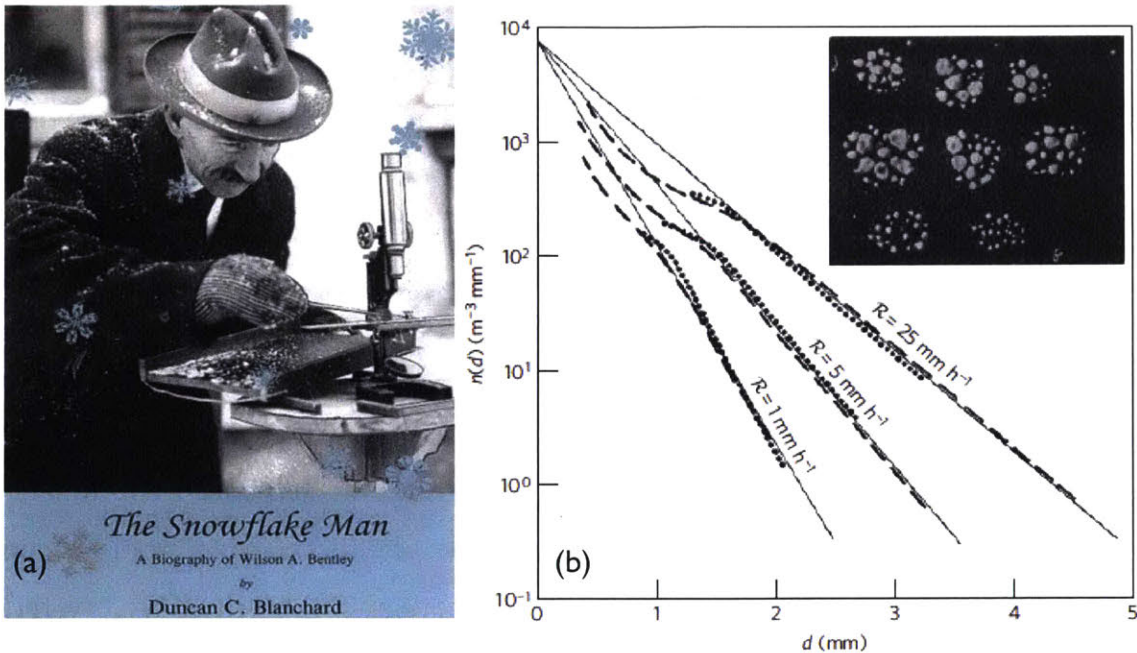


Figure 1-5: (color online). (a) Wilson Bentley (1865-1931) studying the shape of ice crystals [5]. (b) Size distributions of raindrops gathered by Marschall and Palmer [6]. Inset: Image of flour beads formed after impact of raindrops on a bed of flour spread on a screen made of silk tights. This creative method was used by Bentley [7] years before the advent of high speed photography.

Using this method, researchers interested in climate science and meteorology started measuring droplet size distributions in different rain events years before the advent of high-speed photography.

Figure 1-5(b) shows a plot of measured size distributions in different rainfall events from samples gathered by Marschall and Palmer [6]. One can easily notice that for all three set of measurements the droplet size distributions has an exponential behavior at large sizes. In order to understand the nature of the observed size distributions, and to be able to mathematically describe them, we will next provide a brief review on the fragmentation models that are available in the literature. Figure 1-6 shows a pictorial guide to some of the pioneering works in this area. Early, and rather qualitative, observations of symmetry in drop impact patterns by Da Vinci (Figure 1-6(a)), magnificent drawings of atomizing liquid sheets and bells by Savart [9] and Magnus [10] and more recently theories of fragmentation by Kol-

mogorov [65], have all attempted to provide a physical and mathematical model for the process of liquid disintegration.

Giants on Tiny Fragments

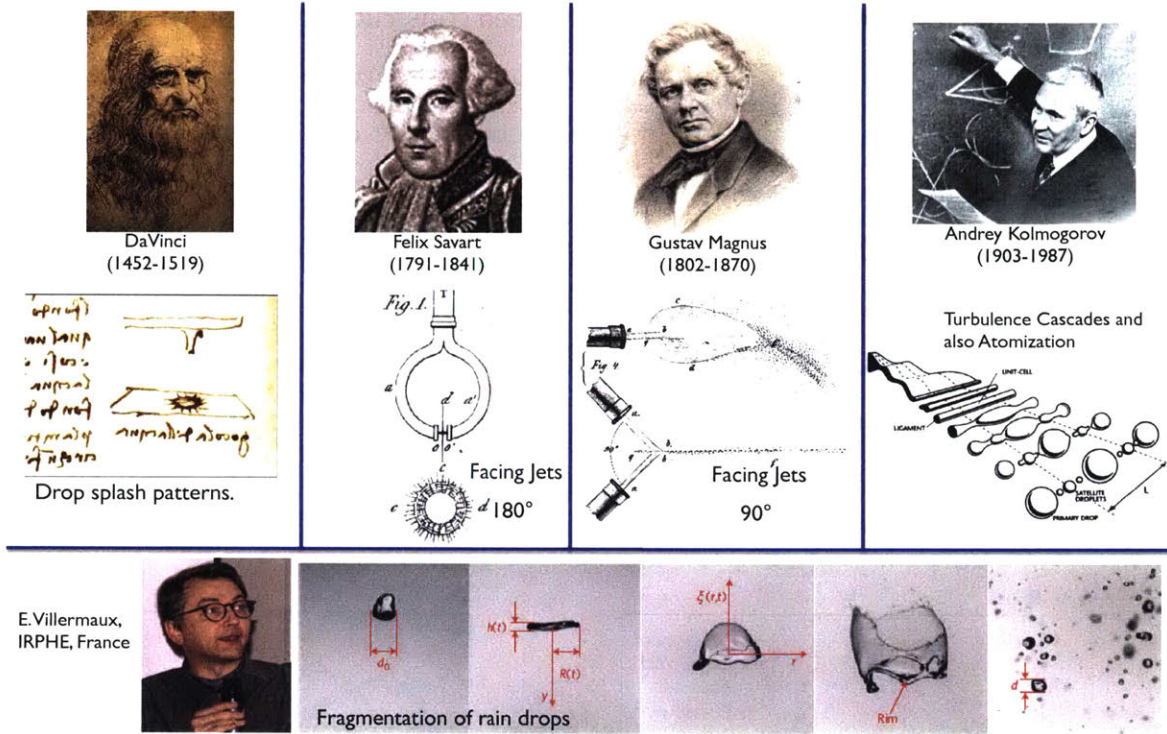


Figure 1-6: (color online). Great scientists studying different aspects of fluid fragmentation through history [8, 9, 10, 11].

The first mathematical model, offered by Kolmogorov [65] in the context of solid fragmentation, relies on considering the fragmentation as a sequence of brittle fracture events in which, for each event, an initial volume will be divided into two new pieces. The volume/mass of each new piece is equal to a random fraction of the original volume. Thus, the size of a fragment after many fracture events will be the multiplication of many random multipliers and consequently the logarithm of the final sizes will be the sum of many random numbers. This indicates a log-normal distribution for the fragment sizes. Despite being relevant to some cases of solid fragmentation, the suggested model by Kolmogorov have been applied rather blindly to the process of liquid fragmentation.

The most recent mathematical model describing different aspects of liquid fragmentation is introduced by Villermaux and coworkers in an extensive series of related studies [66, 67, 13, 11, 8, 62, 68, 69]. The proposed *fragmentation/coalescence* model suggests that liquid fragmentation can be seen as an inverse aggregation process and the dynamics of coalescence between constructing element during the fragmentation plays an important role. Assuming droplet sizes $d_{i=1-N}$ have an average value $\langle d \rangle$ and normalizing the droplet sizes by defining $x \equiv d/\langle d \rangle$, they show that the final droplet sizes follow a Gamma distribution $p(x) = \Gamma(n, x) = (n^n/\Gamma(n))x^{n-1}e^{-nx}$ with an index n that sets the breadth of the distribution [13]. As shown in Figure 1-7, Villermaux [13] demonstrates that the proposed Gamma distribution describes the measurements with better accuracy when compared to the corresponding fits from the older models such as the cascade theory (lognormal distribution) or the maximum entropy (Poisson distribution).

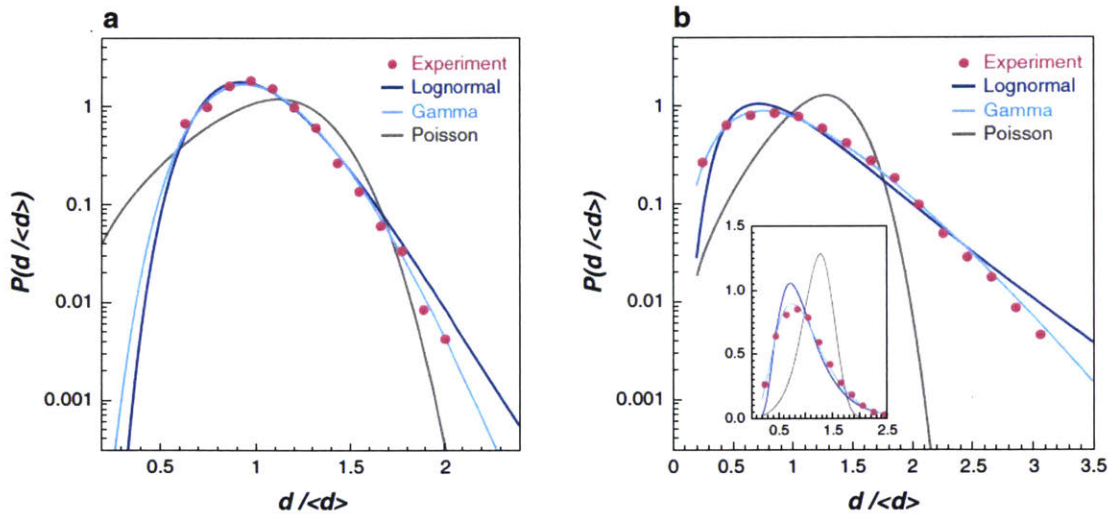


Figure 1-7: (color online). Different droplet size distributions from studies on liquid sheets by Bremond and Villermaux [12] fitted by different models. (a) A narrow size distribution fitted by lognormal, Gamma and Poisson distributions. The order for the Gamma distribution is $n = 17$. (b) A wider size distribution fitted by lognormal, Gamma and Poisson distributions. The order for the Gamma distribution is $n = 4$. Images are taken from [13].

Villermaux showed that the new idea of fragmentation through coalescence can

explain the exponential tails observed by Marschall and Palmer (Figure 1-8(b)). Furthermore, he noticed that the breadth of these size distributions, the index of the Gamma distributions, is determined by the level of geometrical corrugations on the profile of the initial ligaments. This is an example of how far Newtonian fluid fragmentation has come over in the last decades. We want to make similar advances for non-Newtonian liquids and improve our fundamental knowledge about the fragmentation process for these fluids.

1.2.2 Fragmentation of Viscoelastic Liquids

Despite recent developments on the dynamics of Newtonian fluids in fragmentation, there is a paucity of information about atomization/disintegration of viscoelastic liquids/gels.



Figure 1-8: (color online). (a) Snapshot of a high Reynolds number viscoelastic liquid jet at breakup (200 ppm PEO dissolved in water). Image taken from [14]. The original experiments were performed by Hoyt and Taylor [15]. (b) Cover image of the Society of Rheology Bulletin [16]. Images by Keshavarz and McKinley demonstrate the difference between a viscoelastic liquid and its corresponding Newtonian solvent in air-assisted atomization.

With the advent of high-speed photography, many aspects of atomization events were captured and Hoyt and Taylor [15] were among the very first scientists that studied the dynamics of viscoelastic jets and sprays. Figure 1-8(a) shows a snapshot of a high Reynolds number (Reynolds number is defined as $Re \equiv \rho V R / \mu$ and is the ratio of inertia over viscous stresses) viscoelastic jet. The jet becomes unstable due to shear induced instabilities, which rise from the momentum difference between the liquid and air. Following that, stretched and elongated filaments form which show resistance against atomization.

More recent photographic studies of viscoelastic liquids in air-assisted atomization show that, when compared to the Newtonian solvent, the large-scale shear-

induced waves look similar, as shown in Figure 1-8(b) by Keshavarz and McKinley [16]. However, the dramatic difference in the morphology of elongated filaments between these two liquids becomes dominant as the jet travels further away from the nozzle.

As mentioned before, this is a known challenge for coating industry that stems from the “stickiness” of the viscoelastic fluids. As Patton [17] points out, most of the literature lacks a quantitative approach towards the rheological properties of different materials and at best stops at qualitative adjectives such as “tough” or “sticky” materials as contrasted with “thin” or “non-tacky” ones. Figure 1-9 provides a good example of different adjectives used in the coating industry for complex fluids.

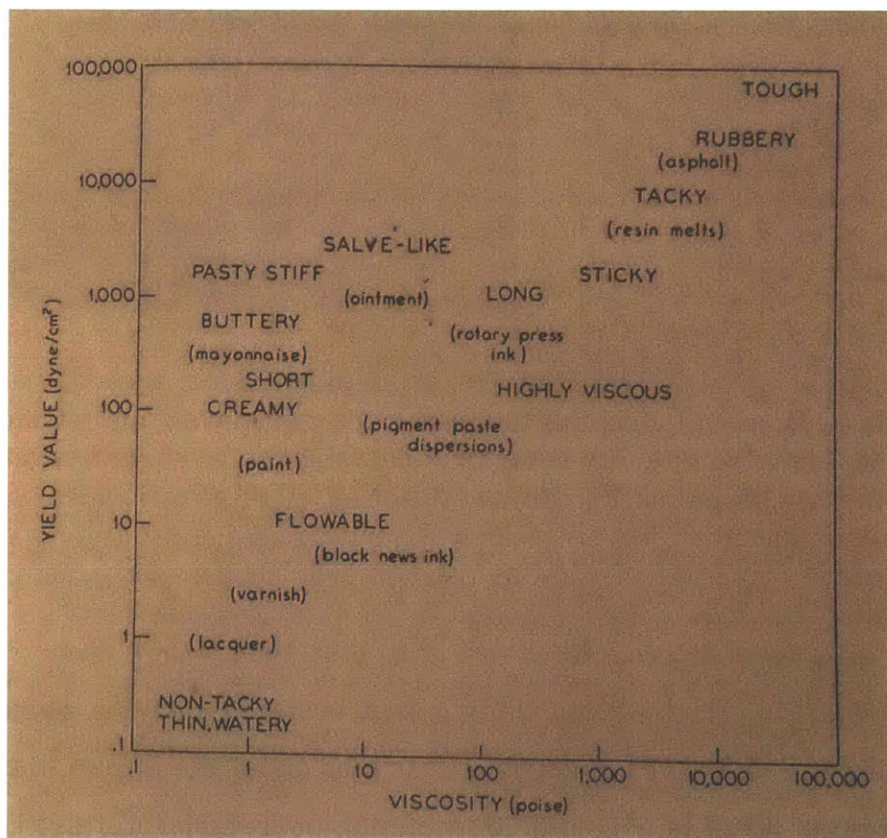


Figure 1-9: (color online). A “rheological” map for different paints and resins used in the coating industry. Image taken from [17].

To address the “stickiness” in a quantitative manner, we need to measure and

report the extensional properties. Knowing that the extensional rheology of many complex fluids can differ dramatically from the corresponding shear rheology, we will next introduce the concept of elongational rheometry.

1.2.3 Extensional Rheology of Dilute Viscoelastic Solutions

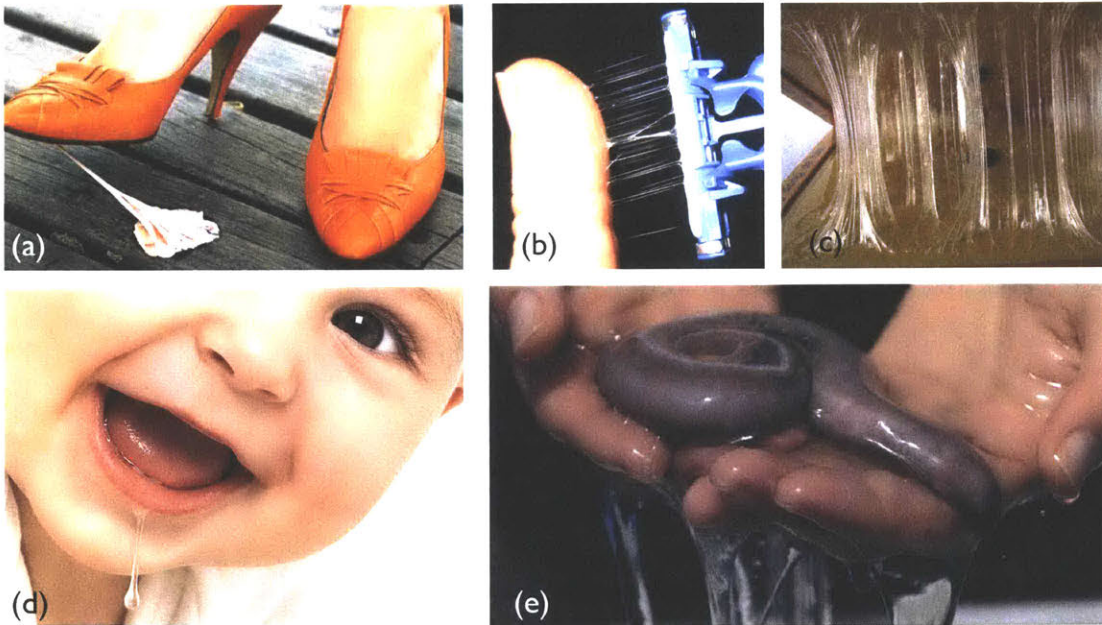


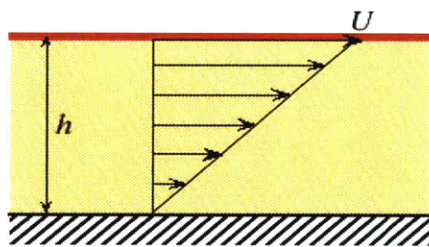
Figure 1-10: (color online). Different daily examples in which the extensional properties (stickiness) of synthetic and biological materials plays an important role: (a) extension of a chewing gum. (b) elongated filaments of a viscoelastic liquid stretching out of the wet strip on a shaving blade holder. (c) large resistance of adhesives in elongational deformations. (d) a saliva drop hold up against gravity by an elongating filament. (e) Hagfish slime is used as a defensive mechanism due to its sticky nature.

As shown in Figure 1-10, our daily experience with chewing gums, shaving blade holder and adhesives gives us a clear idea about the importance of extensional properties for different synthetic materials or chemical additives. The stickiness of these materials can lead to a pleasant smile when we adhere a sticker or an annoying yell when our shoes get entangled with a chewing gum. Human body is known to be a live factory for sticky materials such as saliva and mucus. Some animals, such as hagfish, generate a defensive slime that is also known for its stick-

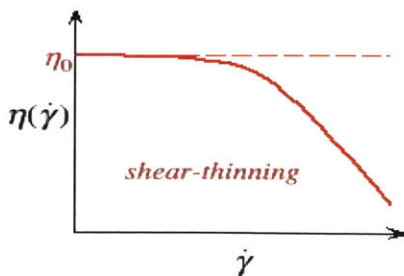
ness (Figure 1-10(e)).

To quantify the “stickiness” of different materials, we need to properly define the corresponding rheological property and seek for proper methods and instruments for measurement purposes. We maybe familiar to the idea of shear viscosity and its corresponding definition in Newtonian liquids. The adjective “slimy” often refers to shear viscosity of different materials and as shown in Figure 1-11(a) it is the ratio between the measured stress and applied rate of shear deformation. Most non-Newtonian liquids exhibit lower values of shear viscosity at higher shear rates, a property known as “shear-thinning” [70, 71]. Figure 1-11(b) also shows a graphic introduction to the idea of an elongational flowfield and the concept of extensional rheology.

- “Slimy”

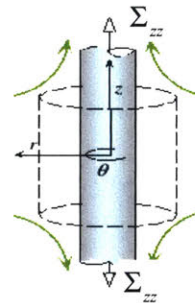


$$\Sigma_{yx} = \eta(\dot{\gamma}) \dot{\gamma}_{yx}$$

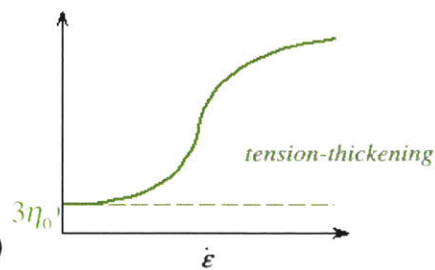


(a)

- “Sticky”



$$\Sigma_{zz} - \Sigma_{rr} = \dot{\epsilon} \eta_E(\dot{\epsilon})$$



(b)

Figure 1-11: (color online). (a) The idea of materials being “slimy” corresponds to their response in shear deformations. (b) “Stickiness” is on the other hand a material property that should be probed in an elongational flowfield.

Unlike the situation in simple shear viscosity, where the subject is rather evolved

and mature, the study of extensional properties is an ongoing challenge especially for dilute solutions [20, 72]. First we need to generate an elongational vorticity-free flowfield. For example, for a velocity field of the form

$$v_x = -\dot{\epsilon}x/2, \quad v_y = -\dot{\epsilon}y/2, \quad v_z = \dot{\epsilon}z, \quad (1.1)$$

in the Cartesian coordinates which corresponds to a flowfield of

$$v_r = -\dot{\epsilon}r/2, \quad v_\theta = 0, \quad v_z = \dot{\epsilon}z, \quad (1.2)$$

form in the cylindrical coordinates, where the $\dot{\epsilon}$ is a constant elongational strain rate, the corresponding stress distribution can be written in the Cartesian coordinates

$$\begin{aligned} \Sigma_{zz} - \Sigma_{xx} &= \Sigma_{zz} - \Sigma_{yy} = \dot{\epsilon}\eta_E(\dot{\epsilon}) \\ \Sigma_{xy} &= \Sigma_{xz} = \Sigma_{yz} = 0 \end{aligned} \quad (1.3)$$

and in the cylindrical coordinates

$$\begin{aligned} \Sigma_{zz} - \Sigma_{rr} &= \Sigma_{zz} - \Sigma_{\theta\theta} = \dot{\epsilon}\eta_E(\dot{\epsilon}) \\ \Sigma_{rz} &= \Sigma_{r\theta} = \Sigma_{\theta z} = 0. \end{aligned} \quad (1.4)$$

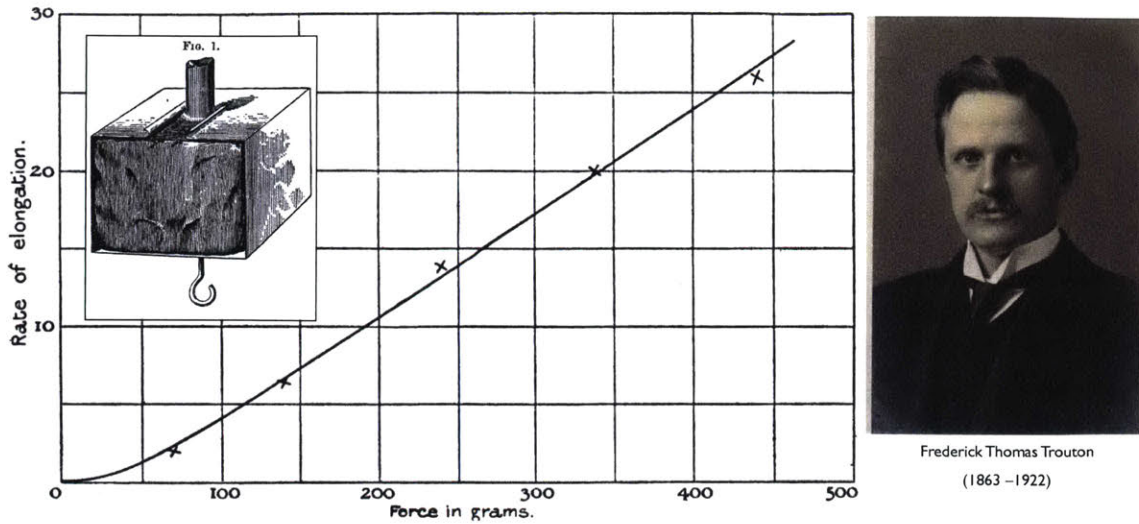


Figure 1-12: (color online). Original (and first) set of measured data for extensional rheology of pitch. The test was performed by Trouton in 1906. [18].

Thus, as shown in Figure 1-11(b), provided we can generate a uniaxial elongational flowfield (Equation 1.1 or 1.2) we can define elongational viscosity as $\eta_E(\dot{\epsilon}) \equiv \Sigma_{zz} - \Sigma_{rr}/\dot{\epsilon}$. Trouton (1863-1922) was the first who measured the elongational viscosity of a material (he studied the extensional viscosity of pitch)[18] and concluded that for Newtonian liquids the extensional viscosity is constant and is three times the corresponding value of shear viscosity. The ratio of the elongational viscosity over the shear viscosity is called the Trouton ratio [73]. Original measurements of Trouton, for the extensional viscosity of pitch, are shown in Figure 1-12. Many polymeric solutions show enhanced values of extensional viscosity at higher elongation rates (see Figure 1-11(b)) which is referred to as strain-rate thickening.

Generating a vorticity-free elongational flowfield is an experimental challenge and depending on the elasticity of the fluid of interest, different methods have been introduced in the literature.

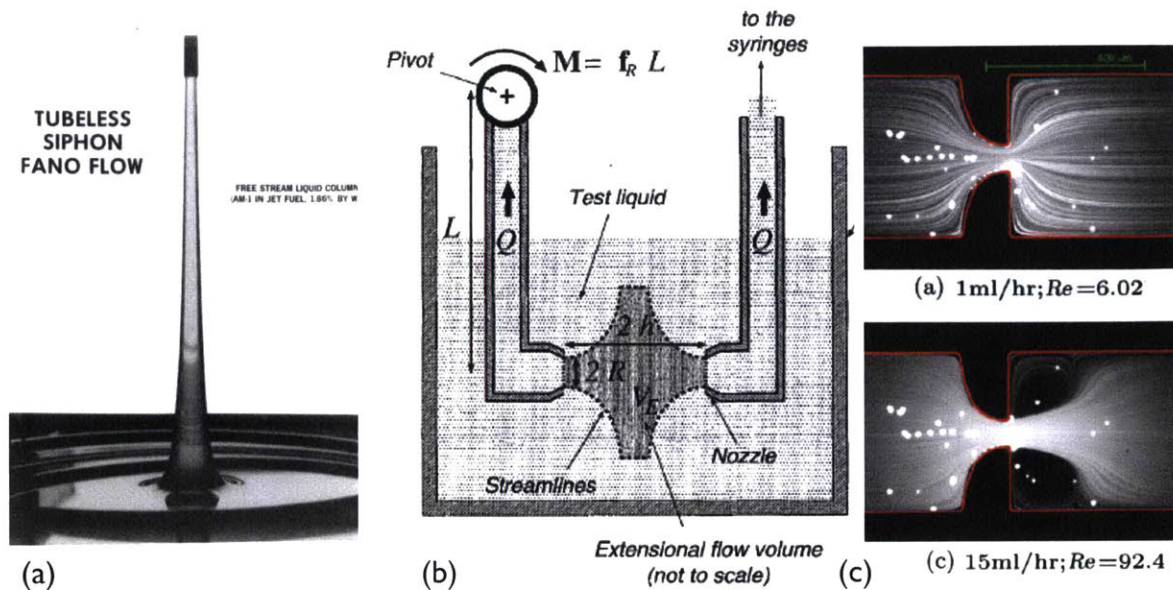


Figure 1-13: (color online). Different methods used in the literature for measuring extensional properties of dilute viscoelastic solutions: (a) tubeless siphon method used by Peng and Landel [19]. Image taken from [20]. (b) Opposed nozzle device used by Dontula et al. [21]. (c) Microfluidic hyperbolic channels used as an extensional rheometer [22].

Figure 1-13 shows few examples of the common devices that are used for extensional rheology. If the liquid is elastic enough, then even a simple test such as the tubeless siphon [19] (Figure 1-13(a)) can be applied. However for more dilute and less elastic solutions, it is not easy to stretch the liquid. Devices such as opposed nozzles (Figure 1-13(b)) and microfluidic channels with hyperbolic wall profile (Figure 1-13(c)) [21, 22] have been introduced but their corresponding measurements are often affected by the fluid inertia.

The challenge of proper measurement of the elongational properties is an ongoing research topic. A close look to the scattered rheological curves in Figure 1-14 which were all measured for the extensional rheology of the same test fluid can be an alarming image for any rheologist [23].

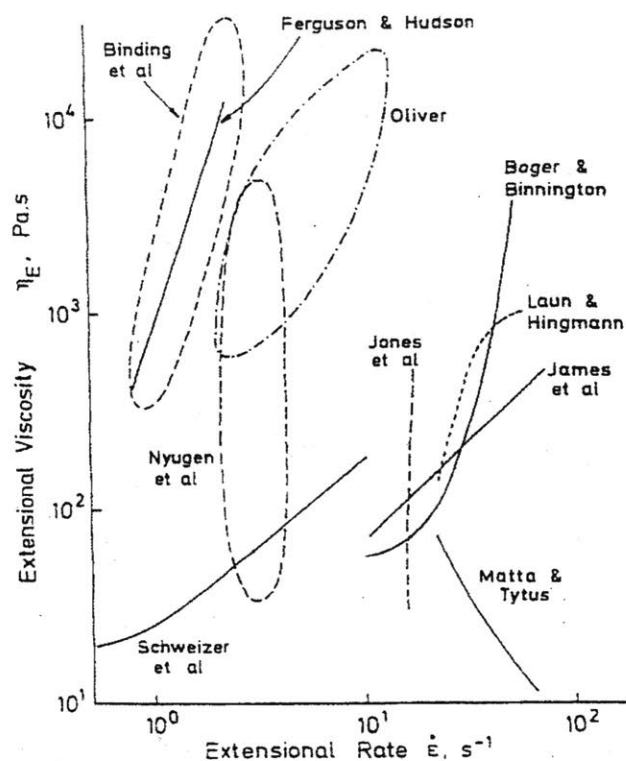


Figure 1-14: (color online). Measurements of extensional rheology for a model fluid (M1) performed by different research groups and labs [23]. This plot is some times referred to as the so-called “M1” muddle.

One other elongational rheometer is the Capillary Breakup Extensional Rheometer (CaBER). Originally proposed by Entov and coworkers [74], and later studied in great detail by McKinley and others [75, 24, 76], CaBER is a simple setup that relies on recording the thinning of a viscoelastic filament under the action of the capillary stresses. Figure 1-15 shows that when a sample of the fluid is placed between two plates and later separated to a final gap a fluid filament can be formed between the two hemispherical volumes of fluid. Due to the extra capillary pressure in the thin filament, an elongational flowfield can emerge in the filament. For the Newtonian liquids, the capillary pressure can be balanced by either the inertia or the viscosity of the fluid. In the presence of a macromolecule, which is the case for viscoelastic liquids, the elongational flowfield will increase in the extension rate up to a critical value, which is the onset of coil-stretch transition in the morphology

of the micro-structure [77]. This critical stretch rate is known to scale as the inverse of the microstructure relaxation time $\dot{\epsilon}_c \sim 1/\tau_E$ in which the relaxation time τ_E is also referred to as the *elongational relaxation time*.

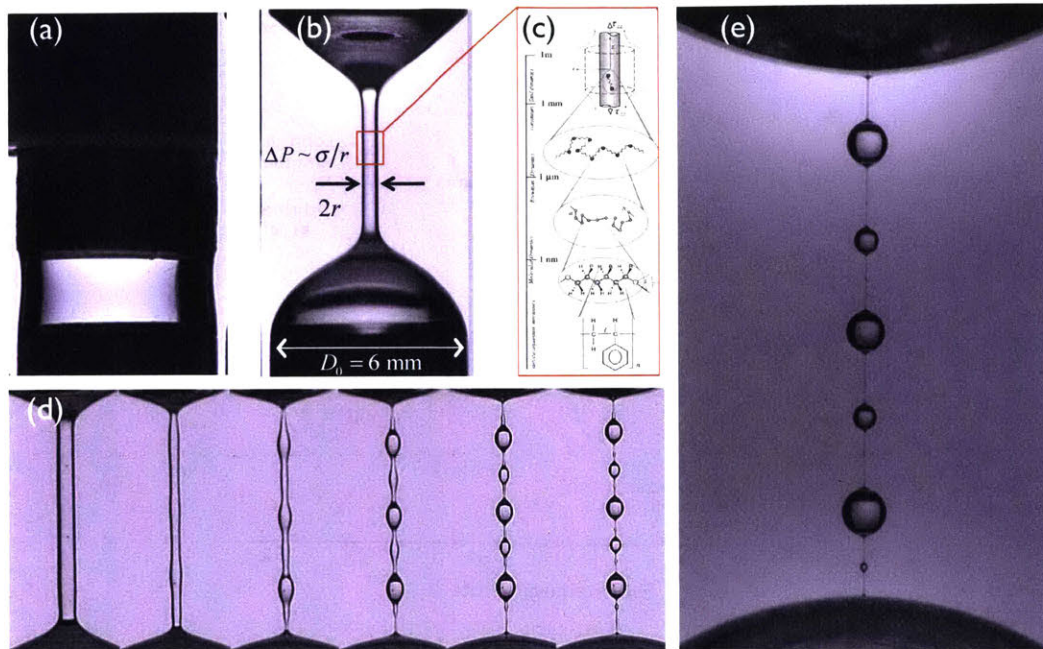


Figure 1-15: (color online). CaBER device: (a) A liquid sample (Bavand’s saliva in this specific figure) sitting between two stationary plates. (b) A filament is formed after the plates are separated from each other. (c) A look into the dynamics of polymer chains in the solvent as they go through elongation. Multiple scales are involved and to get a macroscopic model, from the microscopic properties, several levels of course graining are required. (d) The final stages of breakup can lead to an iterative instability that involves capillarity, elasticity and inertia giving rise to rather beautiful structures (beads-on-a-string). (e) Magnified image showing the thin filament connecting multiple liquid beads. Surface tension is dominant in the bead region while the elasticity is the major force in the thin elongated filaments.

Entov and coworkers [74, 78] show that as the stretch rate approaches this critical value, the flow in the filament will be dominated by a balance between the capillary and the elastic stresses that are excited after the onset of the coil-stretch transition. Assuming a simple rheological model such as Oldroyd-B or FENE-P, with one dominant relaxation time [70], one can find an exact or approximate prediction for the filament diameter evolution during the mentioned elasto-capillary balance. Results show that the diameter of the viscoelastic filament decays expo-

nentially with time [79] and the elongational relaxation time sets the slope of this exponential decay on a log-normal plot.

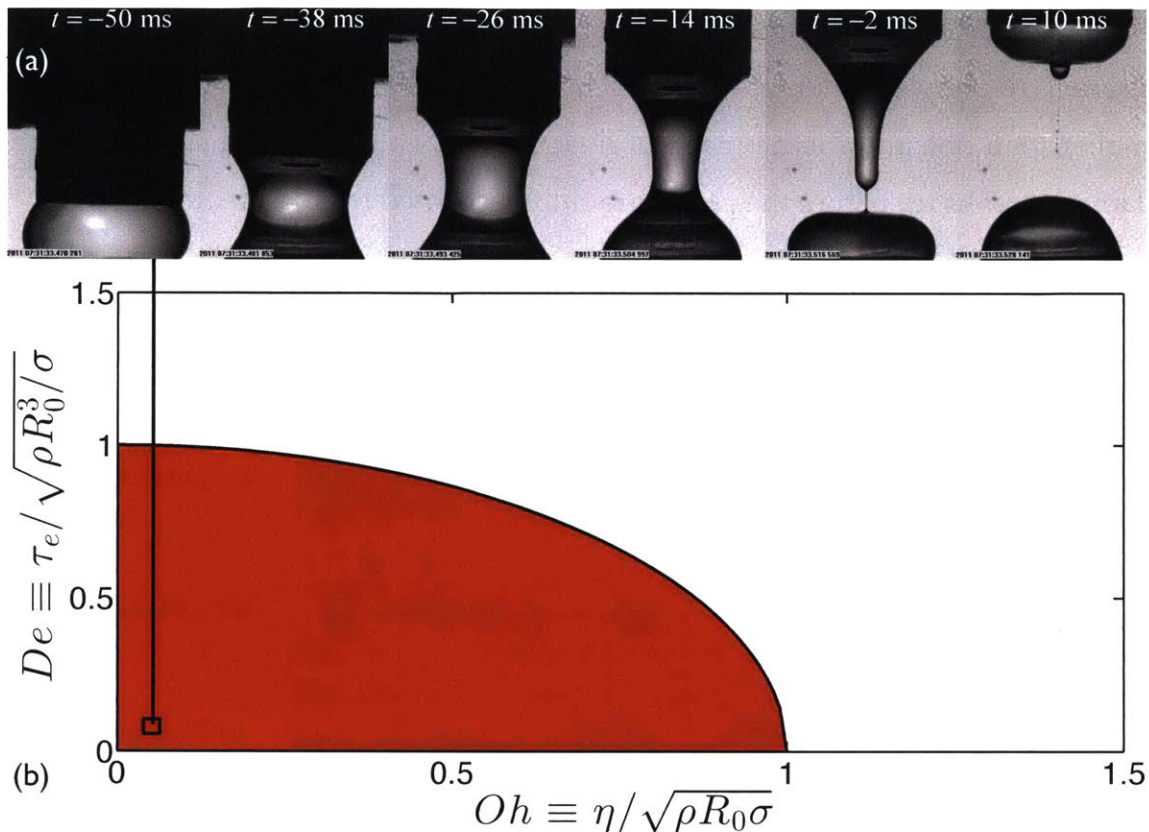


Figure 1-16: (color online). (a) An example of CaBER failing to capture the elasto-capillary balance for a dilute viscoelastic solution (PEO-300K-0.01% wt. in the solvent). The filament breaks during the plate separation stage. (b) An approximate map of operation for the CaBER device based on the corresponding dimensionless numbers. Red region corresponds to solutions that are so dilute and non-viscous for proper testing in CaBER [24].

Knowing that the flow in CaBER is driven by capillary forces one can imagine that the inertia-capillary timescale plays an important role in this process. This timescale, also known as the Rayleigh timescale [80], $\tau_R \equiv \sqrt{\rho R_0^3 / \sigma}$ is set by the density ρ and surface tension σ of the liquid and the initial radius R_0 of the filament. The dimensionless ratio of the elongational relaxation time over the inertia-capillary timescale is known as the Deborah number $De \equiv \tau_E / \tau_R$ which is a measure of the elastic stresses compared to the inertia-capillary ones. Another relevant

dimensionless number is the Ohnesorge number $Oh \equiv \eta/\sqrt{\rho R_0 \sigma}$ which is the ratio of visco-capillary timescale η/σ over the inertia-capillary timescale.

It is known that if the test fluid is not elastic or viscous enough (i.e. $De \leq 1$ and $Oh \leq 1$), CaBER can not report reliable measurements in its normal applications. Figure 1-16 shows a filament for which both Deborah Ohnesorge numbers are smaller than one and the montage of images from CaBER indeed shows that the filament breaks up before the plates are fully separated from each other.

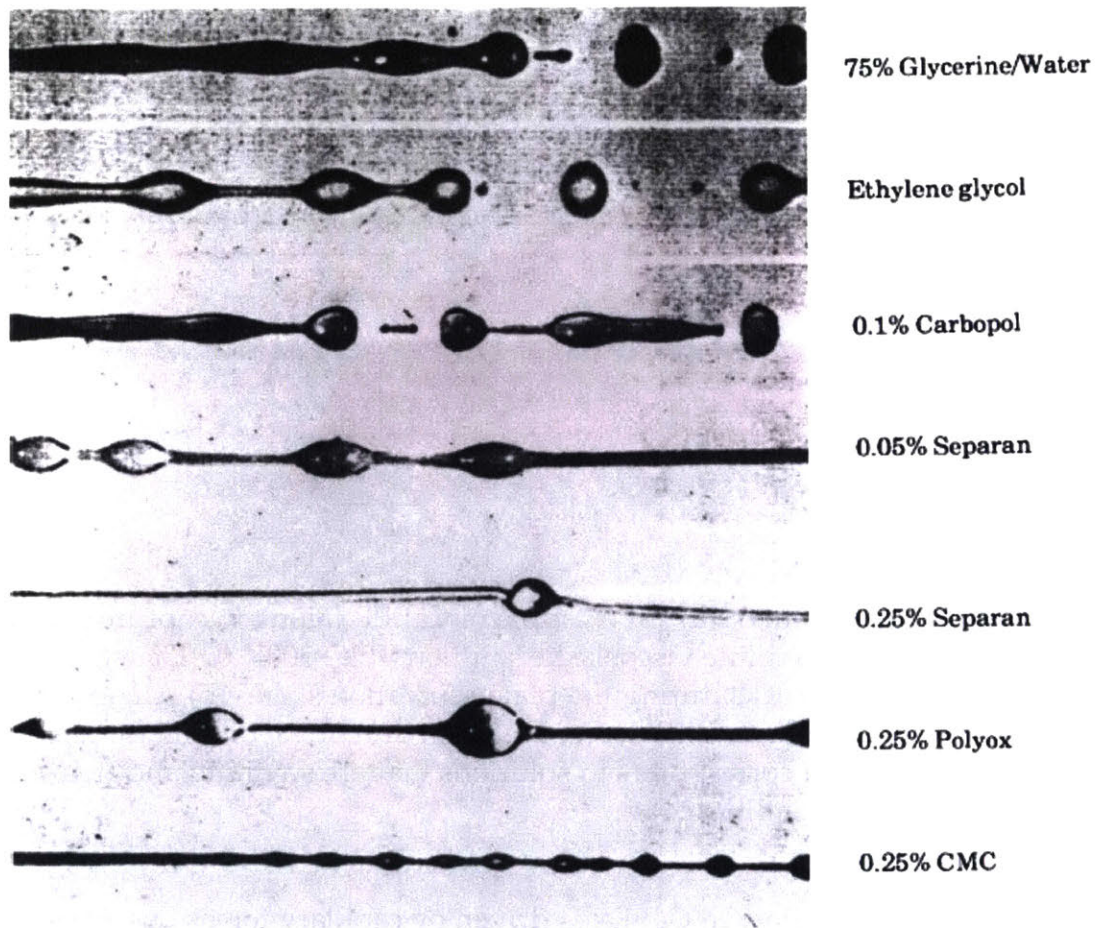


Figure 1-17: (color online). Jet breakup for different Newtonian and viscoelastic liquids. Image taken from [14].

Failure of CaBER in reporting reliable measurement for dilute solutions, has prompted researchers to seek alternative methods by modifying the CaBER device [81, 82]. At the same time, it is known that the capillary breakup of jets can also

be dramatically affected by viscoelastic effects and many have used jet breakup as an “indexer” for extensional viscosity (see Figure 1-17). Schümmer and Tebel [25] studied the behavior of a viscoelastic jet that is subjected to small amplitude perturbations at fixed frequencies. Figure 1-18 shows a summary of their initial measurements. The suggested study focuses on the evolution of the capillary filament that is traveling with the jet velocity. Schümmer and Tebel [25] and later Christanti and Walker [83] both showed that jet breakup studies are indeed a good candidate for elongational rheology of dilute solution.

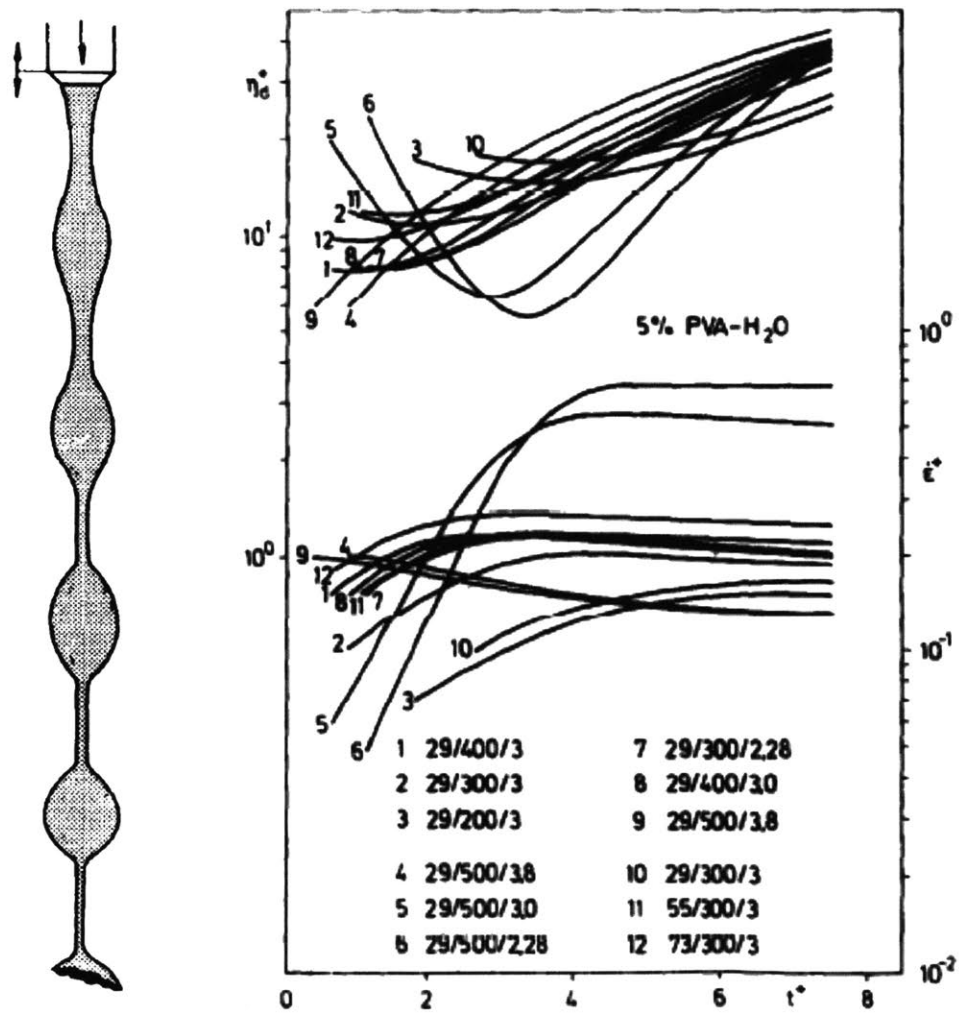


Figure 1-18: (color online). Data from a jet breakup elongational rheometer [25]. The device was originally designed by Schümmer and Tebel [25].

As mentioned, the elongational rheometry for dilute solutions is a an active area of research. In the next chapter we will focus on jet breakup method and microfluidic channels and show that, even for the very dilute solutions, the jet break up studies can report reliable measurements. A comparison between different methods, with more quantitative analysis, is postponed to the next chapter.

1.2.4 Effects of extensional properties on fragmentation

Despite the extensive use of viscoelastic liquids in many industrial applications such as paint coating, emulsification, pharmaceutical sprays, inkjets and anti-misting fuels,our knowledge of the fragmentation dynamics for viscoelastic liquids is still preliminary and qualitative at its best. A more quantitative knowledge can have many potential benefits to many of these industries.

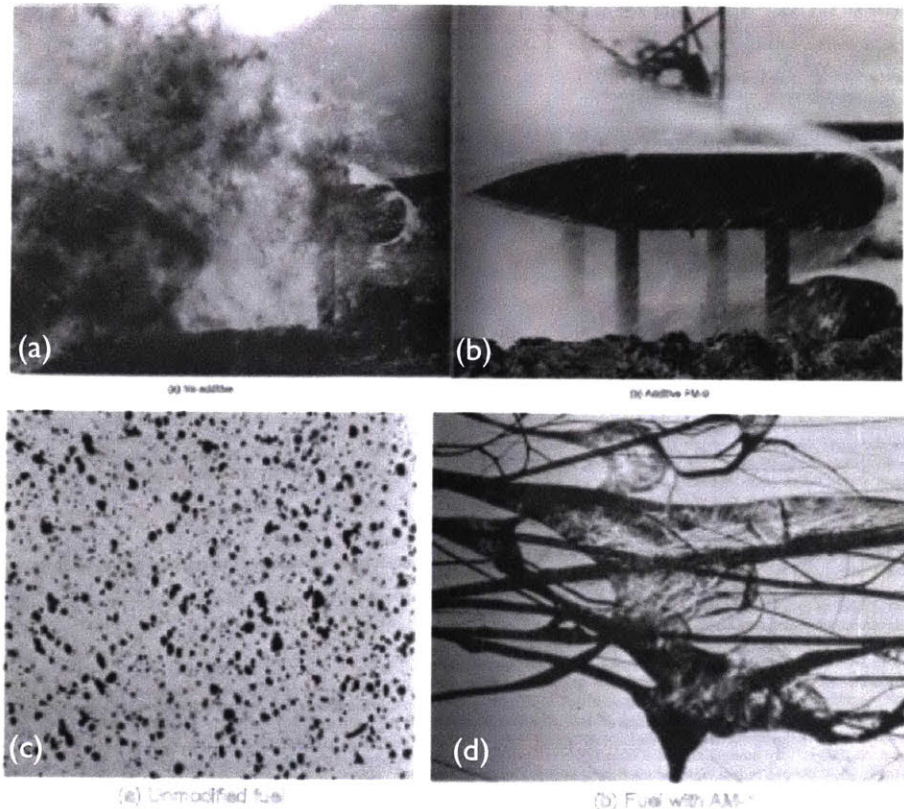


Figure 1-19: (color online). Performance of normal fuel in combustion (a) and atomization (c) compared to the fuel with anti-misting agents ((b) and (d) respectively). Images taken from [26].

Several intriguing results in the literature have emphasized this point in a number of different case studies [26, 84]. As an example, one can note the case of anti-misting fuel agents. These polymers/macromolecules can be added to high octane jet fuels and dramatically help to mitigate fire/explosion hazards by a great factor. Figure 1-19 shows how these agents can suppress the combustion by inhibiting the atomization process. From a biological point of view, the dynamics of mucus and saliva in violent respiratory events such as coughing or sneezing is also enormously affected by the extensional properties of these biological gels/liquids.

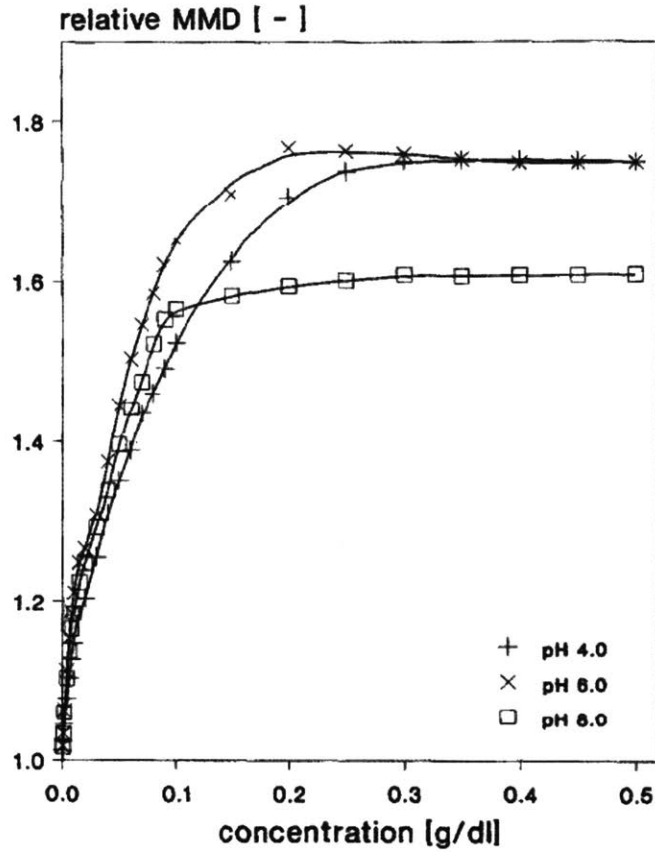


Figure 1-20: (color online). Measurements of relative mass mean diameter (MMD) for viscoelastic sprays performed by Ferguson et al. [27] for a series of PEO solutions.

The lack of quantitative knowledge on this subject in the literature is by no means an indication of lack of interest. On the contrary, it is a sign of the complexity of the topic. To study this subject, one requires both proper knowledge of the extensional viscosity of the test fluids in ideal homogeneous flowfield and this requires proper instrumentation for measuring this material function for dilute solutions. Also essential to this study is a proper set of measurements of fragmentation dynamics and accurate knowledge of the correct models for fragmentation. In short, complex fluids in complex flows can not lead to a simple problem and perhaps this has been a reason that so many qualitative measurements, such as the results plotted in Figure 1-21 by Ferguson et al. [27], stop short of developing a physical model for viscoelastic fragmentation. Most literature also fails to offer any quantitative information and modeling on the effects of viscoelasticity on the

final droplet size distributions.

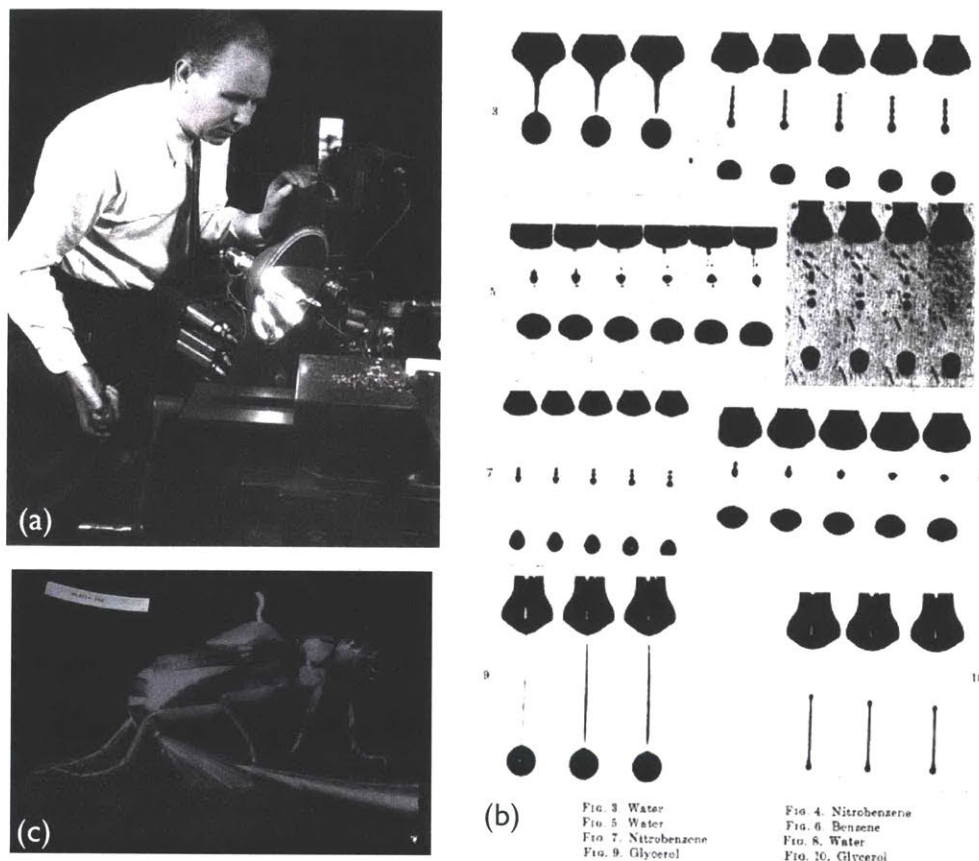


Figure 1-21: (color online). (a) Harold (Doc) Edgerton (1903-1990) performing high speed imaging tests in his lab at MIT. (b) High speed visualization of drop pinch off used by Edgerton et al. [28] to quantify the drop-weight method that is used in liquid surface tension measurements. (c) A bombardier beetle discharging a hot spray as a defensive mechanism. Image taken from MIT museum collection of Edgerton's work <http://video.mit.edu/watch/bombardier-beetles-3185/>.

Addressing challenging problems in natural and industrial processes has been a common theme of research in Massachusetts Institute of Technology (MIT). The pioneering work of Edgerton (1903-1990) on high speed photography proved to be a seminal tool that can be employed for studying many of these problems. As shown in Figure 1-21, many of the problems Edgerton imaged were related to pinch off or droplet breakup of different Newtonian liquids (see Figure 1-21(b)) [28]. At the same time spray/fragmentation of liquids in nature was another topic of interest for Doc Edgerton. Figure 1-21(c) shows a snapshot of a bombardier

beetle releasing a hot spray of liquid as a defensive mechanism for repelling aggressors. This was recorded by Egerton using a high speed camera.

In the same spirit, we aim to address the nonlinear dynamics of complex fluids in fragmentation. For a well known class of viscoelastic test fluids, we show that proper measurements of elongational properties by a novel jet breakup setup can lead to meaningful measurements of elongational relaxation times which capture the relevant material properties of the underlying microstructure. Furthermore, through precise observation, we develop a simple toy model and connect the measured liquid properties such as viscosity and elongation relaxation time to average droplet sizes. We also study the corresponding size distributions and show how viscoelasticity leads to a universal size distribution.

It is noteworthy to mention that while dilute viscoelastic solution are very common in many industrial and natural processed, there are many more complex structured fluids/gels that also go through fragmentation/fracture. Dense colloidal gels used in many resins and paints, food gels, polymer emulsions with a transient network and many other complex fluids have a permanent or temporary physical network in their underlying structure. This network is characterized by a wide range of different length scales and consequently many different timescales are associated with the mechanical response of these gel-like materials [71]. Under rapid deformations the underlying transient network can behave similarly to a soft solid and upon a fragmentation process may experience a brittle like fracture events [33]. In order to understand this limit and be able to predict the mechanical response of these gels in this extreme events we need to introduce a few key ideas about these materials and their linear and nonlinear rheology.

1.2.5 Other complex fluids/gels in nonlinear deformations

Examples of fluids/gels with transient/temporary networks are abundant in both synthetic and biological applications. Figure 1-22 shows microscopic images from the structure of a Polyurethane dispersion at different waiting times. The micro-

gels that constitutes this dispersion can form a fractal like network [29] and its linear rheology under a simple oscillatory deformation will show power law behavior for both elastic and loss moduli [85]. The emergence of power law rheology is a signature of a wide spectrum of relaxation times for these materials and indicates that focusing on the dilute dynamics of a single polymer/macromolecule in a solvent is not the right physical image for these gels [29].

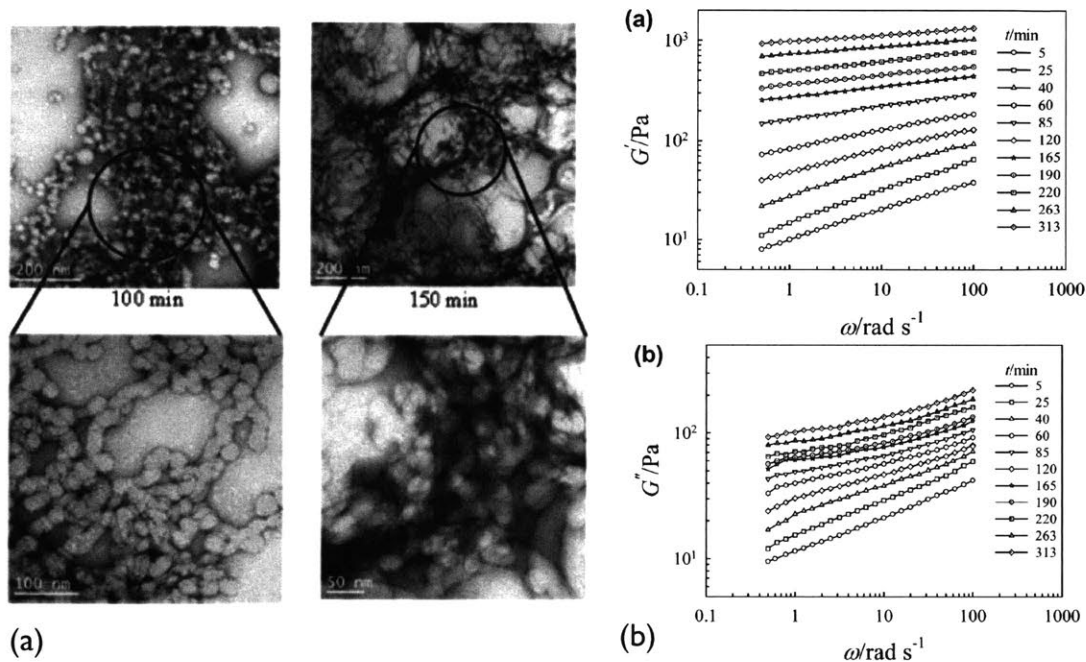


Figure 1-22: (color online). (a) TEM images of waterborne Polyurethane Dispersions at different waiting times. (b) Linear rheology of the same liquids/gels demonstrating a power law behaviour over a wide range of frequencies. Images taken from [29].

Even some of the simple resins provided to us from Axalta Coating Systems, exhibit network-like characteristics in which the breadth of size distributions in the underlying structures leads to a rheological response that is equivalent to multiple modes of relaxation with different time constant [86]. Figure 1-23 shows an example of one of these gel-like resins and a schematic description of the underlying micro structure, comprised of gel like drops that are saturated with low molecular weight chains.

In these materials the underlying network can easily experience fracture in ex-

treme events such as fragmentation. Understanding the linear rheology of these materials and connecting that to the structure of the network within these material is extremely important in a variety of applications and can ideally be used as a guideline for material scientists in designing diverse materials with different properties [87]. At the same time, nonlinear rheology of these materials is an essential element for studying their dynamics in large deformations that are experiences within fracture/fragmentation [88].

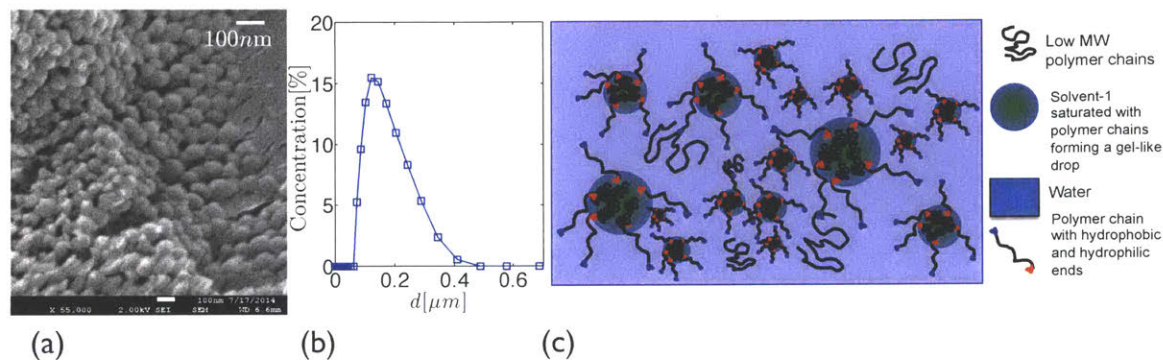


Figure 1-23: (color online). (a) TEM image of a typical resin provided by Axalta Coating Systems. (b) Size distribution of gel-like beads shown in part (a). (c) A physical image of the structure of this specific resin.

The abundance of these gel-like materials in the food and bio-gel industries have prompted many researchers to take some groups of food gels as canonical examples for their experimental studies. Casein acid-induced gels are one class of these materials that exhibit power law linear rheology, strain hardening and softening in their nonlinear rheology and delayed fracture under applied stress or deformation rate [89, 90, 91].

The casein polymer gels are a type of protein gels that have some similarities to casein micelles which are known as the the primary ingredient of yogurt. However, we should emphasize that instead of a colloidal gel structure, which is observed for the casein micelles (Figure 1-24(b)), casein polymer gels show a fibrous cellular structure (see Figures 1-24(c) and 1-24(d)). Protein strands in these structures generate a permanent Network that acts as a flock of mass fractals [89]. Water interacts in these fibrous porous network and the viscous dissipation of these interactions

gives rise to a non-zero loss modulus.

We chose casein protein gels as a good candidate for studying the behavior of soft gels in fracture/fragmentation. Power law rheology, strain hardening and fracture upon applied force/shear rate are all characteristic to the behavior of these gels. Furthermore, the rheological properties of these gels can be easily controlled by fine tuning the chemistry of the acidification process.

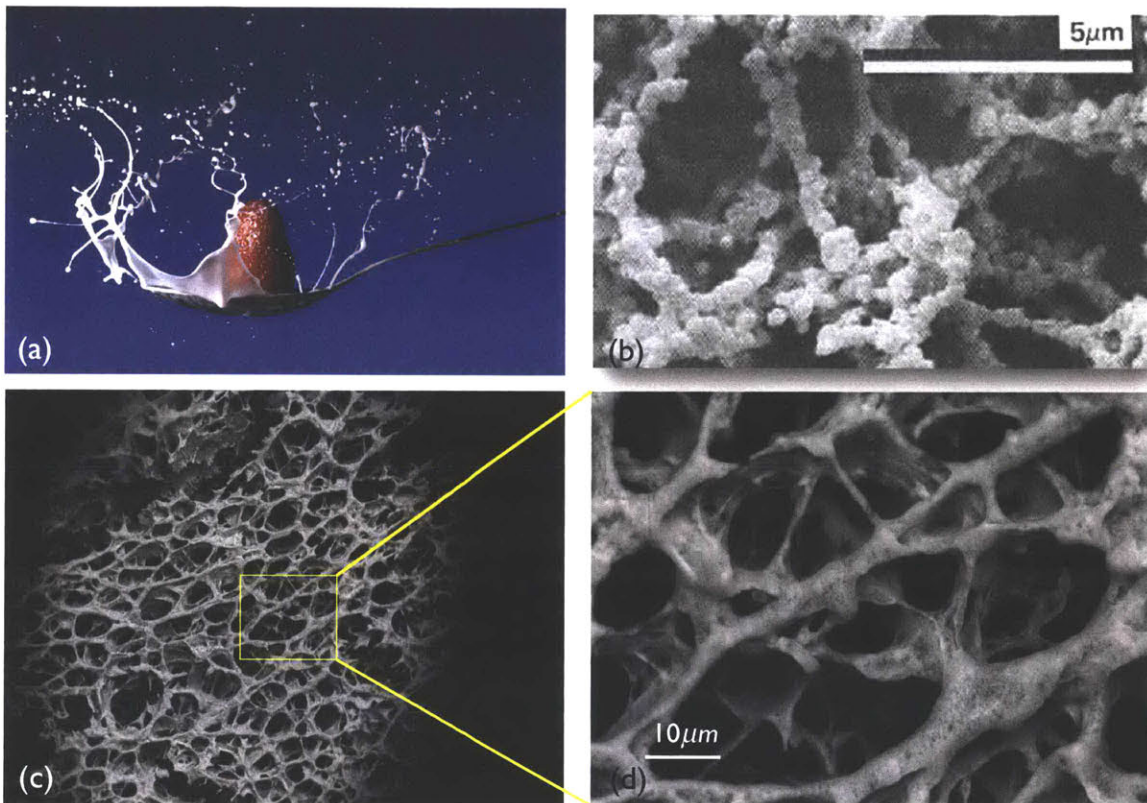


Figure 1-24: (color online). (a) Fragmentation and fracture of a spoonful of yogurt upon the impact of a strawberry. (b) SEM image of yogurt made from unheated skim milk. Casein micelles aggregate in the form of coarse clusters. Image taken from [30]. (c) and (d) ESEM images of a casein acid-induced polymer gel. The thick fibrous strands of this biopolymer gel provide the elastic response of this material in different deformations.

The linear rheology of soft gels is known to be dominated by power law responses in time or frequency [86]. Scott Blair (1902-1987) was one of the first to look at the rheological behavior of many bio-gels and food products. Figure 1-25 shows the relaxation response of a sample of a milk curd after experiencing a step

in strain. Unlike an ideal elastic solid, the measured modulus for this material does decay with time but the the form of this decay is different from the simple exponential decay of Maxwell-Debye type that is predicted for viscoelastic materials with a single relaxation time/mode. To mathematically model this behavior, one requires a mechanical model that incorporates many modes of relaxation with different timescales [92]. Scott Blair found a more sophisticated method for mathematically describing these gels which is based on fractional calculus. Inspired by this idea, and also by the concept of anomalous diffusion, which is experimentally observed in many biological materials [93], Jaishankar and McKinley [86] reintroduced the idea of "fractional rheology" as a useful tool for modeling the linear rheology of soft gels.



G.W. Scott Blair
(1902-1987)

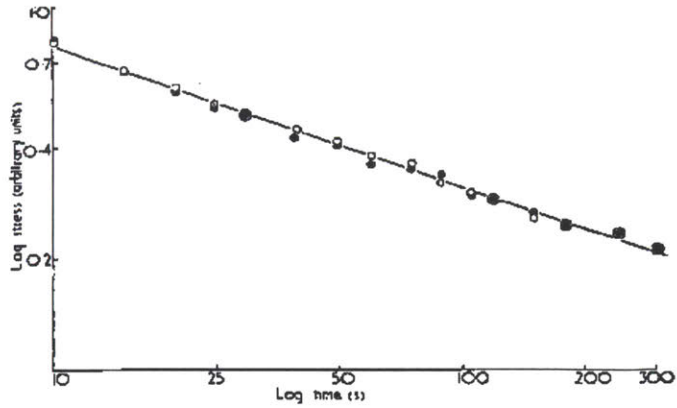


Fig. 2. Relaxation curves (milk curd)
○; ●, duplicate runs.

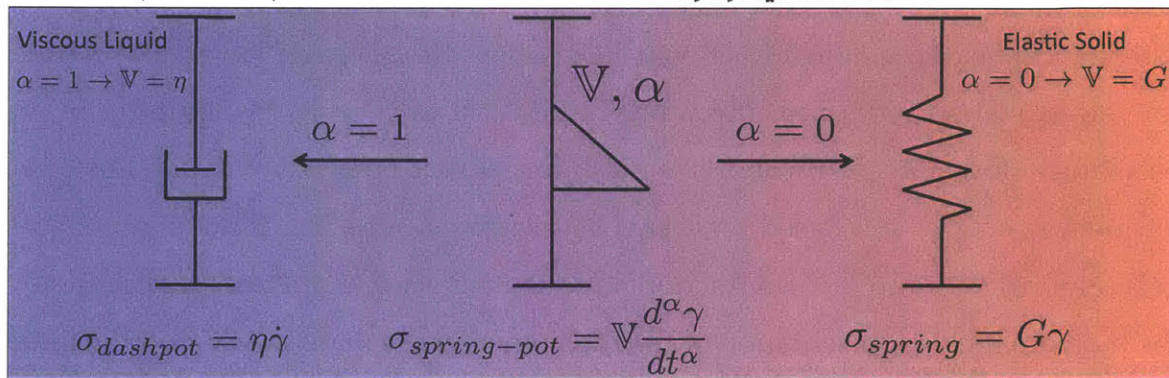


Figure 1-25: (color online). Stress relaxation of milk curd after a step in strain. Data were measured by Scott Blair (1902-1987) [31]. The idea of a *fractional* mechanical element that can generate a power law relaxation response with two model parameters \mathbb{V} and α . As α varies from 0 to 1 one can recover a spectrum of material responses ranging from Hookean solids to Newtonian liquids.

The proposed mechanical element is a *spring-pot* that has a constitutive equation of the form

$$\sigma_{spring-pot} = \mathbb{V} \frac{d^\alpha \gamma}{dt^\alpha} \quad (1.5)$$

where $\frac{d^\alpha}{dt^\alpha}$ is a fractional derivative ¹ of order α defined in the form of a Caputo derivative [95]

$$\frac{d^\alpha}{dt^\alpha} f(t) = \frac{1}{\Gamma(1-\alpha)} \int_0^t (t-t')^{\alpha-1} f^{(n)}(t') dt' \quad (1.6)$$

¹Historically the concept of fractional derivatives was first introduced by Leibniz in a letter to L'Hospital [94].

in which n is the nearest integer bigger than or equal to α , i.e. $n = \lceil \alpha \rceil$ and $f^{(n)}$ is the n th derivative of f .

This fractional model Equation 1.5 has two parameters: a front factor \mathbb{V} which has a dimension of $\text{Pa}\cdot\text{s}^\alpha$ and a dimensionless parameter α that can vary from 0 to 1. While \mathbb{V} sets the strength of the gel, α sets the slope of the power law. By varying values of α from 0 to 1 one can recover an spectrum of rheological responses from a solid to a gel and then a Newtonian liquid. We will show that the value of α is set by the fractal structure of the gel network while \mathbb{V} is strongly affected by the volume fraction of casein dissolved in water.

Rheological response of this fractional element predicts a power law decay in time for the relaxation modulus after a step strain test $G(t) \sim \mathbb{V}t^{-\alpha}$. Similarly in an oscillatory flow, the elastic and loss modulus exhibit power law dependence on frequency $G', G'' \sim \omega^\alpha$. Based on early observations on the linear rheology of soft gels (Figures 1-22 and 1-25), a fractional model seems to be a perfect candidate for the mathematical representation of the rheology of these materials within the limit of linear deformations.

1.2.6 Fracture of soft gels

As described earlier, the cohesion of liquids/gels is characterized the surface energy of the matter. In liquids this quantity is often the surface tension of the fluid and fragmentation of Newtonian liquids is a case in which inertia overcomes the capillary forces. A relevant dimensionless number is called the Weber number $We \equiv \rho V^2 R / \sigma$ which captures the ratio of the inertia over capillary forces. Liquid sheets, jets and drops become unstable at critical values of Weber number [96, 97, 13].

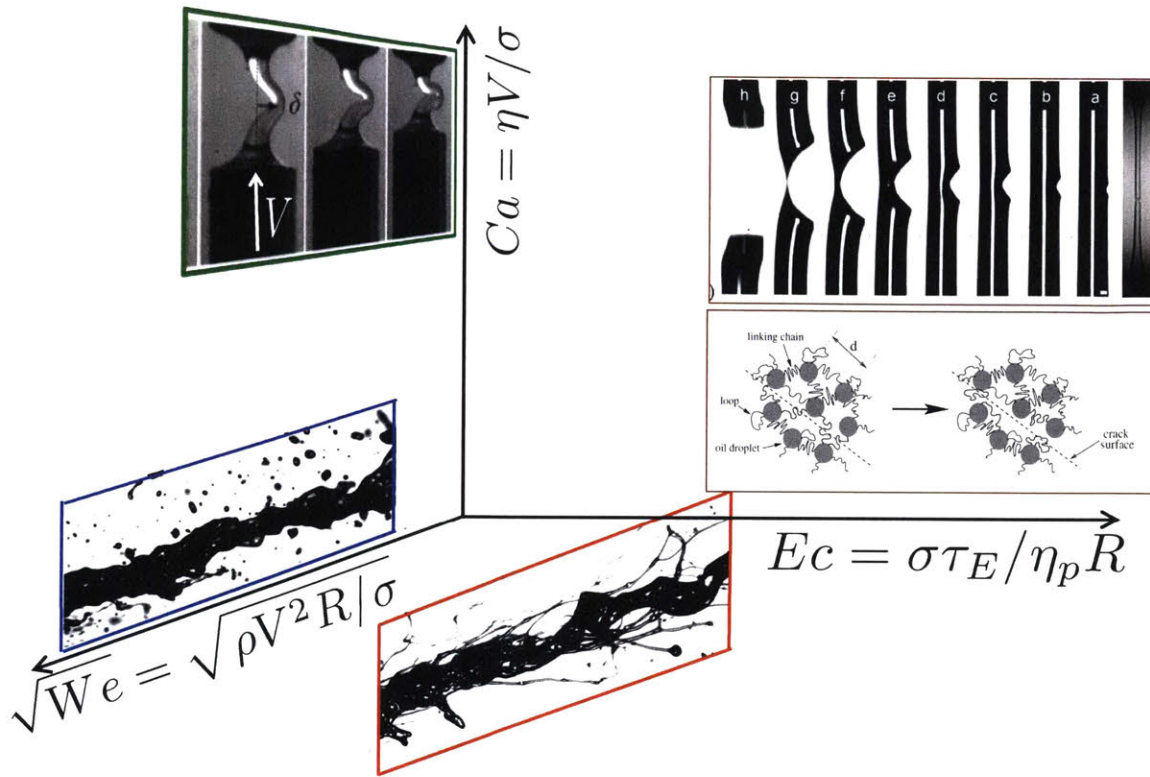


Figure 1-26: (color online). Dimensionless map of fragmentation and fracture for viscoelastic liquids and soft network gels. The $\{\sqrt{We}, Ec, Ca\}$ coordinate system represents dimensionless forms for the inertia, elasticity, and the viscosity of the material. For example in the atomization of non-viscous Newtonian liquids (inset with the blue border), inertia overcomes the capillary forces and the atomization process will be governed by the inertia-capillary balance in the thinning filaments. At the same time, for viscous Newtonian liquids the buckling of a viscous thread which is compressed at a constant velocity V (inset with green borders) is a good example in which viscous stresses can overcome the capillary resistance (at high enough Ca numbers). This results in the buckling of the liquid thread very similar to the buckling of an elastic column under compression. Image is taken from [32]. For viscoelastic liquids/gels, a non-zero relaxation time τ_E leads to high values of elastocapillary number at small length scales. For viscoelastic liquids which do not have a temporary/permanent network this leads to elongated filaments that show enhanced extensional viscosity and inhibit the atomization process (inset image with red borders). However, if the liquid/gel has a temporary/permanent network it is possible that the induced stresses (from either capillary effects, inertia, or external forces) become larger than a critical value that is set by the surface energy of the temporary/permanent network within the material. This can lead to a solid-like fracture of the fluid/gel (inset image with brown borders) [33].

For viscous threads, at certain velocities, viscous stresses dominate over the capillary ones. The Capillary number $Ca \equiv \eta V / \sigma$ is a dimensionless number that compares the strength of viscous forces to the capillary effects. Compressing a viscous thread, fast enough that the capillary number exceeds a certain threshold, leads to the buckling of the filament very much in the similar manner that a compressed elastic beam buckles after a certain deformation [32].

Figure 1-26 shows a dimensionless map for the fragmentation and fracture cases that we aim to study in this thesis. The two mentioned examples of Newtonian fragmentation and viscous buckling sit at the end of two axes of the right vertical plane.

The Ohnesorge number is the ratio of the capillary number over the square root of Weber number. Thus, a trajectory from inviscid Newtonian fragmentation to viscous buckling is equivalent to an increase in Ohnesorge number.

For dilute viscoelastic liquids, the ratio of the Deborah number over the Ohnesorge number is called the elastocapillary number $Ec \equiv De / Oh$. This number shows the relative importance of elastic forces to the visco-capillary effects. Elastic effects start to dominate as the elastocapillary number increases. In fragmentation for viscoelastic liquids as the filaments pinch off and go through a necking instability the radius of the filament in the necking region goes to zero $R \rightarrow 0$, which leads to high values of elastocapillary number and localized flow in the neck region that is dominated by elastic effects.

For gels and fluids with a temporary internal viscoelastic network, the region of high elastocapillary numbers can be considered as a region in which the external stresses (such as capillary pressures in the current scaling) can overcome the cohesive strength of the underlying permanent/temporary network. This may lead to a brittle like fracture in the network of the gel [33, 98].

Unlike the fragmentation of dilute viscoelastic liquids, the brittle-like fracture of soft gels is observed in finite strains. Figure 1-27(a) shows an example of casein gels rupturing in a Couette cell on a stress-controlled rheometer and forming cracks under a constant applied stress. Other examples include rupture of polymeric liquid

[35] and fracture of breast implants [34] in tension.

In all these examples, it is crucial to understand the mechanical response of the material up to the fracture point. Critical values of stress and strain at the rupture point also play an important role in many relevant applications. Understanding linear and nonlinear rheology of the casein gels helps us to develop a general rheological framework that can predict the performance of this class of biopolymer gels in extreme loading conditions. However, we also need to have knowledge about the damage accumulation in these materials. Damage accumulation is due to the irreversible rupture of individual fibers or protein strands in the network of these materials. The idea of damage in these gels is different from the idea of damping in rubber-like materials. The network softening/damping is a reversible process whereas the damage happens in an irreversible manner.

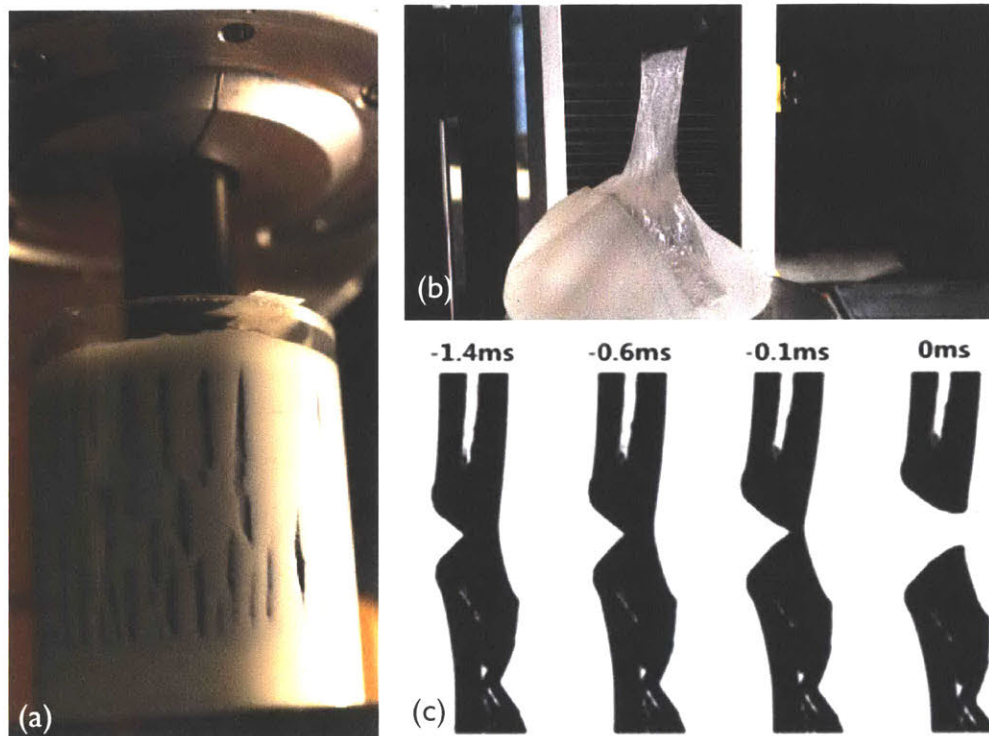


Figure 1-27: (color online). (a) Casein gels under a, constant stress, creep experiment. At a certain failure time macroscopic cracks start to appear in the material. (b) Silicone gel implant rupturing under a tensile test. Image taken from [34]. (c) A polymeric liquid fractures under tension by forming a propagating crack. Image taken from [35].

Damage accumulation is a known mechanism for describing the failure and rupture mechanics for different solids [99]. One of the pioneering studies in this field was performed by Basquin [36] on different metallic alloys. Figure 1-28 shows a summary of the rupture data that he presented in his seminal work. Different metals show a power law dependence between the value of the maximum stress at the rupture point and the number of loading cycles before the fracture. This power law behavior has been observed for many other materials and is widely referred to as the Basquin law [37].

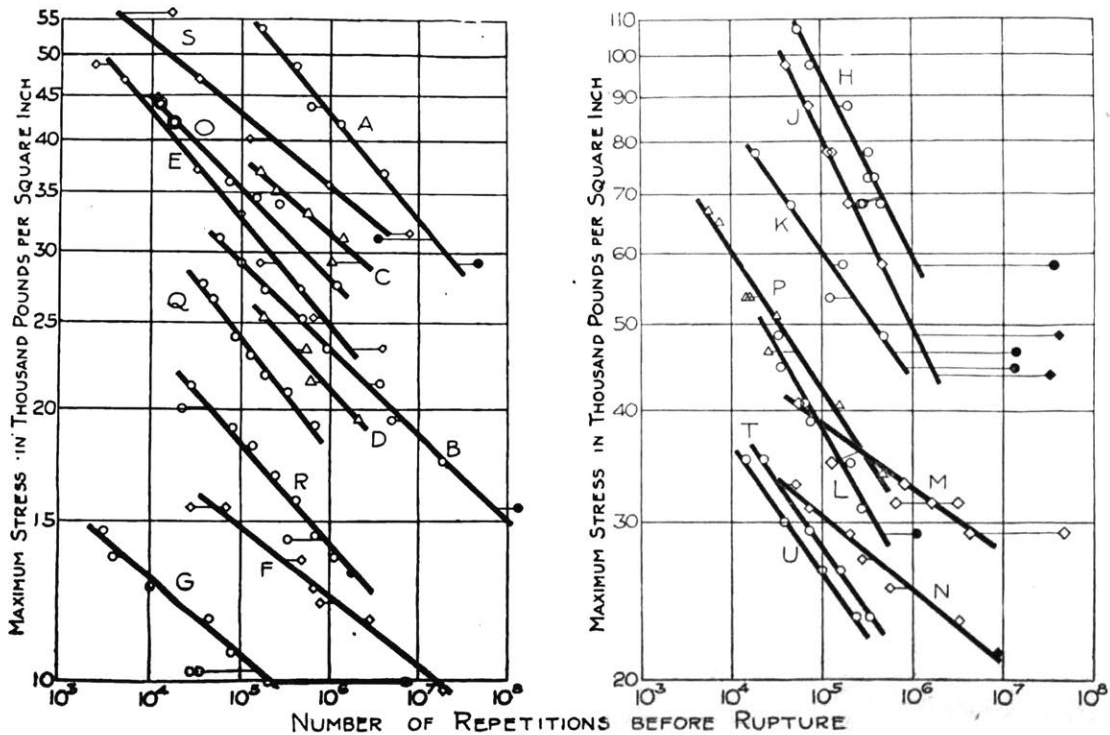


Figure 1-28: (color online). "Fracture toughness" of different metallic materials plotted by Basquin [36]. This is usually referred to as Basquin's law of fatigue [37].

A few years after Basquin, James Bailey (1890-1962) performed extensive series of strength studies on glass. Glass was a valuable commodity at that time for food and drink industry (1939 was well before the introduction of plastics and, for obvious reasons, there was a huge increase in glass demand after prohibition days were over). In his studies, Bailey tried to correlate the strength of glass from some tensile tests to other tests with different loading/deformation protocols. Figure 1-29, for example, shows a summary of his results. As stress rate increases the strength of the material at the fracture point increases. He was able to develop a simple model for damage accumulation that helped him correlate all the different results together. The suggested model for damage accumulation is now known as Bailey durability criteria and it is shown that this can be one of the most general models for correlating fracture data. Freeds and Leonov [39] have recently shown that the Bailey criterion is universally valid for a Markovian stochastic process of

damage which means: irreversibility of the damage process, independence of the various damage accumulations and absence of memory effects in every damage accumulation.



James Bailey
(1890-1962)

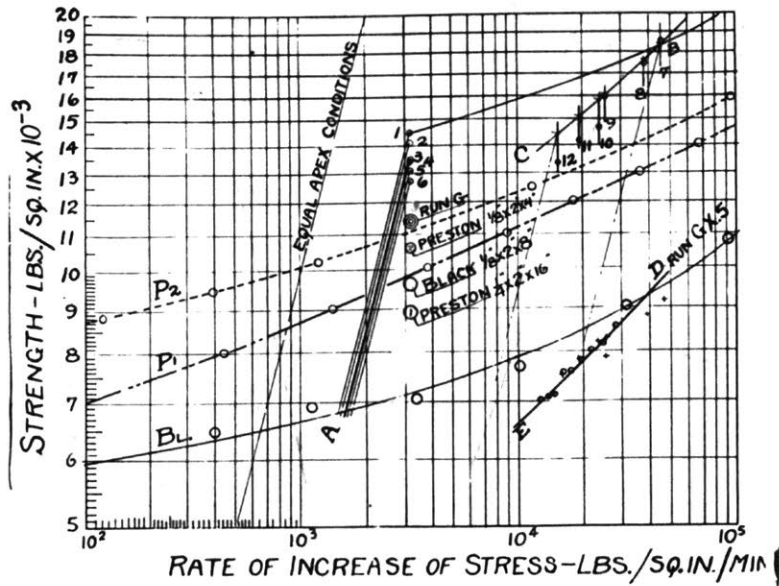


Figure 1-29: (color online). Strength of different glass samples at the fracture point while they experience an increasing load with a constant stress rate. Results from these tests were first analyzed by James Bailey (1890-1962) [38]. His analysis is now referred to as the Bailey criterion [39].

In this thesis we aim to study the dynamics of soft gels and elastic networks in the rupture process. Combining linear and nonlinear rheology, we develop a framework to study the behavior of these materials in large deformations. Our proposed framework is then combined with the concept of damage accumulation and, using the Bailey durability criterion, we provide predictions for the critical stress and strain at the rupture point which are compared with our experimental measurements.

We begin by first introducing our methods of material characterizations in the next chapter. Our rheological are then used in the following chapters to understand the phenomena of fragmentation and fracture for complex fluids.

Chapter 2

Instruments, Test Fluids and Experimental Procedures and Challenges

Accurate and minute measurement seems to the non-scientific imagination, a less lofty and dignified work than looking for something new. But nearly all the grandest discoveries of science have been but the rewards of accurate measurement and patient long-continued labor in the minute sifting of numerical results.

Lord Kelvin

2.1 Scope

In this chapter we present a detailed description for the instruments used in either shear or elongational rheometry. We will focus more on the challenges of performing elongational rheometry for dilute solutions. A brief description of the tested liquids/gels and the preparation procedures will be presented. We will introduce a dimensionless monogram that provides a quantitative description of merits and limits of the described instruments for different liquids.

2.2 Introduction

Rheological measurements for different materials requires a quantitative knowledge of the involved instruments and their corresponding limitations. Studying the rheological response of materials under shear deformations can help us in understanding their behavior in different shear-dominated flows/processes. At the same time, viscoelastic materials are known to show unusual behavior when deformed in an elongational flow field. Commercial rheometers have been optimized through years for precise measurements of shear properties of different materials over a wide range of deformation rates [100]. This level of accuracy in shear rheometry is hardly matched in elongational rheology measurements [60]. This is mainly due to the complexities involved with designing a purely elongational flow field. For highly elastic materials, such as polymer melts or high concentration solutions of high molecular weight polymer chains, several methods are suggested in the literature [101]. However, elongational rheometry for many other fluids, which are considered to be weakly viscoelastic, is an ongoing challenge [102, 24].

Quantifying the elongational rheology of weakly viscoelastic fluids can help us understand the complex fluid dynamical behavior of such materials, which arises due the coupling between microstructure and flow [103, 71]. Mucus, saliva, synovial fluids, and blood are just a few representative examples of such fluids, and many of our vital physiological functions depend on the flow behavior or, in other words, the rheology of these microstructured biomaterials [104, 105, 106]. Similarly, in many important industrial applications such as paint coating, inkjet printing, emulsification and anti-mist fuel combustion, the rheological properties of weakly viscoelastic liquids play a significant role [107, 108, 109, 110].

One important characteristic behavior of viscoelastic liquids is the resistance that the underlying microstructure exhibits to deformation in elongational flows. This resistance is characterized by the extensional viscosity and the value of η_E for viscoelastic solutions can be several orders of magnitude higher than the corresponding shear viscosities [111, 73, 112, 60]. In many biological and industrial applica-

tions such as flow of biological fluids through contractions and valves, the flow of liquid foodstuffs through orifices [113] or atomization of paints in an air-spray nozzle the kinematics of the flow is dominated by elongational deformation leading to dramatic effects of the extensional rheological properties on the flow.

Whether it is the fracture of a gel, in which the connecting strands in the gel network stretch and elongate prior to the rupture, or the fragmentation of a viscoelastic liquid in the atomization process, in which the capillary forces generate an elongational flowfield inside the liquid filaments, understanding the rheological properties of the material in both shear and elongation is of crucial importance. In this chapter, we try to introduce the test materials that are used as test fluids/gels in our experiments and also present a detailed description for different instruments/rheometers that are used to measure the rheological properties of these materials.

2.3 Test Fluids

The test fluids studied in our experiments are all drawn from a well-known class of dilute polymer solutions that show elongational thickening but also exhibit negligible shear thinning [114]. This class of fluids has been widely used to understand the effect of extensional thickening on complex fluid phenomena and separate these effects from other competitive effects rising from nonlinear shear thinning behavior or inertia [115]. Poly (ethylene oxide) (PEO) is widely used as a model viscoelastic fluid in the scientific literature, because the molecules are readily water soluble, available in a wide range of molecular weights and relatively immune to shear-induced or photo-induced degradation. This has helped many researchers develop experimental systems to understand the effect of a deformable material microstructure on the dynamics and instabilities of complex fluids since many of these phenomena are driven by the enhanced values of elongational viscosity [116, 117, 118, 119, 120, 121].

In our first series of experiments we focus on the effects of extensional properties

on atomization and fragmentation for dilute polymer solutions. It is known that dilute polymer solutions such as saliva, fuel anti-misting agents, resins, paints and inks used in inkjetting processes mostly resist fragmentation by enhanced extensional viscosity [122, 123, 124, 108]. Thus, aqueous PEO solutions in moderately viscous solvents were the rational choice for studying the effects of elongational properties on fragmentation, whilst also excluding the confounding effect of shear thinning. We therefore focus on these results here as the materials should be readily available and the results reproducible by future researchers. In each chapter we will provide a detailed description for all the test liquids that were used.

2.3.1 PEO Solutions

In order to quantify the performance of different configurations for extensional rheometry of weakly viscoelastic fluids, we prepared four different dilute polymeric solutions and monitored their flow behavior in hyperbolic channels (EVROC) and in the jet breakup process (ROJER). In addition to these four test fluids, we also tested a concentrated high molecular weight fluid in both the EVROC and CaBER devices to illustrate the similarities and differences when a markedly different viscosity range is probed. Table 1 summarizes the properties of all these test fluids. The viscoelastic fluids are prepared by dissolving small amounts of poly(ethylene oxide) (PEO) of three different average molecular weights (300 kg/mol, 1000 kg/mol, and 4000 kg/mol respectively) in a 60-40%wt. water-glycerol solvent ($\eta_s = 3.0$ mPa.s). The polymer overlap concentrations are respectively $c^* = 0.28\%$, 0.14% and 0.08% for the 300K, 1000K and 4000K solutions. Values of c^* and L (the finite extensibility parameter) are estimated based on the scalings with average molecular weight that are evaluated by Haward et al. [116] for PEO solutions ($L \sim M_w^{1-\nu}$ in which $\nu = 0.56$ for a reasonably good solvent such as PEO in water-glycerol mixture). It is known that at really high deformation rates, flexible polymer chains can be physically degraded due to their finite extensibility [125] and the viscoelastic be-

havior of many complex fluids decrease with time. Thus for each ROJER or EVROC experiment a fresh sample was used and the elapsed time gap between the EVROC and ROJER tests was kept to less than 30 minutes, in order to minimize the possibility of degradation between tests performed with different devices.

Table 2.1: Properties of the viscoelastic test fluids. Different concentrations of poly (ethylene Oxide) (PEO) at three different molecular weights were dissolved in the Newtonian solvent (60-40% wt. Water+Glycerol $\eta_s = 3.0\text{mPa.s}$). Definitions of the Deborah number (De), Ohnesorge number (Oh), Elasticity number (El) and Elasto-capillary number (Ec) that can be spanned by the fluids are described in the text.

M_w	c	c/c^*	$\eta_0[\text{mPa.s}]$	$\tau_E[\mu\text{s}]$	L	De	Oh
0.3M	0.01%	0.036	3.30	72	27	0.72	0.075
1M	0.01%	0.07	3.40	425	50	4.5	0.075
4M	0.0025%	0.03	3.10	957	100	10.5	0.075
4M	0.05%	0.66	3.37	2045	100	21.9	0.095
4M	1%	13.22	700	5.5×10^4	100	595	17

In order to systematically study the effects of viscoelasticity on the atomization, four different dilute polymer solutions were selected as test liquids. All of these solutions are again made by dissolving small amounts of Poly(ethylene oxide) or (PEO) with $M_w = 3 \times 10^5 \text{g/mol}$ and $1 \times 10^6 \text{g/mol}$ respectively (purchased from Sigma Aldrich) in a water-glycerol (60-40 wt.%) solvent ($\eta_s = 3.2\text{mPa.s}$) and the resulting viscometric properties are summarized in Tables 2 and 3.

Table 2.2: Rheological properties of the viscoelastic spray test fluids. Two different concentrations of Poly(ethylene oxide) (PEO) at two different molecular weights were dissolved in the Newtonian solvent (Water+Glycerol 60-40 wt.%) which has a viscosity $\eta_s = 3.2\text{mPa.s}$. The dimensionless parameters Oh and De are defined in the text (see Eqs. (8) and (9)) and are evaluated using $\rho = 1103\text{kg/m}^3$ and $R_l = 85\mu\text{m}$. All the measurements were performed at 25°C .

Mw	c	c/c^*	$\eta_0[\text{mPa.s}]$	$\tau_E[\mu\text{s}]$	L	De	Oh
300K	0.01%	0.036	3.21	60	27	0.2	0.04
300K	0.1%	0.36	3.32	360	27	1.3	0.04
1000K	0.01%	0.07	3.22	996	50	3.6	0.04
1000K	0.05%	0.37	3.31	2800	50	10.0	0.04

Table 2.3: Rheological properties of the viscoelastic fluids tested in Figures 2-3 and 2-4. Two different concentrations of Poly(ethylene oxide) (PEO) at two different molecular weights were dissolved in the Newtonian solvents (water for the 5000K PEO solution and Water+Glycerol 60-40 wt.% for the 2000K solution). The dimensionless parameters Oh and De are defined in the text (see Eqs. (8) and (9)) and are evaluated using $\rho = 1103\text{kg/m}^3$ and $R_0 = 3\text{mm}$. All the measurements were performed at 25°C .

Mw	c	c/c^*	$\eta_s[\text{mPa.s}]$	$\eta_0[\text{mPa.s}]$	$\tau_E[\text{ms}]$	L	De	Oh
5000K	0.15%	1.5	0.9	2.12	36.4	112	1.72	0.005
2000K	0.01%	0.1	3.2	4.21	2.1	71	0.1	0.01

2.3.2 Casein Gels

In the gel fracture tests we needed a gel which is easy to prepare and has relatively constant properties over the time of different experiments (sometimes as long as few days). Acid-induced protein gels with different types of mechanical properties are known to be good test gels for the mentioned purposes. They are prepared by dissolving Caseinate powder (Firmenich) at different concentrations (0.5% – 12%) in deionized water under gentle mixing at 600 rpm and at constant temperature $T = 35^{\circ}\text{C}$. Homogeneous gelation is induced by dissolving a certain amount (0.125% – 12%) of glucono- δ -lactone (GDL, Firmenich) in the protein solution [126]. While still liquid, the protein solution is poured into the gap of a Couette shear cell connected to a strain-controlled rheometer (ARES rheometer). Gelation is achieved within 12 hours after which either a constant strain or a constant shear rate is imposed while the stress is monitored. In both cases, images of the gel are recorded simultaneously to rheology (Canon, EOS7D).

2.4 Shear Rheology Measurements

The shear rheology of the PEO solutions were measured using a stress-controlled rheometer (ARG2; TA Instruments, with either a cone and plate geometry or with a Couette cell), at low shear rates ($10\text{s}^{-1} \leq \dot{\gamma} \leq 1000\text{s}^{-1}$), and using a micro-fluidic rheometer (m-VROC from Rheosense) at higher shear rates ($1000\text{s}^{-1} \leq \dot{\gamma} \leq 200,000\text{s}^{-1}$). Basics of stress-controlled shear rheometry using cone-plate or Couette cells are explained in great detail by Macosko [100]. A description of micro-fluidic measurements and analysis for both shear and elongational rheology will be provided in the next sections of this chapter.

For the casein gels, it is important to visualize the gel prior/during the fracture. Thus, we designed and machined several Couette cells. The outer walls are made of transparent plexi-glass and the inner bobs are made of Delrin. Figure 2-1 (a) shows a drawing of one of the designed cells and Figure 2-1(b) shows the final

assembled version on the ARES (strain-controlled) rheometer. The Casein pre-gel solution is poured in the Couette cell and within the gelation process, the gel is always in contact with the inner/outer walls. After a certain amount of time (3-4 hours for the 4%Casein-1%GDL gel) a white yoghurt-like gel is formed (Figure 2-1(c)). The ARES rheometer is a strain-controlled configuration that changes the strain by precise control of the angular position of the outer wall $\Omega(t)$ and monitors the gels stress response by monitoring the torque $M(t)$ exerted on the inner bob. Figure 2-2 shows a typical response of a 4%Casein-1%GDL gel during the gelation process. The gel is under a linear ($\gamma_0 \ll 1$) oscillation $\gamma(s) = \gamma_0 \sin(\omega_0 s)$ at a fixed frequency ω_0 and the stress response of the gel $\sigma(s)$ is decomposed into elastic (in-phase) and loss (out of phase) moduli, $\sigma(s) = G'(\omega_0, t)\gamma_0 \sin(\omega_0 s) + G''(\omega_0, t)\gamma_0 \sin(\omega_0 s)$. The elastic and loss moduli start to increase close to the gelation point ($t \simeq 5000s$) and grow to constant values after $t \simeq 15000s$.

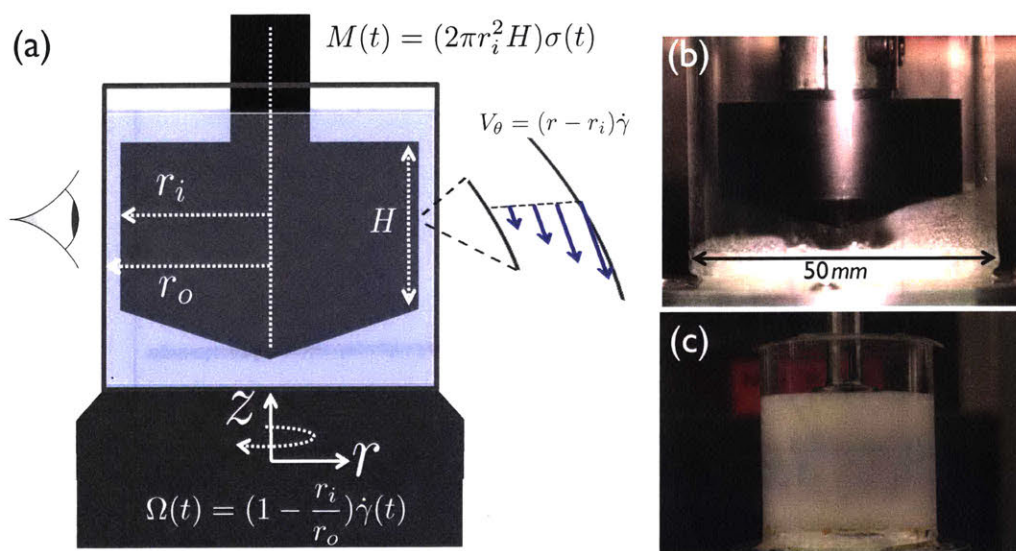


Figure 2-1: (a) and (b): Rheological data for Casein gels were obtained with an ARES-LS strain-controlled rheometer (TA Instrument) using a machined Couette cell made of an outer polished Plexiglas cup of height $H = 20.32$ mm and radius $r_o = 25$ mm which is rotating around a fixed inner bob of radius $r_i = 22.65$ mm made of Delrin, leading to a shear flow in a gap of 2.35 mm. (c) The casein gel formed in the Couette cell on the ARES rheometer.

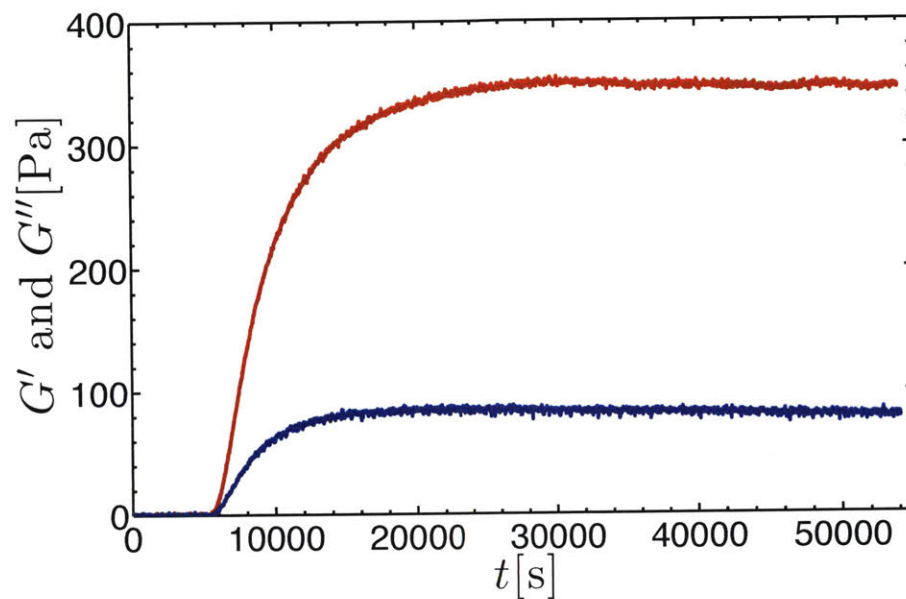


Figure 2-2: Mechanical response of the casein gel (4%casein-1%GDL) during the gelation process monitored by the ARES rheometer. The outer cylinder oscillation creates a linear shear flowfield in the gap that oscillates at a fixed frequency. The torque/stress ($M(t)$ or $\sigma(t)$) response of the gel is monitored vis the fixed inner bob. In and out of phase responses are converted to elastic (red dots) G' and loss modulus (blue dots) G'' respectively.

2.5 Elongational Rheology Measurements

2.5.1 Capillary Breakup Extensional Rheometry (CaBER)

From the early days of extensional rheometry [18] accurate measurement of elongational properties for a wide range of materials/liquids has been reported as an experimental challenge [73, 60, 20] due to the fact that there are few possible geometries/conditions in which uniaxial extensional flows dominate and shear effects are negligible. Although some known established devices such as FISER (Filament Stretching Extensional Rheometer[127]) or SER (Sentmanat Extensional Rheometer[128, 129]) have shown very promising results for sufficiently viscoelastic polymer melts and solutions, there are still many additional challenges for measuring the extensional rheology of very dilute solutions.

Bazilevsky et al. [74] showed that understanding the viscoelastic fluid dynamics of polymeric liquids undergoing capillary breakup can lead to accurate measurements of transient extensional rheology of these dilute solutions at relatively low relaxation times (specifically extensional relaxation times in the range $0.01 \leq \tau_E \leq 1s$). This principle is used in the CaBER instrument and has been studied extensively by many researchers [79, 130, 131, 132]. When two coaxial cylindrical plates are rapidly separated from each other, a liquid filament will be formed between the lower and upper liquid reservoirs. The smaller radius of the fluid filament compared to the radius of the two quasi-static reservoirs causes a higher capillary pressure ($\Delta P \sim \sigma/R(t)$) in the connecting ligament. This extra pressure drives an axial flow from the middle of the filament outward to both ends which progressively drains the filament volume into the reservoirs. The driving effect of capillary stresses inside the filament is resisted by either inertia (inertia-capillary regime) or viscous (visco-capillary regime) stresses in a Newtonian liquid. In polymeric solutions the capillary pressure can also be resisted by elastic stresses resulting in an elasto-capillary balance. For different fluid systems and filament dimensions all three effects of inertia, viscous, and elastic stresses may be in balance with the capillary pressure for some part of the thinning and breakup process [133, 79].

For low viscosity fluids in the initial stage of thinning the flow in the filament will be dominated by inertia; and the local diameter will thin down with a timescale set by an inertia-capillary balance (also known as the Rayleigh timescale):

$$\tau_R \equiv \sqrt{\rho R_0^3 / \sigma} \quad (2.1)$$

in which R_0 is the initial radius of the thinning filament. By a simple scaling argument from the balance of capillary pressure with the inertia terms in the equation of motion the time evolution of the filament radius can be derived to be of the form [42, 133] :

$$R(t) = 0.64 \left(\frac{\sigma}{\rho} \right)^{1/3} (1.95\tau_R - t)^{2/3} \quad (2.2)$$

The predictions from Equation (2.2) can be compared with measurements of the thinning filament radius in CaBER at early inertia-capillary stages (see the solid line in Figure 2-4).

A number of papers (see for example: [74, 78, 79]) have shown that as the filament thins down with time the kinematics of the local flow in the long thin filament evolves into a uniaxial extensional flow [$v_r = (-1/2)\dot{e}r$, $v_\theta = 0$, $v_z = \dot{e}z$] in which the strain rate is given by $\dot{e} = (-2/R(t))dR/dt$. The decrease in the diameter results in the strain rate increasing and the corresponding viscous ($\Sigma_{vis} = \eta\dot{e}$) or elastic ($\Sigma_{elastic} = \eta_E^+\dot{e}$) stresses in the filament become increasingly important. The viscous forces become significant when the ratio of the visco-capillary time-scale ($t_{vis} \sim \eta R(t)/\sigma$) compared to the inertia-capillary time scale ($t_R \sim \sqrt{\rho R(t)^3/\sigma}$) becomes of order unity, i.e. when the local Ohnesorge number becomes close to one (see also [133]):

$$Oh \equiv \eta / \sqrt{\rho\sigma R(t)} \sim O(1) \quad (2.3)$$

Viscoelastic effects can also become significant when the polymer relaxation timescale (τ_E) and the inertio-capillary timescale of the fluid become comparable, i.e. when

the local Deborah number is of order unity:

$$De \equiv \tau_E / \sqrt{\rho R(t)^3 / \sigma} \sim O(1) \quad (2.4)$$

Nonlinear growth in the elastic stresses (i.e. strain-hardening) becomes important when the local Weissenberg number $Wi = \tau_E \dot{\epsilon}$ in the filament exceeds $Wi \geq 0.5$.

Bazilevsky et al. [74] showed that for constitutive equations such as the Oldroyd-B model (in which the polymer chains are infinitely extensible) the elasto-capillary region results in an exponential decay of the filament diameter with time of the form:

$$D/D_0 = (GD_0/4\sigma)^{1/3} \exp(-t/3\tau_E) \quad (2.5)$$

where D_0 is the diameter of the filament, σ is the surface tension of liquid-air interface, G is the elastic modulus of the polymer in the solution ($G = nkT$ for a dilute solution) and τ_E is the relaxation time in the Oldroyd-B model for the liquid. Both experiments and theoretical analyses have shown that because the thinning process is self-similar in the elasto-capillary regime the Weissenberg number remains constant with a value equal to $Wi = 2/3$ [78, 79].

The exponential decay of the filament diameter in CaBER given by Equation (2.5) has been reported by many in the literature for a variety of polymeric liquids used in different applications [134, 135, 131, 136, 76]. However the exponential decay is predicated on infinite extensibility of the polymer chain and as a consequence the thinning filament will never breakup which is, of course, unphysical. Entov and Hinch [78] showed that for constitutive equations which incorporate finite extensibility (such as the FENE-P model for dilute polymer solutions) the elasto-capillary balance and exponential decay in the diameter holds on intermediate timescales but at later times, very close to pinch off, the polymer chains can reach their maximum elongation and the extensional viscosity reaches a plateau. The filament then begins to thin down linearly in a visco-capillary manner once more but with a form given by $D \sim (\sigma/\eta_{E,\infty})(t_b - t)$ where t_b is the final breakup time.

Figure 2-3 shows an example of a successful CaBER test performed for a 5000K

PEO solution at a concentration $c = 1.5wt.\%$. The montage of images show an axially uniform filament (formed between two hemispherical end-caps) which is thinning with time and the measured diameters are fitted best by an exponential expression for a wide range of times ($200ms \leq t \leq 800ms$ in Figure 2-3). Regression of Equation (2.5) enables a precise measurement for the relaxation time for this solution ($\tau_E \simeq 103ms$). However there are also initial and final regions visible in which the exponential decay does not fit the data anymore. In the initial stage (yellow part of Figure 2-3, which endures for a few capillary time scales $\sim 6\tau_R$) the polymer chains have not felt the strong stretching flow yet and the balance is between capillarity and a mixture of inertia and viscous forces combined. On the other hand, at long times the polymer chains reach their maximum extensibility so that they can not extend any more and the polymer contribution to the elongational viscosity will saturate. The data in the orange-shaded region of Figure 2-3 show that the filament diameter deviates from exponential thinning due to finite extensibility and the diameter sharply falls to zero in a linear manner. Also in the final image of the montage in Figure 2-3 it is possible to observe the so-called "beads-on-a-string structure" [137] at the final stages in which the polymers in the connecting filaments between the beads reach their finite extensibility limit and enter a terminal thinning regime [131].

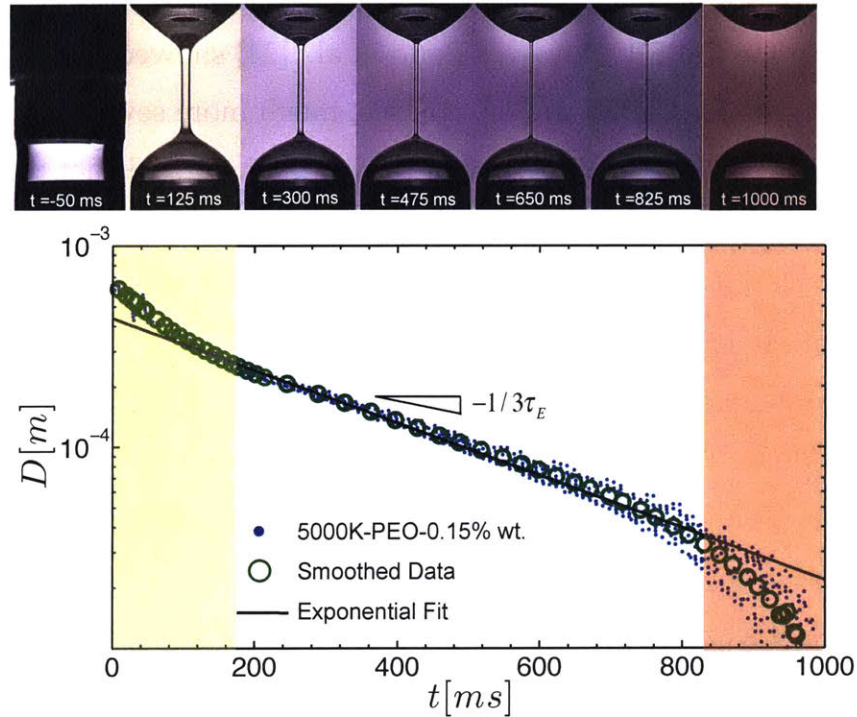


Figure 2-3: CaBER (Capillary Breakup Extensional Rheometry) for a semi-dilute Poly(ethylene oxide) solution (molecular weight $M_w = 5 \times 10^6 \text{ g/mol}$ and 0.15 wt.% concentration, $c/c^* = 1.5$), $Oh = 0.005$, $De = 1.72$. The blue dots are the oversampled data from the laser micrometer while the green circles are the bin-averaged smoothed data. The visualized images of the actual filament thinning with time are at the top. The filament goes through three significant regimes: the initial region (shaded yellow) is still affected by fluid inertia; as the liquid thread thins down under the action of capillary pressure the elastic stresses become increasingly important and an elasto-capillary region emerges. The solid black line indicates an exponential decay with time described by Equation (2.5) (the theoretical prediction for elasto-capillary regime). Finally when the polymer chains in the filament approach their maximum extensibility the diameter approaches zero in a linear manner (shaded orange region).

Ideally every thinning viscoelastic filament would reach an elasto-capillary balance close to pinch off and the CaBER instrument should be able to measure low relaxation times even for very dilute solutions. However there are a number of technical issues which inhibit such measurements [24, 82]. Firstly, it is possible

that the relaxation time is so small that the local Deborah number will approach unity only at very low filament diameters that are below the resolution of the laser micrometer in the CaBER. However Rodd et al. [24] showed that the constraint on measurements for CaBER are, in practice, much more severe than the above-mentioned limit. Using a dimensionless map, they showed that measurements become very hard if the values of both initial Deborah and Ohnesorge numbers (based on the initial radius of the sample plates(R_0)) fall below unity. For a $6mm$ diameter plate and an aqueous solution, measurements will be hard if both the relaxation time and the shear viscosity are below $1ms$ and $60mPa.s$ respectively. This restriction is due to the fact that as the end-plates are separated axially from the initial gap to the final gap there will be shape oscillations in the hemispherical end caps which persist for multiples of the capillary time and these oscillations introduce periodic fluctuations to the laser micrometer readings. If the filament breaks up before these oscillations damp away then the entire life of the thinning filament is corrupted by these end effects. The filament breakup time scales with the larger of the polymer relaxation time (τ_E) or the initial viscous timescale ($t_{vis} = \eta R_0/\sigma$) depending on the magnitude of the elasto-capillary number $Ec \equiv \tau_E \sigma/\eta R_0$. If both of these timescales are shorter than the capillary time-scale of the filament (i.e. $Oh_0 \equiv t_{vis}/\tau_R = \eta/\sqrt{\rho R_0 \sigma} \leq 1$ and also $De_0 \equiv \tau_E/\tau_R = \tau_E/\sqrt{\rho R_0^3/\sigma} \leq 1$) then the filament will break up before the oscillations damp away and the CaBER instrument will fail to report meaningful readings.

Recent work [131, 82] has shown that by modifying the initial rise of the plates to a so-called "slow retraction method (SRM)" the perturbative effects of these inertia-capillary oscillations can be minimized and more accurate measurements are possible for dilute solutions with this new modified approach. However the appearance of the beads-on-a-string structures in CaBER can not be avoided even using the SRM method and Campo-Deaño et al. [82] have proposed following the entire dynamics by high-speed imaging instead of relying on a centrally located laser micrometer read-out alone. An example of a beads-on-a-string structure appearing in a CaBER test with a low viscosity polymer solution is shown in Figure

2-4. As can be seen from the image montage and from the measured diameter $D(t)$ the initial stage is mainly dominated by an inertia-capillary balance (the solid line fitted to the initial data is the fit from inertia-capillary balance, Equation (2.2)) while the rest of the data in the filament thinning region is polluted by the progressive appearance of different generations of beads which appear as the result of an iterated elastic instability [138].

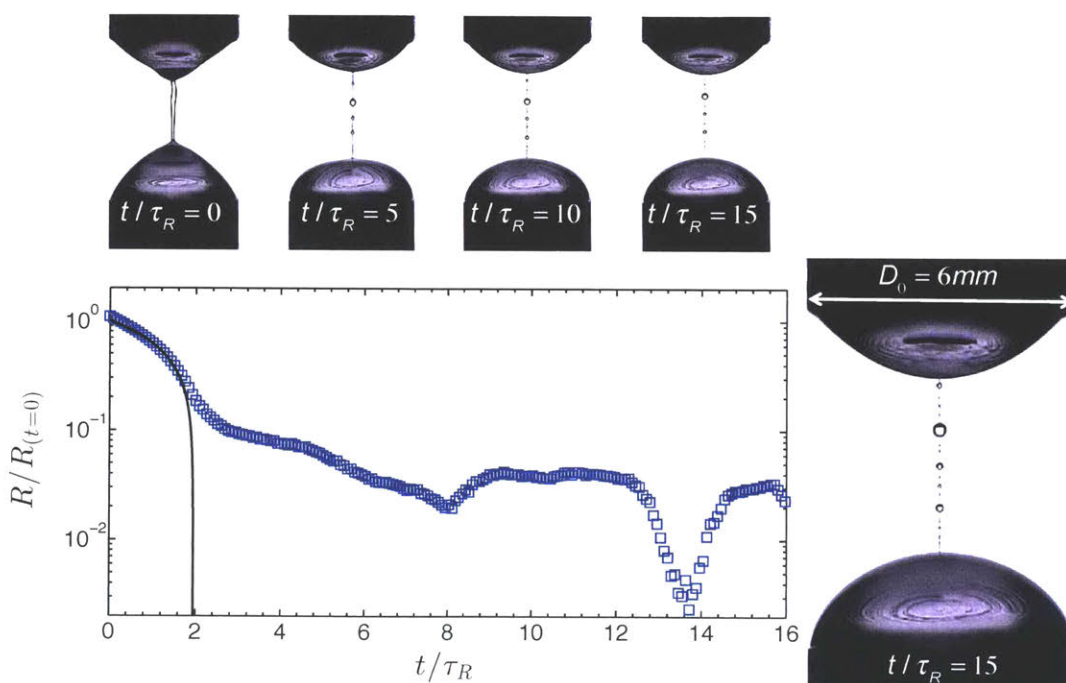


Figure 2-4: CaBER (Capillary Breakup Extensional Rheometry) for a dilute poly ethylene oxide solution ($M_w = 2 \times 10^6 \text{g/mol}$ and 0.01 wt.% concentration $c/c^* = 0.1$), $Oh = 0.01$, $De = 0.1$. The blue squares show the data from the laser micrometer; the normalized filament diameter is plotted versus time normalized by the capillary time-scale ($\tau_R \equiv \sqrt{\rho R_{(t=0)}^3 / \sigma} = 6 \text{ms}$). The solid line is a fit from the expected predictions for inertia-capillary regime (Equation (2.2) in the text). The visualized images of the actual filament thinning with time are shown above. The beads-on-a-string structure that appears in the final stages (picture on the right) makes the measurements of relaxation time almost impossible as the midplane diameter rises and falls with time.

2.5.2 Rayleigh-Ohnesorge Jetting Extensional Rheometry (ROJER)

While the new SRM approach described by [82] can enable CaBER measurements for relaxation times down to $240\mu s$, and recent work by Vadillo et al. [81] has described an approach that extends measurements to less than $80\mu s$, there is still a need for alternative instrumentation that enables facile measurements of low relaxation times for the wide variety of weakly viscoelastic liquids used in many industries such as paint coating, atomization, food and consumer products, inkjet deposition and microfluidic diagnostics used with biopolymeric fluids.

One potential method for probing the elongational properties of a non-Newtonian fluid is to follow the dynamics exhibited during the capillary breakup of a liquid jet. From the pioneering works of Savart [9], Plateau [139] and Rayleigh [80] on the breakup of Newtonian jets there has been a great interest among many researchers in understanding all aspects of this phenomenon [140, 141]. Although the nonlinear capillary phenomenon driving jet breakup has motivated many to develop imaging techniques to capture the phenomena [142, 28, 143] it has also prompted a few researchers to use the process as a tensiometer for evaluating the surface properties of different liquids [144, 145]. Little work focused on non-Newtonian effects until Middleman and coworkers [146, 147, 148] studied the effects of viscoelasticity on jet breakup. Their linear stability analysis showed that viscoelastic effects enhance the instability in the linear (small strain) region. This appears to be a counterintuitive result; however, later nonlinear studies [149] showed that while viscoelasticity enhances the initial disturbance growth, in the nonlinear stage the elongation of the polymer chains resist the capillary thinning process and thus the jet will breakup at longer lengths/times compared to Newtonian liquids of comparable shear viscosities. This enhanced resistance of the viscoelastic jet to breakup in the nonlinear region was studied experimentally by Schümmer and Tebel [150, 151] by perturbing the jet at set frequencies and capturing the resulting filament thinning behavior with high-speed photographic imaging. Their results showed that it is possible to use measurements of the filament diameter evolu-

tion with time in the thinning necks between beads to make estimates of the relaxation time of the fluid using Equation (2.5). Later studies by different authors [152, 153, 154, 83, 155] have further developed the idea of using a thinning viscoelastic jet as an elongational rheometer.

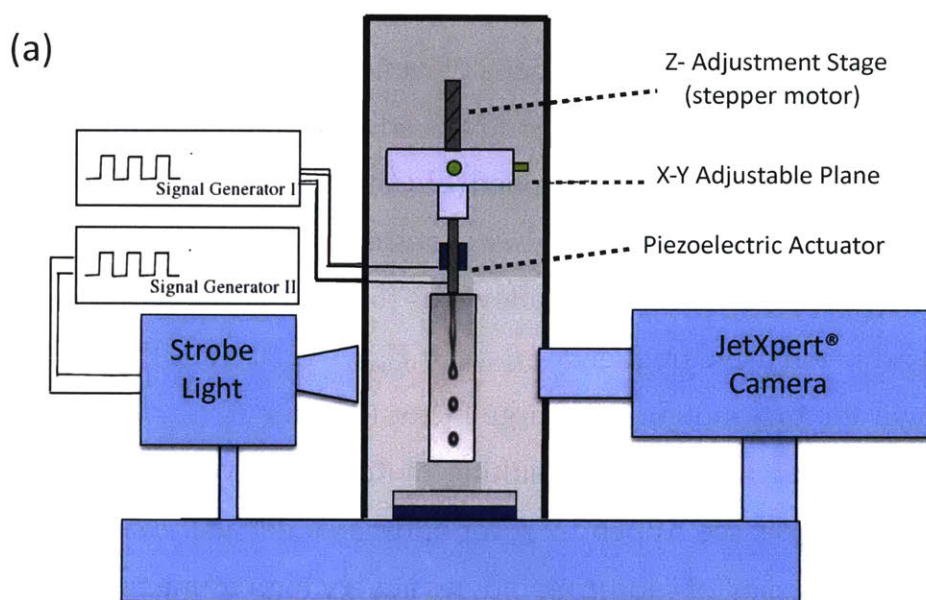


Figure 2-5: (a) The ROJER (Rayleigh-Ohnesorge Jetting Extensional Rheometer) setup. The liquid jet is perturbed by a piezo-electric actuator and then its motion is slowed down and captured using the stroboscope imaging setup.

The ROJER setup is shown in Figure 2-5. A high pressure syringe pump (PHD ULTRA-4400 from Harvard Apparatus) pushes the test fluid through a $150\mu m$ diameter ceramic nozzle. Periodic perturbations are imposed on the fluid before entering the nozzle via an annular piezoelectric actuator. The imposed perturbations introduce very small sinusoidal modulations to the fluid jet with amplitudes less than 1% of the jet diameter over a user-selectable range of frequencies ($0.1Hz \leq f \leq 1 \times 10^5 Hz$). If the wavenumber $k = 2\pi/\lambda$ (where λ is the wavelength) of the imposed perturbations lies in the unstable region of the Rayleigh-Plateau

instability then the amplitude of these modulations will start to grow exponentially with time as the waves are convected downstream with the jet. Due to the periodic nature of the perturbation, the jet modulation is periodic and wave-like with crests and troughs appearing at a frequency identical to the drive frequency of the piezoelectric actuator. This enables us to use stroboscopic imaging to avoid the common challenges of imaging these rapid time-varying phenomena. High speed imaging of jet breakup requires capturing movies at high frame rates and high magnification, consequently the images often have low resolutions or poor illumination due to physical limitations of cameras at these high frame rates. The strobe imaging setup used in this study is adopted from an inkjet visualization device made by JetXpert. The strobed LED light can generate very short and bright light pulses (with less than $1\mu s$ exposure duration) over a wide range of frequencies ($0.1 - 1 \times 10^5 Hz$). This allows us to tune the strobe frequency and set it very close to the drive frequency ($f_{strobe} = f_{piezo} - \Delta f$). Thus the captured movie slows down the real motion by a large factor (e.g. for $f_{piezo} = 6000 Hz$ and a frequency shift of $\Delta f = 0.1 Hz$ the resulting motion is slowed down by a factor of $\Delta f / f_{piezo} \sim 1/60,000$; see Appendix A for additional details). Using this approach we avoid the necessity of capturing movies at very high frame rates and with sufficient memory we can capture sharp and high resolution time-resolved images (1024×778 pixels) of the jet breakup process (see the movie in Supporting Information).

The apparent jet velocity in the captured movies (denoted by V_{app}) is calculated from the expression:

$$V_{app}[m/s] = MF \cdot V_{dig} \cdot FR \quad (2.6)$$

where MF is the magnification factor of the optics in μm per pixel, V_{dig} is the digital velocity of the jet (in pixels traveled per frame), and FR is the frame rate of the captured movie (in frames per second). Although the relationship in Equation (2.6) can be used to find the apparent velocity of a wave crest or droplet from the digital velocity, as a result of the strobe effect the apparent velocity is not the real

velocity at which the fluid is convected. The real jet velocity (assuming almost uniform velocity profile in the jet cross section) can be directly calculated from the flow rate of the pump:

$$V_j = Q/\pi R_0^2 \quad (2.7)$$

where Q is the volumetric flow rate and R_0 is the measured radius of the unperturbed jet after exiting the nozzle and the possible die swell region. Note that the velocity profile will become close to uniform very soon after leaving the nozzle due to the contrast between the air and fluid viscosity and the stress continuity condition at the interface between the air and liquid (see [148]). The real velocity and the apparent velocity are connected to each other by the strobe principle [156] (see Appendix A for derivation):

$$V_{app} = \frac{\Delta f}{f_{piezo}} V_j \quad (2.8)$$

where, as mentioned before, f_{piezo} is the drive frequency and $f_{piezo} - \Delta f$ is the strobe frequency. Similarly to calculate the real elapsed time over which the fluid particle has been moving away from the nozzle we only need to know the axial distance traveled (Z) and from that the time of flight can be calculated:

$$t = Z/V_j \quad (2.9)$$

where Z is the axial position and is equal to $Z_0 + \Delta Z$ in which Z_0 is the location of the top line of the image frame and ΔZ is the relative distance measured from this reference point. This can be measured by precise position tracking of the stepper motor which moves the nozzle that is mounted on a one axis translation stage (see Figure 2-5(a)). Although Equations (2.6) and (2.8) show how the real and apparent velocities are connected, it is more convenient (and also less prone to error propagation) to calculate the time of flight for a fluid element exiting the nozzle by simply using Equations (2.7) and (2.9). Given a specified flow rate (controlled by the syringe pump) the real velocity of the jet can be measured and the actual

elapsed time of flight is calculated by Equation (2.9).

For the instability of interest, i.e. Rayleigh-Plateau instability, the perturbations will be convected downstream with the jet velocity and our assumptions for using Equation (2.9) are correct. This is a result of the fact that instability is convective in nature and theoretical analysis shows that (over the range of tested Weber numbers) there are no absolute instabilities, in which perturbations increase in amplitude at all positions in the jet (see [157] for additional details). Thus the imposed perturbation at a given frequency f_{piezo} will make waves with wavelength $\lambda = V_j/f_{piezo}$ which are convected away from the nozzle with the jet velocity V_j . This means that the dimensionless wavenumber of the imposed disturbance is equal to:

$$kR_0 = 2\pi f_{piezo}R_0/V_j \quad (2.10)$$

in order to see these waves grow rather than decay with time it is crucial to keep the range of the disturbance in the instability margin which lies between $0 \leq kR_0 \leq 1$ [158].

Once the movies have been recorded the captured images are analyzed using image processing codes written in MATLAB and the evolution of the liquid filament diameter with time can be calculated using an edge detection algorithm.

Figure 2-6 shows the measured data from a jetting experiment performed with a very dilute low molecular weight PEO solution (300K PEO $c/c^* = 0.036$). Snapshots of the jet are captured in both the linear and nonlinear regions at different times (Figure 2-6(a)). The imposed perturbations at the nozzle lead to the appearance of waves which are advected to the downstream with a velocity equal to the jet velocity (V_j). As the jet travels further away from the nozzle and the amplitude of the wave grows with time, one can select a Lagrangian point (e.g. a point P at the bottom of a trough) traveling with the jet speed ($Z_P = V_j t$) and record its diameter evolution $D_p(t)$ with time (Figure 2-6(b)). As we show in Figure 2-6(b) this capillary thinning of a fixed Lagrangian element can be described in both the linear and non-linear regions. The initial linear variation is a consequence of the growing

Rayleigh-Plateau instability and is described by the predictions from linear stability analysis (dashed line in Figure 2-6(b)):

$$D_P/D_0 = 1 - \delta \exp(\alpha t) \quad (2.11)$$

in which δ is the ratio of the imposed initial perturbation to the jet diameter ($\delta \equiv d_{\text{perturbation}}/D_0$) and α is the growth rate of the instability derived from the dispersion relation for the Rayleigh-Plateau instability for viscoelastic jets (the details of the linear stability analysis [40] are reviewed in Appendix B).

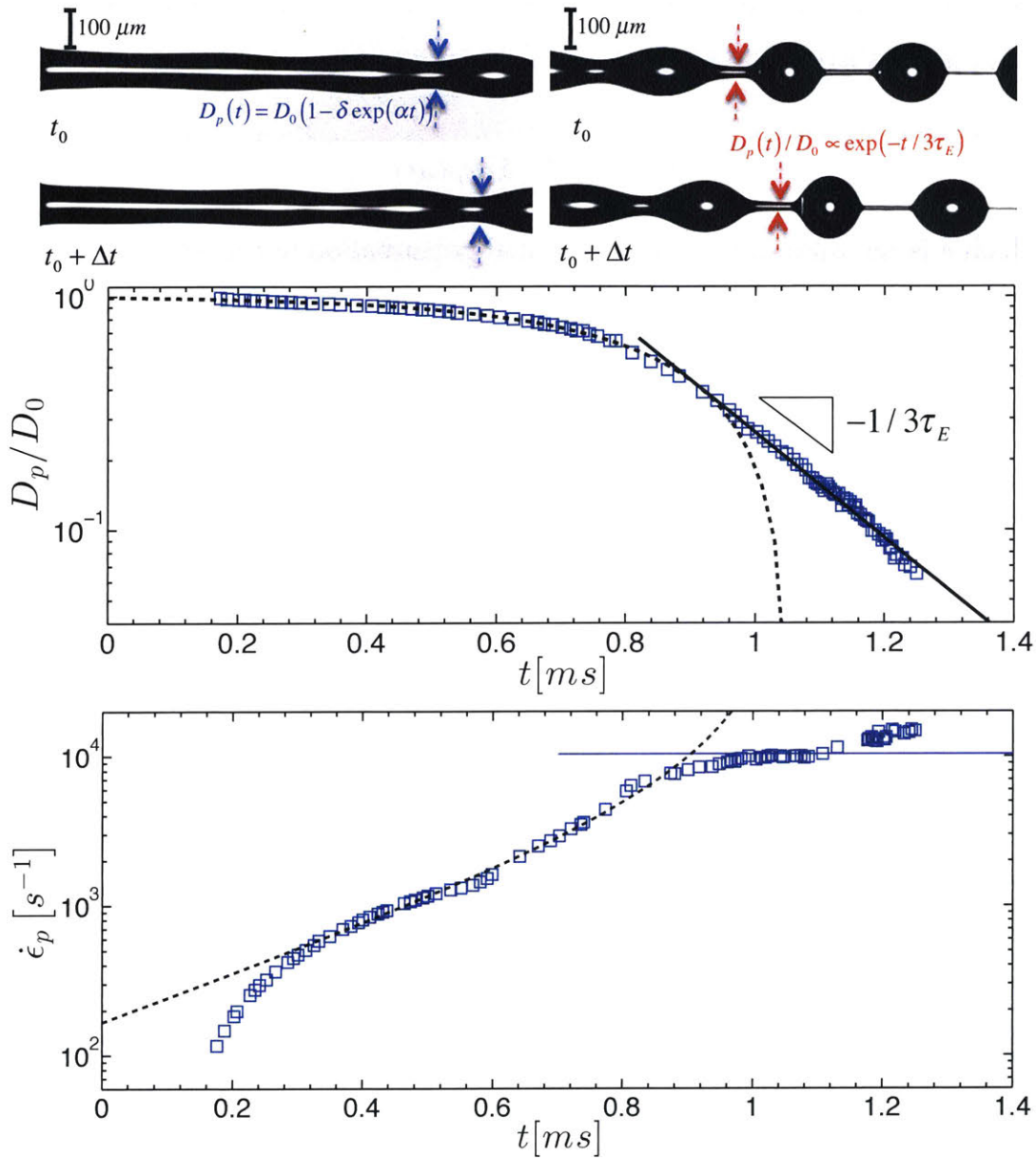


Figure 2-6: Rayleigh-Ohnesorge Jetting Extensional Rheometry (ROJER) analysis for the 300K-PEO solution ($c/c^* = 0.036$); $We_j = 16.9$, $kR_0 = 0.8$, $Oh = 0.075$, $De = 0.72$;(a) Visualized images of the jet going through Rayleigh-Plateau instability; both the linear stage of the instability (left) and the nonlinear stage (right) were imaged using the strobe camera. (b) The measured values for the filament neck diameter plotted against time (blue squares). The dashed line is the fit from the linear stability analysis ($D_p/D_0 = 1 - \delta \exp(\alpha(We, Oh, De)t)$ with $\delta = 0.01$). The solid black line indicates exponential decay with time described by Equation (2.5) as the theoretical prediction for elasto-capillary regime. From fitting the exponential thinning region, the value of the relaxation time is found to be equal to $\tau_E = 60\mu s$. (c) Strain rate in the filament neck ($\dot{\epsilon}_p \equiv (-2/D_p(t)) dD_p(t)/dt$) versus time. The calculated values show a plateau at a critical strain rate equal to $2/3\tau_E$ (solid black line). The initial evolution in the strain rate is described well by the predictions from the linear stability analysis (the dashed line). The deviation at very early times ($t \leq 0.3ms$) arises from the effects of the nozzle exit on the jet diameter and velocity profile

As the instability grows and the filament diameter decreases further, the local trough evolves into a cylindrical filament with an almost uniform diameter. The values of jet diameter in this nonlinear region no longer agree with linear stability predictions (the dashed line in Figure 2-6(b)) and the data suggests higher resistance and a slower decay with time compared to the predictions from linear stability analysis. It is also evident that the diameter of the neck decreases in an exponential manner (the solid line fitted to the data is $D_P/D_0 \sim \exp(-t/3\tau_E)$). Regression of the data to this expression gives a relaxation time $\tau_E = 60\mu s$. At the same time one can examine the extensional kinematics in the filament and track the values of strain rate with time as shown in Figure 2-6(c). The strain rate of the Lagrangian element P as it is convected along the jet is given by $\dot{\epsilon}_P \equiv (-2/D_P(t))dD_P/dt$. The value starts to grow with time in the linear region as the material element in the wave trough contracts until the point at which the nonlinear region of deformations ($t \geq 0.9ms$) starts. In the nonlinear region the value of strain rate experienced by the Lagrangian element reaches a plateau at $\dot{\epsilon}_P = 1.1 \times 10^4 s^{-1}$ which corresponds to a constant critical Weissenberg number, $Wi \equiv \tau_E \dot{\epsilon} = 2/3$. These results are in good agreement with both previous experiments and solutions/simulations in the literature for the nonlinear behavior of viscoelastic filaments during the jet breakup [159, 149, 152, 83, 160].

While the agreement of the measured data with the established linear theory of jets is promising, the more important aspect is the ability of ROJER to serve as an elongational rheometer that can probe very small relaxation times (down to approximately $60\mu s$). There are several advantages in using ROJER for these very dilute solutions compared to a more conventional method such as CaBER; firstly by decreasing the relevant length scale in the instrument from $6mm$ (the plate diameter in CaBER) to the initial nozzle diameter ($2R_0 = 150\mu m$ in ROJER) the inertio-capillary time-scale is reduced by a factor of almost 250. This means that, in principle, ROJER measurements of material relaxation times are possible for any polymeric solution if the relaxation time is of order of few capillary timescales, which will be $O(10\mu s)$ or higher for the current nozzle size ($\tau_R \sim \sqrt{\rho R_0^3/\sigma} \sim 10\mu s$

for $R_0 = 75\mu m$). This simple geometric modification enables measurements over a wider range of relaxation times and viscosities, for which conventional capillary thinning experiments are unable to properly operate (see [24] for an operation map of CaBER). One may argue that this would have also been possible by decreasing the plate size and consequently the capillary timescale in CaBER but it is important to recognize that in a CaBER device there is an initial stage during which the initial gap opens to the final gap separation, and this distance should be of order of the plate size (D_0) if we expect the capillary column to become unstable and undergo capillary breakup. If this transition does not happen fast enough compared to the speed of capillary thinning then the filament will breakup during the initial separation of the plates and CaBER measurements fail. Thus by simple scaling analysis one will find a lower limit for the speed of the plates in CaBER: $\sqrt{\sigma/\rho D_0} \leq V_{CaBER}$. The required minimum speed for the plate actuator in CaBER becomes very large as the plate radius shrinks and with the current technology on CaBER instruments the rise velocity can not exceed $0.1ms^{-1}$ without positional overshoot issues. This instrumentational limit on the rise speed dictates a minimum filament diameter below which the filament may breakup during the plate separation process and before the start of measurements ($D_{min} \sim \sigma/\rho V_{CaBER}^2$ which will be around $6mm$ for a low viscosity liquid like water and a velocity $V_{CaBER} \sim 0.1ms^{-1}$). Recent developments that extend CaBER([82, 81]) platform have overcome many of these limitations by using smaller plates and exploring different separation profiles for the plates. An alternative solution for overcoming inertia-related difficulties and plate separation issues is through studying the behavior of thin flying filaments that form in the jet break-up process. The timescale for such phenomena can be easily reduced by moving to smaller nozzles. Decreasing the characteristic radial length scale of the test sample reduces inertial effects in the fluid and helps us to probe viscoelasticity on much smaller material timescales. furthermore for samples with volatile solvents the ROJER technique has the advantage of minimizing the liquid exposure time to the ambient surrounding and consequently reduces complications arising from solvent evaporation when compared to CaBER related

techniques. Additional benefits of ROJER analysis for very dilute solutions are discussed in the subsequent two sections.

Linear Stability Analysis of Viscoelastic Jets and Satellite Drop Formation

The principles of jet extensional rheometry for measuring fluid relaxation times seem fairly straightforward; however there have been many reports in the literature [83, 161, 162] that also describe satellite formation in both Newtonian and viscoelastic jets. The appearance of large satellite droplets must be minimized in ROJER applications as they modify the desired extensional thinning kinematics. Numerical studies by Ardekani et al. [160] explored nonlinear jet thinning and approach to breakup using the Giesekus constitutive equation to describe the complex fluid rheology. They showed that there is a narrow band of wavenumbers for which periodic forcing of the jet will not lead to formation of satellite droplets and this is the optimal range for elongational rheometry. To investigate the appearance of satellite droplets in a representative viscoelastic liquid (a dilute solution of PEO 300K, $c/c^* = 0.03$), a range of different perturbation frequencies (leading to seven different wavenumbers $k_i = 2\pi f_i/V_j$) were picked and the jet breakup was visualized for all different wavenumbers. As expected from theoretical predictions for the inviscid case [158, 80, 163], the results show that the perturbations are linearly unstable and grow with time if the dimensionless wavenumber ($kR_0 \equiv 2\pi f R_0/V_j$) lies between zero and one (i.e. $0 \leq kR_0 \leq 1$). The jet is stable for shorter waves (higher frequency). By fitting a function of the form prescribed by Equation (2.11) to the initial data for each wavenumber we can determine the corresponding value of the growth rate (α) and the initial perturbation amplitude (δ) at that wavenumber. The experimental values for the growth rate are plotted at different wavenumbers (blue squares) in Figure 2-7. The dashed line is a plot of the predictions from the linear theory for the stability of a viscous jet [158], at corresponding values of Ohnesorge number for our tests, and the solid line is a plot of the dispersion curve described by Brenn et al. [40] for the linear stability of a viscoelastic jet at identical conditions to the experiments performed (i.e. equal values of the Deborah,

Weber and Ohnesorge numbers). It is worth mentioning that the solid line also includes the effects of the inertia of the external air phase on the jet instability and thus requires specification of the value of the Weber number. As predicted by linear theory for viscoelastic jets [147, 149, 40] the polymer solution is more unstable compared to a viscous Newtonian jet having the same values of the shear viscosity. The measured values of growth rate in the linear region match very well with the theoretical predictions for the viscoelastic jet.

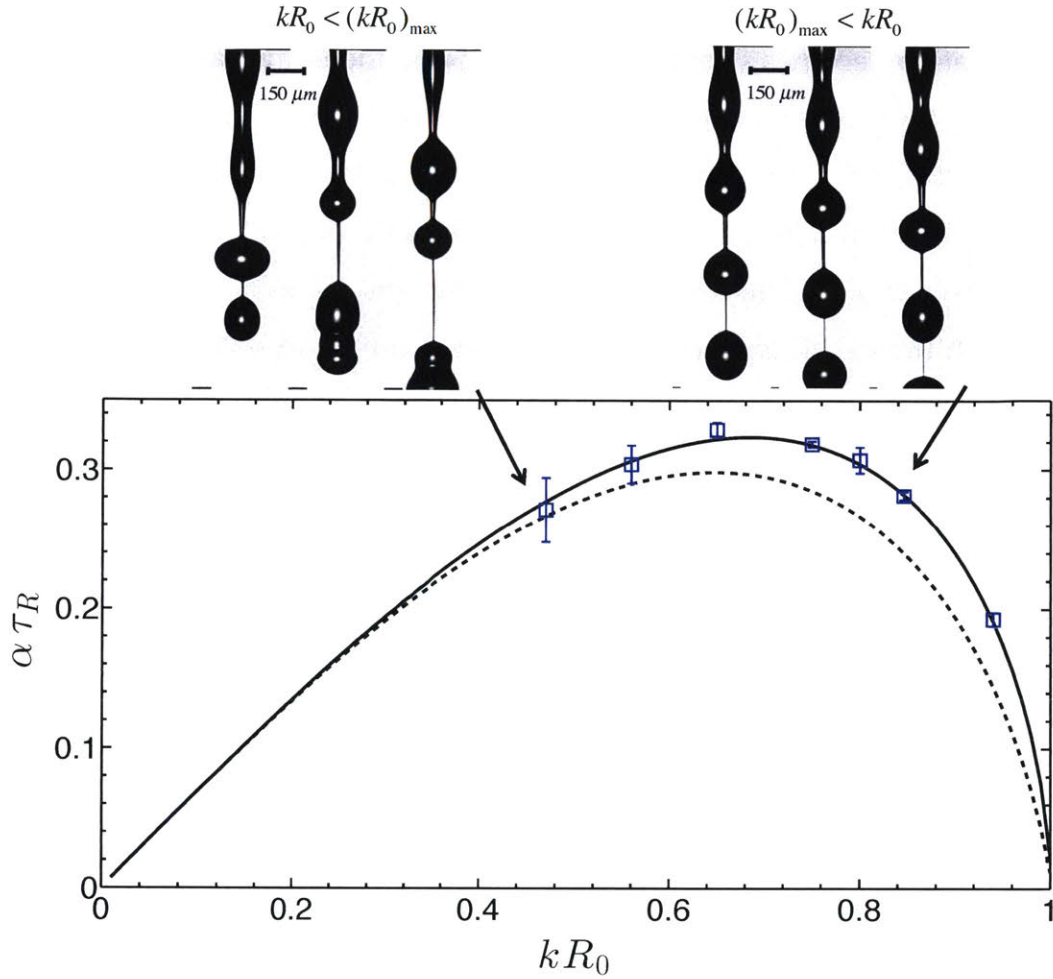


Figure 2-7: Values of dimensionless growth rate ($\alpha \tau_R$ in which $\tau_R = \sqrt{\rho R_0^3 / \sigma}$ is the Rayleigh timescale) for the instability measured from experiments at different dimensionless wave-numbers ($k R_0$) for the viscoelastic jet (PEO 300K) with $Oh = 0.075$, $We = 16.9$, $De = 0.72$, (blue squares) compared with the theoretical dispersion curve for the Rayleigh-Plateau instability: the dashed line shows the dispersion curve for a Newtonian jet ($Oh = 0.075$, $We = 16.9$) and the solid line is for the viscoelastic jet ($Oh = 0.075$, $We = 16.9$, $De = 0.72$). Theoretical results are evaluated from the linear instability analysis of Brenn et al.[40]. Also shown is a montage of images from the final stages of breakup for two different wavenumbers: the left image for $k R_0 = 0.43$ is below the most unstable wavenumber ($k R_0 < (k R_0)_{max}$) and clearly shows the growth of higher wavenumber modes leading to the appearance of a large satellite droplet which later merges into the leading drop, the right image shows a wavenumber of $k R_0 = 0.80$ that is larger than the most unstable mode and for which the satellite droplets do not appear resulting in a smooth beads-on-a-string structure.

The fact that the initial stage of the instability is well described by the linear theory can be further appreciated by investigating the final stages of jet breakup when the deformation becomes strongly nonlinear. Since the perturbation of the piezoelectric actuator can be tuned over a wide range of frequencies then at any given velocity for the jet (V_j) we can perturb the jet over a wide range of wavenumbers ($k = 2\pi f_{piezo}/V_j$). This allows us to ensure that the jet is perturbed in the vicinity of its most unstable wavelengths and a monochromatic disturbance will thus grow rapidly with time such that the nonlinear region can be repeatedly imaged with strobe illumination in a periodic manner. Experiments and computations [160] both show that viscoelastic jets tend to generate satellite droplets if the wavenumber is less than the most unstable one (i.e. $kR_0 \leq (kR_0)_{max}$). The size of these satellite droplets decrease as the wavenumber becomes close to $(kR_0)_{max}$ until they finally vanish if the wavenumber exceeds the critical value (the montage of images in Figure 2-7 illustrate this trend). These observations and computations assist in optimal operation of the jet rheometer and we avoid formation of satellites by perturbing the jet in the narrow band of wavenumbers between the most unstable one and the margin of stability ($(kR_0)_{max} \leq kR_0 \leq 1$). This is essential for precise measurements of rheological material parameters such as fluid relaxation times.

Measurements of Relaxation Time

Once the jet is perturbed at the desired frequency we can track the evolution in the filament profile that is contained in a moving Lagrangian box (the red box in Figure 2-8(a)) that translates downstream with the jet velocity (V_j) so that $Z^{(i)} = Z_0^{(i)} + V_j t^{(i)}$ is the locus of each pixel in the box. The thin translating ligament in the box, which is connected to the two adjacent wave peaks, will have a history identical to a stationary filament in CaBER that connects the two hemispherical end caps to each other. This is illustrated in Figure 2-8(b) by taking the filament profiles contained in the descending red box shown in Figure 2-8(a) and arranging them in a time sequence array (time in this figure is equal to the time of flight for the moving Lagrangian box and is simply calculated by $t \equiv z/V_j$). The blue squares in

Figure 2-8(c) show the decay of the filament in both the linear and the non-linear region. The dashed lines again show the predictions for the exponentially growing perturbation from linear theory:

$$D_{min}/D_0 = 1 - \delta \exp[\alpha(De, Oh, We, kR_0)] \quad (2.12)$$

in which the growth rate at the tested conditions (De, Oh, We, kR_0) is directly calculated from the theoretical dispersion relationship coming from the linear stability analysis of Brenn et al. [40] (see appendix B) and the values of δ lie in the range $0.001 \leq \delta \leq 0.01$.

On the other hand the solid line fitted to the data in Figure 2-8(c) is an exponential fit of the form in Equation (2.5). Fitting this model to the data gives us a value of $60\mu s$ for the relaxation time (τ_E) . The dynamics of the thinning filament in ROJER are thus identical to the elastocapillary balance established in CaBER and this rheological test can be viewed as a "flying CaBER" which translates downstream with the speed of the jet. The important distinguishing feature of ROJER is the fact that by avoiding the inertia-related issues inherent in CaBER tests we can now measure extremely low relaxation times.

From this analysis it is evident that the externally imposed velocity of the jet serves only as a flow parameter that sets the translation speed of the reference frame. If the ROJER instrument is to be thought of as an extensional rheometer then the analysis must be Galilean-invariant and the measured relaxation times should not depend on the jet velocity. To check this, a series of tests were performed at three different velocities (and consequently different Weber numbers) for the same test fluid (PEO-300K-0.01 wt.%). The results are summarized in Figure 2-8(c) and one can see that for each test the decay of the filament in the non-linear region matches well with the expected exponential decay and the measured relaxation time for each test is equal to $60 \pm 3\mu s$.

This invariance is expected to be valid over a wide range of Weber numbers. If the imposed jet velocity is in the vicinity of the dripping to jetting transition (i.e.

$We_j \leq O(1)$) then the force balance in the thinning filament will be different and the analysis used here must be modified to a new balance which involves the weight of the drop; this has been discussed in detail by Clasen et al. [164]. Conversely, at very high velocities, the aerodynamic forces of the external air column excite the jet to become unstable in different wind-induced modes compared to the well-known Rayleigh-Plateau mode [165]. This transition happens at gas-phase Weber numbers ($We_{gas} \equiv \rho_{gas} V_j^2 / \sigma \approx 0.4$) which in our experiments with water (for which $\rho_w / \rho_a = 1000$) correspond to liquid-phase Weber numbers higher than $We_j = 400$.

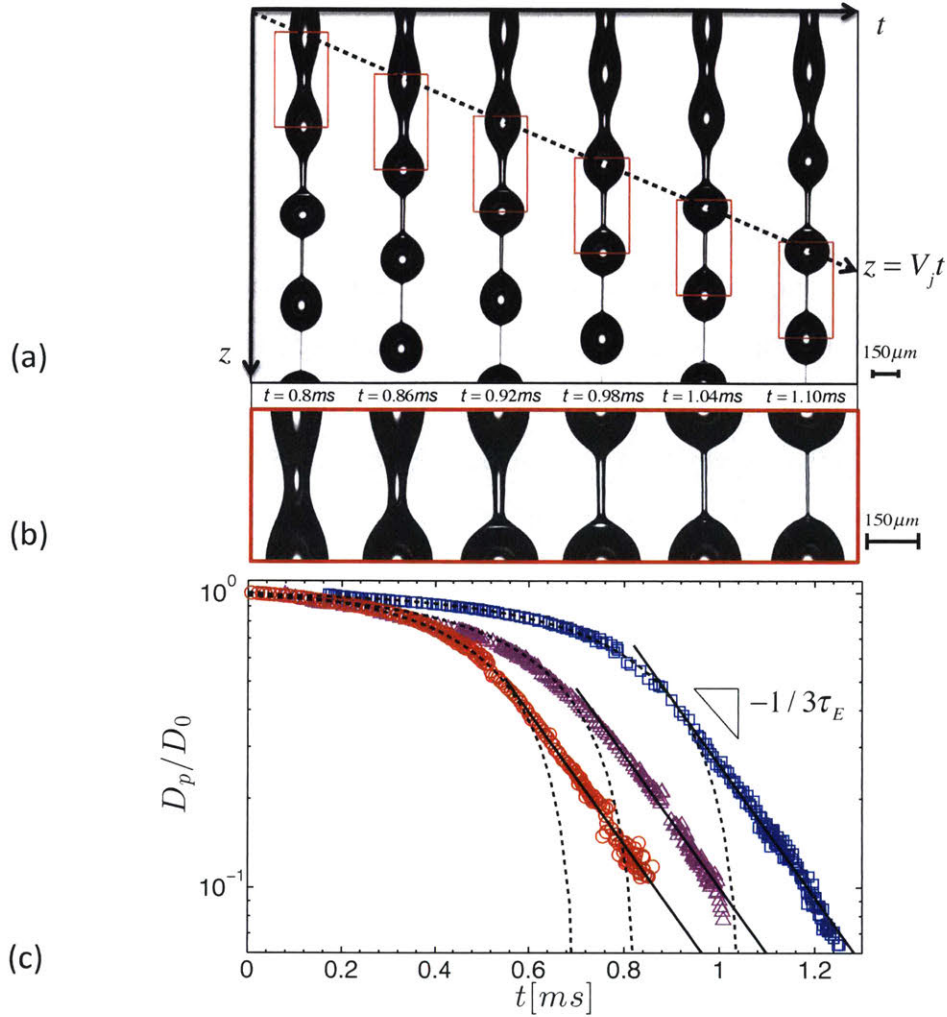


Figure 2-8: (a) Montage of images obtained at different times from the jet breakup experiment ($We_j = 16.9, kR_0 = 0.8, Oh = 0.075, De = 0.72$) following a fixed Lagrangian fluid element (i.e. the section of the jet shown in the red box) which moves with constant velocity ($V_j = 2.6\text{ms}^{-1}$). (b) Sitting in a moving frame translating with constant velocity (V_j) the Lagrangian element becomes stationary and the filament thins down as a result of capillarity in a way that is reminiscent of the dynamics of the filament in CaBER. (c) The normalized diameter versus time for PEO-300K-0.01 wt.%($Oh = 0.075, De = 0.7$) at three different jet velocities: red circles ($V_j = 3.9\text{ms}^{-1}, We = 39.6, kR_0 = 0.66$), magenta triangles ($V_j = 4.7\text{ms}^{-1}, We = 54.5, kR_0 = 0.80$), blue squares ($V_j = 2.6\text{ms}^{-1}, We = 16.9, kR_0 = 0.80$). The dashed lines are the corresponding fits from the linear instability analysis ($D/D_0 = 1 - \epsilon \exp(\alpha(We, Oh, De)t)$) and the solid lines each show an exponential decay ($D/D_0 \sim \exp(-t/3\tau_E)$) with $\tau_E = 60\mu\text{s}$ for each line. The measured relaxation times from ROJER analysis are thus independent of jet velocity.

Measurements of relaxation times were also performed for all of the other PEO-based solutions and the resulting values are tabulated in Table 1. Figure 2-9 shows both a montage of images (Figure 2-9(a)) and filament diameter data (Figure 2-9(b)) for two solutions of PEO of different molecular weights (300K and 1000K) but at similar levels of dilution ($c/c^* = 0.36$ for 300K PEO and $c/c^* = 0.37$ for 1000K PEO). The evolutions in the neck diameters in the nonlinear region each show an exponential decay that can be fitted by Equation (2.5) (solid lines in Figure 2-9(b)). As can be seen from the montage of images and the corresponding diameter measurements the lower molecular weight fluid jet (green squares) thins more rapidly, as compared to the higher molecular weight (red triangles). This is reflected in the values of the relaxation times for these two solutions. For the 1000K PEO solution (red triangles) we obtain a value of $\tau_E = 2.8 \times 10^{-3}s$ for the relaxation time, whereas the 300K solution (green squares) at a similar value of c/c^* shows a much lower relaxation time with $\tau_E = 3.6 \times 10^{-4}s$. The longest relaxation time in dilute polymeric solutions can be estimated from the molecular weight of the polymer using Rouse-Zimm theory [166]:

$$\tau_{Zimm} \sim \frac{[\eta]\eta_s M_w}{RT} \quad (2.13)$$

in which $[\eta]$ is the intrinsic viscosity which is connected to the molecular weight through the Mark-Houwink expression:

$$[\eta] = 0.072 M_w^{3\nu-1} \quad (2.14)$$

where the solvent quality parameter is $\nu = 0.55$ for PEO solutions in glycerol water mixture [24]. Combining Equations (2.13) and (2.14) it is apparent that the longest relaxation time for dilute solutions should scale with molecular weight as:

$$\tau_E \sim M_w^{3\nu} \quad (2.15)$$

This scaling is valid for very dilute solutions ($c/c^* \ll 1$) but Tirtaatmadja et al. [167] have shown that even at higher (constant) values of c/c^* the dependency on molec-

ular weight remains similar to Equation (2.15). Based on these scaling arguments we expect that for solutions tested in Figure 2-9(b) the ratio of relaxation times should be: $\tau_{1000K}/\tau_{300K} = (1000/300)^{3 \times 0.55} = 7.30$. The experimental measurements show a ratio of $\tau_{1000K}/\tau_{300K} = 2800/360 = 7.77$, and are thus in good agreement within the expected accuracy of the reported values of solvent quality and polymer nominal molecular weight.

As discussed, the measured scaling dependency of relaxation times on the nominal molecular weight agrees well with the suggested scalings from polymer physics but one can also directly contrast the numerical values that arise from measurements and theory. Using Equation (2.13) the numerical values for the longest relaxation time in the dilute limit (at $c/c^* \ll 1$) is $\tau_{Zimm} = 34\mu s$ for the 300K PEO solution and $\tau_{Zimm} = 252\mu s$ for the 1000K PEO solution. The ratio of these estimates agrees well with the ratio of the measured values from ROJER, but the individual numerical values of the relaxation time are much smaller than the measured ones. This is simply due to the fact that the value of c/c^* for these two solution is finite ($c/c^* \sim 0.36$ for both molecular weights). Tirtaatmadja et al. [167] have shown that at higher (constant) values of c/c^* the dependency on molecular weight is similar to Equation (2.15) with an extra prefactor which grows linearly with c/c^* because it also takes the rod/coil drag scaling into account. Using the new scaling the correction factor for the Zimm relaxation time will be around 10 [167] which gives estimates of relaxation time to be $340\mu s$ for the 300K PEO solution and $2520\mu s$ for the 1000K PEO solution. These new corrected values are definitely much closer to the measurements of relaxation time obtained from jet rheometry experiment.

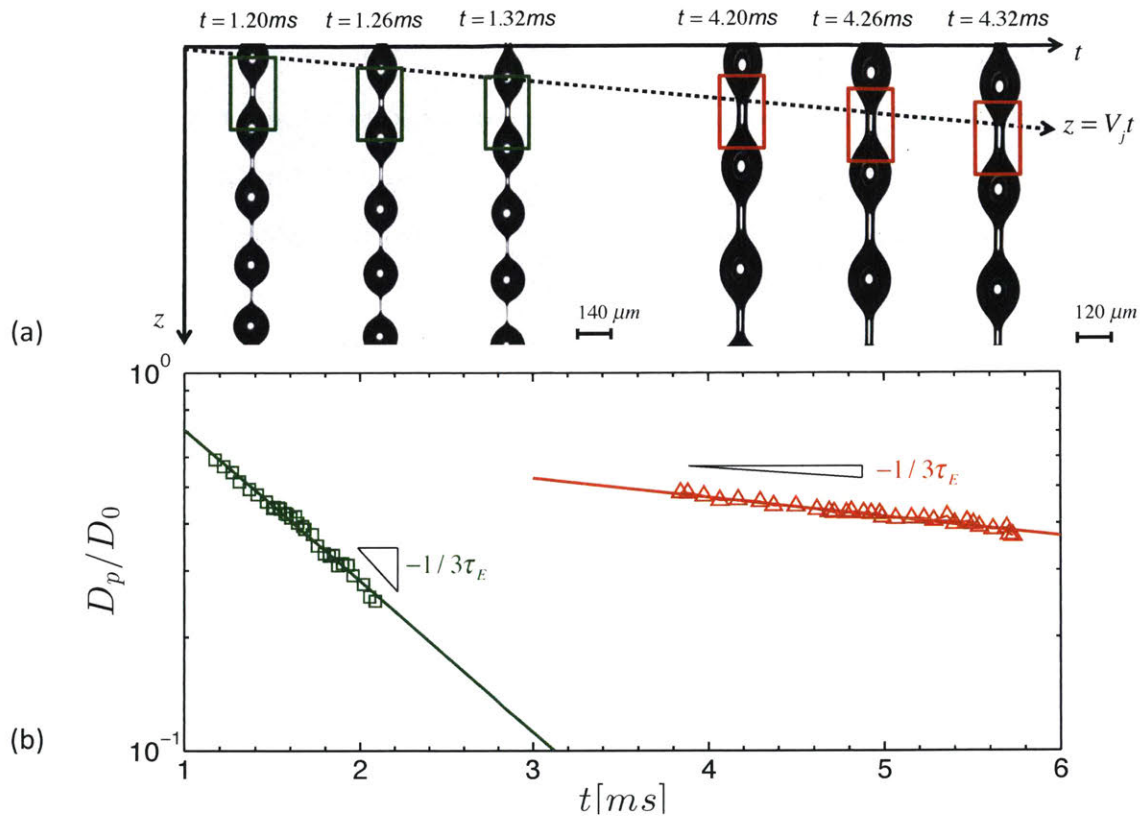


Figure 2-9: (a) Montage of images from ROJER test for two different molecular weight polymer solutions (left images are for PEO-300K-0.1 wt.% and the right images are for PEO-1000K-0.05 wt.% $We_j = 8.5, kR_0 = 0.77, Oh = 0.075$) at different times following a Lagrangian fluid element (the section of jet in the green and red boxes respectively) which moves with constant velocity ($V_j = 0.87\text{ms}^{-1}$). (b) The normalized diameter versus time for PEO-300K-0.1 wt.% (green squares) and for PEO-1000K-0.05 wt.% (red triangles). The solid lines show exponential decays fitted to Equation (2.5) with $\tau_E = 360\ \mu\text{s}$ for PEO-300K-0.1 wt.% and $\tau_E = 2800\ \mu\text{s}$ for PEO-1000K-0.05 wt.%.

Measurements of Elongational Properties

This can be achieved by analyzing the evolution in filament diameter for a fixed material element in the viscoelastic liquid (red filled circles in Figure 2-10(a)) with the corresponding Newtonian solvent (blue open circles in Figure 2-10(a)). This difference in thinning can be quantified, as discussed in detail in previous sections, by fitting the exponential decay in the viscoelastic case (black solid line in Figure 2-10(a)) and the linear visco-capillary thinning observed in the solvent (dashed line in Figure 2-10(a)). From the fits one can evaluate the values of strain rate and the tensile stress difference in the thinning material element from the following expressions [79]:

$$\dot{\epsilon}_P = \frac{-2}{D_P(t)} \frac{dD_P(t)}{dt} \quad (2.16a)$$

$$\Delta\Sigma(t) = \Sigma_{zz} - \Sigma_{rr} = 2\sigma/D_P(t), \quad (2.16b)$$

Using the relationships in Equations (2.16a) and (2.16b) explicit relationships can be found for the time-varying apparent elongational viscosity in the thinning jet:

$$\eta_E^+ \equiv \frac{\Sigma_{zz} - \Sigma_{rr}}{\dot{\epsilon}_P} = \frac{-\sigma}{dD_P(t)/dt} \quad (2.17)$$

From this expression it is apparent that by measuring the evolution in the filament diameter with time for a fixed material point P we can calculate both the strain rate and the instantaneous elongational viscosity at that specific strain rate. Using the ROJER data from Figure 2-10(a) the corresponding values of elongational viscosity are calculated and plotted versus strain rate for the PEO-300K-0.01 wt.% fluid. Figure 2-10(b) shows a comparison between the shear (triangles) and elongational (circles) viscosity for the viscoelastic solution (red filled symbols) and the Newtonian solvent (blue open symbols). The shear viscosity shows negligible increase with addition of dissolved polymer and no dependence on shear rate; by contrast there is a considerable increase in the extensional viscosity of the PEO solution. The Newtonian solvent shows a constant value of elongational viscosity equal to

$3\eta_s$ which is in agreement with the expected Trouton ratio for Newtonian liquids [18]. The PEO solution shows very similar values of the elongational viscosity to the solvent at low strain rates, but then starts to increase when the strain rate approaches a critical value, which is close to the relaxation rate of the polymer chains in the elongational flow (τ_E^{-1}). The Weissenberg number of the flow at this point corresponds to the coil to stretch transition for the dissolved polymer chains, $Wi = \tau_E \dot{\epsilon} \simeq 0.5$ [168]. The experimental results for the PEO solution also show good agreement with the FENE-P (finite extensibility nonlinear elastic dumbbell) model proposed by Peterlin [169, 168] in both shear (dashed line in Figure 2-10(b)) and extension (solid line in Figure 2-10(b)). The parameters used in evaluating the predictions of the FENE-P model are the measured values of zero shear viscosity (η_0), the solvent viscosity (η_s) and the relaxation time (τ_E) along with the extensibility parameter ($L \simeq 27$) which is computed from the known molecular parameters for the PEO chains [116]. The FENE-P model predicts negligible change in the shear viscosity for the dilute solution but a considerable increase in the extensional viscosity for $Wi \geq 0.5$. Due to the nonlinear nature of the FENE springs the extension of the individual polymer chains are constrained by the extensibility parameter (L). Once fully extended the chains act like an anisotropic suspension of rigid rods and the extensional viscosity in the bulk reaches a plateau value at high strain rates ($\lim_{\tau_E \dot{\epsilon} \gg 1} \eta_E \rightarrow 3\eta_s + 2(\eta_0 - \eta_s)L^2$). It should be noted that the values of extensional viscosity from ROJER measurements are, in principle, transient measurements and the FENE-P predictions plotted in Figure 2-10(b) are for the steady state values of the extensional viscosity. However, since in the ROJER experiment the liquid relaxation time ($60\mu s$) is very small compared to the timescale of the measurements ($O(1ms)$) the transient behavior will very rapidly approach to the steady response and thus the measured extensional viscosities agree well with the predicted steady state values obtained from the FENE-P model.

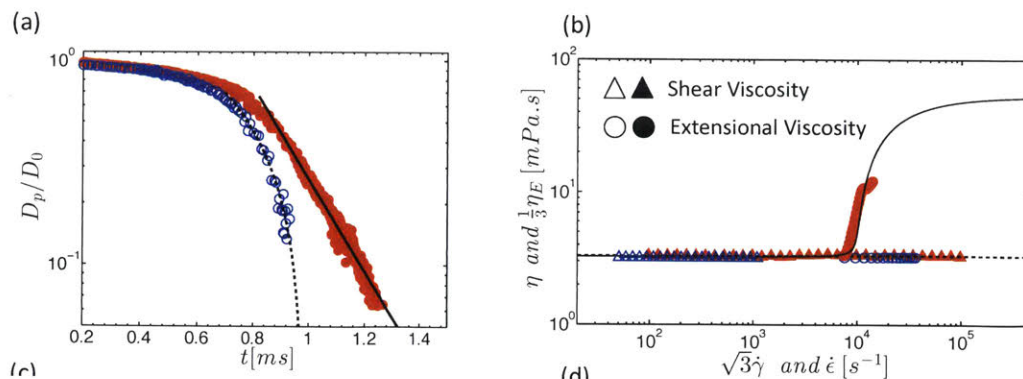


Figure 2-10: (a) The ROJER measurements of the thinning filament diameter as a function of time for both the viscoelastic liquid (PEO-300K-0.01 wt. %-red filled circles) and the corresponding Newtonian solvent (water and glycerol ,60-40 wt. %-blue open circles). Solid line shows the exponential fit for the elasto-capillary regime (Equation (2.5)) and the dashed line is the linear fit for the visco-capillary regime for filament thinning ($D(t) = 0.072 (\sigma/\eta_s) (t_b - t)$). (b) Shear (triangle) and extensional rheology (circle) for both the Newtonian solvent (blue open symbols) and the viscoelastic solution (PEO-300K-0.01 wt. %)(red filled symbols). The solid and dashed lines show respectively the FENE-P predictions using model parameters in Table 1 for the extensional and shear viscosities. The transient elongational viscosity data are extracted from the jet thinning dynamics shown in Figure 10(a).

2.5.3 EVROC

A different class of instruments for probing elongational properties of dilute solutions are based on steady flow of viscoelastic fluids through a contraction or a contraction/expansion[170, 171, 172]. Imposing a sudden contraction on a fully developed channel flow induces streamwise extensional kinematics that can cause significant stretching in the microstructure of the fluid, which then results in an extra pressure drop across the contraction/expansion. Essentially this is the microfluidic analog of the “orifice plate” widely used for inline measurement of the flow rate of Newtonian fluids (with constant rheology). Early studies of polymeric flows in contractions [173, 174, 175, 176, 177, 178, 179] showed many promising aspects and its relevance to commercial polymer processing operations such as injection molding established the contraction flow as a ubiquitous “rheological index” for elongational properties. Several recent studies[180, 22, 181, 182, 41], benefiting from advances in fabrication techniques for microfluidic channels, have

focused on the flow of complex liquids in hyperbolic contraction geometries asserting that the hyperbolic profile will aid in maintaining the apparent stretch rate $\dot{\epsilon}_a$ constant throughout the contraction [183, 180]. The recent study by Ober et al. [41] investigated a microfluidic hyperbolic expansion/contraction flow for a variety of different low viscosity test fluids and outlined methods based on two-dimensional lubrication theory to measure elongational properties based on pressure drop measurements across the contraction.

Considering the recent developments in microfluidic devices/flows for biological applications and the fact that many of the relevant liquids are of a weakly viscoelastic nature [184, 185, 186, 187, 188, 170, 171] it is important for the rheologist to develop a comprehensive understanding of the relative merits of different devices available for measuring the elongational rheology of dilute solutions. This situation is complicated by the knowledge that the extensional viscosity of a microstructured material is typically a time-varying function of both the strain rate $\dot{\epsilon}(t)$ and the total strain $\epsilon = \int_0^t \dot{\epsilon}(t') dt'$ imposed on a material element [73, 101]. This can lead to difficulties in unambiguously determining the true extensional viscosity and in comparing results obtained with different instruments. Thus, in this study, we attempt to measure the elongational properties of a family of dilute polymer solutions by using two separate devices representing the different classes described above. Results from a microfluidic hyperbolic contraction device or "extensional viscometer-rheometer-on-a-chip" (EVROC), similar to the device used by Ober et al. [41], are compared with jet breakup studies performed with the ROJER setup. This latter configuration focuses on the transient growth in the extensional viscosity for an unknown viscoelastic test sample at a single (nominally) constant strain rate that is set by the viscoelastic and interfacial properties of the fluid. By contrast, the former (EVROC) configuration considers a steady Eulerian flowfield with the total strain on a material element defined by the precise converging shape of the hyperbolic die and the 2D or 3D nature of the flowfield. In such an instrument, the strain rate can be systematically controlled by varying the flow rate through the device.

So far in this chapter, we have highlighted the limits of CaBER and benefits of ROJER, for the rest of discussions we focus on the limits of EVROC and compare that to ROJER in quantitative measurements of the elongational properties of the fluid and develop simple physical scalings that can help elucidate the operational parameter space of each device. We represent our results in terms of an operating diagram or *nomogram* that delineates the regions of parameters where viscoelastic fluid properties can be successfully measured. The findings from this study provide practical guidance to microfluidic researchers who are interested in quantifying the elongational rheology of a wide range of industrial and biological liquids that exhibit weak viscoelastic behavior.

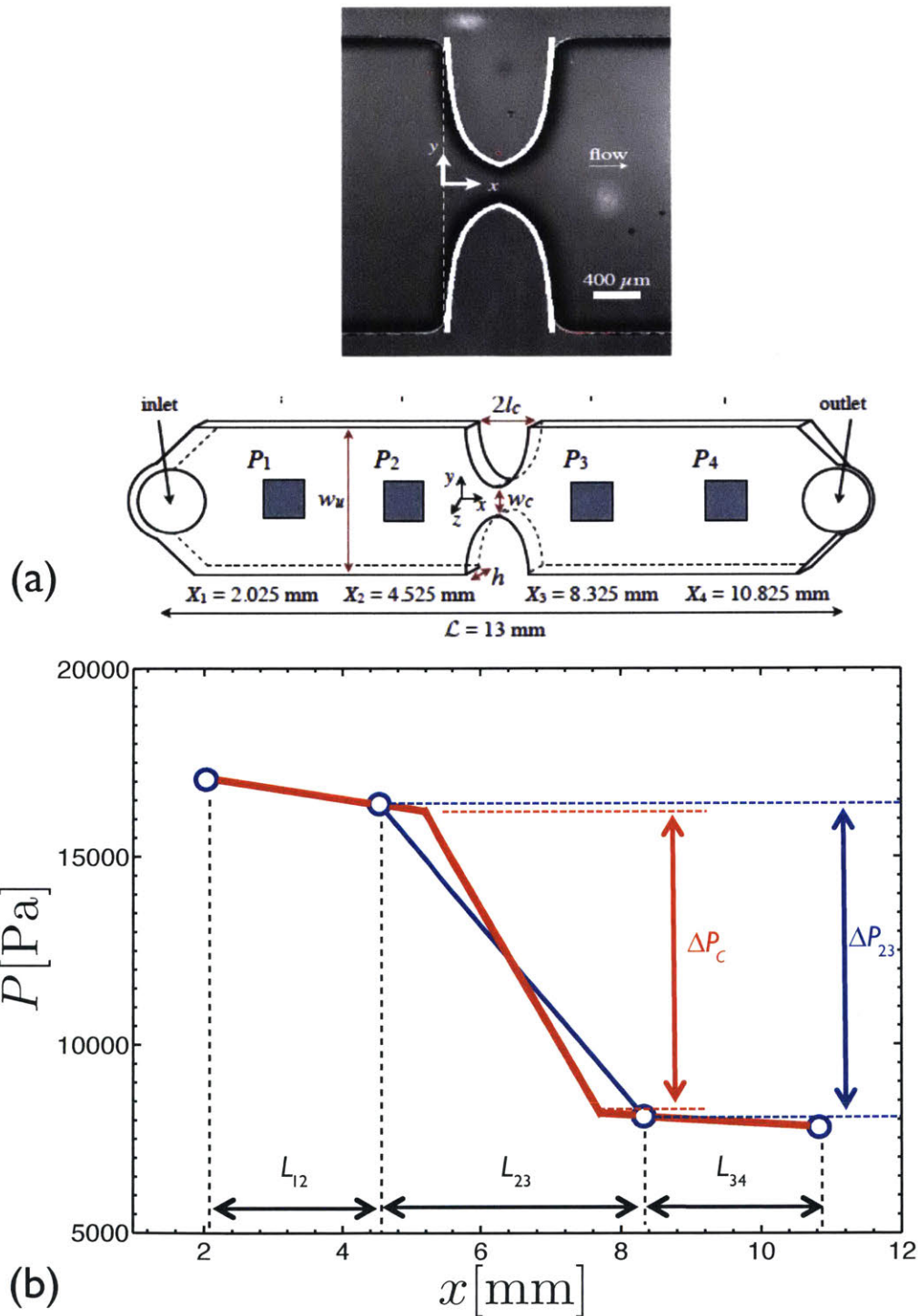


Figure 2-11: (color online). (a) SEM image of the hyperbolic contraction and the dimensions of the entire geometry. Taken from Ober et al. [41] with permission (Reproduced with permission from Rheologica Acta 52, 6 (2013). Copyright 2013 Springer.). (b) Pressure measurements, for the PEO-4000K-0.05% wt. solution. Four flush-mounted pressure transducers are located along the channel axis. The magnitude of the pressure drop across the contraction/expansion between sensors 2 and 3 (ΔP_c) is an indication of elongational effects.

EVROC Setup

The microfluidic planar hyperbolic contraction used in this study was fabricated by RheoSense (San Ramon Ca., USA)[189]. The channel geometry and dimensions are shown in Figure 2-11 (a). The channel height (h) is constant throughout the geometry. The flow upstream is pushed by a syringe pump through a straight channel region with constant width w_u to establish a fully-developed shearing flow before reaching a symmetric contraction/expansion $0 \leq x \leq 2l_c$ in which the width varies as $w(x) = K/(x_0 - |x - l_c|)$ where $x_0 = l_c w_u / (w_u - w_c)$ and $K = l_c w_c w_u / (w_u - w_c)$. At an imposed flow rate Q , the average streamwise velocity at any plane x , will vary as $\langle u(x) \rangle = Q/hw(x)$, so if we focus on the flow along the midplane of the device, the apparent extension rate $\dot{\epsilon}_a$ is

$$\dot{\epsilon}_a = \frac{Q}{l_c h} \left(\frac{1}{w_c} - \frac{1}{w_u} \right) \quad (2.18)$$

leading to a value of the average Hencky strain ϵ_H that is experienced by a fluid element following through the contraction given by:

$$\epsilon_H(x) \equiv \int_0^{t(x)} \dot{\epsilon}_a dt' \quad (2.19)$$

where the limit of integration corresponds to the time at which the material element is at a location x along the constriction. This function reaches a maximum value of $\epsilon_H = \ln(w_u/w_c)$ when the material element reaches the throat of the contraction, $x = l_c$.

Before and after every test, the channels are flushed with water/ethanol to make sure that there is no residue from previous tests. For every measurement the channel was filled with the test fluid for 10-15 minutes and measurements are then started after pumping 3-5 ml of the sample through the EVROC fixture and monitoring the approach to steady state values for the pressure signal recorded by each transducer. Figure 2-11(b) shows the raw pressure measurements for one of the viscoelastic test solutions (PEO-4000K-0.05%wt.). The pressure drop across the

hyperbolic contraction ΔP_c is evaluated from the pressure difference measured between the 2nd and 3rd sensors ΔP_{23} with a minor extrapolation upstream and downstream of the pressure transducers to correct for the fact that they are not located exactly at the throat entrance/exit of the converging/diverging region[41]. From Equations (4.6) and (2.19) it is clear that by varying the flow rate in the channel the apparent extension rate in the constriction is controlled, and measuring the pressure drop across the contraction then gives a direct measure of the viscoelastic effects involved in the deformation of material elements as they flow through the contraction/expansion.

Shear Viscosity Measurements with EVROC

Before characterizing the elongational properties of the test fluids (with composition shown in Table 1) by both EVROC and ROJER instruments we performed a series of tests with a commercial stress-controlled rheometer (DHR-3 from TA Instruments New Castle DE) in a double-wall Couette geometry (inset image in Figure 2-12(a)) to characterize the shear rheology of each fluid. Measurements were performed over a wide range of shear rates. The limits of the shear viscosity measurements are set by the minimum torque ($\mathcal{T}_{min} = 0.05 \mu\text{N.m}$) that the instrument can control/measure at lower rates and the maximum strain-rate is set by the onset of inertially-induced secondary flows in the Couette cell. The inner cup has a 28.0 mm diameter, the rotor has an inner diameter of 29.5 mm and an outer diameter of 32 mm and the outer cup is 34 mm in diameter.

Figure 2-12(a) shows the results for the shear viscosity measured for the Newtonian solvent (black symbols) and two of the viscoelastic solutions formulated from 4000K PEO at both a very low concentration $c/c^* = 0.03$ (magenta symbols) and also at a much higher concentration $c/c^* = 13.22$ (orange symbols). Open circles show results from the double-wall Couette geometry and the filled triangles show results from EVROC measurements. The microfluidic chip can be used to determine the shear viscosity of the fluid by focusing only on the pressure difference measured between sensors 1 and 2 which are located in the region of steady fully-developed

channel flow before the hyperbolic contraction. Assuming a fully developed 2D flow, it is known that the wall shear stress Σ_w is related to the pressure drop ΔP_{12} between the two upstream flush-mounted sensors by the expression[189]:

$$w_u h \Delta P_{12} = 2L_{12}(w_u + h)\Sigma_w \quad (2.20)$$

At the same time, for a given flow rate Q imposed by the syringe pump, the apparent shear rate can be calculated as $\dot{\gamma}_a = 6Q/w_u h^2$. However, to determine the true wall shear rate which captures the effects of shear-thinning fluid rheology on the velocity profile we use the Weissenberg-Rabinowitsch-Mooney (WRM) equation [100, 189, 111]:

$$\dot{\gamma}_{true} = \frac{\dot{\gamma}_a}{3} \left[2 + \frac{d(\ln \dot{\gamma}_a)}{d \ln(\Sigma_w)} \right] \quad (2.21)$$

Using Equations (4.5 and 4.1) for a given flow rate, knowing the channel geometry and the pressure drop between the first two sensors ΔP_{12} one can calculate the true shear viscosity $\eta(\dot{\gamma}_{true}) \equiv \Sigma_w/\dot{\gamma}_{true}$ at each imposed shear rate.

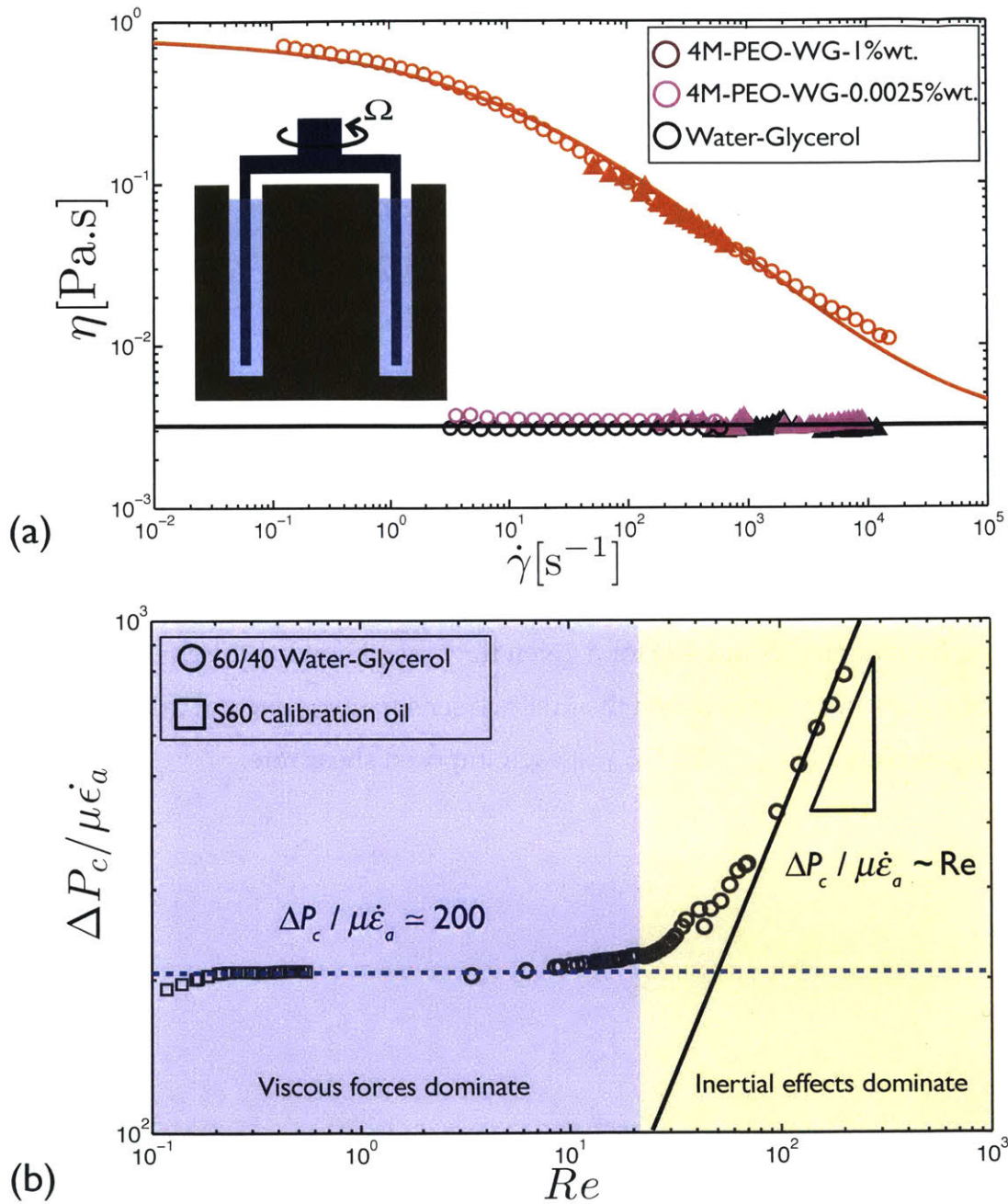


Figure 2-12: (color online). (a) Shear viscosity measurements plotted for three different test fluids: the Newtonian solvent (\circ and \blacktriangle), 4M-PEO-0.0025%wt. (magenta open circles \circ and magenta filled triangles \blacktriangle) and 4M-PEO-1%wt. (\circ and \blacktriangle). Open circles are data measured in a double-wall Couette geometry and the filled triangles are shear viscosity measurements from the EVROC device calculated from the measured pressure difference upstream between sensors 1 and 2. (b) Pressure difference across the hyperbolic contraction ΔP_c measured at different flow rates and plotted in a dimensionless form ($\Delta P_c / \mu \dot{\epsilon}_a$) vs. Reynolds number Re for different Newtonian liquids: S60 calibration oil (\square) and water-glycerol solvent (60-40 wt.%) (\circ).

As shown in Figure 2-12(a) the values of the shear viscosity obtained from the EVROC microfluidic device are in good agreement with the measured values from the double-wall geometry in the conventional stress-controlled rheometer. The results for the very dilute solutions ($c/c^* \ll 1$) show very little difference from the solvent viscosity, but for the higher concentration a pronounced shear thinning behavior can be observed (brown data). The data for the high concentration PEO solution is fitted by a Carreau-Yasuda model [100]:

$$\frac{\eta - \eta_s}{\eta_0 - \eta_s} = [1 + (\tau_s \dot{\gamma})^a]^{(n-1)/a} \quad (2.22)$$

where η_0 and η_s are, respectively, the zero shear-rate and solvent viscosity, τ_s is a timescale that sets the onset of shear thinning at $\dot{\gamma}^* \simeq 1/\tau_s$, $n - 1$ sets the power law slope and a sets the breadth of the transition region. Fixing $\eta_0 = 0.8$ Pa.s, $\eta_s = 0.003$ Pa.s and also setting the value of τ_s to be equal to the relaxation time measured in the capillary breakup experiment (described below) $\tau_s = \tau_E = 55$ ms one can see that a good fit of the model (solid line in Figure 2-12(a)) can be obtained with $n = 0.3$ and $a = 0.4$.

Elongational Viscosity Measurements with EVROC

As mentioned before, one signature of elastic effects in converging flows of a complex fluid is the enhanced pressure drop across the contraction [173, 176, 41]. However, extra care must be taken in interpreting the extra pressure drop because of additional effects arising from viscous stresses, inertia and the unsteady nature (in a Lagrangian sense) of the flow experienced by a material element flowing through the hyperbolic contraction. Connecting the measured pressure drop to the true extensional viscosity is a known challenge in microfluidic extensional rheometry [190, 191, 171].

One of the major complications is related to the nonlinear effects of fluid inertia. Figure 2-11(b) shows the pressure drop ΔP_c across the hyperbolic contraction measured for different Newtonian fluids over a wide range of Reynolds numbers. The

Reynolds number on the abscissa is defined as $Re \equiv \rho d_h l_c \dot{\epsilon}_a / \eta_0$ where ρ is the fluid density, η_0 is the zero shear viscosity (in case of Newtonian liquids $\eta_0 = \mu$), $l_c \dot{\epsilon}$ is the local increment in velocity at the throat arising from the constriction, and $d_h = 2hw_c/(h + w_c) = 267\mu\text{m}$ is the hydraulic diameter defined at the throat of the contraction. The true pressure drop across the contraction ΔP_c is related to the measured pressure difference between sensors 2 and 3 by the expression [41]

$$\Delta P_c = \Delta P_{23} \left\{ 1 - \frac{1}{2} \left(\frac{1}{\mathcal{P}} - 1 \right) \frac{L_{23} - 2l_c}{L} \right\} \quad (2.23)$$

where $L_{23} = 3.8\text{ mm}$, $L = L_{12} = L_{23} = 2.5\text{ mm}$, $l_c = 400\mu\text{m}$ are properties of the specific geometry and the fraction of the total pressure drop across the device that arises from the converging/diverging flow is denoted $\mathcal{P} = \Delta P_{23}/\Delta P_{14}$. Simple scaling arguments show that, for Newtonian liquids, in the limit of very low Re the pressure drop will scale with the viscous stress $\Delta P_c \sim \mu \dot{\epsilon}_a$, and at high Re , inertial effects will dominate so that the pressure drop should scale with the inertially induced stresses in the liquid $\Delta P_c \sim \rho V^2 \sim \rho(Q/wh)^2$. The Newtonian data in Figure 2-11(b) show a similar trend; at low Re the dimensionless pressure drop in the device normalized by a characteristic viscous stress is constant at a value set by the geometric dimensions of the channel[41] $\Delta P_c/\mu \dot{\epsilon}_a \sim 200$ and at high Re numbers the normalized pressure drop scales linearly with Reynolds number $\Delta P_c/\mu \dot{\epsilon}_a \sim Re$ suggesting that for high Reynolds number flows, enhancements in the pressure drop measured across the contraction do not arise from the extensional viscosity but rather from fluid inertia. For the specific geometry used in this study, transition between the viscous- and inertia-dominated regions occurs at $Re_c \sim O(10)$, consistent with the separate study by Ober et al. [41].

Because of the nonlinear inertial effects at high Reynolds numbers ($Re \geq O(10)$) it is clear that proper extensional rheometry measurements are not possible in this limit (yellow shaded area in Figure 2-11(b)). Analyzing the pressure drop data above this limit and connecting that to the elongational properties of a liquid can be very misleading [191]. In the same way increases in the torque measured in a

Taylor-Couette device at high shear rates may be erroneously interpreted as shear thickening in the fluid rheology when it in fact arises from secondary flows. If a strongly extensionally-thickening fluid is analyzed it may result in true elastically dominated increases in the pressure drop before these inertial effects set in at $Re \sim O(10)$. However, one can imagine that for many weakly-elastic fluids the critical strain rate at which elongational rheological properties start to dominate over inertial effects may be high enough that in a device such as EVROC the corresponding values of Re would approach the limit of inertially-dominated flows. Thus the response of the unknown material in this range of strain rates would be a mixture of inertial and elastic effects. Decoupling these effects from one another is hard, if not impossible.

2.5.4 Comparison Between Different Instruments (EVROC and ROJER)

In order to probe the sensitivity limit of EVROC we tested the 60-40 wt. water-glycerol solvent (Table 1) along with one concentrated and four dilute PEO solutions. Figure 2-13(a) shows a summary of these data. Preliminary results for all of the fluids are plotted in terms of normalized pressure drop measured at different values of Re . It is clear that, within the operational limits of EVROC ($Re \leq Re_c$), for the three most dilute solutions (green, blue and magenta data points) the normalized pressure drop is indistinguishable (within the experimental limits) from the corresponding values for the Newtonian solvent. Subtle differences emerge for some of these solutions at higher strain rates but the onset of these distinctions lie in the region where the pressure drop data are already polluted by inertial effects (yellow-shaded area). For the most dilute and lowest molecular weight PEO solution (300K-0.01%wt.), the measured pressure drop values remain indistinguishable from the Newtonian solvent even up to the upper limit of flow rates ($Q_{max} = 15.2$ ml/min; $\dot{\gamma}_a = 1.2 \times 10^4$ s⁻¹) achievable by the syringe pump (compare the black and green symbols in Figure 2-13(a)).

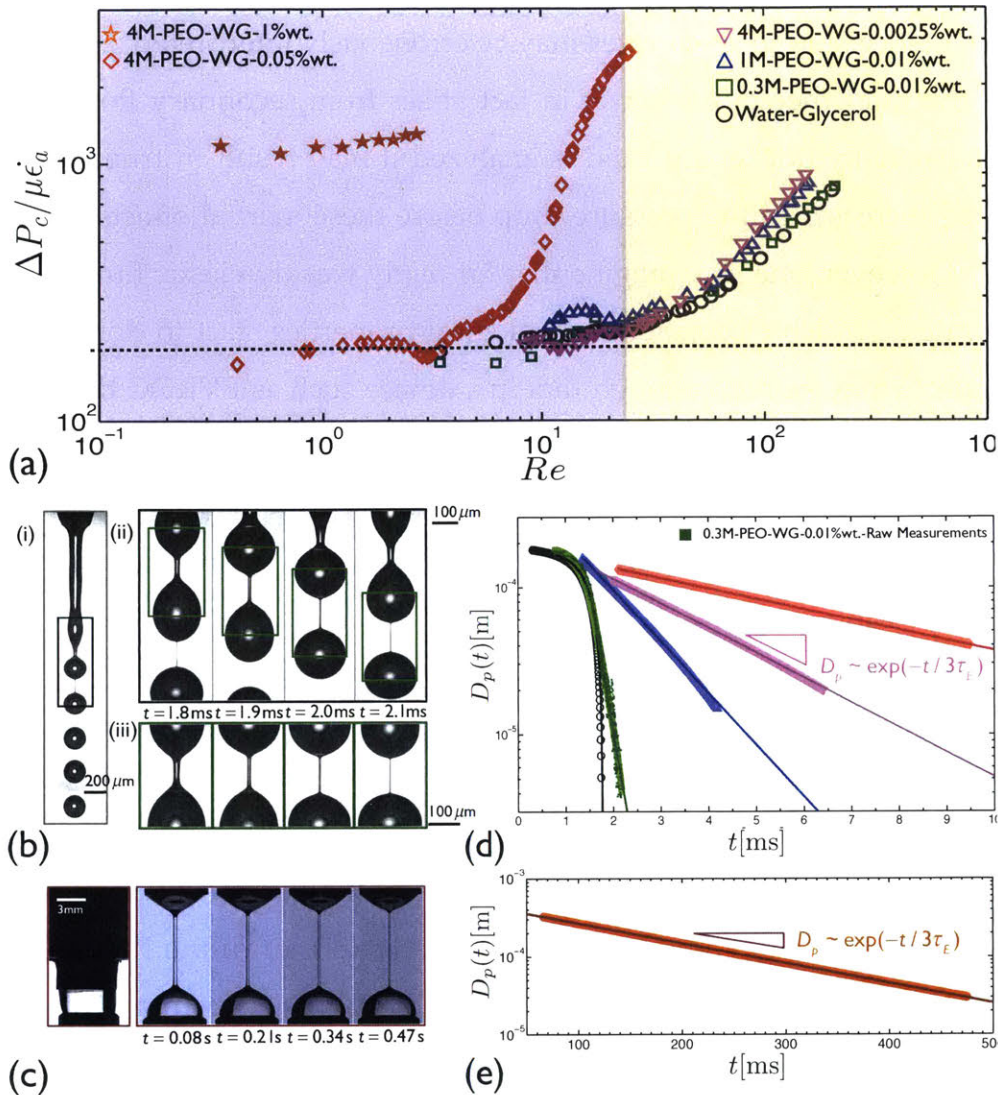


Figure 2-13: (a) Pressure drop across the hyperbolic contraction in EVROC tests measured at different flow rates and plotted in a dimensionless form, $\Delta P_c / \mu \dot{\epsilon}_a$ versus Re , for different fluids: the Newtonian solvent (\circ), 300K-PEO-0.01%wt. (\square), 1000K-PEO-0.01%wt. (\triangle), 4000K-PEO-0.0025%wt. (magenta inverted triangles ∇), 4000K-PEO-0.05%wt. (\diamond), 4000K-PEO-1%wt. (\star). (b) Snapshots of the jet breakup process for the 300K-PEO-0.01%wt. solution in the ROJER setup: (i) An image of the entire process showing the jet exiting the nozzle and breaking up into individual droplets. (ii) A time sequence of enlarged snapshots showing the emergence of a cylindrical filament that can be followed by the Lagrangian box (in green) that is moving downstream with the jet velocity. (iii) Time evolution of the filament in the Lagrangian box shows elasto-capillary thinning. (c) Snapshots demonstrating the elasto-capillary thinning regime in the CaBER device for the 4000K-PEO-1%wt. solution. (d) Time evolution of the filament neck diameter $D_p(t)$ is plotted for different fluids tested in the ROJER setup: the Newtonian solvent (\circ), 300K-PEO-0.01%wt. (\square), 1000K-PEO-0.01%wt. (\triangle), 4000K-PEO-0.0025%wt. (magenta inverted triangles ∇), 4000K-PEO-0.05%wt. (\diamond). (e) Results from CaBER test for the 4000K-PEO-1%wt. solution (\circ). Solid lines in both (d) and (e) show fits of the exponential decay expected from theory (Equation 2.5). Raw measurements of $D_p(t)$ for the 300K-PEO-0.01%wt. solution (\blacksquare) are also plotted, to provide an indication of typical fluctuations in the diameter measurements.

It is only for the two solutions with higher concentrations of 4000K PEO (red and orange data points) that measurable differences from the Newtonian solvent emerge before inertia effects start to dominate. The data for the 4000K-0.05% solution (red symbols) shows the onset of extensional thickening at a critical extension rate, as expected for dilute polymer solutions. Interestingly the data for the 4000K-1%wt. solution (orange symbols) shows a relatively constant value for the pressure drop across the contraction/expansion which is an order of magnitude higher than the corresponding asymptotic value for the inertia-less Newtonian limit (dashed black line). The relaxation time for this fluid $\tau_E \sim 55$ ms is high enough that even at the very lowest flow rates tested in the EVROC device $Q \simeq 0.05$ ml/min corresponding to $\dot{\epsilon} \simeq 20$ s⁻¹ the induced stretch rate is higher than the relaxation rate of the microstructure $\dot{\epsilon} \geq 1/2\tau_E$. Thus the viscoelastic contribution to the pressure drop dominates over viscous effects and leads to the enhanced pressure drop across the contraction for all test conditions.

This dataset shows that although the EVROC has clear potential for measuring the extensional properties of sufficiently viscoelastic solutions, there also exists a certain group of weakly viscoelastic liquids for which EVROC measurements, if not completely impossible, are at least heavily polluted by inertia effects. In section XX we quantify the dimensionless criteria that delineate these different regions.

In order to compare the EVROC performance with ROJER/CaBER, we studied the behavior of all of the test fluids using capillary thinning and jet breakup. For the very concentrated PEO solution (4000K-1%wt.), the test liquid was sufficiently elastic that measurements could be performed with a conventional CaBER device. As a result of their very low shear viscosities, measurements for the Newtonian solvent and the other four dilute polymer solutions were carried out using our ROJER setup.

In Figure 2-13(b-i) we show a snapshot of the viscoelastic jet for the 300K-0.01%wt. solution at $Q = 4$ ml/min corresponding to $V_j = 1.4$ m/s. Due to the small dimension of the jet ($D_0 \simeq 175$ μ m) the entire jet breakup process happens in a remarkably small length ($l_{break-up} \sim O(1$ mm)) and time scales ($t_{break-up} \sim l_{break-up}/V_j \sim$

($O(1 \text{ ms})$). Using a macro imaging lens one can optically zoom and magnify the image (up to a certain optical limit that depends on the magnification and numerical aperture of the lens) to gain a better view of the region of interest, which corresponds to the region from the onset of filament formation till the jet breaks up into discrete droplets. The black rectangle in Figure 2-13(b-i) indicates this region and a time series of the optically-zoomed view of this region (with a resolution of approximately $2 \mu\text{m}/\text{pixel}$) are shown in Figure 2-13(b-ii). As is clear from Figure 2-13(b-ii), the thinning dynamics of a Lagrangian element which is moving downstream with jet velocity V_j (e.g. elements inside the green box) can be tracked accurately and the evolution in filament diameter for a fixed Lagrangian point P are recorded with time in the same way as for the CaBER instrument (Figure 2-13(b-iii)).

The results are plotted in terms of the filament diameter $D_p(t)$ for the neck region in Figure 2-13(d) (raw measurements of the filament diameter are first smoothed by a moving average scheme from Matlab and then plotted). It is clear that for all dilute solutions tested with ROJER the thinning filaments exhibit an elasto-capillary regime at intermediate times in which the diameter decays with time exponentially (Equation 2.5). This is significantly different from the trend that is observed for the Newtonian solvent (black circles). The data for the Newtonian solvent follow the predictions of the initial linear instability analysis (solid black line, see Keshavarz et al. [108] for details) for almost the entire observable window and only show a narrow visco-capillary balance in the final stages of breakup. When compared to the Newtonian data, even the very dilute 300K-0.01%wt. solution (green symbols) shows a clear deviation in the diameter evolution with time and the final stages of breakup show an exponential decay in diameter consistent with the elasto-capillary balance. For the concentrated solution (4000K-1%wt.) the pressure drop required to force the fluid through the jet nozzle and piezo-tube is too large for the syringe pump. However the fluid is sufficiently viscous that CaBER measurements could be performed and the results are shown in Figures 2-13(c) and 2-13(e). Due to the much higher relaxation time for this concentrated solution the

duration of the capillary breakup event is resolvable using CaBER measurements ($t_{break-up} \geq O(0.1 \text{ s})$).

Analysis for the EVROC Data

To convert the pressure drop ΔP_c measured in the EVROC tests into a rheologically meaningful quantity such as the extensional viscosity one has to isolate the viscoelastic contribution of the pressure drop. As discussed, the nonlinear effects of inertia for $Re \geq Re_c$ make this complicated and it is recommended to measure the pressure drops in the limit of negligible inertia ($Re \leq Re_c$). However, even for measurements performed in the viscous-dominated regime one must be cautious in analyzing experimental pressure drop data. For inertialess flows of viscoelastic liquids, the calculated pressure drop across the contraction has two main components that we decompose additively so that $\Delta P_c = \Delta P_e + \Delta P_v$ where ΔP_e is the viscoelastic component of interest for computing the elongational viscosity and ΔP_v is a viscous component due to shearing at the walls. [174, 175, 41]. In order to measure/calculate elastic component ΔP_e one needs to have an accurate expression for the viscous component ΔP_v . For a non-Newtonian fluid sample this can be done by considering the flow of an inelastic fluid such as a phenomenological power law model (for which $\eta = m\dot{\gamma}^{n-1}$) [111]. An analytical expression for the viscous pressure drop across the hyperbolic contraction using a power-law model ($\Delta P_{c,v}^{PL}$) is given by Ober et al. [41]:

$$\Delta P_{c,v}^{PL} = \frac{2^{n+2}}{n+1} \left(\frac{2n+1}{n} \right)^n \left(\frac{l_c}{h} \right)^{n+1} \left\{ \left(\frac{w_u}{w_u - w_c} \right)^{n+1} - \left(\frac{w_c}{w_u - w_c} \right)^{n+1} \right\} m \dot{\epsilon}_a^n \quad (2.24)$$

From the measured shear rheology shown in Figure 2-12 we can thus calculate $\Delta P_e = \Delta P_c - \Delta P_{c,v}^{PL}$. To connect the remaining pressure drop $\Delta P_e(Q)$ to the extensional viscosity first Collier et al. [192] (for a semi-hyperbolic converging die) and later Ober et al. [41] (for the EVROC device used in this study) show that by assuming an incompressible flow and using a simple energy dissipation argument one can connect the rate of work done by the pressure drop occurring across

the contraction to the viscous losses induced by extensional stress differences in the fluid. After some simplifications the following expression for an ideal planar elongational flow is suggested by Ober et al. [41] for measuring the apparent extensional viscosity in a microfluidic contraction device at each imposed strain rate:

$$\eta_{E,app}^+(\dot{\epsilon}_a, \epsilon_H) = \frac{1}{\epsilon_H} \frac{\Delta P_e}{\dot{\epsilon}_a} = \frac{1}{\epsilon_H} \frac{(\Delta P_c - \Delta P_{c,v}^{PL})}{\dot{\epsilon}_a} \quad (2.25)$$

Analysis for the ROJER Data

In EVROC measurements, one adjusts the imposed extensional deformation rate by controlling the flow rate through the device and then monitors the extensional stress difference that develops in the fluid by recording the pressure drop across the contraction. This is different from the corresponding measurement procedure and analysis appropriate for devices based on capillary thinning such as ROJER or CaBER. As the filament thins under the action of capillarity, the normal stress difference in the thinning thread balances with the capillary pressure which is naturally set by the surface tension so that $(\Sigma_{zz} - \Sigma_{rr}) = 2\sigma/D(t)$. The thinning filament is being elongated with a local stretch rate that can be measured by analyzing the time evolution of the filament diameter:

$$\dot{\epsilon}_p = \frac{-2}{D_p(t)} \frac{dD_p}{dt} \quad (2.26)$$

This allows us to calculate the local transient extensional viscosity of the fluid at each instant:

$$\eta_{E,app}^+ = \frac{-\sigma}{dD_p/dt} \quad (2.27)$$

This material function thus varies with both imposed strain $\epsilon = \int_0^t \dot{\epsilon} dt'$ as well as the strain rate in the filament at that instant in time. In the elastocapillary thinning regime (given by Equation (2.5)) the strain rate is in fact constant. This can be directly verified by substituting Equation (2.5) in Equation (2.26) to give $\dot{\epsilon}_p = 2/3\tau_E$. In this region we thus expect the apparent extensional viscosity approaches the

true material function expected in a homogeneous extensional flow.

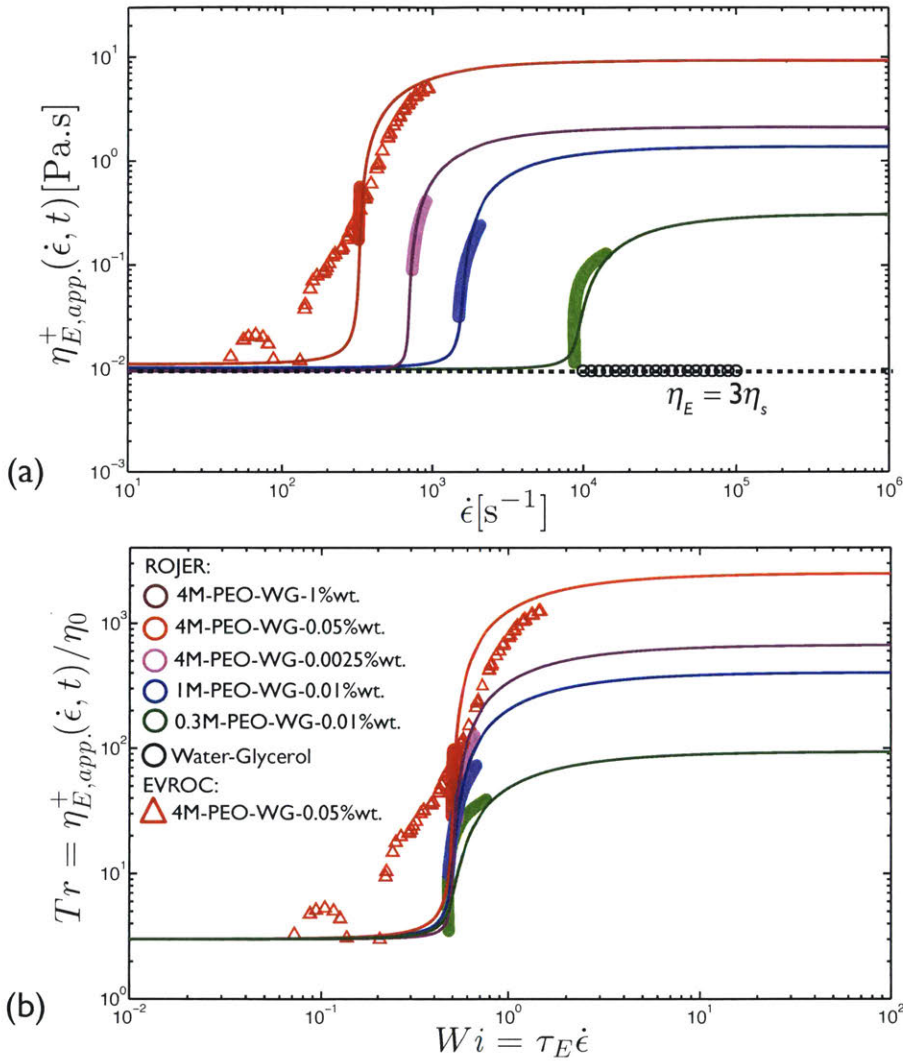


Figure 2-14: (color online). (a) Circles show the apparent extensional viscosities measured from ROJER experiments for the Newtonian solvent (\circ), 300K-PEO-0.01%wt. (green circles \circ), 1000K-PEO-0.01%wt. (blue circles \circ), 4000K-PEO-0.0025%wt. (magenta circles \circ), and the 4000K-PEO-0.05%wt. (red circles \circ) solutions. Open triangles show the EVROC measurements for the 4000K-PEO-0.05%wt. solution (red triangles Δ). The solid lines are predictions of FENE-P theory plotted for each liquid with the corresponding parameters from Table 1. (b) Same data shown in (a) but plotted in dimensionless form: Trouton ratio $Tr \equiv \eta_{E,app}^+(\dot{\epsilon}, t) / \eta_0$ versus the Weissenberg number $Wi \equiv \tau_E \dot{\epsilon}$.

Figure 2-14(a) shows a plot of the apparent extensional viscosity for all of the dilute polymer solutions studied (the 4000K-1% wt. solution with $c/c^* = 13.2$ is clearly not in the dilute regime, and since the primary focus of our study is on weakly viscoelastic fluids we postpone a discussion on the extensional rheology of this entangled semi-dilute solution to the Appendix XX[193]). The circles show data analyzed from ROJER tests and the red triangles are the EVROC results for the 4000K-0.05%wt. solution. Equations (2.26) and (2.27) are used to calculate the stretch rate and apparent elongational viscosity for ROJER tests ¹ and Equations (4.6) and (2.25) are used to calculate the values of average stretch rate and apparent extensional viscosity from the corresponding values of flow rate and pressure drop across the contraction in the EVROC test. Our results are also compared with the predictions of the FENE-P (finitely extensible nonlinear elastic) model, assuming the Peterlin statistical closure for the restoring force [111, 169](solid lines in both Figure 2-14(a) and 2-14(b)). Unlike simpler constitutive equations such as the Oldroyd-B model, which treats the polymer chains as ideal Hookean springs that are infinitely extensible, the FENE-P model assumes that the macromolecules have a finite extensibility and, once they are stretched to this fully unraveled limit, they will add no extra contribution to the extensional viscosity [111]. It is easy to show that the Oldroyd-B and FENE-P models differ primarily in their predictions of the steady extensional viscosities at stretch rates just above the critical coil-stretch transition rate. At steady state, the quasilinear Oldroyd-B model predicts the unphysical result that the extensional viscosity diverges at $\dot{\epsilon}_c = (1/2\tau_E)$. The FENE-P model corrects this shortcoming by incorporating the finite extensibility of the molecule (captured by a finite extensibility parameter L) into a nonlinear evolution equation for the viscoelastic stresses [111, 194]. The FENE-P model pre-

¹In calculating the extension rates for both Figures 2-14(a) and 42-14b) we multiplied the stretch rates calculated from Equation (2.26) by a factor of 0.75 ($\dot{\epsilon} = (3/4)\dot{\epsilon}_p$). This factor comes from the fact that the stretch rate in the elasto-capillary balance plateaus around a critical value $\dot{\epsilon}_p = 2/3\tau_E$ while the predictions for elongational viscosity from constitutive equations such as Oldroyd-B/FENE-P show that the coil-stretch transition happens at a lower critical strain rate $\dot{\epsilon}_c = 1/2\tau_E$. In order to make a quantitative one-to-one comparison between the ROJER data and known constitutive equations all the stretch rate data from ROJER for each of the test fluids were multiplied by $(1/2)/(3/2) = 3/4$.

dicts that the steady elongational viscosity $\eta_E(\dot{\epsilon})$ remains bounded once the chains are fully extended. The stretched chains act like an anisotropic suspension of rods with the extensional viscosity in the bulk reaching a plateau value at high stretch rate ($\lim_{\tau_E \dot{\epsilon} \rightarrow \infty} \eta_E^+ = 3\eta_s + 2(\eta_0 - \eta_s) L^2$).

The solid lines in Figure 2-14(a) show predictions from the FENE-P model for each liquid using the corresponding parameters $(\tau_E, \eta_s, \eta_0, L)$ from Table 1. All of the ROJER data show good agreement with the predictions from the FENE-P model. The apparent viscosity extracted from the EVROC test also shows a trend that agrees qualitatively with the predictions of the FENE-P model, but the agreement is not quantitative. The observed difference arises due to the fact that in the EVROC device material elements in different planes experience different deformation histories as they flow through the contraction/expansion. These local variations in the stretch rate of different material elements smear out the critical extension rate. By using computational shape optimization for the design and fabrication of cross-slot microfluidic devices, Haward et al. [116] showed that a homogeneous elongational flowfield can be achieved, by minimizing this inhomogeneity in the flow history of different material elements. Experimental results from such optimized microfluidic devices show a much better agreement with the FENE-P model [116, 172].

Figure 2-14(b) shows the extensional viscosities represented in dimensionless form with a Trouton ratio η_E^+/η_0 plotted as a function of the Weissenberg number $Wi = \tau_E \dot{\epsilon}$. Due to the high extensibility of the molecules ($L \sim M_w^{1-\nu}$ where ν is the solvent quality exponent [138, 116]) Trouton ratios as high as $Tr \sim 1000$ can be achieved by these dilute polymer solutions at high molecular weights. These high values of the extensional viscosity can dramatically change the filament thinning dynamics at high strain rates and small length scales in a number of important application such as inkjetting, atomization, microfluidic cell sorting etc [107, 109, 184]. Measurements with the EVROC device for the low viscosity solutions (green, blue and magenta colors in Figure 2-13(a)) are largely polluted by nonlinear inertia effects, but Figures 2-14(a) and 2-14(b) clearly show that jetting rheometry is a reliable

alternative for determining the extensional rheology of very dilute polymer solutions. The ROJER instrument not only differentiates between the extensional rheology of the different solutions in a qualitative manner (Figure 2-13(d)) but also quantitatively measures elongational properties in the elasto-capillary regime at constant strain rate that agree well with predictions of microstructural constitutive equations such as the FENE-P model.

Measurements of the extensional viscosity were performed for a number of viscoelastic polymer solutions using two microfluidic test configurations; a microfabricated hyperbolic converging/diverging flow and a micromachined piezoelectric nozzle. Our results show that for dilute solutions that have both low shear viscosities and low relaxation times, the flow in the hyperbolic contraction is affected by nonlinear inertial effects before any signature of elasticity emerges. However, the EVROC is still a functional method for characterizing more viscous and more elastic solutions. The fact that many industrial and biological samples are indeed dilute solutions of large macromolecules in a low viscosity solvent encouraged us to find an alternative method for performing extensional rheometry of dilute solutions. The ROJER instrument, which is based on understanding the capillary thinning and breakup in a sub-millimeter scale physically-forced jet proves to be a valuable additional method that can discriminate between the relaxation times of the different viscoelastic solutions used in the present study. The results obtained from the ROJER and EVROC techniques also compare well with the predictions of a canonical model such as the FENE-P constitutive equation. Depending on the intrinsic properties of the specific fluid being tested, one or other of these two microfluidic rheometry methods can thus help us to determine the elongational properties of an unknown complex fluid. The question for practicing rheologists is to know where exactly are the limits and boundaries of operation for each of these two distinctly different instruments. As we show below, by knowing the intrinsic properties of a liquid we can provide guidance on deciding *a priori* which instrument to use.

2.6 Operating Limits of the EVROC Device

As we have shown in this chapter, the flow of a viscoelastic liquid in a microfluidic channel can be affected by three different mechanisms: elastic effects due to elongation of macromolecules passing through the contraction, viscous effects due to viscous shear stresses at the walls, and finally adverse inertial effects due to acceleration of the material elements passing through the contraction/expansion. If we pick a characteristic length scale such as the hydraulic diameter (denoted generically by R) for this device, we can identify three important timescales, each characterizing one of the three different aforementioned mechanisms:

$$\tau_{elas.} = \tau_E \quad : \text{Elongational relaxation time} \quad (2.28a)$$

$$\tau_{visc.} = R^2 \rho / \eta_0 \quad : \text{Viscous diffusion time scale} \quad (2.28b)$$

$$\tau_{conv.} = R/V \quad : \text{Convective time scale} \quad (2.28c)$$

where $V = Q/wh$ is the characteristic scale for the velocity in the channel. Having identified three important timescales, it is apparent that the flow of any liquid in the device can be described by two dimensionless numbers:

$$\text{Reynolds Number} \quad Re = \tau_{visc.} / \tau_{conv.} = \rho V R / \eta_0 \quad (2.29a)$$

$$\text{Weissenberg Number} \quad Wi = \tau_{elas.} / \tau_{conv.} = \tau_E V / R \quad (2.29b)$$

Equations (4.6a and 4.6b) clearly show that for a given liquid and hyperbolic channel geometry (fixed values of τ_E, ρ, η_0 and R), changes in the flow rate lead to both Re and Wi increasing proportionally such that their ratio (given by the elasticity number[195] $El \equiv Wi/Re = \tau_E \eta_0 / \rho R^2$) remains constant. In other words in the two-dimensional space spanned by $Re - Wi$ (the operating plane for EVROC) changing the velocity corresponds physically to moving away from the origin on a line with fixed slope (or a fixed angle θ in polar coordinates) and the velocity provides a measure for the radial distance from origin (similar to r in polar coordinates).

dinates). In order to observe elastic effects, and to be able to characterize them, one has to stretch the dissolved polymers sufficiently fast, compared to their relaxation rate ($V/R \geq 1/\tau_E$), or in other words the viscoelastic timescale should dominate over the convection time scale so that the Weissenberg number of the flow is $Wi = \tau_E V/R \geq O(1)$. Thus for any fluid with relaxation time τ_E and test geometry R , there exists a certain velocity $V_c \sim R/\tau_E$ above which the elastic effects we seek to measure begin to emerge. However, the challenge is to ensure that this (large) velocity is still small enough that the Reynolds number characterizing the flow stays lower than the critical value for onset of inertia effects (i.e. $Re = \rho V R/\eta_0 \leq O(1)$). One can easily see that by combining these two criteria then the ratio of the Weissenberg number over Reynolds number should be larger than unity; i.e. $Wi/Re \geq O(1)$. In Figure 2-15(a) a line of constant elasticity is shown as a dashed blue arrow in the $Wi - Re$ plane.

The magnitude of the elasticity number thus provides a criterion for EVROC measurements. Given a specific hyperbolic channel design (i.e. a given microfluidic length scale R) and fixed liquid properties (η_0, τ_E , and ρ) one can calculate *a priori* whether the criterion for EVROC measurements (i.e. $El = \tau_E \eta_0 / \rho R^2 \geq O(1)$) is satisfied or not. From this expression it becomes apparent that in dilute polymeric liquids, such as the ones tested in this study, in which both the relaxation time and the shear viscosity are small, EVROC measurements are often impossible or contaminated by inertial effects. One possible pathway for circumventing this constraint is to fabricate even smaller microfluidic geometries (because decreasing the corresponding length scale increases the elasticity number). For the present design the length scale is $R \equiv d_H \simeq 267 \mu\text{m}$. However, the large pressure drop that result from very small length scales (cf. Equation 2.24) can lead to fabrication failure and pumping issues. Additionally the characteristic device length scale R can not approach the length scale of the microstructure in the liquid otherwise wall effects lead to hindered chain deformation and hydrodynamic screening complications[196].

Having determined the appropriate limits of EVROC, we now consider our alter-

native jet-based extensional rheometer and probe the operational boundaries for the ROJER device.

2.6.1 Limits of ROJER

ROJER, or other related capillary-thinning methods for extensional rheometry (such as CaBER or modified versions of CaBER [197, 81, 82]), exploit the dynamics of the Rayleigh-Plateau instability and often rely on optical devices such as high-speed/strobe cameras, lenses and bright field illumination strategies to record the evolution in the filament diameter with time. A liquid thread with a known initial radius R that is connected at both ends to hemispherical liquid reservoirs (as in either of the ROJER/CaBER configurations) experiences higher capillary pressures inside the filament neck compared to the pressure in the hemispherical reservoirs. This pressure imbalance leads to the drainage of liquid from the filament into the reservoirs and induces an elongational flow within the filament. For a viscoelastic liquid four different physical mechanisms can be important: Elastic, viscous and inertial effects can all play a significant role, similar to the discussion above for flow in the hyperbolic contraction. In addition to these three effects, the capillary effects play an essential role in extensional flows with free surfaces. Thus one must consider an additional timescale that captures the effect of surface tension or capillarity in this problem

$$\tau_{cap.} = \sqrt{\rho R^3 / \sigma} : \text{Capillary time scale.} \quad (2.30)$$

This capillary time scale was first introduced by Rayleigh [80, 163] in his studies of liquid jets and is therefore also known as the Rayleigh time scale τ_R . It is also the timescale observed in the vibration of a liquid droplet/jet due to capillary effects[198].

It is easy to construct an appropriate dimensionless number comparing the mag-

nitudes of the capillary and convective timescales:

$$\sqrt{We} = \tau_{cap.}/\tau_{conv.} = V\sqrt{\rho R/\sigma} \quad (2.31)$$

This ratio is the square root of the Weber number which is widely used in studies of drop/jet breakup in inkjetting and atomization operations[57].

Thus in ROJER four competing timescales are involved (Equations ((2.28)and 2.30)) which leads to a set of three important dimensionless numbers (\sqrt{We} , Re , Wi). A new coordinate \sqrt{We} is therefore also required to determine the locus of each fluid being tested in the ROJER instrument. In Figure 2-15(a) we represent this concept by plotting an $\{x, y, z\}$ three dimensional space with $\{\sqrt{We}, Re, Wi\}$ coordinates respectively.

To characterize the performance of ROJER we need to understand how the dynamics of a thinning filament are governed by the different physical mechanisms involved. Inertial effects are damped out by viscous effects if the capillary timescale is larger than the viscous diffusion time scale ($\tau_{cap.} \geq \tau_{visc.}$). The ratio of these two timescales is known as the Ohnesorge number $Oh \equiv \tau_{cap.}/\tau_{visc.} = \eta_0/\sqrt{\rho\sigma R}$ [199] and for viscous effects to dominate over fluid inertia we require $Oh \geq O(1)$. Similarly, in order to probe viscoelastic effects in the thinning thread the elongation rate of the filament resulting from capillary action should exceed the relaxation rate of the polymer (i.e $1/\tau_{cap.} \geq 1/\tau_{elas.}$). The ratio of the elastic timescale to the capillary time is an intrinsic Deborah number and we thus require $De \equiv \tau_{elas.}/\tau_{cap.} = \tau_E/\sqrt{\rho R^3/\sigma} \geq O(1)$.

One additional benefit of ROJER as compared to EVROC is the fact that unlike the hyperbolic channel flow in which the characteristic length scale R is fixed and not changing with time, in ROJER the appropriate length scale $R(t)$ is evolving with time and decreases steadily from the initial value toward the final instant of breakup. By studying the functional form of the relevant dimensionless numbers such as the Deborah and Ohnesorge numbers one can see that as $R(t)$ decreases, local estimates of the the relevant force balances increase as we approach

the breakup point. This means that as we follow the evolution of the thinning filament with time there exists a certain point at which elastic effects start to dominate the flow. Provided the local diameter at this crossover point is larger than the optical resolution of the setup (which we denote $l_{resolution}$) then ROJER measurements are feasible. However if this crossover point lies below our resolution limit then ROJER will not be able to resolve the elasto-capillary balance that is established close to breakup.

The practical constraints of physical optics mean that most imaging systems have a lower resolution of a few microns, $l_{resolution} \sim O(1 \mu\text{m})$. We also know that for most complex fluids, the zero shear viscosity will not be much smaller than the viscosity of water (unless we consider supercritical solvents such as liquid CO_2). Thus for most low viscosity liquids (with $\eta_0 \geq 10 \text{ mPa}\cdot\text{s}$) the visco-capillary regime is accessible within the optical resolution that is achievable ($l_{resolution} \sim O(1 \mu\text{m})$). To determine the operating boundaries of ROJER in elongational rheometry we can assume that a failed test means that elastic effects do not emerge in the thinning filament even on the finest length scale that is resolvable $R(t) \sim l_{resolution}$. In other words, even in the final moments of filament thinning the rate of stretching is not as high as the relaxation rate of the microstructure, so that $\dot{\epsilon} = (-2/R) \cdot (dR/dt) < 1/\tau_E$. If an elasto-capillary balance has not emerged yet then for most practical liquids in the final moments of thinning a visco-capillary balance starts to emerge and, consequently, the maximum rate of thinning that is optically accessible scales as $\dot{\epsilon}_{max} \sim V_{cap.}/R \sim \sigma/\eta_0(1/l_{resolution})$.

Therefore for a viscoelastic liquid, in a device such as ROJER, to reach a critical stretch rate which is faster than the relaxation rate of the microstructure the following criteria should be met:

$$1/\tau_E \leq \dot{\epsilon}_{max} \simeq \frac{1}{l_{resolution}} \frac{\sigma}{\eta_0} \quad \text{or} \quad \frac{l_{resolution}}{R_0} \lesssim \frac{\tau_E \sigma}{\eta_0 R_0} \quad (2.32)$$

This dimensionless grouping that controls ROJER performance may be referred to as an elasto-capillary number, which can also be written in terms of De and Oh as

$\tau_E \sigma / (\eta_0 R_0) = De/Oh = Ec$ [200]. An alternate, easier, justification for this criterion for successful ROJER testing is to consider the stresses involved in the thinning filament. The elasto-capillary balance starts on a length scale R_{EC} , when the capillary stresses become as large as polymer elastic stresses: $\sigma/R_{EC} \sim \eta_0/\tau_E$. This simply tells us the condition for ROJER performance is $l_{resolution} \leq R_{EC} \approx \sigma\tau_E/\eta_0$ which is equivalent to $l_{resolution}/R_0 \lesssim Ec$.

Equation (2.32) shows that in ROJER, just as in EVROC, the criterion for successful elongational rheometry can be expressed by a single dimensionless number based on the geometry, optical resolution and intrinsic properties of the liquid (which here includes the relaxation time, surface tension and zero shear viscosity). Combining these two separate criteria for successful operation of the microfluidic hyperbolic channel and jet breakup measurements (EVROC and ROJER respectively) the entire dimensionless space in Figure 2-15(a) can be navigated for different liquids through a two dimensional state diagram or nomogram which tells us what instrument is suitable in each region .

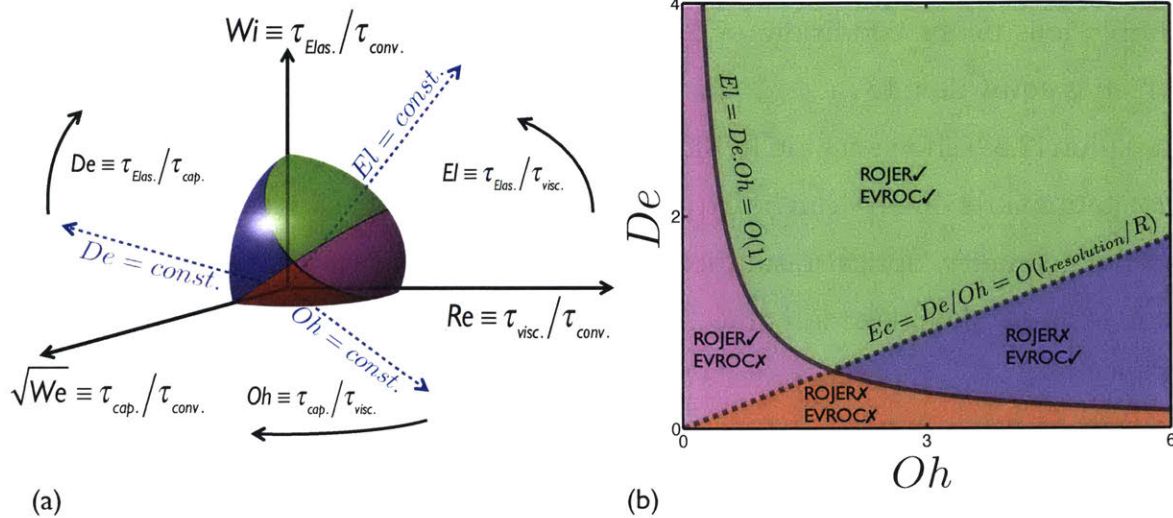


Figure 2-15: (color online). (a) Measurement nomogram in 3-dimensional space for different liquids with coordinate axis x, y, z constructed from $\{\sqrt{We}, Re, Wi\}$ combination. Lines of constant elasticity El , Ohnesorge Oh and Deborah De numbers are shown by blue dashed arrows. The black arc arrows show the direction at which El, Oh and De increase in their corresponding $Re - Wi, Re - \sqrt{We}$, and $\sqrt{We} - Wi$ planes. One eighth of a unit sphere is plotted in the corner of the coordinates. Every material location in the x, y, z parameter space can be radially projected onto the surface of this sphere. Shaded colors show regions in which EVROC and the ROJER instrument can/cannot perform. (b) Measurement nomogram based on the key intrinsic properties of the fluid plotted in a 2D representation. The angular orientation of every point in the 3D parameter space sketched in (a) can be uniquely mapped onto this 2D representation ($De - Oh$). The solid and dashed lines are lines of constant elasticity number El and elasto-capillary number Ec respectively. The green area indicates where both ROJER and EVROC are possible ($Ec \geq O(l_{resolution}/R)$ and $El \geq O(1)$). The magenta area is where ROJER is possible and EVROC is impossible ($Ec \geq O(l_{resolution}/R)$ and $El < O(1)$). The blue area is where ROJER is impossible and EVROC is possible ($Ec < O(l_{resolution}/R)$ and $El \geq O(1)$). The red area is where both ROJER and EVROC are not possible ($Ec < O(l_{resolution}/R)$ and $El < 1$).

2.6.2 Operating Nomogram for Microfluidic Extensional Rheometry

Looking at Figure 2-15(a) one can see that (as we first noted for the elasticity number) both the Deborah and Ohnesorge numbers characterizing the fluid are also independent of the velocity and thus represent the slopes of rays passing through the origin and projected onto their respective $Wi - \sqrt{We}$ and $\sqrt{We} - Re$ planes. The black arcs in Figure 2-15(a) show the direction in which each of these dimensionless groups increase. It is also noteworthy that although the parameters $\{\sqrt{We}, Re, Wi\}$ form an independent set of coordinates, the $\{El, Oh, De\}$ set are not independent and indeed any one of the three can be expressed in terms of the other two through the relationship $El = Oh.De$. A good way to understand the difference between these two different sets of dimensionless numbers is to think of Cartesian and spherical coordinates. The dimensionless groups \sqrt{We}, Re, Wi all grow linearly with velocity and thus correspond to orthogonal coordinates in Figure 2-15(a). By contrast El, Oh, De are all independent of velocity and represent the slopes of the position vector projected onto the three base orthogonal coordinate planes. Thus as we increase the velocity and keep other parameters constant we move radially away from origin on a fixed line and orientation in space. To uniquely specify a point in space using spherical coordinates we only need two angles (θ and ϕ) and a radial distance (r) from origin. This tells us that only two dimensionless numbers from the set of El, Oh, De are needed to uniquely describe the *orientation* of any material line/vector in space. Increasing the characteristic velocity of the fluid in the device, and keeping these two angles constant, we travel on a fixed ray away from the origin. If we pick the Deborah and Ohnesorge numbers to describe the orientation of material lines then we can project our results onto the two dimensional map plotted in Figure 2-15(b) which is a one-to-one transform of the outer surface of the spherical segment shown in Figure 2-15(a).

This two-dimensional nomogram representing intrinsic viscoelastic fluid properties can help us understand where different materials are located at different length

scales. For example the abscissa ($De = 0$) corresponds to all Newtonian phenomena starting from the inviscid limit close to the origin and moving towards very viscous fluids on the far right. The region close to, but not on, the ordinate axis represents low viscosity but elastic liquids, such as the very dilute solutions of high molecular weight polymers considered in the present work. Other examples include "stringy materials" such as saliva, printing inks and paints that are often highly problematic in atomization and breakup phenomena.

The two criteria derived above for EVROC and ROJER operation can be drawn as two separate lines in this space given by the expressions $El = De.Oh = O(1)$ and $Ec = De/Oh \simeq l_{resolution}/R$ on this two dimensional plane (as shown by the solid and dashed lines in Figure 2-15(b)). These two lines divide the entire region into four subregions. In each of these subregions extensional rheometry with either EVROC and or ROJER may be possible depending on the values of these two groups. Different areas are shaded by different colors as follows:

1. Green: regions in which both criteria are met ($El \geq O(1)$ and $Ec \gtrsim l_{resolution}/R$). In simple words, these fluids are both elastic and viscous enough that both ROJER and EVROC can be used for extensional rheometry.
2. Magenta: regions in which jetting rheometry is possible but EVROC is not successful ($Ec \gtrsim l_{resolution}/R$ and $El < O(1)$). In simple words, these fluids are of such low viscosity that inertial effects dominate in the microfluidic contraction, but they are sufficiently elastic that they will form a thread during jet breakup.
3. Blue: regions in which the criterion for EVROC is met but jetting is not possible ($El \geq O(1)$ and $Ec \lesssim l_{resolution}/R$). In simple words, these liquids are sufficiently viscous that they generate a viscoelastic contribution to the pressure drop ΔP_c across the contraction, but insufficiently elastic for the elastic stresses to balance capillary pressure in the jet until the length scale falls below the optical resolution limit.
4. Orange: regions in which neither criterion for either EVROC or ROJER are

met ($El < O(1)$ and $Ec \lesssim l_{resolution}/R$). In this region the fluid is insufficiently viscoelastic for either class of device to operate successfully.

2.6.3 Nomogram for Measuring Extensional Viscosity

Figure 2-16 shows an alternate, log-log representation of the proposed nomogram in Figure 2-15(b). The viscoelastic liquids studied in the present work are located on this nomogram based on their corresponding values of Ohnesorge and Deborah numbers (Table 1 in the main text). It is clear that for the three most dilute solutions (300K-PEO-0.01%wt., 1000K-PEO-0.01%wt., and 4000K-PEO-0.0025%wt. each shown by triangles located in the magenta-shaded region showing) measurements in the EVROC fail due to inertial effects. The other two viscoelastic solutions (a dilute 4000K-PEO-0.05%wt.(\circ) solution and a semi-dilute entangled 4000K-PEO-1%wt.(\bullet) solution) are located in the green-shaded area where both EVROC and ROJER/CaBER instruments can perform measurements of the extensional viscosity.

In studying the limits of performance for jetting rheometry, a quantitative estimate of the limiting conditions can be made by estimating the slope of the dashed line in Figure 2-15(b). For our ROJER system $l_{resolution} \sim 1.5\mu m$ and $R_0 \sim 90\mu m$ which shows that the actual slope of the dashed line is very small. The orange region indicated in Figure 2-15(b) is thus also very small and this is a very promising reason to believe that microfluidic jet breakup studies are a viable option for many dilute viscoelastic liquids. Finally it is also necessary to point out that ROJER fails for certain liquids that are very viscous but have an extremely small relaxation time (blue region in Figure 2-15(b)). Examples of these liquids can be found in concentrated solutions of low molecular weight polymers which are sometimes used in food thickeners. For these liquids, the EVROC device benefits from the dominant viscous characteristics and can probe both the viscous response as well as any additional elastic contributions to the pressure drop without dealing with inertia-related issues [41].

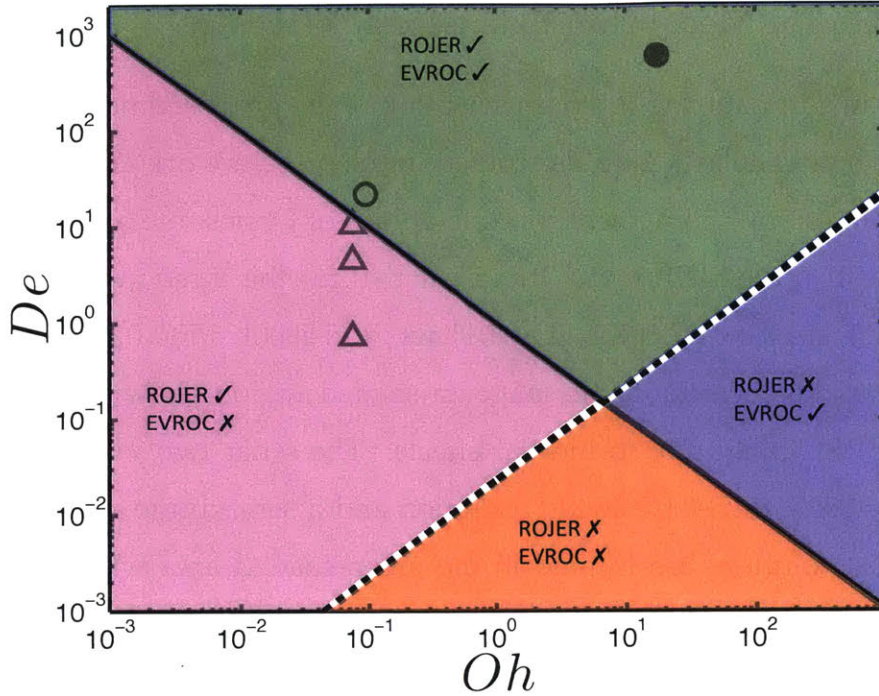


Figure 2-16: (color online). Extensional rheometry nomogram based on the key intrinsic properties of the fluid plotted in a 2D representation. The green area indicates where both ROJER and EVROC are possible ($El \geq O(1)$ and $Ec \geq O(l_{resolution}/R)$ using $l_{resolution} \simeq 2\mu m$ and $R_0 \simeq 90\mu m$). The magenta area is where ROJER is possible and EVROC is impossible ($Ec \geq O(l_{resolution}/R)$ and $El < O(1)$ respectively). The blue area is where ROJER is impossible and EVROC is possible ($Ec < O(l_{resolution}/R)$ and $El \geq O(1)$). The red area is where both ROJER and EVROC are not possible ($El < 1$ and $Ec < O(l_{resolution}/R)$). The locus of each test fluids is located on the nomogram based on the corresponding values of Deborah and Ohnesorge numbers (calculated in Table 1 in the main article). For three of the dilute polymer liquids (300K-PEO-0.01%wt., 1000K-PEO-0.01%wt., and 4000K-PEO-0.0025%wt.) measurements were possible using the ROJER instrument while the EVROC data could not be analyzed due to dominant inertial effects (Δ). One dilute solution, 4000K-PEO-0.05%wt.(\circ), and a semi-dilute entangled solution, 4000K-PEO-1%wt.(\bullet) are located in the green region and both EVROC and ROJER measurements give meaningful values for the apparent extensional viscosity of these liquids.

Chapter 3

Effect of elongational properties on the average diameter of the fragments observed in the atomization

A beautiful blonde is chemically three-fourths water, but what lovely surface tension.

— Anonymous

3.1 Scope

We introduced different methods for elongational rheology of dilute solutions in the previous chapter. In this chapter we show how these measured elongational properties can change the dynamics of fragmentation and atomization even for very dilute viscoelastic solutions. We chose a canonical fragmentation process known as air-assisted atomization, which is widely used in the spray and coating industry. After introducing the atomization process and presenting the experiments, we proceed to develop a simple toy model for the dynamics of the liquid filaments in the final stages of atomization. This model is based on the behavior of the filaments in a sudden stretch test which is devised and observed in detail using high-speed photography. Finally we compare the results of our toy model with the experimental measurements.

3.2 Introduction

Jet atomization and the physics of liquid breakup has been a source of scientific curiosity and industrial applications for many years and over the past century there have been many developments in understanding the fluid mechanics involved in jetting and atomization of the Newtonian liquids [140]. However, most liquids of commercial relevance have a complex microstructure and do not completely follow Newtonian behavior; polymer melts, fuels, paints, and our own saliva are just a few examples. There are many applications in which these non-Newtonian solutions experience jet breakup or atomization such as paint spraying, inkjet printing, cosmetics preparation, spray drying of foods, and disease transfer through sneezing; however by comparison to the depth of knowledge about the atomization of Newtonian liquids [57, 42] little is known about the complexities encountered in the atomization of viscoelastic liquids [201].

Accurately measuring the extensional response of low viscosity fluids and understanding the importance of extensional stresses in complex flow fields is a research challenge that Ken Walters and colleagues focused on intensely for several decades. In a wide-ranging plenary paper for the 11th ICR in Brussels (1992) [102], Walters pointed out when discussing the challenges inherent to measuring the extensional properties of mobile liquids that "the task is therefore to generate a flow which is dominated by extension and to address the problem of how best to interpret the data in terms of material functions that are rheologically meaningful". He went on to note that (after he first expanded on this philosophy at an earlier 1984 European Congress) "...to say that it did not meet with unbridled enthusiasm would be an under-statement!" However, inspired by this conviction, and undeterred by such reservations we investigate air-blast atomization of complex fluids by seeking to understand and quantify the break up dynamics of a non-Newtonian jet.

Previous studies have shown that addition of viscoelasticity can lead to significant changes in both jet break up and atomization processes [202, 203, 15, 204].

These modifications occur mainly when the fluid element reaches the large strains and rapid nonlinear deformation rates that are generated in the final breakup and pinch off stages (Figure 3-1). Chao et al.[203] showed that addition of polymers to jet fuels can lead to anti-misting properties which can be extremely beneficial to aviation safety. In some other applications such as spray or roll coating [205] these "anti-misting" properties which result from the added viscoelasticity may inhibit the sprayability of a liquid and be undesirable. Thus, understanding and quantifying these effects is an important scientific goal; better knowledge of these phenomena is sufficiently important that it has been suggested that the future of industries such as rapid manufacturing of biological materials via drop-on-demand printing or jet engine propulsion are dependent on new developments and deeper understanding of jetting phenomena in complex fluids [206, 58, 207, 208].

Attempts to understand the effects of viscoelasticity on atomization [201, 209] have faced challenges in measuring the behavior of the non-Newtonian liquid in the strong nonlinear deformation and high strain rates that characterize the spray. Dilute polymeric solutions are known to show nonlinear behavior in large deformations and demonstrate higher resistance against elongational deformations [111]. Spray visualizations show that the added viscoelasticity does not lead to any significant change in the early stages of breakup dynamics, when the liquid is still close to the nozzle. Here the deformations are still small and disturbances are in the linear stage (compare Figures 3-1(a) and 3-1(c)). However significant differences start to emerge when viscoelastic ligaments are stretched and elongated into the air stream far from the nozzle (compare Figures 3-1(b) and 3-1(d)). This has motivated many researchers to focus on the extensional rheological properties of the fluid, in order to better understand the effects of viscoelasticity on the liquid's performance in atomization [203, 136, 210]. These findings have shown qualitatively that the additional resistance against elongational deformations for viscoelastic solutions will lead to poor atomization. As discussed in chapter 2, precise measurements of elongational properties such as the fluid relaxation time or the magnitude of the elongational viscosity are essential for a quantitative study of

these effects, but elongational rheology for dilute solutions is a well-known challenge [73, 23, 24, 60, 20, 133]. While true extensional rheometers such as the Filament Stretching Extensional Rheometer (FISER) work well for very elastic melts, gels and viscous polymer solutions [101] there are only a few extensional rheometers that can be used for dilute polymer solutions and low viscosity complex fluids. In the previous chapter we presented a detailed descriptions for these rheometers. Corresponding limits for each of these instruments were shown and discussed in detail in Chapter 2.

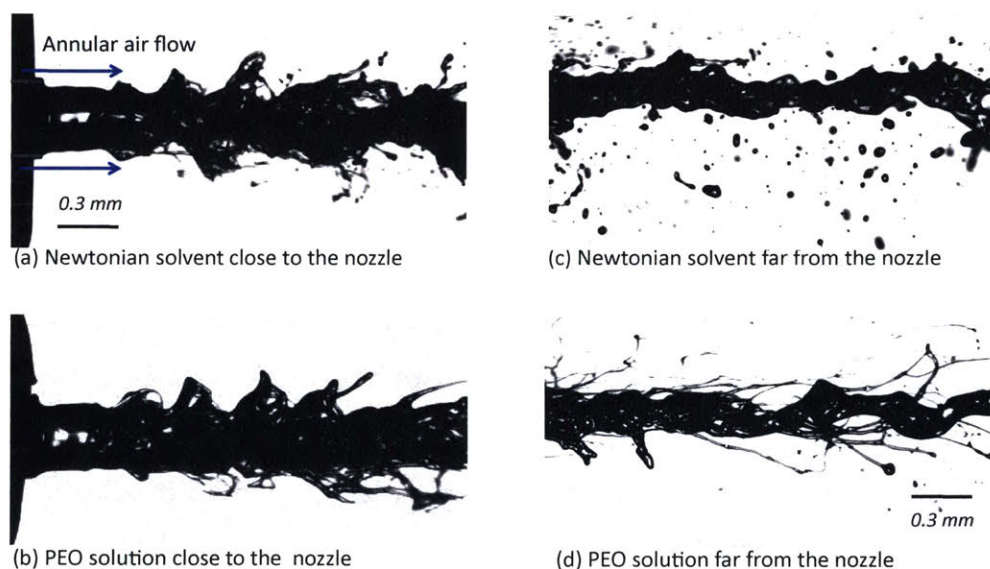


Figure 3-1: (a) Spray visualization images for the Newtonian solvent close to the nozzle. (b) Spray visualization images for the viscoelastic solution (PEO-300K-0.01 wt.% in the solvent) close to the nozzle. (c) Spray visualization images for the Newtonian solvent far from the nozzle. (d) Spray visualization images for the viscoelastic solution (PEO-300K-0.01 wt.% in the solvent) 5mm away from the nozzle.

To understand the dominant effects of complex fluid rheology on atomization, researchers have tried to understand the key fluid mechanical features of sprays and study the dynamical response of well-characterized fluids in the spray. Air-assisted atomization is a commonly-used method for spraying viscoelastic flu-

ids in many industrial coating applications. As shown in Figure 3-2(a), a high-momentum annular air jet destabilizes the low momentum liquid jet and finally atomizes the liquid jet into small droplets/fragments. Recent research on air-assisted atomization has shown that, for a Newtonian fluid at least, this process can be described as a well characterized sequence of instabilities that help to finally disintegrate the liquid into small fragments (Figure 3-2). Marmottant and Villermaux [42] have shown that in air-assisted atomization the liquid jet passes through three distinct instabilities. Initially the low momentum core liquid jet experiences a relatively high shear rate at its surface induced by the surrounding annular flow of air (which has a much higher velocity and kinetic energy). This will lead to the generation of waves on the surface of the liquid jet due to the well-known Kelvin-Helmholtz instability (Figure 3-2) [158]. As the wave crests grow, the acceleration of the less dense medium, i.e. air, into the more dense medium results in a second instability, known as Rayleigh-Taylor instability, that elongates ligaments of fluid into the air stream. Finally the stretched ligaments thin down in the neck region that still connects them to the core liquid jet as a result of Rayleigh-Plateau instability and they ultimately detach from the jet after stretching to a certain length. Beyond this point the detached ligament can fragment into a cascade of small droplets which form the final spray mist.

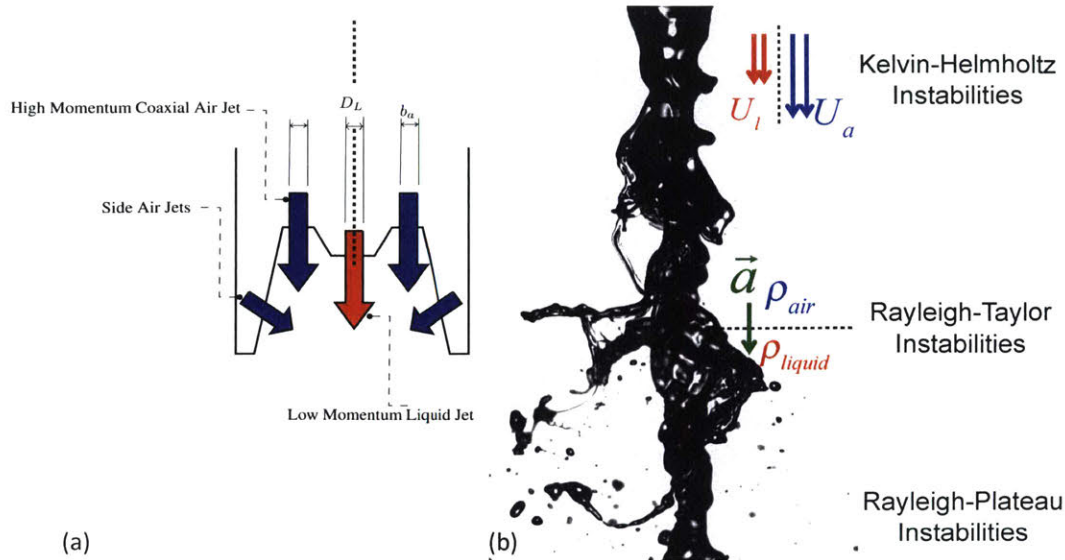


Figure 3-2: (a) Schematic of the industrial spray nozzle used in the experiments with $D_L = 1.5\text{mm}$, $b_a = 1.5\text{mm}$. A low momentum liquid jet (red color) is surrounded by a coaxial high momentum jet of air (blue color). The oblique air jets are low momentum and only help confine the primary jet in a narrow plane. (b) Spray visualization of water; three different successive instabilities make the liquid jet unstable and finally atomize it into a fine mist of droplets.

For measurements of elongational properties in very low viscosity “mobile liquids”, Christanti and Walker [83, 210] used a novel method, originally suggested by Schümmer and Tebel [25] that focused on understanding the fluid mechanics of the jet breakup process itself. By studying the jet breakup of dilute polymeric solutions they showed that there is a correlation between the measured relaxation times and the average droplet diameters measured in air-assisted atomization. Studies of sprays of viscoelastic solutions by Christanti and Walker [210], building on earlier work by Ferguson et al. [27], have shown qualitatively that there is an initial increase in average droplet diameters denoted by $\langle d \rangle$ with increasing relaxation times followed by a saturation at higher values of the fluid relaxation time.

Despite the growing interest in fragmentation and atomization of very dilute poly-

meric solutions, there is still a lack of quantitative knowledge about the effects of viscoelasticity on atomization in this limit. In this chapter we study a selection of dilute Poly(ethylene oxide) (PEO) solutions at moderate molecular weights and concentrations well below coil overlap conditions. We show that careful analysis of jet breakup for these liquids can help us make precise measurements of their elongational properties. These model solutions are also tested in a commercial air-assisted atomization gun that is used in the paint coating industry. The changes in the measured mean droplet size from the spray tests are related to the measured fluid relaxation times by a simple physical argument describing the fluid dynamics of the thinning and elongating ligaments that develop close to individual pinch off events in the spray.

3.3 Test liquids

In order to systematically study the effects of viscoelasticity on the atomization, four different dilute polymer solutions were selected as test liquids. All of these solutions are made by dissolving small amounts of Poly(ethylene oxide) or (PEO) with $M_w = 3 \times 10^5 g/mol$ and $1 \times 10^6 g/mol$ respectively (purchased from Sigma Aldrich) in a water-glycerol (60-40 wt.%) solvent ($\eta_s = 3.2 mPa.s$) and the resulting viscometric properties are summarized in Table 1. The values of surface tension for all the viscoelastic solutions are close to the solvent value ($\sigma \simeq 60 \pm 3 mN/m$). Using the expressions given in [24, 190] the overlap concentrations (c^*) are respectively 0.28 wt.% and 0.14 wt.% for 300K and 1000K solutions. Values of the extensibility parameter for these PEO solutions are calculated based on the constants reported in [116] for flexible PEO chains ($L \sim M_w^{1-\nu}$ in which $\nu = 0.56$ for a reasonably good solvent such as PEO in water/glycerol). Because of the dissolved polymer, the shear viscosity of the solutions show a slight increase at low rates ($\eta_0 = 3.3 mPa.s$) and asymptotically approach the solvent value at high shear rates ($\eta_\infty = 3.2 mPa.s$ at $\dot{\gamma} \simeq 10^5 s^{-1}$). The small increase in the zero shear viscosity is due to the very low concentration of the PEO in the solvent for this solution ($\eta_0 \simeq \eta_s (1 + c/c^*)$) and for

Table 3.1: Rheological properties of the viscoelastic spray test fluids. Two different concentrations of Poly(ethylene oxide) (PEO) at two different molecular weights were dissolved in the Newtonian solvent (Water+Glycerol 60-40 wt.%) which has a viscosity $\eta_s = 3.2mPa.s$. The dimensionless parameters Oh and De are defined in chapter 2 and are evaluated using $\rho = 1103kg/m^3$ and $R_l = 85\mu m$. All the measurements were performed at $25^\circ C$.

Mw	c	c/c^*	$\eta_0[mPa.s]$	$\tau_E[\mu s]$	L	De	Oh
300K	0.01%	0.036	3.21	60	27	0.2	0.04
300K	0.1%	0.36	3.32	360	27	1.3	0.04
1000K	0.01%	0.07	3.22	996	50	3.6	0.04
1000K	0.05%	0.37	3.31	2800	50	10.0	0.04

the $M_w = 300K$ solution, $c/c^* = 0.036$). Although the addition of small amounts of PEO to a Newtonian solvent will keep the shear viscosity almost unchanged, the extensional viscosity can increase substantially beyond a critical deformation rate [114]. This increase in the extensional viscosity arises from the coil-stretch transition of the dissolved macromolecules in a strong extensional flow [111]. One important measure for quantifying the onset of strain hardening is the elongational relaxation timescale (τ_E) of the fluid which varies with the molecular weight and concentration of dissolved polymer. The measured relaxation times for all the viscoelastic solutions determined through jet breakup studies are tabulated in Table 1.

3.4 Experimental Setup

The spray experiments were carried out using an air-assisted atomization nozzle (Figure 3-2(a)). The liquid jet is released at moderate speeds ($1 \leq V_{liquid} \leq 10ms^{-1}$) through a cylindrical nozzle $D_L = 1.5mm$ and this core flow is surrounded by a high speed annular flow of air ($V_{air} \sim 80 - 120 ms^{-1}$)(Figure 3-2(a)). The initial sep-

aration between the liquid jet and the annular flow of air is about $760\mu\text{m}$. The destabilized liquid jet will then form a so-called “spray fan”; two auxiliary low speed jets of air are blown from the sides to keep the vertical axis of the spray fan as stable as possible. Visualization of the droplets after breakup are carried out using a LaVision imaging setup. A $1.5\text{mm} \times 1.5\text{mm}$ field of view is illuminated using laser back-lighting and digital images of the droplets were taken as they pass through the frame (Figure 3-3(b)). Image-processing and size distribution measurements of the droplets in the captured images were carried out by the LaVision image analysis package. Five different positions in the spray plane were selected as the sampling sites for all of the tested liquids and more than one thousand droplets were counted in each sampling. All the tests were performed for a fixed flow/geometry and similar environmental conditions in terms of temperature and humidity.

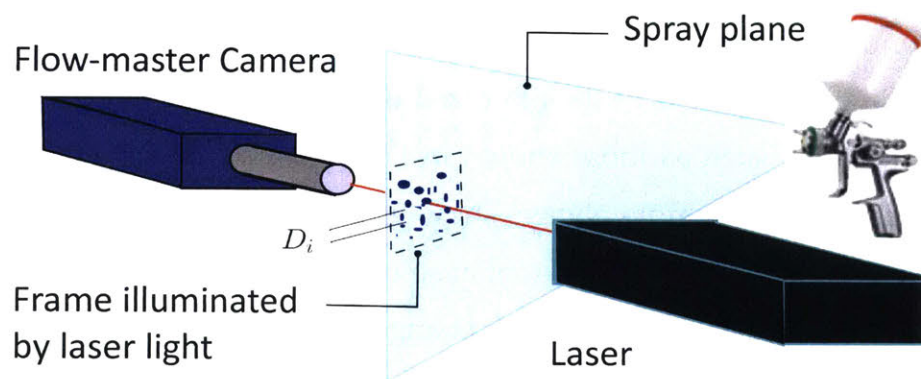


Figure 3-3: The LaVision spray visualization setup. A $1.5\text{mm} \times 1.5\text{mm}$ frame is illuminated using laser back-lighting and a Flowmaster camera captures individual snapshots from the droplets in the spray fan.

The viscometric properties of the fluids were measured using a stress-controlled rheometer (ARG2 with a 4mm cone geometry with 2° degree cone angle; TA Instruments), at low shear rates ($10\text{s}^{-1} \leq \dot{\gamma} \leq 1000\text{s}^{-1}$), and using a micro-fluidic rheometer (m-VROC from Rheosense) at higher shear rates ($1000\text{s}^{-1} \leq \dot{\gamma} \leq 200,000\text{s}^{-1}$). Exten-

sional rheological properties are measured using capillary thinning rheometry and a free jet rheometer (ROJER) which was discussed in Chapter 2.

3.5 Shear and elongational rheology of the spray fluids

The shear and elongational rheology of these solutions are discussed in Chapter 2. The steady shear viscosity do not exhibit any significant difference between the tested solvent and the viscoelastic solutions but ROJER visualization of the filament thinning dynamics with time do show a significant change even for very dilute solutions. This enhanced resistance of the viscoelastic solution to stretching in elongational flows plays a key role in controlling the dynamics of the filaments close to the breakup point from the rapidly deforming liquid core during the atomization process. This additional resistance leads to the appearance of elongated filaments connecting the large beads to each other. A signature of this effect can be seen by looking at snapshots of the atomized droplets in any ligament-mediated atomization process such as those shown in Figure 3-4(a). Images of the atomized viscoelastic liquid sample always show greater numbers of both large and small droplets compared to the Newtonian solutions (compare Figures 3-4(a) and 3-4(b)); i.e. the droplet size distribution is changed due to the extensional rheology of the test fluid. To explore the effects of viscoelasticity we next calculate the first moment of this size distribution to understand how the average droplet size $\langle d \rangle$ depends on the intrinsic Deborah number of the test fluid.

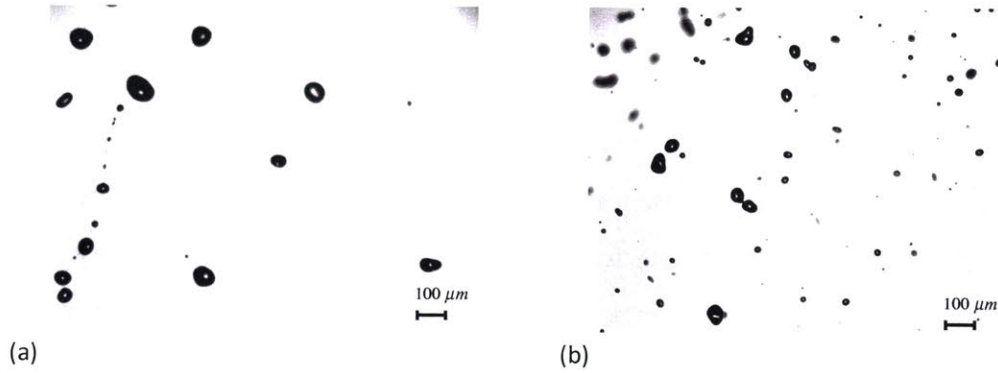


Figure 3-4: (a) Visualization of viscoelastic droplets (PEO-300K-0.01 wt.%) undergoing fragmentation in opposed jet atomization ($Re = 620, We = 300$). (b) Visualization of Newtonian solvent droplets (water and glycerol 60-40 wt.%, $Re = 620, We = 300$) during fragmentation in opposed jet atomization.

3.6 Effect of elongational properties on atomization

As noted in the introduction, the increase in the average droplet size observed during atomization of viscoelastic liquids is a key feature that has been observed by many previous authors in the literature [201, 209, 210, 123, 122, 211, 154] but most previous attempts to connect this increase with the fluid relaxation timescale have not been very successful [210, 154, 201, 122]. This has been primarily due to the fact that the proposed models can not capture one other key feature, which is the saturation of the effect at large values of the relaxation time. Previous analyses have argued that the droplet average size should be proportional to the wavelength of the final instability process during the atomization event, and a combination of linear stability analyses for the different instability modes in the air spray should predict the measured values for the mean droplet diameter $\langle d \rangle$ [212, 57]. Although this scaling may work for inviscid jets, recent work by Marmottant and Villermaux [42] for viscous Newtonian fluids shows that the effects of viscosity on the lifetime of the ligaments that form in the final stages of detachment from the core liquid jet play a dominant role in setting the average droplet size in the spray. In their tests, Marmottant and Villermaux showed that by increasing the Newtonian viscosity of the atomized fluid, the thinning neck that connects elongating ligaments to the

core liquid jet will have more time to breakup. This viscous retardation of the capillary thinning and breakup process enables the filament to uniformly elongate into the surrounding air phase due to the external shear stresses exerted by the air stream. This additional extension reduces the thickness of the ligament (which controls the average droplet size following breakup). More viscous liquids thus form longer and thinner filaments, which also agrees with our common experience of long and thin syrup filaments that arise when we pour such liquids from relatively high heights. During this thinning process the volume of the filament remains constant (and equal to the initial volume) i.e. $V(t) = V_0 \sim d_l^3$. What Mar-mottant and Villermaux [42] show can be summarized in the following scaling for the average droplet sizes based on the breakup time of the neck of the filament:

$$\langle d \rangle / d_l \simeq t_a / t_b \quad (3.1)$$

in which d_l is the initial characteristic size of the ligament before the elongation process, t_b is the breakup time of the neck of the filament and $t_a \equiv (d_l / V_{air}) (\rho_{liquid} / \rho_{air})^{1/2}$ is a characteristic timescale for the acceleration arising from the air dragging the ligament away from the core liquid jet. Eq. (3.1) shows that the average diameter and the neck breakup time are inversely proportional since the viscous fluid ligament will continue to uniformly stretch while the neck is thinning with time. Figures 3-5(a) 3-5(b) present an illustrative description of the mentioned process.

In order to understand this mechanism better, especially for viscoelastic solutions, we consider the experiment shown in Figure 3-5 (c), which is designed to emulate sudden extensional effects in the spray. Viscoelastic liquid samples with fixed initial volume (V_0) were placed between the two plates of the CaBER and the two plates were separated from each other at relatively high strain rates to mimic the fast extensional action of the airstream during the ligament stretching and subsequent atomization phenomena. A similar configuration has been used by Villermaux and his coworkers in mimicking fragmentation processes for Newtonian flu-

ids [42, 213].

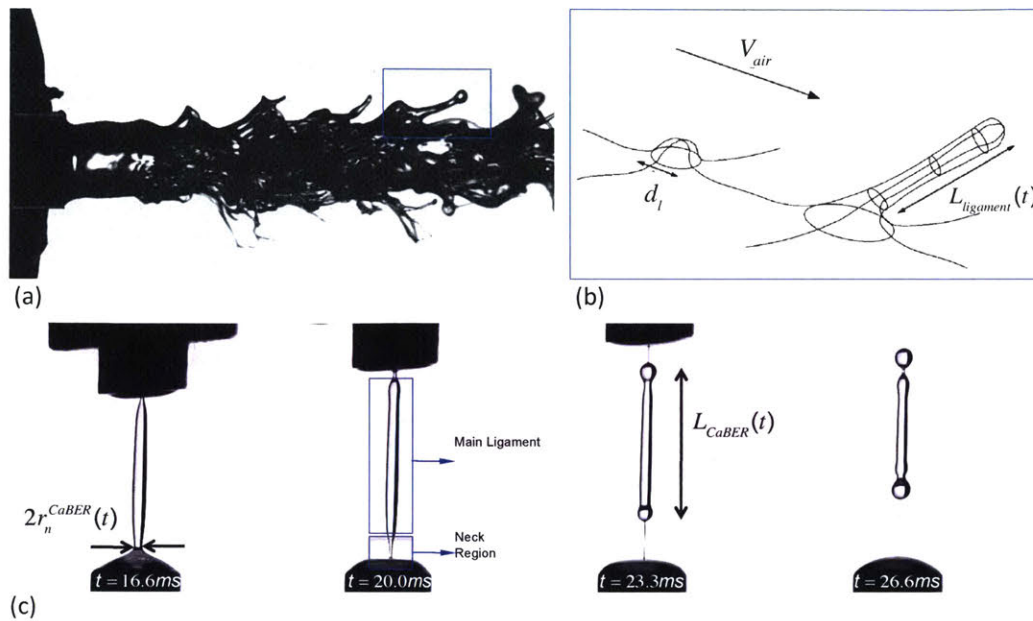


Figure 3-5: (a) Spray visualization image for the viscoelastic polymer solution (PEO-300K-0.01 wt.% in solvent) close to the nozzle. A ligament can be seen in the blue box which is elongated by the air stream (b) Schematic of the suggested model by Marmottant and Villermaux [42] for analyzing the dynamics of the ligament, (reproduced with permission). (c) Montage of images from sudden step-extension test for the viscoelastic solution (PEO-300K-0.01 wt.% in the solvent) in a CaBER instrument. As soon as the flow in the neck region reaches the elasto-capillary balance ($t \geq 20.0ms$) subsequent deformation is localized in the neck while the main ligament stops stretching ($dL_{CaBER}/dt \simeq 0$) and a capillary wave propagates along the filament.

To analyze the effects of viscoelasticity on the average droplet sizes, a simple scaling model which is similar to the one used by Marmottant and Villermaux [42], is introduced in the next section.

3.7 Toy model

In order to emulate the dynamics of ligaments close to pinch off in the atomization process (see Figure 3-5(a) and 3-5(b)) a sudden “step-stretch” test has been devised

using the CaBER platform in conjunction with high speed video image analysis. In this test we impose a very rapid axial displacement of the upper plate in the CaBER device. Because of fluid inertial effects, the liquid sample cannot respond rapidly enough to form a uniform liquid bridge. This may preclude analysis of the self-similar capillary thinning required in CaBER analysis, but it closely emulates the rapid formation and acceleration of fluid ligament that can be seen in the jet image shown in Figure 3-5(a). This process has been considered in detail by Marmottant and Villermaux [42] for Newtonian fluids, and we follow their analysis for viscoelastic fluid ligaments. Specially we observe the formation of a primary or main ligament $L_{ligament}(t)$ (or $L_{CaBER}(t)$ in our replicated experiment) that is connected by a thinning neck region (of diameter $2r_n^{CaBER}(t)$) to the primary drop (or hemispherical end-cap region in our replicated experiment). Figures 3-5(c) and 3-6(a) in the main text show a montage of images for a step stretch test with the 300K-PEO-0.01 wt.% solution. For an inviscid fluid, Marmottant and Villermaux [42] show that the lifetime of this neck is independent of the stretch rate and depends only on the inertio-capillary timescale of the initial ligament. In our notation (based on radius rather than diameter) this lifetime is $\sim \sqrt{8}\tau_R$ (see Figure 3-6 in [42]).

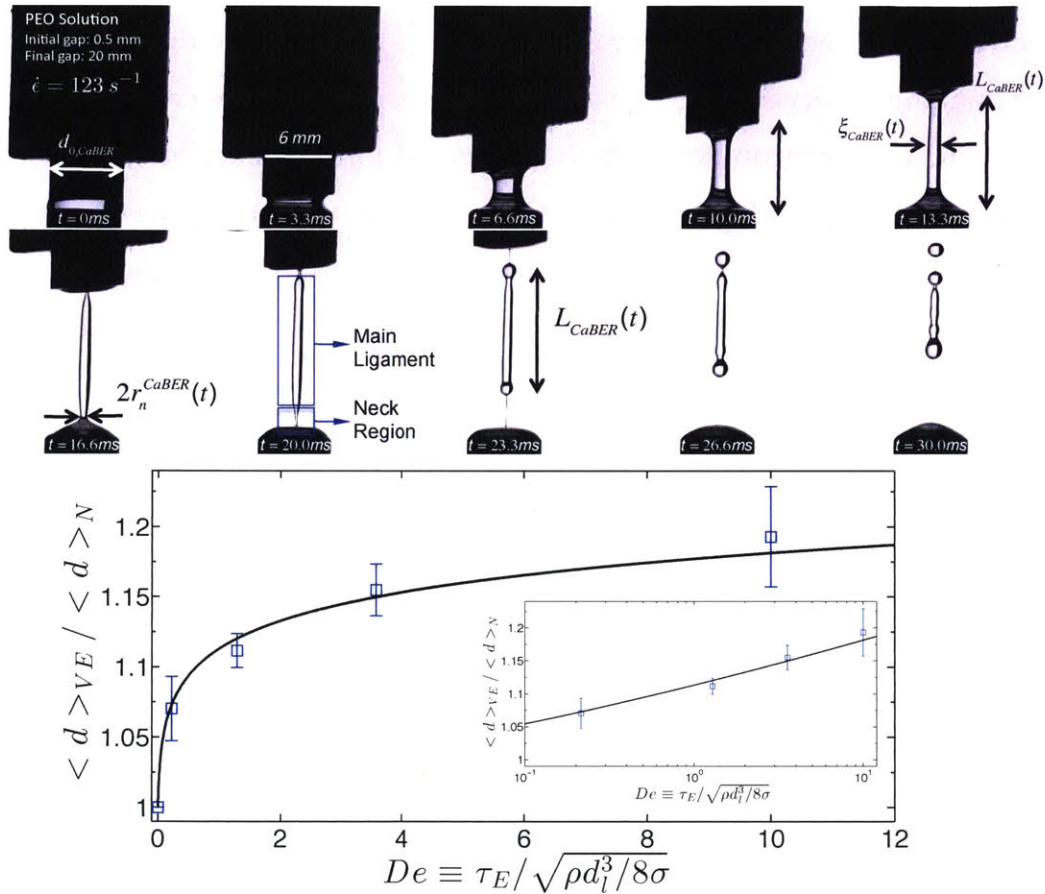


Figure 3-6: (a) Montage of images from the sudden stretch experiment for PEO-300K-0.01 wt.%. (b) Blue squares are average sizes for the viscoelastic solutions normalized by the average diameter for solvent drops as a function of the Deborah (De) number in the ligament ($De \equiv \tau_E / \sqrt{\rho d_l^3 / 8\sigma}$ in which d_l is the characteristic ligament size and is estimated from the average diameter, $\langle d \rangle_N$). The solid black line shows the predictions from the model described in the text (Eq. (3.9)).

Repeating the test for different viscoelastic solutions shows that in all of the step-stretch tests the additional viscoelasticity increases the lifetime of the neck region and the neck clearly forms an elongated microfilament close to its pinch off (see for example the image at $t = 23.3ms$ in the test). This means that the local flow in the neck must reach a critical strain rate close to break up that corresponds to a critical Weissenberg number of $Wi \sim O(1)$. The interesting result from our video imaging observations is the fact that before reaching this critical Weissenberg number the neck contributes little to the overall force balance and serves principally to maintain the integrity of the primary ligament fixed at the bottom/top. In the early images of Figure 3-5(c) (i.e. for times $t \leq 23ms$) it is clear that the primary ligament continues to stretch (i.e. $dL_{CaBER}/dt > 0$). However when the neck suddenly pinches down, and the extensional flow in the neck reaches the critical Weissenberg number, the main ligament is effectively isolated from the deformation being imposed at the end plates. The main ligament no longer elongates (i.e. $dL_{CaBER}/dt \rightarrow 0$). A capillary wave now starts to propagate along the isolated ligament and leads to an increasingly corrugated shape that eventually fragments into droplets. This result, repeatable over many tests, is distinctly different than observations for viscous Newtonian liquids, in which the main ligament and the thin connecting neck both thin down continuously under a visco-capillary balance such that the extensional deformation is a rather uniform process along the ligament axis. By contrast for viscoelastic solutions, when the local flow inside the neck reaches an elasto-capillary balance then the resulting deformation is located in the (very thin) neck, rather than in the primary ligament, and the main body of the ligament will experience negligible subsequent deformation.

To understand the effect of this sudden cessation of the stretching in the main ligament on the average diameters of droplets formed in the spray in a quantitative way we need to analyze the local flow in the neck more accurately. We assume that close to pinch-off, fluid inertia will be negligible compared to viscous effects and we start our analysis before the flow in the filament reaches the elasto-capillary region (i.e. we start from the onset of a visco-capillary pinch). The flow in the

thinning neck will be a simple force balance between the viscous and capillary stresses:

$$-3\eta\frac{2}{r(t)}\frac{dr(t)}{dt} = c\sigma\left(\frac{1}{r(t)} - \frac{1}{R_l}\right) \quad (3.2)$$

in which $r(t)$ is the local midpoint radius of the thinning neck and $R_l = d_l/2$ is the radius of the initial volume of fluid ligament undergoing the stretch. In this process the local neck is not (at first) a long cylindrical filament in which we can simply assume that the two principal radii of curvature are $R_1 = r(t)$ and $R_2 \rightarrow \infty$ but instead is a short neck connected to a hemispherical reservoir (or droplet) with radius of R_l at the base; we therefore take the radii of curvature as $R_1 = r(t)$ and $R_2 = -R_l$ respectively. The coefficient of proportionality appearing in Eq. (3.2) is expected to be of order of unity. In their original analysis Entov and Hinch [78] take $c = 1$ and in the limit of long thin filaments ($r/R_l \ll 1$) the self-similarity solution or viscocapillary thinning derived by Papageorgiou gives $c = 0.42$ [214]. We retain c as a single fitting constant in our subsequent analysis. Integrating Eq. (3.2) yields an evolution equation for the diameter of the neck in the visco-capillary region:

$$\frac{r}{R_l} = 1 - \exp\left(\frac{c}{6\tau_{vis}}\left(t - t_b^{(VC)}\right)\right) \quad (3.3)$$

in which τ_{vis} is the characteristic visco-capillary timescale $\tau_{vis} = \eta R_l / \sigma$ and the visco-capillary breakup time is shown as $t_b^{(VC)}$. In order to find an estimated value for the breakup time $t_b^{(VC)}$, we only need to have a physical estimate for the radius at the start of the visco-capillary region $r(t=0)/R_l$. Eggers and Villermaux [140] have shown that the visco-capillary region starts when the local Ohnesorge number ($\eta/\sqrt{\rho\sigma r(t)}$) becomes of order unity and using this assumption the value of $r(t=0)/R_l$ can be estimated to be around $\eta^2/\rho\sigma R_l$, thus one can find a meaningful estimate for the breakup time of the ligament in the visco-capillary regime:

$$t_b^{(VC)} = -\frac{6\tau_{vis}}{c} \ln(1 - Oh_{R_l}^2) \sim \frac{6\tau_{vis} Oh_{R_l}^2}{c} \quad (3.4)$$

in which Oh_{R_l} is the initial(small) value of the Ohnesorge number based on the

initial size of the fluid ligament:

$$Oh_{R_l} \equiv \frac{\eta}{\sqrt{\rho\sigma R_l}} \ll 1 \quad (3.5)$$

As a side note, by Taylor series expansion of Eq. (3.3), we can investigate the predictions of the suggested model in the limit of times close to the break up $(t_b^{(VC)} - t) \rightarrow 0$ or equivalently from a geometrical viewpoint in the limit of small values of $r(t)/R_l$:

$$\frac{r(t)}{R_l} = 1 - \left(1 + \frac{c}{6\tau_{vis}} (t - t_b^{(VC)}) + \dots\right) \simeq \frac{c}{6\tau_{vis}} (t_b^{(VC)} - t) \quad (3.6)$$

This expression shows that the proposed scaling model leads, in the limit of thin and slender neck region ($r(t)/R_l \ll 1$), to the expected similarity solution for viscopillary thinning of Newtonian slender filaments [215, 214, 216].

The addition of viscoelasticity has a significant effect on this process, as shown in the montage of images presented in Figure 3-6(a). The main ligament in the viscoelastic filament stops stretching after the neck locally attains an elasto-capillary balance and the bulk of the remaining deformation is localized in the thin neck after that point. The criterion for onset of this process can be estimated by comparing the strength of the flow in the filament neck ($\sim \dot{\epsilon}_{neck}$) to the relaxation time of the liquid; when $Wi_{neck} \equiv \tau_e \dot{\epsilon}_{neck} \sim O(1)$ the polymer chains are extended faster than the rate at which they can relax. Elastic stresses will therefore dominate and grow and arrest the pinch-off process. The subsequent deformation happens primarily in the neck while being arrested in the main ligament (which will now undergo capillary recoil and formation of a satellite drop). To find an estimate for the starting time of the elasto-capillary region in the neck we use the visco-capillary model obtained above (Eq. (3.6)) and follow the evolving strain rate; the stretching in the main ligament stops when the value of the strain rate in the connecting neck reaches a critical value close to the relaxation rate of the polymer i.e. the time at which $\dot{\epsilon}_{neck} \sim 1/\tau_E$. If we denote this time by $t_{pinch}^{(EC)}$ using Eq. (3.6) then we can find an expression for the strain rate from which $t_{pinch}^{(EC)}$ can be evaluated as a function of

relaxation time (τ_E) and other parameters in the model:

$$t_{pinch}^{(EC)} = t_b^{(VC)} - \frac{6\tau_{vis}}{c} \ln \left(1 + \frac{c\tau_E}{3\tau_{vis}} \right) \quad (3.7)$$

The addition of viscoelasticity (i.e. nonzero values of τ_E) thus reduces the critical time ($t_{pinch}^{(EC)}$) at which the flow in the neck attains an elasto-capillary balance; consequently the span of time for which the main ligament is stretching in the air will be reduced. If the lifetime of the thinning filament for a viscous Newtonian fluid is estimated as $\sqrt{8}\tau_R + t_b^{(VC)}$ where $\sqrt{8}\tau_R$ is the initial time required for the flow in the neck to reach the visco-capillary balance (as shown by Marmottant and Villermaux [42] this initial time is set purely by the inertio-capillary timescale since in this initial stage inertial and capillary stresses are the dominant ones in balance) then the new (reduced) lifetime become $\sqrt{8}\tau_R + t_{pinch}^{(EC)}$ for viscoelastic solutions.

Less stretching leads to shorter and thicker viscoelastic ligaments which will end up breaking up into bigger (average size) droplets. This trend agrees with the qualitative observations of average sizes in the atomization of viscoelastic liquids shown in Figure 3-6(b). For a more quantitative comparison we combine Eqs. (3.1), (3.4) and (3.7) to obtain the following expression for the effect of fluid elasticity on the average drop sizes:

$$\frac{\langle d \rangle_{VE}}{\langle d \rangle_N} = \frac{(\sqrt{8}c/6)\tau_R + \tau_{vis}.Oh_{Rl}^2}{(\sqrt{8}c/6)\tau_R + \tau_{vis}.Oh_{Rl}^2 - \tau_{vis} \ln \left(1 + c\tau_E/3\tau_{vis} \right)} \quad (3.8)$$

where $\langle d \rangle_{VE}$ denotes the average droplet size in the viscoelastic spray and $\langle d \rangle_N$ denotes the corresponding value for a Newtonian spray.

Eq. (3.8) can be further simplified into a form that only incorporates the dimensionless Ohnesorge and Deborah numbers with $c = 4.1$ as a fitting parameter:

$$\frac{\langle d \rangle_{VE}}{\langle d \rangle_N} = \frac{(\sqrt{8}c/6)Oh_{Rl}^{-1} + Oh_{Rl}^2}{(\sqrt{8}c/6)Oh_{Rl}^{-1} + Oh_{Rl}^2 - \ln \left(1 + cDe_{Rl}/3Oh_{Rl} \right)} \quad (3.9)$$

Marmottant and Villermaux [42] have shown that for a Newtonian liquid measured average diameter and the initial ligament scale d_l are related by: $\langle d \rangle / d_l = We_{d_l}^{-1/2} = (\sigma / \rho V_{air}^2 d_l)^{1/2}$. Using this expression and the measured value of the average droplet size $\langle d \rangle_N$, for a Newtonian liquid at a typical air speed of $V_{air} \simeq 100 m.s^{-1}$ we can evaluate the ligament size as $d_l = 2R_l \simeq 170 \mu m$. Because elastic effects are unimportant at early stages we assume this value is unchanged for the weakly elastic polymer solutions. We can plot the evolution in this scaling model prediction (Eq. (3.9)) for different relaxation times (τ_E) measured using ROJER and compare the model with the experimentally measured sizes from atomization tests. The solid line in Figure 3-6 (b) shows the theoretical predictions from this simple model (with the constant $c = 4.1$) compared with the measured average sizes for the tested viscoelastic solutions (all the solutions tabulated in Table 1) normalized by the corresponding value for the Newtonian solvent under identical conditions $\langle d \rangle_N = 16 \mu m$. The average droplet diameters were calculated from ensemble averages over large number of droplets (typically more than five thousand droplets) at five different sampling positions in the spray fan. All of the spray parameters were kept constant for all of the tested liquids.

The model captures very well both the initial increase of sizes at low intrinsic Deborah numbers (based on the length scale of the elongated ligament $De_{R_l} = \tau_E / \sqrt{\rho R_l^3 / \sigma}$) and also the saturation observed at higher De_{R_l} . The same plot with a linear ordinate axis and a logarithmic abscissa is shown as the inset image in Figure 3-6 (b) and it is clear that the average drop size changes approximately linearly with $\ln(De)$. For the cases considered here $\tau_R = \sqrt{\rho R_l^3 / \sigma} = 101 \mu s$, $\tau_{vis} = 4 \mu s$ and $Oh_{R_l} = 0.04$. Even for a maximum fluid relaxation time of $6000 \mu s$, the logarithmic term is smaller than the initial terms $((\sqrt{8}c/6)Oh_{R_l}^{-1} + Oh_{R_l}^2)$ in the denominator, and thus the expression in Eq. (3.9) can be Taylor-expanded as:

$$\frac{\langle d \rangle_{VE}}{\langle d \rangle_N} \simeq 1 + \frac{\ln(1 + cDe_{R_l}/3Oh_{R_l})}{(\sqrt{8}c/6)Oh_{R_l}^{-1} + Oh_{R_l}^2} \quad (3.10)$$

which in the limit of $cDe_{R_l}/3Oh_{R_l} \gg 1$ is equivalent to a linear dependency of the

mean drop size $\langle d \rangle$ on $\ln(De_t)$ ($1.9 \leq cDe_{R_i}/3Oh_{R_i} \leq 92.6$ in our tests) which is in good agreement with our experimental observations.

3.8 Conclusions

We have shown that a periodically forced viscoelastic jet combined with a strobe-based digital video imaging system can form the basis of an extensional rheometer that is suitable for studying weakly viscoelastic fluids. Operation of this jetting rheometer requires an understanding of the interplay of viscous, inertial and elastic forces in the jet and we therefore refer to this as a Rayleigh-Ohnesorge Jet Extensional Rheometer (ROJER).

The shear and extensional rheology of several dilute PEO solutions were studied using the ROJER. Flow visualization studies of the performance of these fluids in air-assisted atomization were also performed. The shear rheology of these dilute polymeric solutions did not suggest any significant difference in their atomization performance whereas both the flow visualization and drop diameter measurements from our spray tests showed an increase in the mean drop size. The extensional rheology for these solutions was measured using both CaBER and ROJER and we showed that due to the inertia-capillary timescale there is a lower limit for measurements of relaxation times in a CaBER device. This limit can be circumvented by studying the dynamics of capillary breakup using the ROJER device because of the much smaller length and time scales involved. Measurements obtained from ROJER in terms of both linear stability and nonlinear elasto-capillary thinning analysis of the jet were verified using known theoretical and numerical predictions and it was shown that quantitative agreement can be obtained with existing stability theory. The values of relaxation times extracted from this analysis were used to quantify the performance of the test fluids in the air-assisted atomization process. Using our observations, a new and relatively simple model was developed for understanding the viscoelastic dynamics of the ligament thinning process close to their final detachment from the core liquid jet. Using the mea-

sured relaxation times within the framework of the suggested model a physical prediction for the average droplet size $\langle d \rangle_{VE}$ during atomization of a weakly viscoelastic fluid was obtained and the experimental results with four different PEO solutions were found to agree well with the model predictions.

This study helps us understand the subtle effect of extensional rheology on the breakup and the atomization of weakly viscoelastic liquids which are widely used in many biological and industrial applications. For Newtonian liquids, two different scalings for ligament sizes are suggested based on linear stability analysis [212, 54]. The difference between the two scalings arises from the Rayleigh Taylor stability analysis, in which the direction of air acceleration relative to the liquid/air interface can change at different air/liquid flow rate ratios. The competing effect of viscosity and surface tension on the average droplet size in an air atomizer can be understood by a simplified version of the original scaling from Aliseda et al. [212]:

$$\frac{d_l}{D_0} \simeq 1.2 \left(\frac{\sigma}{\rho V_{air}^2 D_0} \right)^{1/2} [1 + We^{1/6} Oh^{2/3}] \quad (3.11)$$

where d_l is the size of ligament being accelerated away from the jet and the Weber and Ohnesorge numbers in Eq. (3.11) are calculated based on the diameter of the nozzle D_0 .

Marmottant and Villermaux [42] have shown that due to the viscous slowing of the filament break up, viscous Newtonian filaments stretch more than inviscid ligaments do in the air stream. Using a similar approach to the analysis carried out in section 9 one can suggest a scaling for the average droplet size for the atomization of viscous Newtonian liquids:

$$\frac{\langle d \rangle_N}{d_l} = \frac{(\sqrt{8c/6}) Oh_{R_l}^{-1}}{(\sqrt{8c/6}) Oh_{R_l}^{-1} + Oh_{R_l}^2} = \frac{(\sqrt{8c/6})}{(\sqrt{8c/6}) + Oh_{R_l}^3} \quad (3.12)$$

where now the value of the Ohnesorge number is based on the characteristic length scale in the ligament. We also have shown how the final average droplet size and the ligament thickness d_l is modified in the presence of weak fluid elastic-

ity through a result of the form shown in Eq. (3.9). This expression is found to agree well with our experimental measurements for a number of PEO solutions. The simplest way to include all of the competing effects of viscosity, surface tension and elasticity on overall mean droplet sizes is by combining Eqs. (3.11), (3.12) and (3.9) which results in an expression of the form:

$$\frac{\langle d \rangle_{VE}}{D_0} \approx 1.2 \left(\frac{\sigma}{\rho V_{air}^2 D_0} \right)^{1/2} [1 + We^{1/6} Oh^{2/3}] \times \left[\frac{(\sqrt{8}c/6) Oh_{R_l}^{-1}}{(\sqrt{8}c/6) Oh_{R_l}^{-1} + Oh_{R_l}^2 - \ln(1 + cDe_{R_l}/3Oh_{R_l})} \right] \quad (3.13)$$

This suggested scaling is the first attempt to address in a complete way the different effects of fluid viscosity and elongational relaxation time on the average droplet size produced in air atomization for weakly viscoelastic solutions. The model incorporates all of the essential fluid properties and geometry dimensions. Quantitative predictions from this model agree well with experimental results for the four tested PEO solutions. A similar combination of classical linear stability theory, scaling arguments and benchmark experiments were used by Middleman and coworkers [147, 146] to systematically understand the effects of surface tension, viscosity and weak elasticity on the breakup length of viscoelastic jets. Jet rheometry of mobile liquids using the ROJER instrumentation thus provides a pathway to realize the concept originally outlined by Walters some 30 years ago of "...a flow dominated by extension that can be analyzed in a quantitative fashion to extract material functions that are rheologically meaningful". The rheologically meaningful functions here are the extensional relaxation time $\tau_E(c, M_w)$ and the instantaneous apparent Trouton ratio $\eta_E^+(\dot{\epsilon}, t)/\eta_0$. We have demonstrated that quantitative measurements of relaxation times as small as $60\mu s$ can help us understand the key role of nonlinear viscoelasticity in modifying the mean droplet size in an air-assisted atomization process. It will be of interest to see if these rheological properties can also help understand other features of this important industrial process such as changes in the shape and breadth of the droplet size distribution

in the final spray fan.

Chapter 4

Droplet Size Distributions in Fragmentation of Viscoelastic Liquids

*Can you imagine young people nowadays making a study of trigonometry for the fun of it?
Well I did.*

Clyde Tombaugh

4.1 Scope

The breakup and atomization of complex fluids can be markedly different than the analogous processes in a simple Newtonian fluid. Here we investigate the ligament-mediated fragmentation dynamics of viscoelastic fluids in three different canonical flows. In this chapter we report the size distributions that are measured in each viscoelastic fragmentation process and show a systematic broadening from the Newtonian solvent. In each case the droplet sizes are well described by Gamma distributions which correspond to a fragmentation/coalescence scenario. We use a prototypical axial step strain experiment together with high-speed video imaging to show that this broadening results from the pronounced change in the corrugated shape of viscoelastic ligaments as they separate from the liquid core. These corrugations saturate in amplitude and the measured distributions for viscoelastic liquids in each process are given by a universal probability density function,

corresponding to a Gamma distribution with $n_{min} = 4$. The breadth of this size distribution for viscoelastic filaments is shown to be constrained by a geometrical limit which can not be exceeded in ligament-mediated fragmentation phenomena.

4.2 Introduction

Fragmentation and droplet formation from a viscoelastic jet or sheet is a fundamental component of many industrial and biological processes [84, 217]. Atomization of paint, combustion of fuels containing anti-misting agents and pharmaceutical sprays as well as involuntary physiological processes such as sneezing are common examples in which the atomized liquid contains synthetic or biological macromolecules that result in viscoelastic fluid characteristics. One important metric of a fragmentation process is the final droplet size distribution, and understanding the role of material properties (e.g. fluid viscosity and relaxation time) on the polydispersity of such distributions is of crucial importance in many applications [57, 218].

The process of liquid fragmentation for simple Newtonian liquids in natural phenomena such as the distribution of rain drops has fascinated scientists from ancient times [61] to modern [64, 13, 63]. Recent studies by Villermaux and coworkers [219, 66, 13, 11] have shown that old paradigms for understanding disintegration of Newtonian liquids, based primarily on either cascade theory [220] (leading to log-normal size distributions) or maximum entropy theories [221] (leading to Poisson size distributions) do not adequately capture all physical aspects of these atomization processes. Villermaux et al. [66] show that the atomization process for Newtonian liquids can be precisely described by a *fragmentation/coalescence scenario* [222]. The final droplet size distribution predicted from this fragmentation/coalescence scenario is a Gamma distribution in which the probability density function (PDF) for a given droplet size [13] is given by

$$p(x = d/\langle d \rangle) = \Gamma(n, x = d/\langle d \rangle) \equiv \left(n^n / \Gamma(n) \right) x^{n-1} e^{-nx} \quad (4.1)$$

where $\langle d \rangle$ is the mean or average size. The scale factor n determines how narrow the size distribution is: large values of n indicate a narrow distribution around the average value and small values of n describe a broader distribution with proportionally larger numbers of both small and large droplet sizes. The reported values of n for fragmentation processes of Newtonian liquids are typically in the range of $6 \leq n \leq 9$ [13].

In complex fluids, studies of many capillary-related phenomena (such as capillary breakup of filaments [223, 120] and liquid sheets [119]) have shown interesting and counterintuitive elastic effects. However, there is a paucity of fundamental quantitative knowledge regarding the dynamics of fragmentation. Experimental studies [202, 122, 123, 209, 27, 224, 124] have shown that addition of viscoelasticity can inhibit fragmentation in atomizers, and results in higher values of the average diameter $\langle d \rangle$ for viscoelastic liquid droplets. Most recently, work by Keshavarz *et al.*[108] has made use of scaling arguments to develop a model predicting the evolution in $\langle d \rangle$ as a function of dimensionless parameters such as the Ohnesorge ($Oh \equiv \eta/\sqrt{\rho\sigma R_0}$) and Deborah ($De \equiv \tau_E/\sqrt{\rho R_0^3/\sigma}$) numbers which characterize viscous and elastic effects in the spray process. Here η is the shear viscosity of the liquid, σ is the surface tension and τ_E is the characteristic relaxation time for the viscoelastic liquid. The model predicts a slow, logarithmic growth of $\langle d \rangle$ with De , which agrees with experimental spray measurements. However none of these studies address the role of viscoelasticity on changing the *distribution* of droplet sizes. The few attempts in the literature to address the size distributions for polymeric liquids [225, 226] base their assumptions on older paradigms such as cascade or maximum entropy theories, which do not correspond to the physical picture described by the fragmentation/coalescence scenario that quantifies the Newtonian size distributions [13, 140].

The dramatic change in the inertio-elastic breakup of a high speed jet during air-assisted atomization is illustrated in Fig. 4-1. As previously noted [15], the large scale features remain unchanged but the addition of a high molecular weight polymer results in finer scale structures such as atomized droplets that remain con-

nected to the core jet by thin viscoelastic ligaments. The lifetime of these ligaments depends on the extensional viscosity of the fluid, and it is well known that adding dilute amounts of a high molecular weight flexible macromolecule to a Newtonian solvent will keep the shear viscosity almost unchanged, whereas the extensional viscosity will increase dramatically [114, 227].

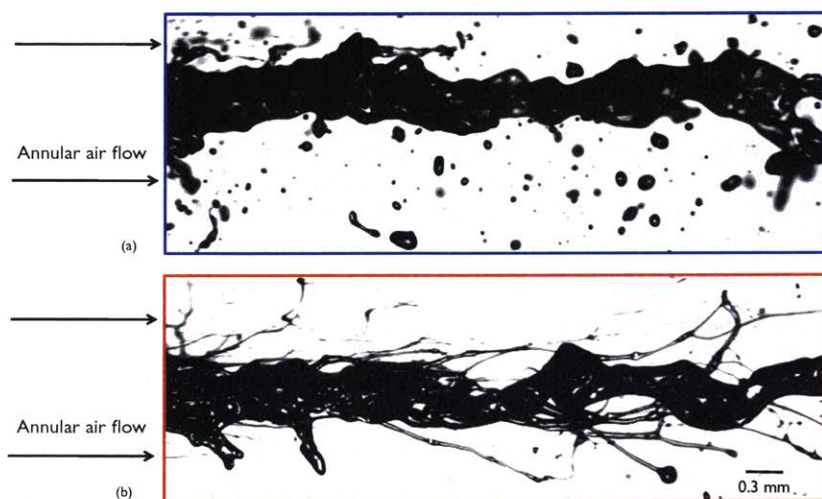


Figure 4-1: (color online). Snapshot of the liquid jet in the air-assisted atomization for (a) the Newtonian solvent and (b) the viscoelastic solution (PEO-300K-0.01% wt. in the solvent).

4.3 Test Fluids

Test fluids that are studied in this chapter are the same ones described in Chapter 2. However, we provide a summarized description for them in this chapter as well: All of the test solutions are made by dissolving small amounts of poly(ethylene oxide) or (PEO) with $M_w = 3 \times 10^5 g/mol$ and $1 \times 10^6 g/mol$ respectively (purchased from Sigma Aldrich) in a water-glycerol (60-40 wt.%) solvent ($\eta_s = 3.2 mPa.s$) and the resulting viscometric properties are summarized in Table 1. The values of surface tension for all of the viscoelastic solutions are close to the solvent value ($\sigma \simeq 60 \pm 3 mN/m$). Using the expressions given in [24, 190] the overlap concentrations (c^*) are respectively 0.28 wt.% and 0.14 wt.% for 300K and 1000K solutions. The values of the chain extensibility parameter ($L \sim M_w^{1-\nu}$ in which $\nu = 0.56$ for

a good solvent), which is a measure of the maximum attainable macromolecular extension, are also calculated based on the physical constants reported in [116] for the PEO chains.

Table 4.1: Properties of the viscoelastic test fluids. Two different concentrations of poly (ethylene oxide), (PEO) at two different molecular weights were dissolved in the Newtonian solvent (Water+Glycerol 60-40% wt.)

Mw	c	c/c^*	$\eta_0[mPa.s]$	$\tau_E[\mu s]$	L	De	Oh
300K	0.01%	0.036	3.21	60	27	0.2	0.04
300K	0.1%	0.36	3.32	360	27	1.3	0.04
1000K	0.01%	0.07	3.22	996	50	3.6	0.04
1000K	0.05%	0.37	3.31	2800	50	10.0	0.04

All four solutions are made by dissolving small amounts of poly(ethylene oxide) (PEO) of different average molecular weights (300 kg/mol and 1000 kg/mol) in a water-glycerol (60-40%wt.) solvent. The coil overlap concentrations are respectively $c^* = 0.28\%$ and 0.14% for the 300K and 1000K solutions. An important measure for the extensional properties of these fluids is the timescale characterizing the chain unraveling process in an elongational flow [228], referred to as the elongational relaxation time (τ_E). We showed in chapter 2 that beyond a critical strain rate ($\dot{\epsilon} \gtrsim \tau_E^{-1}$) the extensional viscosity of these solutions increases dramatically. This critical strain rate varies with the molecular weight and concentration[77, 229, 116]. It can easily be exceeded in the final stages of atomization for many complex fluids in which capillary-driven pinch off processes lead to thin threads ($R(t) \rightarrow 0$) and extremely high values of the local strain rate $\dot{\epsilon}(t) \sim -2\dot{R}/R(t)$. Thus, when compared to the corresponding Newtonian solvent, the enhanced extensional viscosity of a dilute solution will inhibit the capillary-driven thinning of liquid ligaments and may be anticipated to retard the subsequent atomization process.

To illustrate the fragmentation/coalescence process we show in Fig. 4-2(a) the

break up of a single fluid filament (drawn rapidly out of a bath of fluid) into a set of droplets. This process is a capillary-dominated competitive phenomena between the neighboring liquid blobs that initially emerge on the ligament (shown as magenta circles). The geometry of the precursor liquid thread sets the size distribution of these initial blobs.

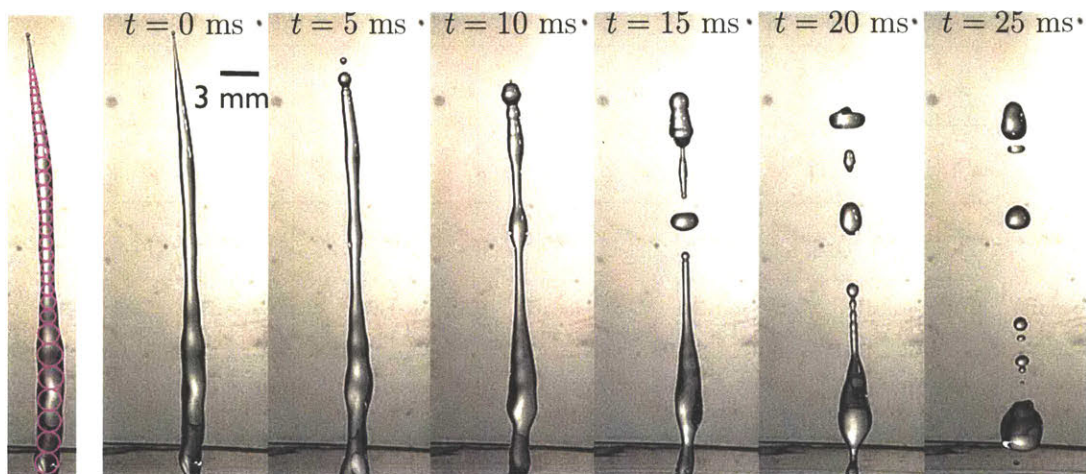


Figure 4-2: (color online).(a) Images from the fragmentation process for a Newtonian ligament. The coalescence of the neighboring blobs in the ligament at $t = 0$ (magenta circles on the left image) results in the final distribution of droplet sizes at $t = 25$ ms.

4.4 Size Distributions in Air-Assisted Atomization

Knowing that the geometry of the initial ligaments determines the final droplet size distribution in a Newtonian spray [13], we analyzed the droplet size distribution for the Newtonian solvent and all four viscoelastic solutions, gathering a set of almost five thousand droplets for each liquid. In Fig. 4-3 we show the PDF for the Newtonian solvent and for all four viscoelastic test fluids (corresponding to $0.2 \leq De \leq 10$). Remarkably, the viscoelastic solutions show a universal behavior which is independent of both the molecular weight and the concentration of the dissolved polymer. All show a size distribution that is well described by a Gamma distribution; however it is clear that the polymer solutions have a much broader size distribution. The viscoelastic data is characterized by a Gamma distribution

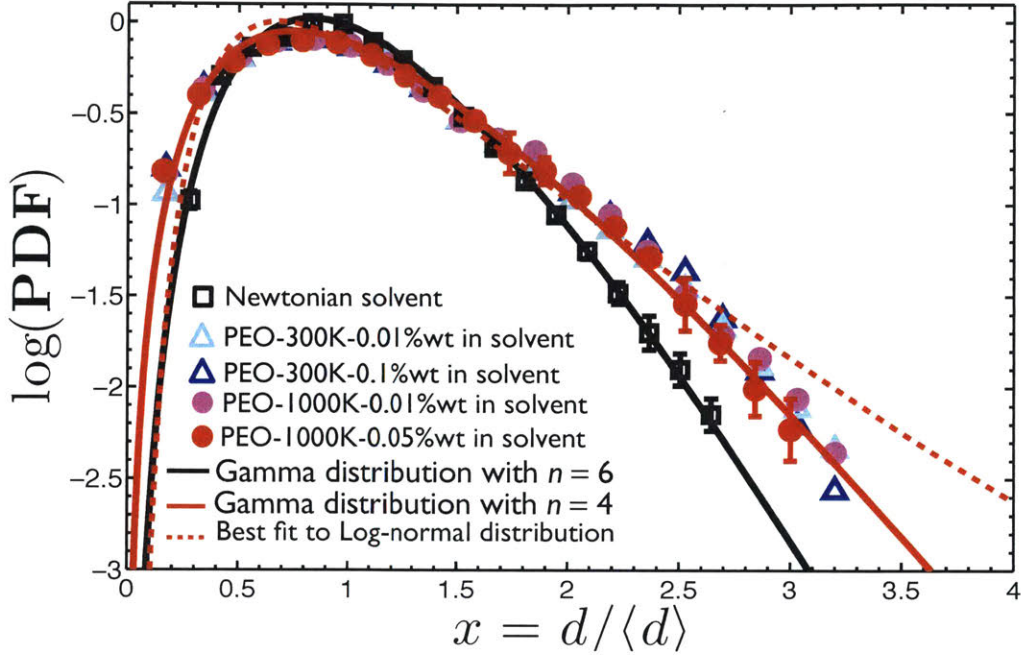


Figure 4-3: (color online). (a) Droplet size distributions for all tested liquids in the air-assisted atomization process. For each fluid we specify the values of Ohnesorge and Deborah number, $\{Oh, De\}$: $(\square)\{Oh = 0.04, De = 0\}$, $(\triangle)\{0.04, 0.2\}$, $(\triangle)\{0.04, 1.3\}$, $(\bullet)\{0.04, 3.6\}$, $(\bullet)\{0.04, 10.0\}$. Solid lines are Gamma distributions for $n = 6$ (black) and $n = 4$ (red).

with $n = 4$ (compared to $n = 6$ for the Newtonian solvent). As in the Newtonian case, the corresponding best fit from a Log-normal distribution fails to correctly capture the probability distributions at large sizes (identical trends are obtained in atomization tests with paint ‘resins’ consisting of aqueous polymer dispersions; see the S.I. for details).

Fig. 4-4 shows the measured droplet size distribution ($N \geq 5000$ for each figure) for different viscoelastic liquids compared with the Newtonian solvent. It is clear that the PDF for the viscoelastic size distributions are broader than the corresponding Newtonian PDF within the measured error-bars (the error-bars show the measured standard deviation between values of the PDF for droplet size distributions measured in five different regions of spray). A Gamma distribution with $n = 4$ describes the PDF for all the viscoelastic cases (compared to $n = 6$ for the Newtonian solvent). By increasing the polymer concentration (Fig. 4-4(a)) or molecular weight (Fig. 4-4(b)) the final droplet size distributions in air-assisted atomization

does not change and is well-described by a Gamma distribution with $n = 4$.

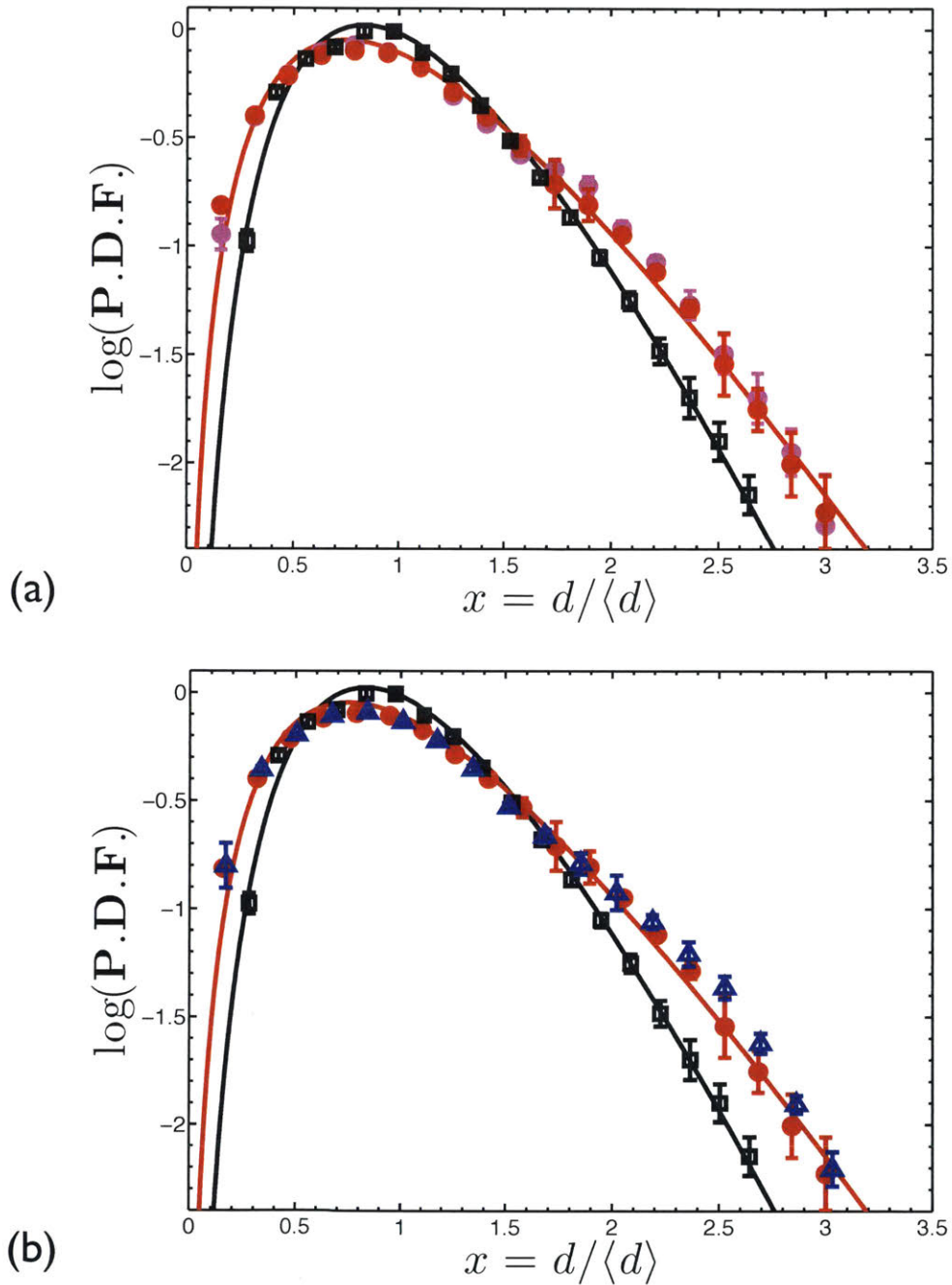


Figure 4-4: (color online). Droplet size distributions for different liquids examined in the air-assisted atomization process: (a) Newtonian solvent (\square) $\{Oh = 0.04, De = 0\}$ compared with PEO-1000K-0.01% (\bullet) $\{Oh = 0.04, De = 3.6\}$ and PEO-1000K-0.05% (\bullet) $\{Oh = 0.04, De = 10.0\}$ Solid lines are Gamma distributions for $n = 6$ (black) and $n = 4$ (red). (b) Newtonian solvent (\square) $\{Oh = 0.04, De = 0\}$ compared with PEO-300K-0.1% (\triangle) $\{Oh = 0.04, De = 1.3\}$ and PEO-1000K-0.05% (\bullet) $\{0.04, 10.0\}$ Solid lines are Gamma distributions for $n = 6$ (black) and $n = 4$ (red).

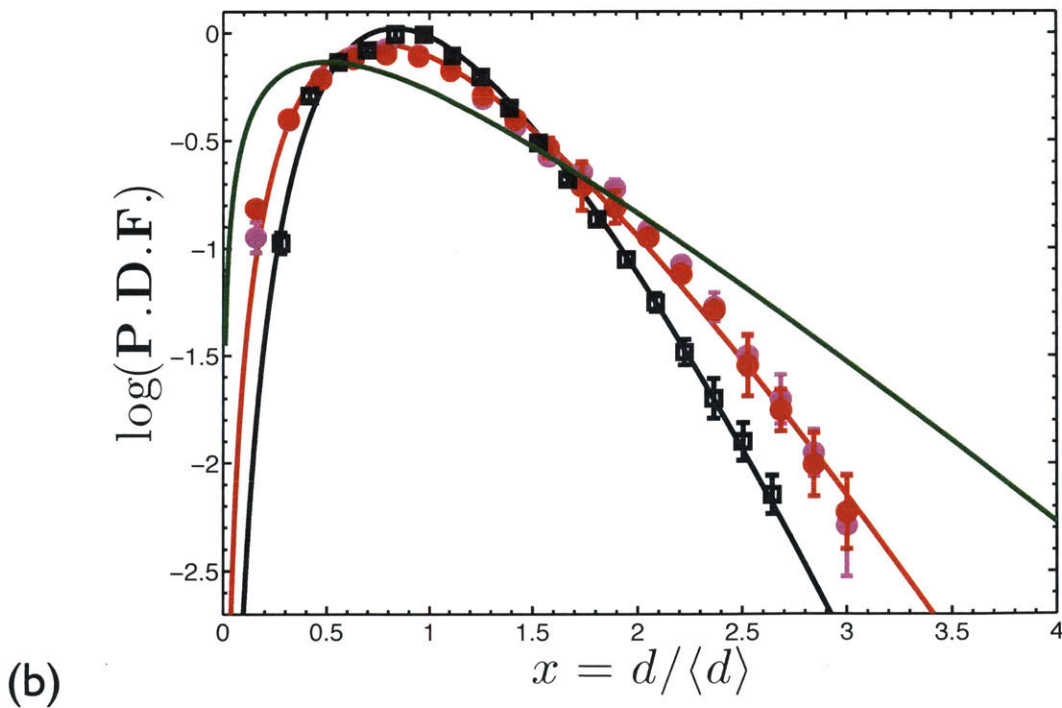
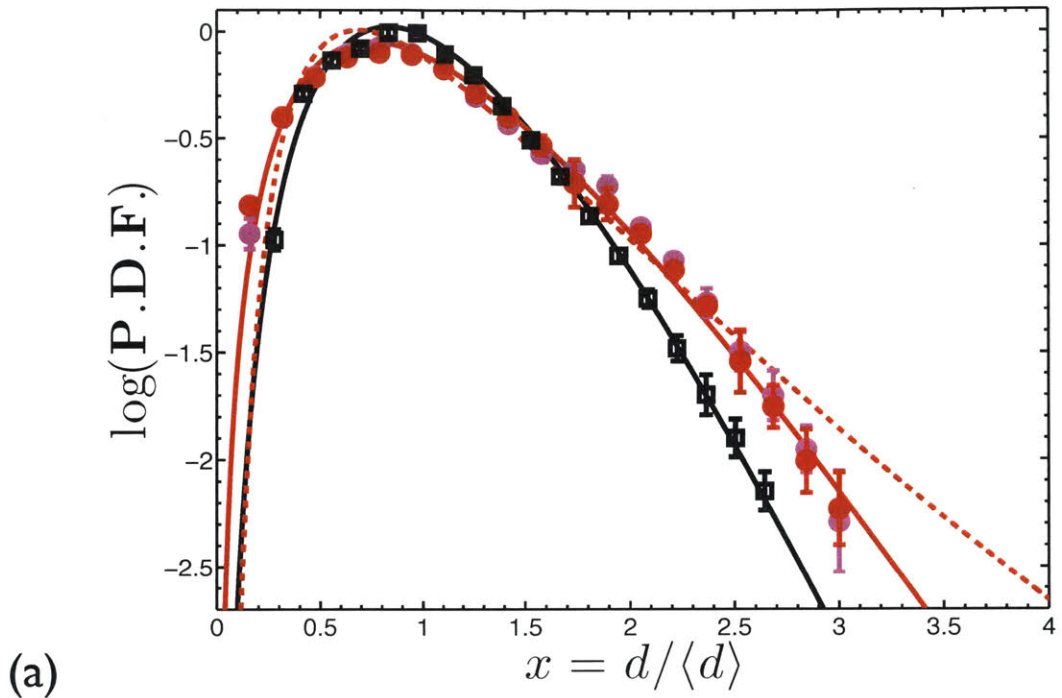


Figure 4-5: (color online). Droplet size distributions for different liquids tested in the air-assisted atomization process: Newtonian solvent (\square) $\{Oh = 0.04, De = 0\}$ compared with PEO-1000K-0.01% (\bullet) $\{Oh = 0.04, De = 3.6\}$ and PEO-1000K-0.05% (\bullet) $\{0.04, 10.0\}$ Solid lines are Gamma distributions for $n = 6$ (black) and $n = 4$ (red). (a) The dashed red line is the best fit to a log-normal distribution. (b) The solid green line is a Gamma distribution with $n = 2$ and is shown solely for comparative purposes.

Attempts to fit the viscoelastic size distributions with a log-normal distribution or a Gamma distribution of lower order $n = 2$ are shown in Fig. 4-5(a) and 4-5(b) respectively. For viscoelastic data, the best fit to a log-normal distribution (dashed red line in Fig. 4-5(a)) clearly overestimates the number of droplets at large sizes (the right tail) and also underestimates the number of droplets measured at smaller sizes (to the left of the maximum). At the same time it is noteworthy to see that the captured size distributions do not become broader with increasing viscoelasticity and as shown in Fig. 4-5(b), remain well-described by a Gamma distribution with $n = 4$ and do not follow the predictions of Gamma PDF with a lower value of n (the green solid line shows, for example, $n = 2$).

To quantify the error values in different fits we use the following log mean error norm:

$$\sigma_{error} \equiv \sqrt{(1/N) \sum_1^N (\log p_i(x_i) - \log f(x_i))^2} \quad (4.2)$$

in which $p_i(x_i = d_i/\langle d \rangle)$ is the measured probability density function and $f(x_i = d_i/\langle d \rangle)$ is the prediction from a corresponding fit. Obviously a low value of the error parameter for a fit shows that the fit has captured the phenomena accurately. Fig. 4-6(a) shows a comparison between different applied fits for all different viscoelastic liquids. It is clear that the Gamma distribution with $n = 4$ has the lowest error parameter when compared to the best fit to a log-normal distribution and the expected Newtonian Gamma distribution (with $n = 6$). Furthermore, one can compare predictions of Gamma distributions at different values of n with the measured data and see how the error parameter evolves with n for each liquid. Fig. 4-6(b) shows that for all viscoelastic liquids the best fit (i.e. the one with the minimum value of the error norm) is a Gamma distribution with $n = 4$. A corresponding analysis for the Newtonian solvent shows that $n = 6$ leads to a minimum error parameter suggesting that a Gamma PDF with $n = 6$ is the best fit for the Newtonian data.

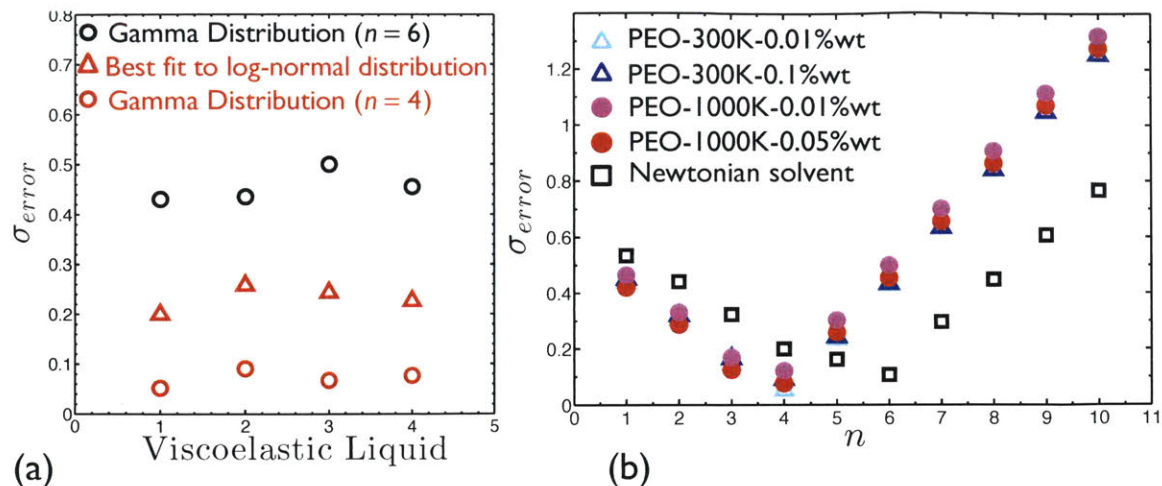


Figure 4-6: (color online). (a) Computed error in fitting different types of PDF to measured droplet size distributions of four different viscoelastic liquids. The red circles correspond to a Gamma distribution with $n = 4$, red triangles show the log mean square error for the best fit to a log-normal distribution and the black circles are for a Gamma distribution with $n = 6$. (b) Computed error in fitting PDF from Gamma distribution at different values of n for all four viscoelastic liquids. For all liquids the error is minimized for a Gamma distribution with $n = 4$.

Studies by Villermaux and coworkers [11, 66, 42] for Newtonian fluids have shown that the value of n characterizing the final Gamma distribution is determined by the smoothness of the initial ligaments when they detach from the core liquid jet. In other words, the index n is a measure of the corrugation in the initial ligaments which the final spray of droplets inherits in its size distribution. They show that the value of n can be predicted just by recording the geometrical shape of the initial ligament:

$$n \equiv \langle d \rangle_0^2 / (\langle d^2 \rangle_0 - \langle d \rangle_0^2) \quad (4.3)$$

in which $\langle \dots \rangle$ indicates a number average and $d_i = 2r_i$ are the diameters of the proto-blobs that one can fit in the profile of the ligament at the instant of pinch-off from the core liquid jet (shown with magenta circles in Fig. 4-2 and by the dashed circles in Fig. 4-7(c) above). A very uniform ligament at $t = 0$ (in which axial fluctuations in the local blob diameters are almost negligible) leads to a very large value of n and, consequently, a very narrow final droplet size distribution. By contrast, a highly corrugated initial ligament in which fluctuations in the local blob diameters

are large, leads to smaller values of n and broader size distributions.

4.5 Sudden Stretch Test

The universal decrease in the values of n for viscoelastic sprays arises from the high extensional viscosity which changes the geometry of initial ligaments from smooth to more corrugated shapes. Tracking the geometry of ligaments in high speed processes such as atomization is an ongoing visualization challenge. A much simpler test, which still illustrates these effects of fluid rheology on the ligament shape at initial times, is an axial ‘step-strain’ test, consisting of a liquid sample confined between two cylindrical plates which are then separated at relatively high stretch rates. The dynamics of fragmentation can be properly replicated through such a test [42] and we use this geometry to study the configuration of viscoelastic ligaments at short times after separation from the liquid core. Fig. 4-7(a) shows a montage of images for the PEO 300K solution ($c/c^* = 0.36$). The fast dynamics of the initial capillary thinning forms capillary waves on the ligament as soon as it separates from the liquid cusps that develop due to the strong squeezing flow in the necks of the ligaments. In contrast to Newtonian liquids (where capillary thinning rapidly leads to droplet pinch off), in viscoelastic ligaments the squeezing flow leads to a localized high strain rate in the neck and the elongating liquid elements resist pinch off due to the enhanced extensional viscosity [223]. This localized elongational flow leads to a highly corrugated beads-on-a-string morphology [138, 223, 120, 137]. The viscoelastic ligament in Fig. 4-7(c) has a more corrugated shape compared to the corresponding Newtonian case and axial variations in the diameter of local blobs $d_i(z)$ are much larger than the corresponding Newtonian case. As shown in Fig. 4-7(b), the distribution of blob sizes can be determined by identifying space filling spheres located at positions where the wavy profile is locally a peak or a trough; thus the radius of the i^{th} blob is $r_i = r_0 + \xi_i$ in which r_0 is the radius of the undisturbed ligament and ξ_i is the deviation of the peak ($\xi_i > 0$) or

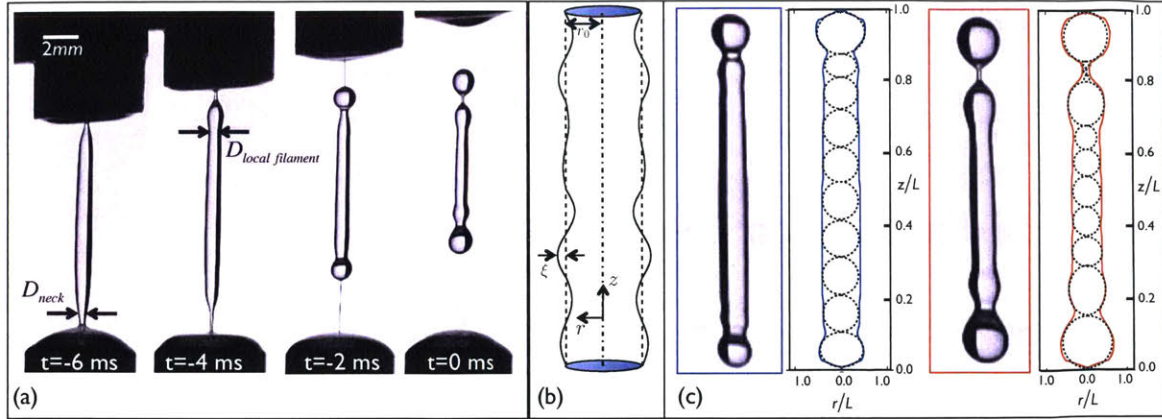


Figure 4-7: (color online). (a) Sudden stretch experiment for a viscoelastic solution at high strain rates ($\dot{\bar{\epsilon}} \simeq 120s^{-1}$). (b) Schematics of a cylindrical ligament with initial radius r_0 corrugated by perturbations with similar wavelengths but varying amplitude ξ . (c) Ligament profiles for the Newtonian solvent (blue curve) compared with the viscoelastic solution (red curve) at the breaking point from the liquid hemispherical reservoirs ($t = 0$). The dashed circles indicate the local proto-blobs inside each ligament.

trough ($\xi_i < 0$). The resulting values of n are calculated using Eqn.(4.5) and show a drastic decrease from $n \simeq 51$ for the Newtonian solvent to $n \simeq 4$ for the viscoelastic solution ¹. These changes in the distribution of corrugations are triggered in all of the viscoelastic fluids, regardless of either polymer concentration or molecular weight, because of the diverging nature of the local strain rate $\dot{\epsilon}(t)$ in the necking filament, which ultimately induces coil-stretch transition in all of the polymer solutions studied.

4.6 Proof for Minimum Value of Smoothness Parameter

To understand the universal saturation in the atomization behavior ($n \rightarrow 4$) we investigate the origins of the corrugations in more detail. Interfacial disturbances on

¹Obviously the fact that aerodynamic effects from the surrounding annular air flow do not appear in the sudden stretch test results in the Newtonian ligament having a very smooth initial profile and a higher value of n compared to a real fragmentation processes

a ligament can be generated from a combination of capillary and shear instabilities. The resulting ligament profile deviates from cylindrical $r(z) = r_0$ by wave-like modulations of the form $\xi_i \cos(2\pi z/\lambda)$ [230, 231]. These perturbations change the distribution of the initial blobs in a ligament from a monodisperse distribution ($n \rightarrow \infty$) on a perfectly smooth cylinder to broader distributions with progressively lower values of n . The amplitude of the perturbations can not exceed the radius of the ligament (thus we expect $-r_0 \leq \xi_i \leq r_0$) and due to the random wavy nature of corrugations we also expect $\langle \xi_i \rangle = 0$. Upon substituting these expressions, Eqn.(4.5) simplifies to

$$n \equiv \langle d \rangle_0^2 / (\langle d^2 \rangle_0 - \langle d \rangle_0^2) \quad (4.4)$$

can be simplified by replacing $d = 2r$ and then substituting $r_i = r_0 + \xi_i$ with $\langle \xi_i \rangle = 0$ due to the wavy nature of the corrugations. The simplification is expanded here:

$$n \equiv \langle d \rangle_0^2 / (\langle d^2 \rangle_0 - \langle d \rangle_0^2) = \frac{\langle r \rangle_0^2}{(\langle r^2 \rangle_0 - \langle r \rangle_0^2)} = \frac{r_0^2}{[\langle (r_0 + \xi_i)^2 \rangle - r_0^2]} = \frac{r_0^2}{[\langle (r_0^2 + 2r_0\xi_i + \xi_i^2) \rangle - r_0^2]} \quad (4.5)$$

which, knowing that $\langle \xi_i \rangle = 0$, simplifies into $n \equiv r_0^2 / \langle \xi_i^2 \rangle$. While the geometrical constraint $|\xi_i| \leq r_0$ gives a minimum value of $n_{min} = 1$ for randomly distributed fluctuations, such a tortuous profile is physically impossible since the corrugated shape would contain a higher volume than the original cylindrical ligament. To satisfy conservation of volume inside the isolated ligament, an additional constraint must be imposed on the third moment of the blob radii distribution, giving $\langle r_i^3 \rangle \leq (3/2)r_0^3$ ².

The undisturbed ligament (as shown in Fig. 4-8(a)) is similar to a cylindrical liquid column with constant radius r_0 . Before the ligament separates from the core jet, the amplitude of capillary corrugations increase with time and the ligament forms a series of N neighboring spherical proto-blobs with individual radii r_i ($i := 1 - N$). No extra volume is added into the ligament so the sum of the individual volumes for proto-blobs in the corrugated ligament can not exceed the initial volume:

²The 3/2 factor comes from the fact that the liquid volume in the initially undisturbed ligament is the volume inside a cylinder with radius r_0 which is 3/2 times higher than the sum of identical neighboring spherical blobs with radius r_0 .

$(4/3)\pi \sum r_i^3 \leq N(2r_0)\pi r_0^2 \Rightarrow \langle r_i^3 \rangle \leq (3/2)r_0^3$. We use the inequality because in addition to all the proto-blobs, there is some (small) additional mass in the very thin liquid borders between neighboring spheres (which is shown with the blue color in Fig. 4-8). As shown in Fig. 4-8(b), the disturbances can grow in amplitude and consequently some of the additional mass goes into the proto-blobs leading to a more corrugated ligament with a conserved total mass/volume. The connection between the volume of sphere and cylinders and the factor of 3/2 is actually initially attributed to Archimedes [232]. Archimedes regarded his proof for this theorem to be his most profound discovery and a sculpted sphere and cylinder were placed on his tomb at his request [233].

Substituting $r_i = r_0 + \xi_i$ and averaging, this new constraint can be simplified to $3r_0\langle \xi_i^2 \rangle + \langle \xi_i^3 \rangle \leq (1/2)r_0^3$. By introducing a new dimensionless amplitude parameter ($-1 \leq \alpha_i \equiv \xi_i/r_0 \leq 1$) the constraints on the initial blob size distributions can thus be rewritten as:

$$\langle \alpha_i \rangle = 0 : \text{random wavy nature of corrugations} \quad (4.6a)$$

$$3\langle \alpha_i^2 \rangle + \langle \alpha_i^3 \rangle \leq 1/2 : \text{conservation of volume} \quad (4.6b)$$

Recognizing that $n = 1/\langle \alpha_i^2 \rangle$, the last constraint in Eqn.(4.6) can be rewritten as $\min\{6/(1 - 2\langle \alpha_i^3 \rangle)\} \leq n$. The minimum value of the function $6/(1 - 2\langle \alpha_i^3 \rangle)$ will thus set the minimum for the index n in a geometrically constrained ligament with constant volume. This minimum is obviously achieved when $\langle \alpha_i^3 \rangle$ attains its most negative value, also subject to Eqn.(4.6a). By trigonometry, introducing a simple transformation of $\alpha_i = \cos(\theta_i)$ we can rewrite $\langle \alpha_i^3 \rangle = \langle \cos^3(\theta_i) \rangle = (1/4)\langle [\cos(3\theta_i) + 3\cos(\theta_i)] \rangle$. Using the first condition in Equation 4.6, this reduces to $\langle \alpha_i^3 \rangle = (1/4)\langle \cos(3\theta_i) \rangle$, which lies between $-1/4$ and $+1/4$. Thus it is clear that the exponent n can not be lower than the minimum value of $n_{min} = 6/(1 - 2\langle \alpha_i^3 \rangle) = 4$. This proof for a minimum value of $n_{min} = 4$ is consistent with earlier scaling arguments that the geometric roughness of the initial ligaments will reach a saturation limit which is set purely by geometry and volume constraints [140].

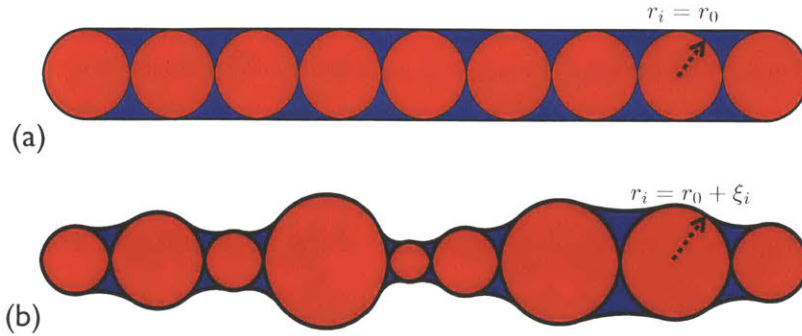


Figure 4-8: (color online). (a) An undisturbed axi-symmetric ligament with a total volume of V_0 consisting of 9 proto-blobs with equal radius ($r_i = r_0$ for $i = 1 - 9$) leading to a value of $n = \infty$. The red area shows the liquid volume within the proto-blobs and the blue area represents the additional volume in the liquid borders between neighboring spheres. (b) A corrugated ligament with a total volume V_0 identical to the undisturbed ligament in (a) and a corrugation amplitude set $\{\xi_i/r_0\}_{i=1-9} = \{-0.2, 0.1, -0.3, 0.5, -0.5, -0.2, 0.4, 0.3, -0.1\}$. The growth of disturbances have rearranged some of the additional volume (blue in (a)) into the new set of proto-blobs. The resulting ligament has a value of $n = 9.6$.

4.7 Other Ligament-Mediated Fragmentation Flows

Knowing that pronounced viscoelastic effects in dilute solutions are manifested in strong elongational flows we performed similar fragmentation tests in two other ligament-mediated fragmentation processes. First we studied drop impact experiments in which a liquid drop ($D \sim 4mm$) impacts on a small target of comparable diameter at high Weber numbers ($We = \rho V^2 D / \sigma \gtrsim 400$). As shown in Fig. 4-9(a), following impact, a curtain of liquid expands outwards from the target and finally bursts into a set of tiny droplets. We also considered jet impact atomization consisting of two identical liquid jets (same liquid, velocity and diameter) that collide with each other at a fixed angle (shown in Fig. 4-9) [234]. Villermaux and coworkers [235, 8] have shown for Newtonian fluids that ligament-mediated fragmentation also occurs in these types of atomization.

Fig. 4-9(a) shows a schematic of the jet impact atomization setup. Two identical jets collide with each other at a given angle and generate a thin liquid film. This configuration was first studied by G. Magnus [10] (Fig. 4-9(b) and 4-7(c)). Depending on the inertia of the impacting jets, at low Weber numbers the liquid film can show shapes which are similar to a “bay leaf” and a “fish-bone” (Fig. 4-9(d) and

4-9(e)). At higher Weber numbers the fluid sheet becomes unstable and filaments go through a fragmentation process breaking into a set of droplets (Fig. 4-9(f)).

The test configuration for studying drop impact of viscoelastic liquids on a small target is similar to the setup used by Villermaux and Bossa [236] for the Newtonian case. Movies 3 and 4 (electronic S.I.) show side and top views of this process in the case of a Newtonian drop. Upon impact the drop will form a curtain that spreads radially outward and at a certain point breaks into small droplets. Movie 5 shows the top view for a viscoelastic drop (300K PEO-0.01% wt). The viscoelastic liquid forms large and small beads connected with each other by elongated filaments (beads-on-a-string structures). A montage of images selected from these movies are shown in the main manuscript.

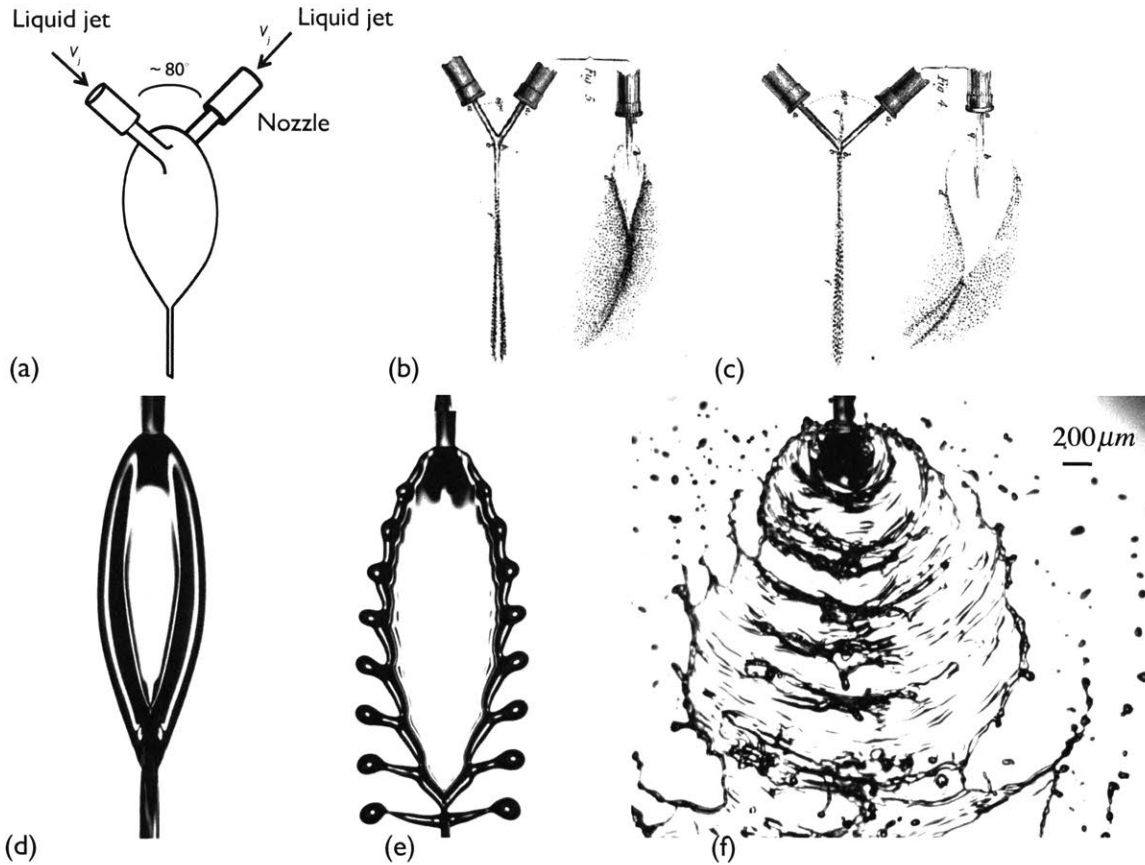


Figure 4-9: (color online). (a) Schematics of the jet impact atomization test. The two identical nozzles face each other with an intersection angle $\theta \sim 80^\circ$. (b) and (c) Original hand drawings for a similar setup used for studying the atomization of Newtonian jets by G. Magnus [10] at different angles ($\theta \sim 60^\circ$ and $\theta \sim 90^\circ$ respectively). (d), (e) and (f) Visualization of the jet impact test for the Newtonian solvent $Oh = 0.02$ at different jet velocities corresponding to $We \equiv \rho V_j^2 D / \sigma = 1.5, 12.5$ and 150 respectively. The jets impact and form morphologies which resemble a “bay leaf”, and a “fish-bone” at lower speeds and finally result in atomization forming filaments and droplets at higher speeds as shown in Fig. 4-9(f).

Droplet visualization in both processes shows that viscoelasticity again leads to larger numbers of both big and small drops in the final fragments (Figs. 4-10(a-ii) and 4-10(b-iii)), whereas in the Newtonian case the drop sizes are narrower. A summary of the measured breadth of the droplet size distributions for these two new tests, along with data from air-assisted atomization is shown in Fig. 4-10(c). We show the computed values of the Sauter Mean Diameter ($SMD \equiv \sum d_i^3 / \sum d_i^2$) normalized by the average diameter ($\langle d \rangle$) versus the measured values of n obtained from fitting Gamma distributions to the measured PDF for each experiment (each

consisting of $N \geq 5000$ droplets). For a Gamma distribution $SMD/\langle d \rangle = 1 + 2/n$ and the solid line in Fig. 4-10(c) shows this analytical prediction compared with the experimental measurements. In all three flows, the addition of viscoelasticity decreases the value of n from that observed in the same flow for a Newtonian fluid. Even for weakly elastic polymer solutions with relaxation times as low as $60\mu s$, the size distributions universally approach $n = 4$ in each flow.

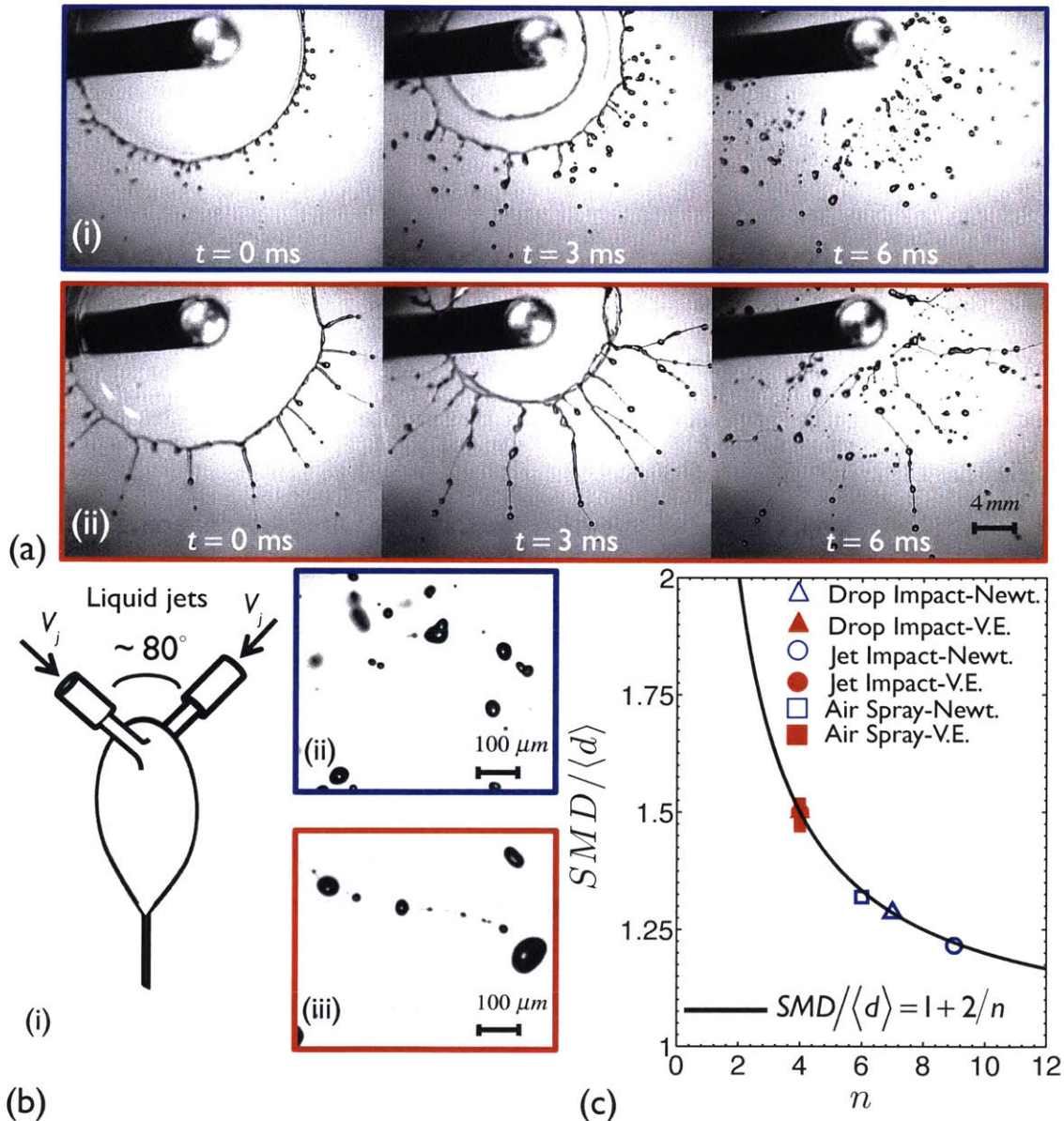


Figure 4-10: (color online). (a) Fragmentation after drop impact on a small target. Montage of images for (i) the Newtonian solvent and (ii) a polymer solution (PEO 300K). (b) Snapshots of the droplets captured after fragmentation by jet impact atomization for (i) the Newtonian solvent and (ii) viscoelastic solution. (c) Summary of the measured values of the dispersity $SMD/\langle d \rangle$ in three different fragmentation processes for both the Newtonian solvent (blue) and the viscoelastic solutions (red) compared with the theoretical prediction (solid line).

4.8 Size Distribution of Ligaments

We now present the ligament size distributions in all the studied processes for both the Newtonian solvent and for one of the viscoelastic test fluid. Fig. 4-11(a) presents the size distributions of the ligaments in our air-assisted atomization experiments. For both the Newtonian and the viscoelastic liquid the measured distributions are very narrow compared to the final droplet size distributions that we have measured and that are reported in Fig. 4-3. The ligament sizes show an even narrower distribution in the jet impact atomization and the drop impact tests (Fig. 4-11(b)). Similar trends for ligament size distributions have been observed in the literature for *Newtonian* liquid fragmentation in all of these geometries [54, 13, 12, 236].

Furthermore, we also analyze the size distribution of the droplets that emerge from an individual ligament fragmentation in the sudden stretch tests (shown in Fig. 4-7(c)). Fig. 4-11(c) shows the measured size distributions for both the Newtonian solvent and the viscoelastic liquid. Measured droplet sizes are gathered after image analysis for approximately 30 ligaments, each of which fragments into a few droplets. It is clear that the smoothness of the Newtonian ligaments at early times leads to a relatively narrow final size distribution (the blue line in Fig. 4-11(c) shows a fit to a Gamma distribution with $n = 30$). Viscoelastic ligaments on the other hand, exhibit a more corrugated geometry/profile as they detach from the hemispherical caps (Fig. 4-7) and their corresponding droplet sizes after the ligament goes through the fragmentation process shows a much broader distribution (the red line in Fig. 4-11(c) shows a Gamma distribution with $n = 4$). These results indicate that the breadth of the droplet size distributions in the viscoelastic spray is most strongly affected by the dynamics of each individual ligament fragmentation. As shown in Fig. 4-7 and Fig. 4-11, even in the sudden stretch test (in which the absence of air flow leads to ligaments with a smoother profile than in a real atomization process) the addition of viscoelasticity leads to geometrical corrugations on an individual ligament profile that reduce the value of the smoothness parameter

to the minimum $n_{min} = 4$ (Fig. 4-7(c)). This broadens the droplet size distribution in a single ligament fragmentation process compared to a Newtonian fluid (Fig. 4-11(c)). However, when we convolve this single ligament distribution with the narrow ligament size distribution shown in Fig. 4-11(a) and Fig. 4-11(b) (red lines) we obtain a final droplet size distribution in the actual spray process (Fig. 4-3). As we show by the (+) symbols in Fig. 4-11(c) below this convolution is indistinguishable from the complete Gamma distribution. Given the narrow distribution of the ligament sizes, if one calculates the convolution integral numerically, the final result (red cross symbols) will be very close to the Gamma distribution observed in the fragmentation of an individual ligament.

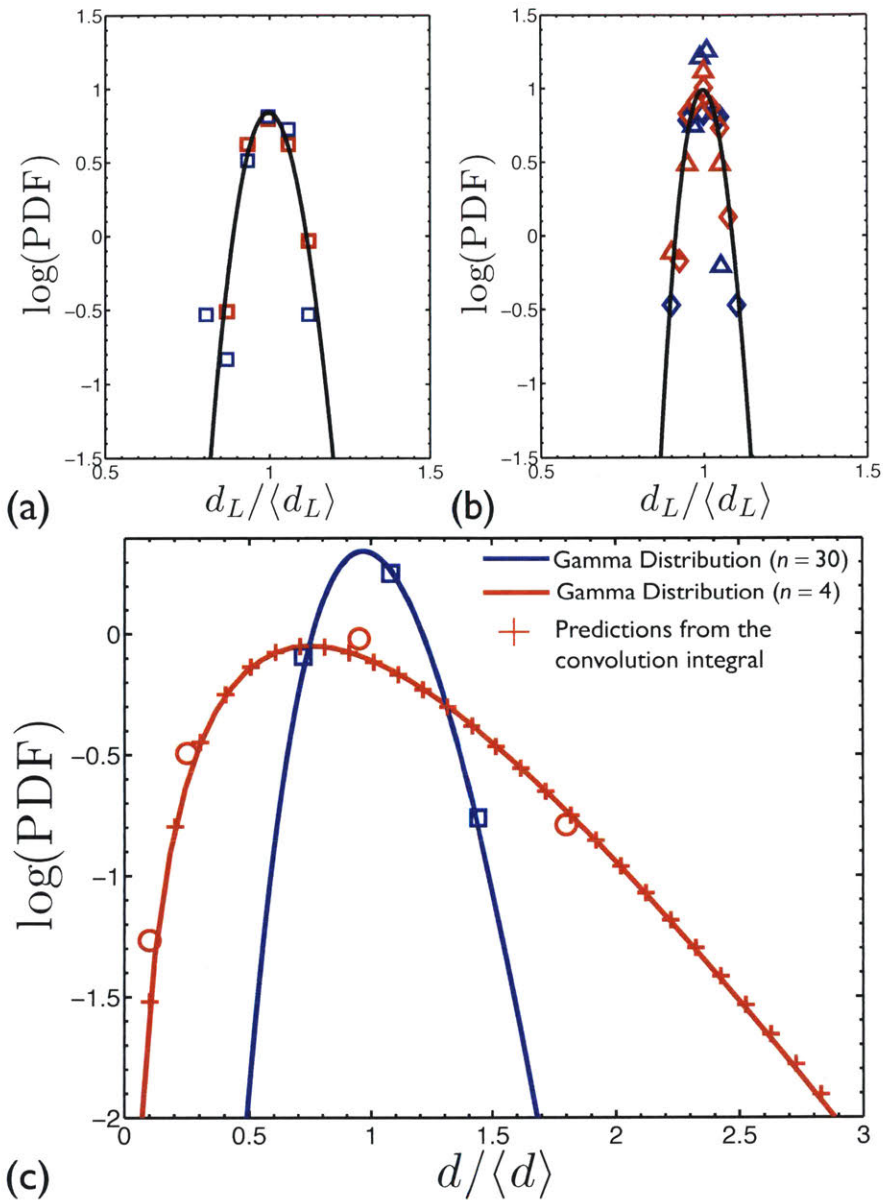


Figure 4-11: (color online). (a) Ligament size distributions in air-assisted atomization for the Newtonian solvent $\{Oh = 0.04, De = 0\}$ (\square) and the PEO-300K-0.1%wt. solution $\{Oh = 0.04, De = 1.3\}$ (\square). The solid black line shows the fit of a very narrow Gamma distribution with $n = 300$. (b) Ligament size distributions in drop-impact fragmentation (\triangle, \triangle) and the jet impact atomization tests (\diamond, \diamond) for the Newtonian solvent $\{De = 0\}$ (\triangle, \diamond) and the PEO-300K-0.1%wt. solution $\{De = 1.3\}$ (\triangle, \diamond). The black solid line shows a narrow Gamma distribution with $n = 600$. (c) Droplet size distributions in individual ligaments in the sudden stretch test (stretched ligaments in Fig. 4-7(c)) for the Newtonian solvent $\{Oh = 0.04, De = 0\}$ (\square) and the PEO-1000K-0.05%wt. solution $\{Oh = 0.04, De = 10.0\}$ (\circ). The solid blue and red lines are Gamma distributions with $n = 30$ and $n = 4$ respectively. The red cross symbols show the numerical calculation of the convolution integral between the fits for the droplet size distribution in a ligament (red solid line) and the fit for the measured ligament size distribution in the spray (black solid line in (a)).

4.9 Discussion

Our results indicate that this viscoelastic broadening mechanism is driven by the local dynamics of the strong extensional flow in the filament necks. Although viscoelasticity monotonically increases the average droplet size $\langle d \rangle$ in ligament-mediated fragmentation phenomena [108], the distribution of sizes about the mean value are uniquely determined by a broad Gamma distribution with $n = 4$. This geometrical limit is triggered by the enhanced elongational viscosity experienced during the capillary pinch off process (provided that the concentration of the microstructure is above the ‘infinite dilution limit’ [135]) and results in highly corrugated ligaments. The final size distribution is constrained entirely due to geometry and conservation of volume. Recognizing and understanding this bound is essential in guiding the design of many processes that involve breakup and fragmentation of complex liquids such as emulsification, spray painting and even biological processes such as pathogen transfer resulting from violent expiration [237].

Chapter 5

Rotary atomization of Newtonian and viscoelastic liquids

Let no-one ignorant of geometry enter.

Plato

5.1 Scope

We study the kinematics and dynamics of fragmentation for different Newtonian and viscoelastic liquids in rotary atomization. Centripetal acceleration is responsible for pushing the liquid at the rim of a spinning cup, producing and destabilizing a liquid torus in a process similar to Rayleigh-Taylor instability. The resulting ligaments leave the liquid torus with a remarkably repeatable spacing that scales linearly with the inverse of the rotation rate. Filaments then follow a well-defined geometrical path-line that is described by the involute of a circle. Starting from the geometry of our system, we derive the detailed kinematics of this process and compare it with our experimental observations. We show that the ligaments elongate tangentially following the involute of a circle and thin radially as they separate from the cup. A theoretical form is derived for the spatial variation of the filament deformation rate. Far from the cup, the deformation rate becomes comparable to the critical rate of capillary thinning and the filaments break into droplets.

Coupling the derived kinematics with known properties for Newtonian and viscoelastic liquids, we provide a physical analysis of the fragmentation process that is compared in detail with our experiments.

5.2 Introduction

Animals drying their wet fur by rapidly shaking their body and rotary atomization in paint coating are just a few examples in which centripetal acceleration is used to disintegrate liquid films into smaller fragments. The interest in this type of atomization goes back to the pioneering studies in Germany on different combustion and spray drying designs. Peter Bär [43] (son of the famous Julius Bär, founder of the Swiss Julius Bär private banking group) designed a “centripetal atomizer”. Figure 5-1(a) shows a picture of Bär setup. This simple design, used for a new type of spray-dryer at its time, consists of a tube that delivers the fluid of interest into a rotating cup. More recent designs still follow the same basic idea (Figure 5-1(b)). The gradually increasing industrial interest, encouraged different researchers to study this type of atomization in more detail. Hinze and Milborn [45] performed a series of experiments with different Newtonian liquids and provided several semi-empirical correlations for the performance of this atomizer. Early high-speed visualizations of Hinze and Milborn showed that, in certain ranges of rotation speeds and fluid delivery rates, evenly-spaced ligaments emerge on the edge of the spinning cup (Figure 5-1(c) and (d)).

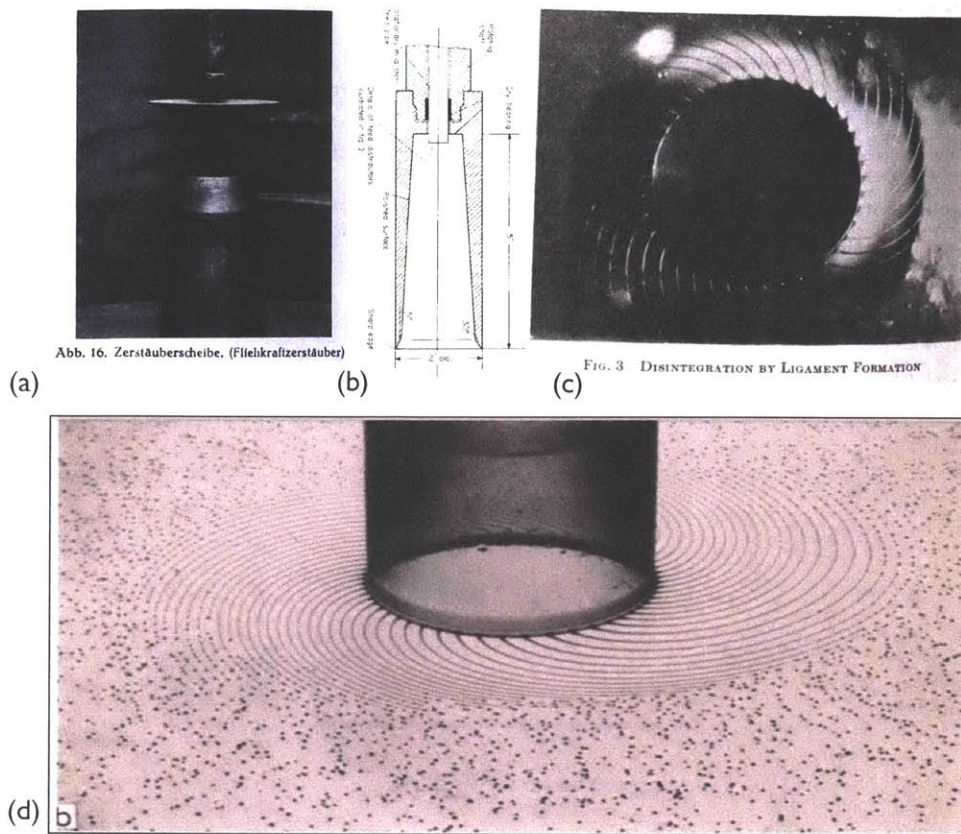


Figure 5-1: (color online). Examples of rotary atomizers in the literature: (a) The “atomizer disc” or the “centripetal atomizer” which was studied by Peter Bär [43]. (b) The rotary atomizer used by Fraser *et al.* [44]. (c) Snapshot of the evenly-spaced ligaments that are formed around the rotating cup by Hinze and Milbourn [45]. (d) Ligaments formation and breakup into a relatively mono-disperse cloud of droplets, captured by Fraser *et al.* [46]

Narrower size distributions and well-defined geometrical fluid pathlines (similar to the involute of a circle) are the main advantages of this type of atomization as compared to air-assisted atomization [44, 46, 47]. Despite these inherent advantages, there is a paucity of fundamental knowledge about the roles of fluid rheology in this process. In this chapter, we study the effects of viscosity and viscoelasticity by performing rotary atomization tests on different Newtonian and dilute polymeric liquids.

5.3 Setup

We designed a rotary atomization setup which is very similar to the one suggested by Fraser *et al.*[44, 46]. As shown in Figure 5-2, the fluid is delivered to the rotating cup through a swivel joint at the back of the cup. The fluid then gets accelerated to the rim of the cup. A high-speed camera (Phantom Miro series) is mounted in front of the spinning cup and enables us to record the fragmentation process at high spatial (1400×800 pixels) and temporal (4000 fps recording speed) resolution.

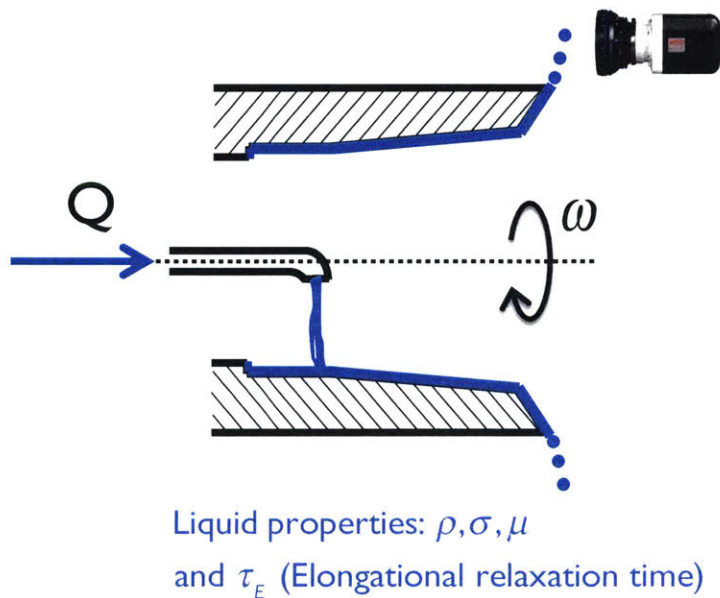


Figure 5-2: (color online). Schematics of the visualization setup. A cup with diameter $D = 2R = 3.18$ cm, rotating at an angular speed ω , is supplied with liquid at a volumetric flow rate Q . Due to the centrifugal forces, the liquid is pushed to the rim of the cup and then disintegrates into smaller fragments. A high-speed camera (Phantom-Miro) is used to visualize the fragmentation event.

In order to spin the cup at a desired rate of rotation, a mechanical assembly was designed and fabricated in the MIT machine shop. Figures 5-3((a) and (b)) show CAD drawings of the design while the final prototype is pictured in part (c).

A stepper motor controls the rotation of the cup through a timing belt pulley, the liquid is delivered through a swivel joint that allows the transfer of liquid from a fixed tube to the rotating cup. A Harvard PHD ULTRA syringe pump is used to feed the liquid into the cup at a constant volumetric flow rate $Q = 0.1 - 200$ ml/min. The entire setup is then mounted and fixed in a transparent glass box (see figure 5-3(d)) which minimizes the spread of fragments while optically being accessible for imaging purposes.

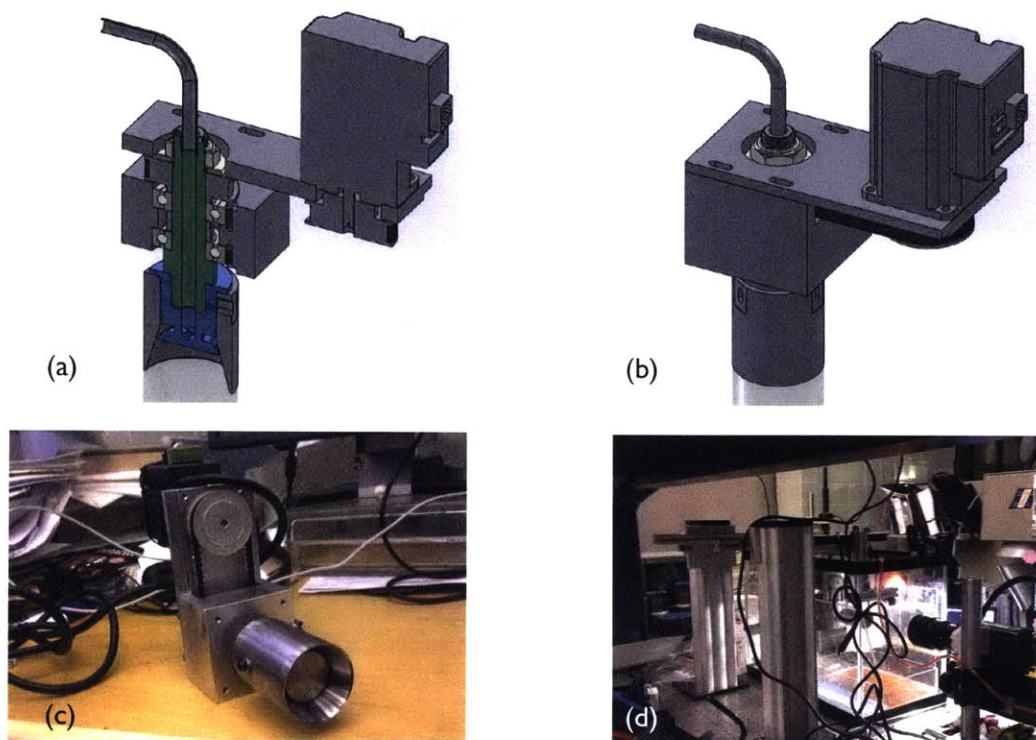


Figure 5-3: (color online). (a) and (b) Solidworks CAD drawings of the initial design for the rotary atomizer. (c) The final prototype. (d) The atomizer is fixed on a set of stands inside a transparent glass box that minimizes the spread of the generated mist but allows optical access for imaging purposes.

Fast motion of the cup and the liquid drops/ligaments can lead to optical blur, especially at high rotation rates. To avoid this, we chose relatively small values of exposure times in our high-speed recordings ($\sim 20 \mu\text{s}$). Using back-lighting technique, we were able to provide ample illumination for recordings at these low

values of exposure time. A bright halogen lamp with an optical diffuser were fixed behind the rim of the cup and the shadow of the fragmentation event was recorded. Figure 5-4 is a typical frame from a recorded movie that shows the atomization of silicone oil ($\nu = 100$ cSt). The outer profile of each filament/drop is seen as a dark shadow with a high contrast compared to the bright background. The bright inner strips/circles that can be detected within filaments/drops is due to the known lens effect that cylindrical/spherical transparent object can generate. All the important features of the phenomena, such as sizes and numbers of ligaments, can be easily captured by simple image-processing schemes in Matlab or ImageJ. The fact that the entire fragmentation event happens in the fixed plane of the cup circle is extremely helpful in imaging and analysis.

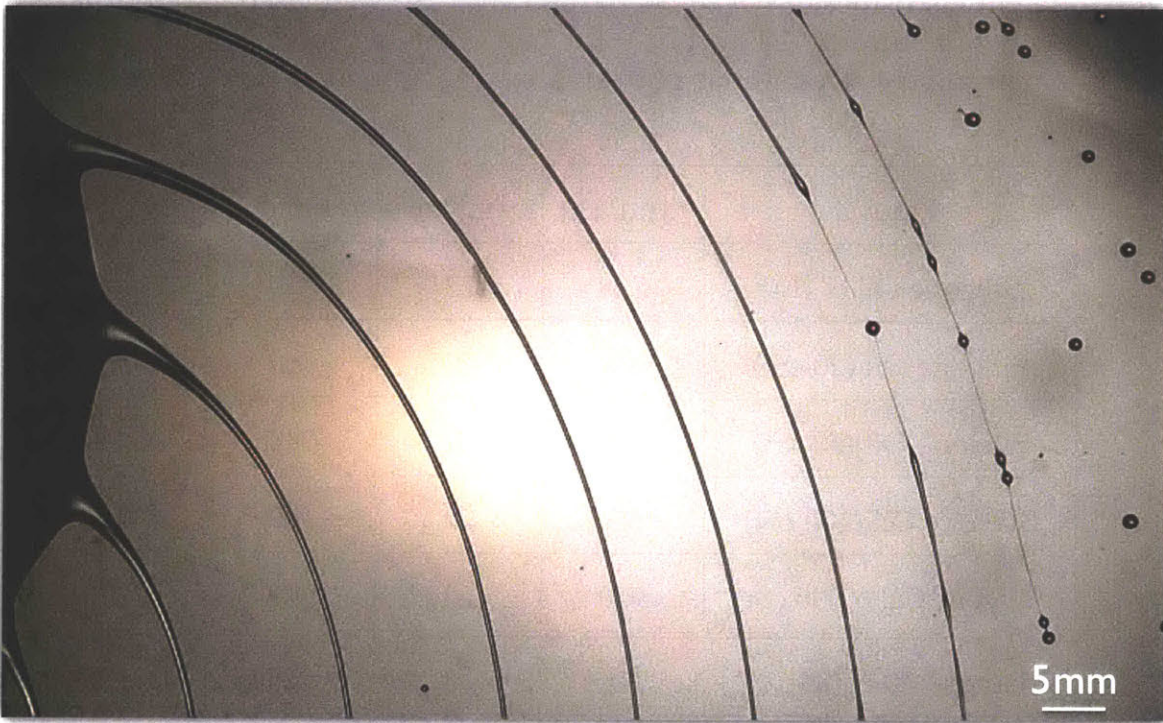


Figure 5-4: (color online). Silicone oil ($\nu = 100$ cSt) flows into the the rotating cup ($\omega = 62.8$ rad.s⁻¹) at a constant volumetric flow rate ($Q = 60$ ml/min). The liquid forms a thin torus-like film on the rim of the spinning cup which then, due to the centripetal acceleration, becomes unstable and forms a series of evenly-spaced continuously elongating ligaments. All ligaments form a similar spiral-like pattern. Capillary forces then make the individual Ligaments unstable and consequently break them into small droplets.

5.4 Test Fluids

We prepared several different Newtonian liquids for our study and used certain subsets of them in different tests. Five different silicone oils were purchased from Gelest and a Newtonian solvent was prepared by mixing ethanol and water with a 90-10% weight ratio. Properties of these Newtonian liquids are tabulated in Table 5.1.

Table 5.1: Properties of the Newtonian test fluids. Five different silicone oils (S.O.) with different viscosities ($\nu = 7, 20, 50, 100$ and 1000 cSt) were used in our tests. An ethanol-water mixture (90-10% wt. $\eta_s = 1.0$ mPa.s) was also prepared to be used as a Newtonian solvent. Definitions of the Ohnesorge number (Oh_R) is described in the text.

Liquid	μ [mPa.s]	σ [mN.m]	ρ [kg/m ³]	Oh
Silicone Oil (7 cSt)	6.44	22	920	0.011
Silicone Oil (20 cSt)	19	22	950	0.033
Silicone Oil (50 cSt)	48	22	960	0.082
Silicone Oil (100 cSt)	96	22	960	0.166
Silicone Oil (1000 cSt)	970	22	970	1.667
Ethanol-Water (90-10%)	1	23	825	0.001

In order to study the effect of viscoelasticity on the rotary fragmentation, we also dissolved Poly(ethylene oxide) (PEO) in the ethanol-water mixture and prepared three dilute solutions. Two of the viscoelastic solutions contained a 300K M_w PEO, dissolved at a concentration of 0.01% and 0.05% wt. into the solvent. The third viscoelastic solution was made with a 1M M_w PEO at 0.01% wt. concentration. The properties of the viscoelastic test fluids are tabulated in Table 5.2. For these dilute solutions the shear viscosity is almost constant and close to the corresponding value for the solvent but, as discussed in previous chapters, the elongational viscosity can be dramatically higher. Measurements of the elongational relaxation times were carried out using the ROJER technique [238] and are reported in Table 5.2.

Table 5.2: Properties of the viscoelastic test fluids. Three different dilute polymer solutions were then prepared by dissolving small amounts of PEO (Poly(ethylene oxide)) in the Newtonian solvent (ethanol-water mixture). Definitions of the Deborah number (De_R), and Ohnesorge number (Oh_R), are described in the text.

Liquid	M_w	c(wt.)	c/c^*	η_0 [mPa.s]	σ [mN.m]	τ_E [μ s]	De_R	Oh_R
1M-0.01%	1M	0.01%	0.07	1.08	23	900	0.005	0.001
300K-0.05%	0.3M	0.05%	0.18	1.16	23	109	0.0006	0.001
300K-0.01%	0.3M	0.01%	0.04	1.04	23	68	0.0004	0.001

5.5 Dimensionless Operational Map

To understand the underlying physics of rotary fragmentation, we can analyze the different timescales that are involved in this phenomenon. A Newtonian liquid with density ρ , viscosity μ and surface tension σ is delivered, by a volumetric rate Q , into a cup of size $D = 2R$ that is rotating at rate ω . Four timescales can be identified: a rotation timescale $1/\omega$, a convection timescale R^3/Q , a capillary timescale $\sqrt{\rho R^3/\sigma}$ and a viscous timescale $\mu R/\sigma$. From these, we can construct three dimensionless groups by comparing the capillary timescale to the other characteristic timescales. We thus obtain:

$$\begin{aligned}
 We_{rotation} &\equiv \left(\frac{\sqrt{\rho R^3/\sigma}}{1/\omega} \right)^2 = \frac{\rho R^3 \omega^2}{\sigma} \\
 We_{convection} &\equiv \left(\frac{\sqrt{\rho R^3/\sigma}}{R^3/Q} \right)^2 = \frac{\rho Q^2}{R^3 \sigma} \\
 Oh &\equiv \left(\frac{\sqrt{\rho R^3/\sigma}}{\mu R/\sigma} \right)^{-1} = \frac{\mu}{\sqrt{\rho R \sigma}}
 \end{aligned} \tag{5.1}$$

The first two are effectively the Weber numbers that arise based on the rotational (ω) and convective (Q) momentum of the fluid respectively. Both these groups

compare the ratio of the inertially generated stresses in the flow to the resisting capillary ones at the air/liquid interface. In this chapter We refers to the rotation Weber number $We_{rotation}$. The last dimensionless group that emerges from this analysis is the familiar Ohnesorge number that describes the ratio of viscous to the inertia-capillary stresses [199].

As mentioned, many liquids of interest in rotary atomization are complex fluids such as paints or inks which can be considered viscoelastic liquids. These complex fluids have an underlying microstructure that can resist the generated elongational deformations associated with the pinch off phenomena in rotary atomization. Thus, for viscoelastic fluids, the presence of an elongational relaxation timescale τ_E gives rise to a new dimensionless number:

$$De_R \equiv \left(\frac{\sqrt{\rho R^3 / \sigma}}{\tau_E} \right)^{-1} = \frac{\tau_E}{\sqrt{\rho R^3 / \sigma}}. \quad (5.2)$$

Hinze and Milborn [45] were one of the first to use these dimensionless numbers (Equation (5.1)) in their study of the rotary atomization for Newtonian liquids. In their studies they found that by increasing either the rotation rate for the cup or the flow rate of the fluid three separate regimes emerge. Figure 5-5 is a visual guide for these regimes: (a) At low rotation/flow rates only few single drops are formed at the edge of the cup ("*single drop formation*"). Due to the centripetal acceleration these drops finally pinch off and distance from the cup. (b) At larger values of rotation/flow rate many evenly-spaced similar ligaments appear on the cup and each ligament follows a spiral-like geometry in space ("*ligament formation*"). Due to the action of capillary forces, the stretching ligaments finally break up into groups of droplets that are relatively mono-disperse in size thanks to the repeatable and organized geometry of the ligaments. (c) At large enough rotation/flow rates a liquid sheet emerges on the edge of the cup ("*film formation*"). This liquid sheet rotates with the cup and is destabilized due to the inertia of its motion in the air. The sheet forms an unstable rim, this time far from the cup, that breaks into droplets with a wide range of sizes.

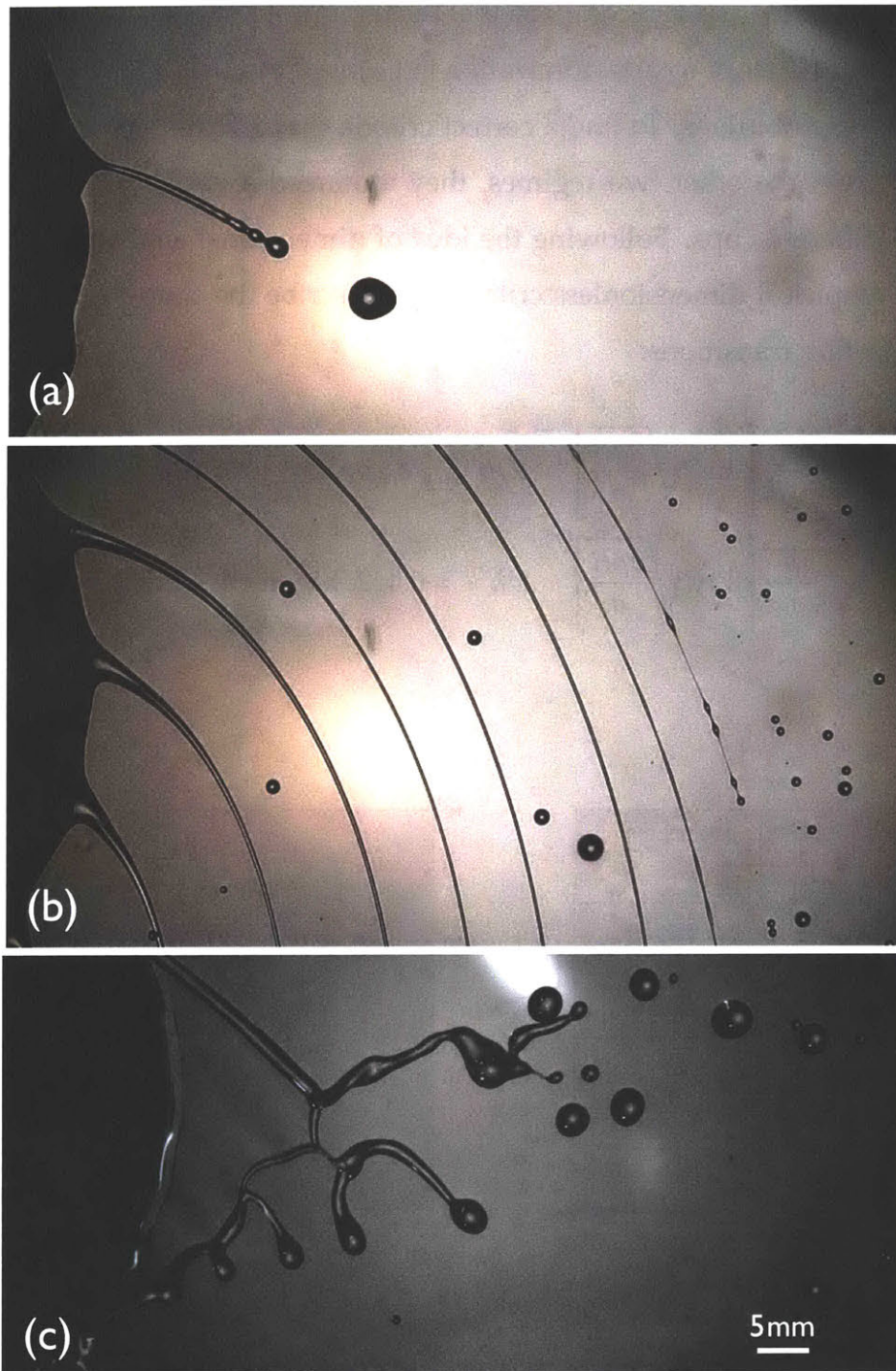


Figure 5-5: (color online). A visual guide showing the formation of single drops (a) ligaments (b) and fluid film (c) for silicone oil ($\nu = 50$ cSt) as the flow rate increases from (a) to (c). The cup is rotating at the same rate for the three images and the corresponding dimensionless groups $\Pi_1 \equiv \omega D \sqrt{\rho D / \sigma}$ and $\Pi_2 \equiv (Q/D) \sqrt{\rho / (\sigma D)} (\mu / \sqrt{\rho \sigma D})^{1/6}$ are: (a) $\{\Pi_1 = 1.95 \times 10^2, \Pi_2 = 1.64 \times 10^{-3}\}$, (b) $\{\Pi_1 = 1.95 \times 10^2, \Pi_2 = 1.64 \times 10^{-2}\}$ and (c) $\{\Pi_1 = 1.95 \times 10^2, \Pi_2 = 9.83 \times 10^{-2}\}$

Hinze and Milborn [45] recognized that the regime of ligament formation yields the best performance of rotary atomization in terms of mono-dispersity in the final droplet size distributions. To find a correct criteria that differentiates the ligament formation from the other two regimes, they atomized a variety of different liquids with different cups. Following the idea of dimensional analysis, they found that semi-empirical dimensionless criteria can describe the drop-to-ligament and ligament-to-film transitions:

$$\frac{Q}{2R} \sqrt{\frac{\rho}{2\sigma R}} \left[2\omega R \sqrt{\frac{2\rho R}{\sigma}} \right]^{0.25} \cdot Oh^{1/6} = 2.88 \times 10^{-3} : \text{Drop-Ligament}$$

$$\frac{Q}{2R} \sqrt{\frac{\rho}{2\sigma R}} \left[2\omega R \sqrt{\frac{2\rho R}{\sigma}} \right]^{0.6} \cdot Oh^{1/6} = 0.442 : \text{Ligament-Film}$$
(5.3)

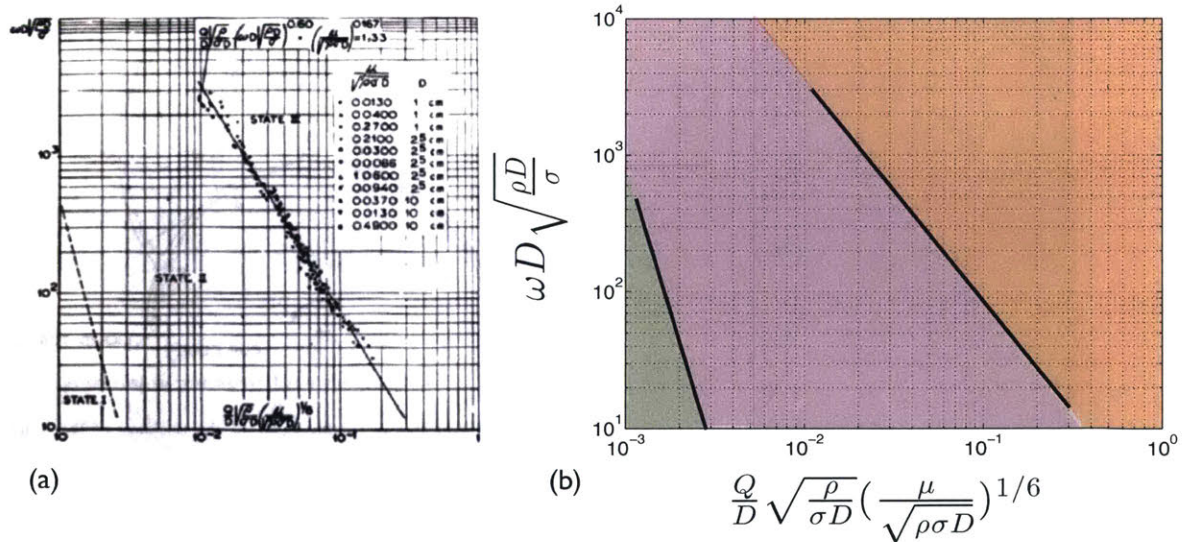


Figure 5-6: (color online). (a) The proposed dimensionless map of rotary atomization by Hinze and Milborn [45]. Different lines outline the corresponding criteria that differentiate possible morphologies such as drop, ligament and film generation from each other.

Figure 5-6(a) is a copy of the original result reported by Hinze and Milborn [45]. The same criteria are replotted in Figure 5-6(b) leading to a dimensionless operational map for the different regimes: drop formation (shaded in green), ligament

formation (shaded in magenta) and film formation (shaded in red).

5.6 Rotary Atomization of Newtonian Liquids

As described before, the optimal regime of operation is the ligament formation. Thus, for the rest of this chapter, we mainly focus on this regime for both Newtonian and then viscoelastic fluids.

5.6.1 Average Droplet Sizes

Several studies in the literature have found empirical correlations for the average droplet diameter measured in rotary atomization of Newtonian liquids [47, 48, 49, 50, 51].

<i>Reference</i>	<i>Liquid</i>	<i>Flow-rate Q</i>	<i>Rotational speed, n</i>	<i>Diameter, D</i>	<i>Liquid viscosity, μ</i>
Hege ⁴	Various	-	-1.0	-0.50	-0.083
Oyama <i>et al.</i> ²⁰	Water	0.20	-1.0	-0.30	-
Kamiya and Kayano ²¹	Water	0.33	-1.0	-0.50	-
Ryley ¹⁹	Water	0.19	-1.41	-0.66	-1.41*
Present work	Oil	0.334	-1.32	-1.22	-0.1

* Denotes values inferred by dimensional analysis.

Figure 5-7: (color online). Dependency of the average droplet size on different properties. The table, taken from Dombrowski and Lloyd [47], provides a summary of the empirical power law exponents that are suggested in the literature. Results from Hege [48], Oyama *et al.* [49], Kamiya and Kayano [50], Ryley [51] and Dombrowski and Lloyd [47] show approximate values for the corresponding exponents.

Figure 5-7, taken from Dombrowski and Lloyd [47], summarizes the empirical power law exponents that are suggested in the literature. One can easily see the apparent discrepancy between suggested results from different works in this

specific field of atomization and fragmentation. It should also be emphasized that dimensional analysis can not really add certainty to any of the proposed correlations. We thus aim to understand the involved phenomena in more detail and provide a physical model for predicting the average sizes.

5.6.2 Parameter Study

Measured average droplet sizes at different rotation and flow rates are plotted in Figure 5-8 (a) and (b), respectively, for the Newtonian solvent (ethanol-water mixtures).

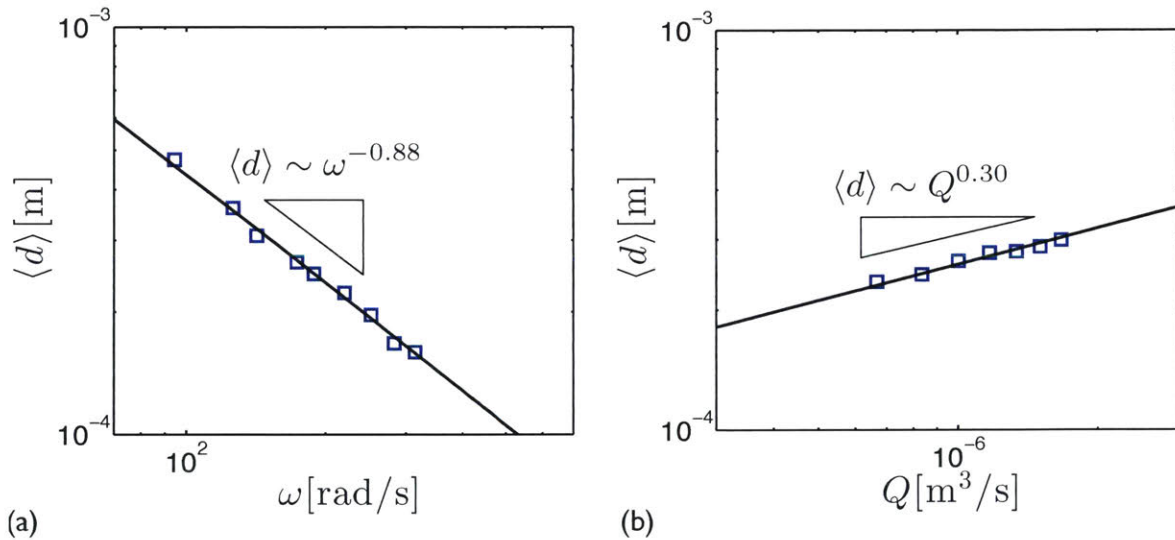


Figure 5-8: (color online). Measured values of the average droplet diameter for the ethanol-water (90%-10% wt.) mixture. Dependency of the average droplet diameter $\langle d \rangle$ on: (a) the rotation rate of the cup ω at a fixed value of volumetric flow rate $Q = 60$ ml/min and (b) the volumetric flow rate Q at a fixed rotation rate $\omega = 172.7$ rad/s.

Results clearly exhibit certain power law dependencies between the average diameters and the applied rotation/flow rates. The measured average droplet size decreases with increasing rotation rate $\langle d \rangle \sim \omega^{-0.88}$ and shows an opposite trend when increasing the volumetric flow rate $\langle d \rangle \sim Q^{0.30}$. This power law exponents are around the same values reported in the literature [47] but yet again fail to give

us a complete physical image.

In order to understand the nature of the observed correlations for the ligament formation regime, we start by understanding the mechanism of ligament generation and focus on the flow kinematics.

5.6.3 Formation of Ligaments

The centripetal acceleration $R\omega^2$ is the driving force for this fragmentation process. Inside the cup, the liquid elements are pushed towards the edge and finally reach the rim of the cup. Then a liquid torus is formed around the edge that has a tendency to preserve its shape due to surface tension. However, if the fluid elements feel enough acceleration and the resulting inertia stresses win over the resisting capillary ones, then the torus becomes unstable and forms elongated fingers that turn into ligaments when they are fully stretched. This mechanism is exactly identical to the well-known Rayleigh-Taylor instability [239, 240, 158, 241]. Replacing the centripetal acceleration with gravity, we can clearly see the similarity with the stability analysis for an interface separating a heavier liquid at the top from a lighter one at the bottom. As proposed by Plesset and Whipple [242], a simple balance of stresses at the interface can give us a physical scaling for the most unstable wavelength. We imagine that the interface is perturbed by a wave with wavelength λ which has an infinitesimally small amplitude. The respective downward and upward displacement of the heavier and lighter liquid is favored by the downward direction of the gravity and in the absence of any resisting mechanism every wave with any arbitrary wavelength grows in amplitude and is unstable. However, the presence of surface tension develops a resisting capillary pressure at the interface which tends to keep the interface between the two liquids flat. Thus, the driving stress for this mechanism scales with $\rho g a$ where a is the amplitude of the wave and the resisting rises from the capillary pressure that scales with surface tension and the curvature of the wave $\sigma a/\lambda^2$. Simple balance between these two suggests that the critical wavelength scales with the capillary length $\lambda_c \sim \sqrt{\sigma/\rho g}$.

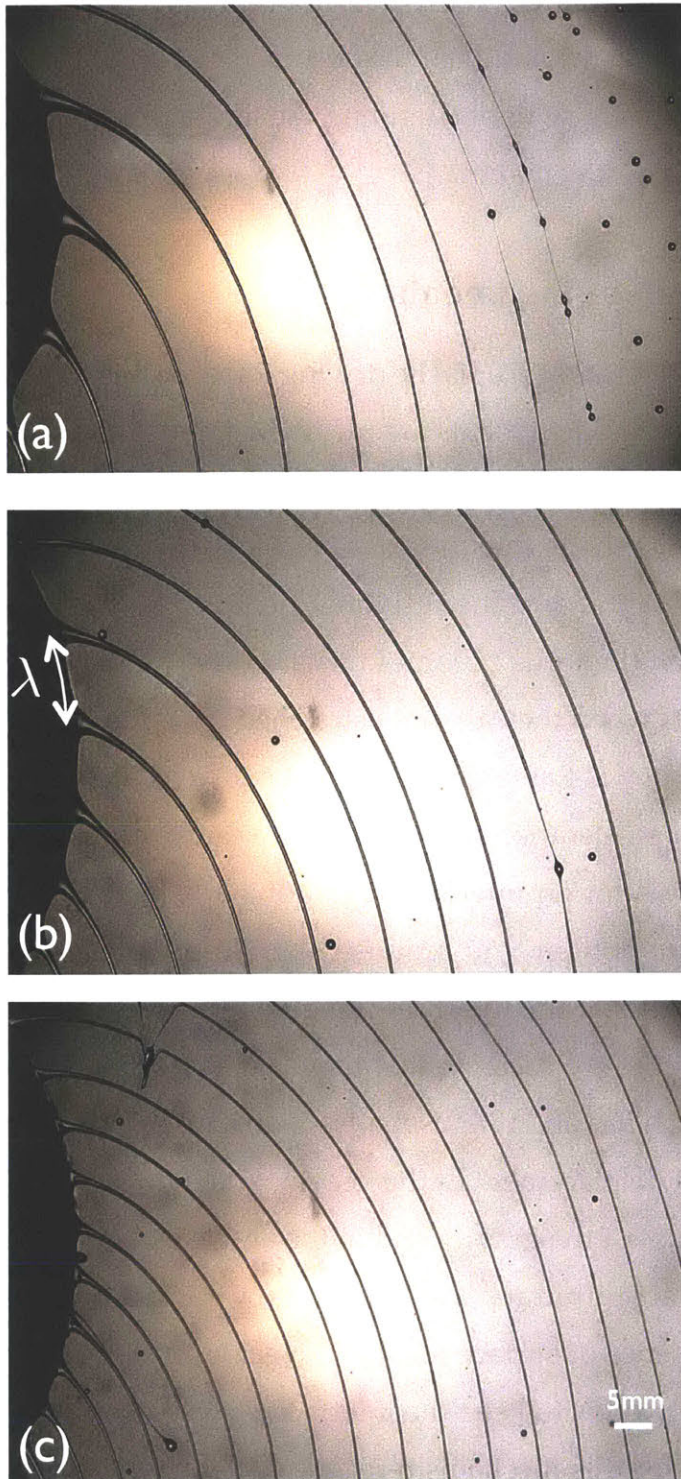


Figure 5-9: (color online). Silicone oil ($\nu = 100$ cSt) is delivered to the cup at a constant flow rate ($Q = 60$ ml/min). Three snapshots show the number of formed ligaments at three different values of rotation rate: (a) $\omega = 62.8$ rad/s, $We \equiv \rho R^2 \omega^2 / \sigma = 100$, (b) $\omega = 94.2$ rad/s, $We \equiv \rho R^2 \omega^2 / \sigma = 225$ and (c) $\omega = 157$ rad/s, $We \equiv \rho R^2 \omega^2 / \sigma = 625$.

To apply the mentioned scaling to rotary atomization we need to replace the gravity term g with the centripetal acceleration $R\omega^2$:

$$N = \frac{2\pi R}{\lambda} \sim \omega \sqrt{\frac{\rho R^3}{\sigma}} \rightarrow N \sim \sqrt{We}. \quad (5.4)$$

where N is the number of ligaments formed around the cup. In fact Eisenklam [243], inspired by a lecture from G. K. Batchelor, was the first to make this analogy in his study of rotary atomization. He showed that, based on the theoretical solution of Taylor [240], the scaling relationship described in Equation (5.4) has a numerical coefficient:

$$N = \frac{1}{\sqrt{3}} \sqrt{We}. \quad (5.5)$$

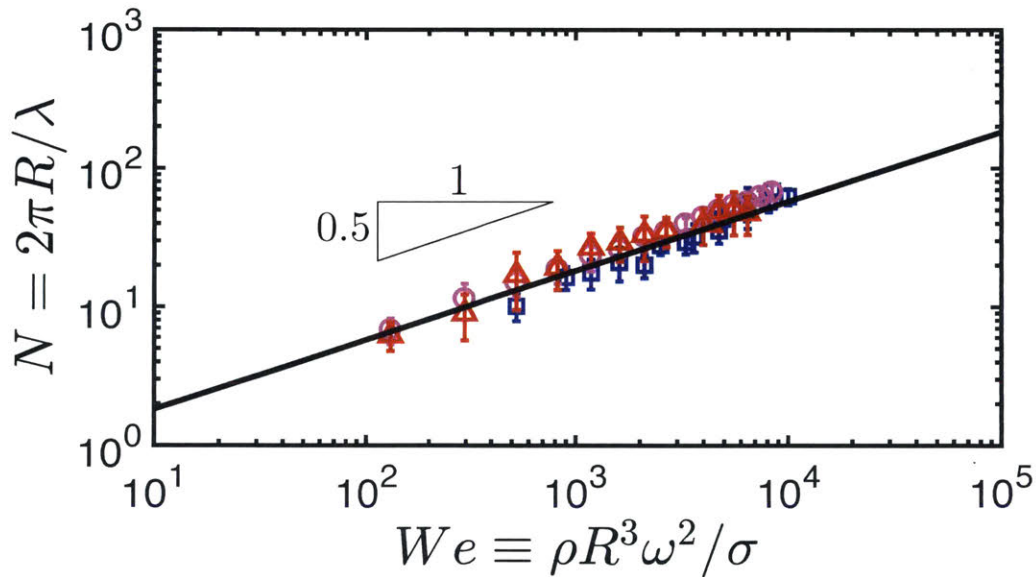


Figure 5-10: (color online). Number of ligaments N vs. the rotational Weber number $We \equiv \rho R^3 \omega^2 / \sigma$ plotted for three different silicone oils: (\square) $\{\nu = 7 \text{ cSt}, Oh_R = 0.01\}$, (\circ) $\{\nu = 100 \text{ cSt}, Oh_R = 0.14\}$, (\triangle) $\{\nu = 1000 \text{ cSt}, Oh_R = 1.4\}$. The solid black line shows the predictions of the Rayleigh-Taylor instability analysis $N = (1/\sqrt{3})\sqrt{We}$.

Figure 5-9 shows how the number of ligaments for silicone oil increases from (a) to (c) with increasing rotation rate. This qualitatively agrees with the theoretical

prediction in Equation (5.5). We further tested this analysis by measuring ligaments at different rotation rates for three different silicone oils ($\nu = 7, 100, 1000$ cSt). Figure 5-10 shows a summary of the measured data plotted in a dimensionless form. Number of ligaments are measured at different rotational Weber numbers. Results for all three viscous liquids agree very well with the prediction of the theoretical model (plotted as solid black line).

5.6.4 Geometry of a Single Ligament

In order to understand the kinematics of the flow we need to further investigate the geometry of individual ligaments. As shown in Figure 5-11, each fluid element leaves the cup with a tangential velocity component $V_\theta = R\omega$. Assuming a non-zero radial velocity at the departure point $V_r(r = R) = 0^1$, we can see that particles have simple straight path-lines that are plotted as dashed gray lines in Figure 5-11. As it is clear from this schematics, close to the cup the velocity of a fluid element is dominated by the tangential component V_θ , while the radial component V_r is negligible. However V_r gradually increases as the fluid element distance from the cup, becoming the dominant component of the velocity at large values of r/R . At any instant of time, the ligament profile given by the superposition of the current position of all the different fluid elements which have left the cup at different times in the past (similar to a "streak-line") forms a spiral-like shape. This geometrical shape is known as the "*involute of a circle*" and has been extensively studied in different fields of science. Some of the noteworthy examples include the pioneering work of Christiaan Huygens [244, 245] in his study of clocks for addressing the longitude problem in naval navigation and also the design of impulse-less transmission gears by Leonard Euler[246]. In Cartesian coordinates the involute of a circle has the following parametric equation:

$$\begin{aligned} x/R &= \cos \phi + \phi \sin \phi \\ y/R &= -(\sin \phi - \phi \cos \phi) \end{aligned} \tag{5.6}$$

¹Later on, we will relax this assumption.

where $\phi = \omega t$ is the rotation angle of the cup.

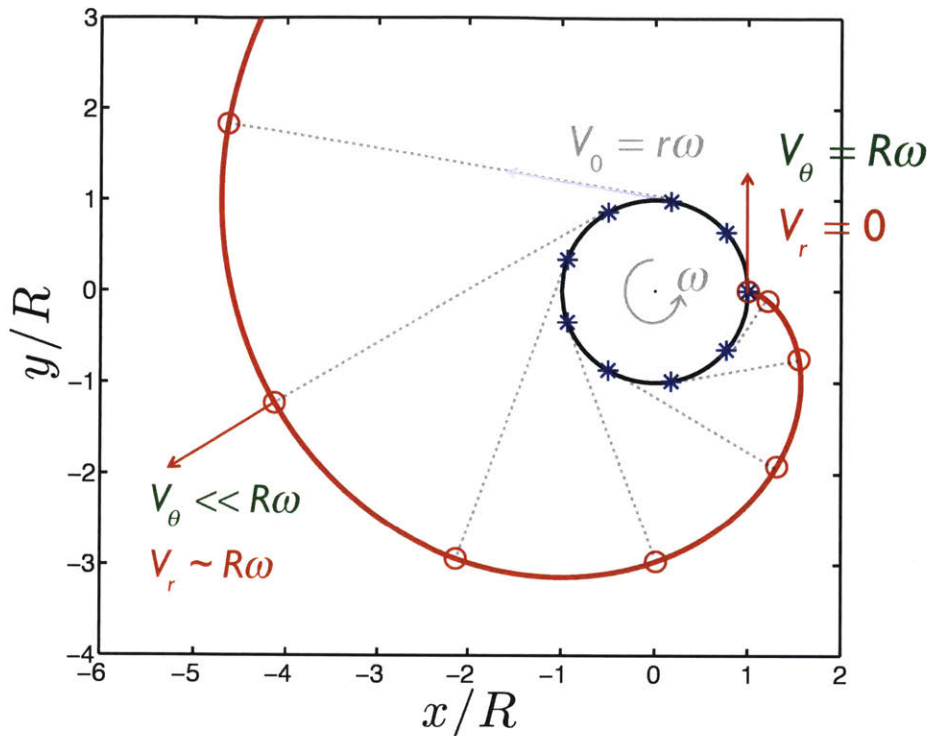


Figure 5-11: (color online). A simple schematics for the geometry of the ligaments formed in rotary atomization. The black line shows the rotating cup. Individual fluid elements ($*$) leave the rim of the cup, at different times, with a constant $V_0 = R\omega$ speed tangent to the cup and each follow a straight path-line (dashed gray lines) that is tangent to the circle at the corresponding point of departure. However, at the current time, the instantaneous positions of all different fluid elements (\circ) form a continuous spiral pattern (solid red line) that is known as the "involute of a circle".

Figure 5-12 shows the profile of ligaments that are formed in the rotary atomization of a viscous resin. Blue circles are a plot of the involute of a circle, described by Equation (5.6) which agree well with the observed spatial trajectory of individual ligaments. The agreement suggests that, even for complex fluids such as paints and resins, the kinematics of the flow is very close to the simple description that can be developed based on tangential departure of fluid elements from the rotating cup.

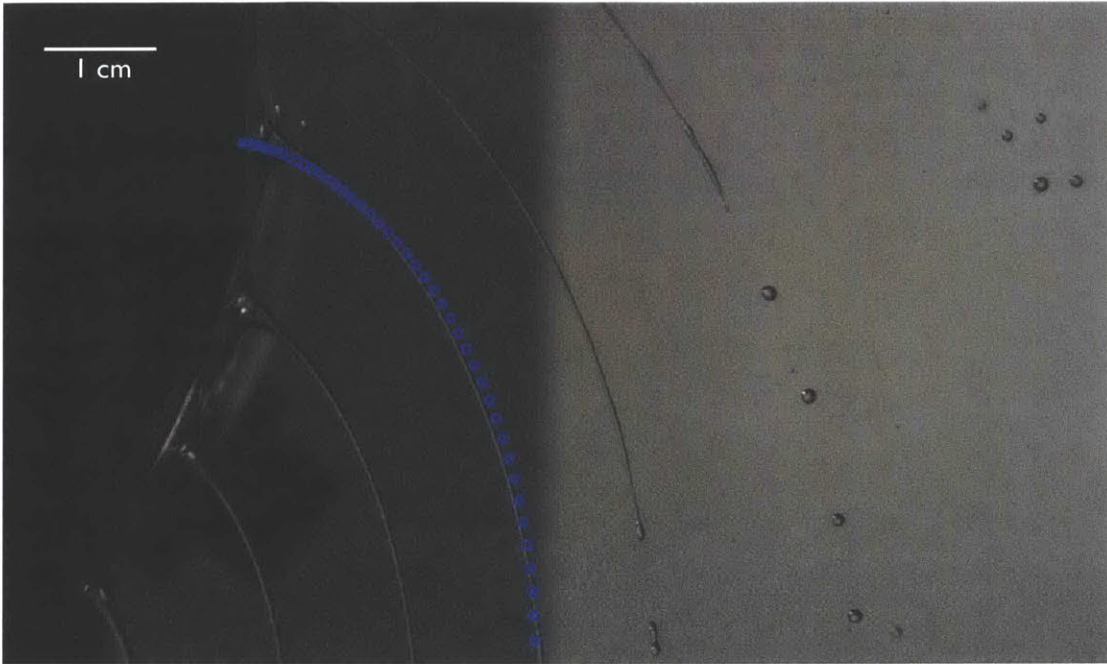


Figure 5-12: (color online). A comparison between the theoretical prediction for the involute of a circle based on Equation (5.6) (blue circles) and the experimental profile of a single ligament observed in the rotary atomization of an industrially used viscous resin (Resin B). The cup rotation rate is $\omega = 125.6$ rad/s and the Resin B with a zero shear rate viscosity of $\eta_0 = 100$ mPa.s is pumped into the cup by a volumetric rate of $Q = 60$ ml/min.

5.6.5 Kinematics of the Flow

To determine the kinematics of the flow such as spatial variations of the velocity profiles and involved strain-rates, we first assume that each fluid element leaves the cup with a zero radial velocity and tangential velocity equal to the speed of the cup surface. Figure 5-13 (a) shows a schematic of this model. We should emphasize that this simple kinematic model may not be apparent when we just look at the spiral-like geometry of a single ligament (Figure 5-13 (a)). The velocity of every fluid element on the spiral-like ligament is a constant vector with fixed magnitude $R\omega$. However, the corresponding values of the radial and the tangential components of the velocity vary as the fluid distances from the spinning cup. A simple geometrical projection provides the following:

$$\begin{aligned} V_r/R\omega &= \frac{\sqrt{r^2 - R^2}}{r} \\ V_\theta/R\omega &= \frac{R}{r} \end{aligned} \quad (5.7)$$

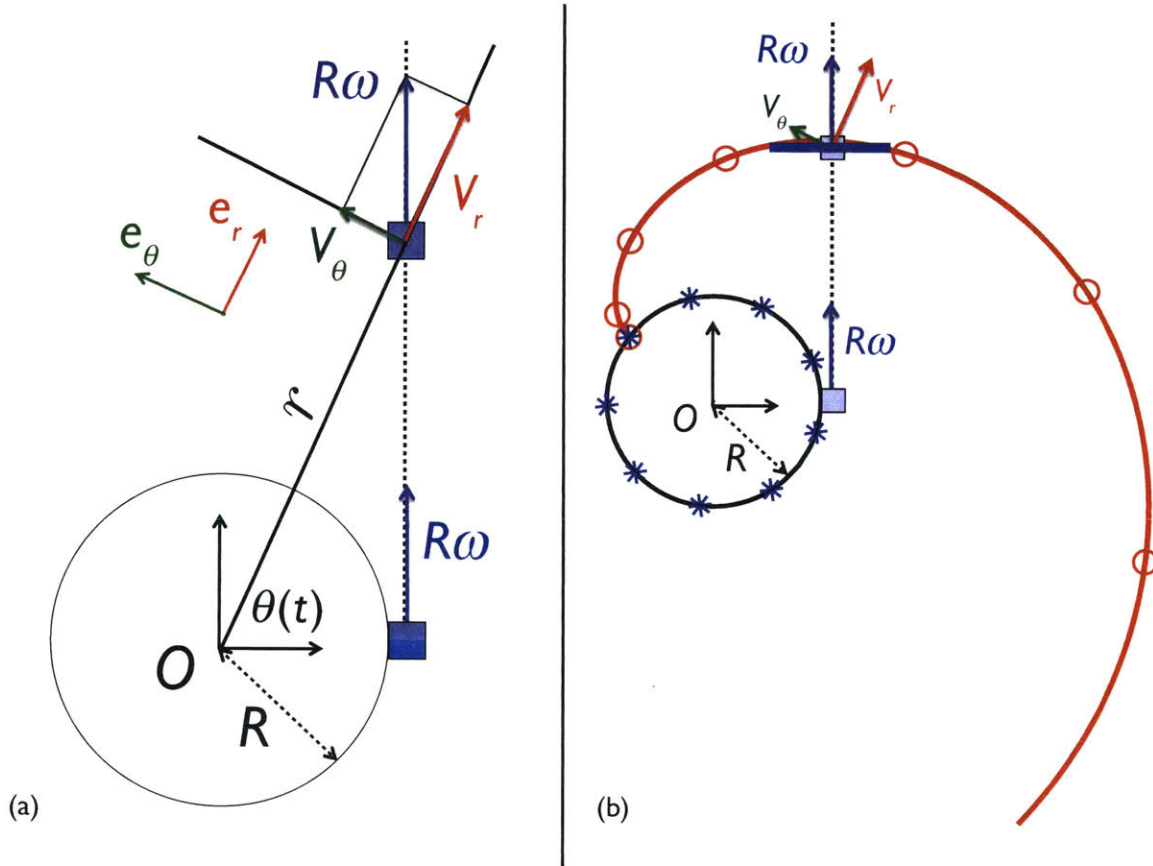


Figure 5-13: (color online). (a) Schematics of the kinematics of a single fluid element. The constant velocity vector of the fluid element with magnitude $R\omega$ is projected on the radial and tangential directions and at every moment, based on the radial position r , the corresponding velocity components V_r and V_θ can be calculated.

The calculated velocity field leads to an a flow field that is purely elongational along the symmetry axis of the ligament, with a strain rate $\dot{\epsilon}(r)$ that varies spatially with the following functional form:

$$\dot{\epsilon}(r)/\omega = \frac{\omega}{\sqrt{(r/R)^2 - 1}} \quad (5.8)$$

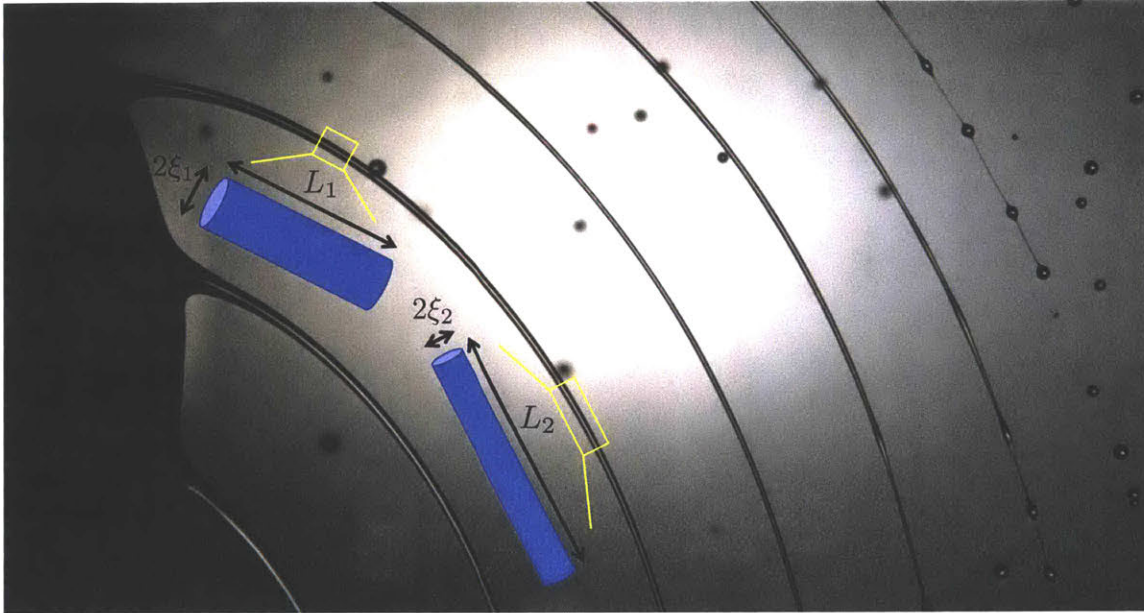


Figure 5-14: (color online). Illustration of the continuous elongation of fluid elements as they distance from the cup and move to larger radial positions. The profile of each ligament is the involute of a circle and fluid elements, on the involute, continue to stretch along the local symmetry axis of the ligament. In order to conserve the volume of liquid in the element, the axial stretch leads to the gradual thinning of the ligament. Thus, the local thickness of each ligament decreases with r/R .

In other words, as the fluid elements leave the cup, due to the flow kinematics they are continuously stretched along the local axis of the ligament. As shown in Figure 5-14, to conserve the volume of each fluid element, the elongation along the ligament (increase of L from L_1 to L_2) leads to a related contraction in thickness (decrease of ξ from ξ_1 to ξ_2). As shown by Equations (5.7) and (5.8), the rate of elongation decreases radially and becomes negligible at large values of r/R . This qualitatively agrees with the physical picture that changes in velocity components are much greater in regions close to the cup.

This simplified model, although qualitatively in agreement with our experimental observations, shows a singularity at the edge of the cup for $r/R = 1$. Figure 5-15 shows a plot of the velocity components and their corresponding spatial variation. It is clear that the radial velocity has an infinite tangent at the edge of the cup $\partial V_r / \partial r \rightarrow \infty$ as $r/R \rightarrow 1$. This singularity is also inherited in the strain field and

Equation (5.8) simply diverges at $r/R = 1$. This mathematical singularity is not physical and it rises from the assumption of zero radial velocity at the edge of the cup. The radial velocity at $r/R = 1$, despite being negligible compared to the tangential velocity, is non-zero. The unphysical assumption of $V_r(r/R = 1) = 0$ leads to the mathematical singularity and unphysical diverging values of stretch rate at regions very close to the cup.

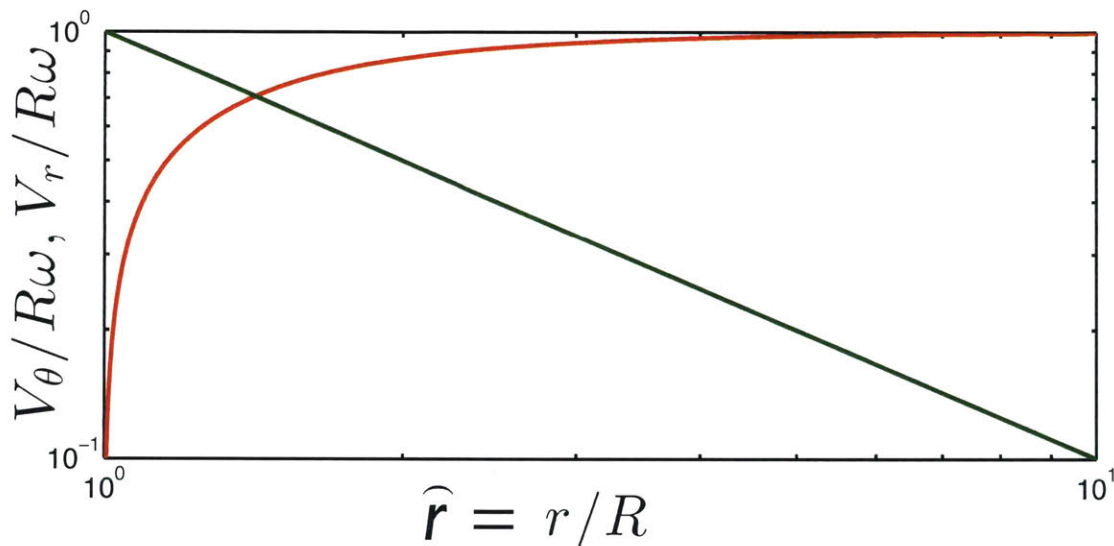


Figure 5-15: (color online). Dimensionless plot of the radial (red) and tangential (green) components of the velocity as a function of r/R .

To establish a more physical model and compensate for the nonzero radial velocity at the cup, we assume that fluid elements leave the cup with a velocity that has both radial and tangential components. As sketched in Figure 5-16, the tangential velocity is identical to the cup speed $R\omega$ while the radial velocity, $eR\omega$, is a fraction e of the cup speed. As we show in Figure 5-16, a simple geometrical trick allows us to find the kinematics of the fluid elements in this new model. Continuing the velocity vector of a single fluid element into the cup, we can find a smaller circle tangent to it. The kinematics of the flow in the new model is therefore identical to that of our previous model (Equations (5.7) and (5.8)) if we replace the original cup (solid black circle in Figure 5-16) with a smaller imaginary cup (dashed circle) that has a modified radius $R' = R/\sqrt{1+e^2}$ and rotation rate $\omega' = \omega(1+e^2)$.

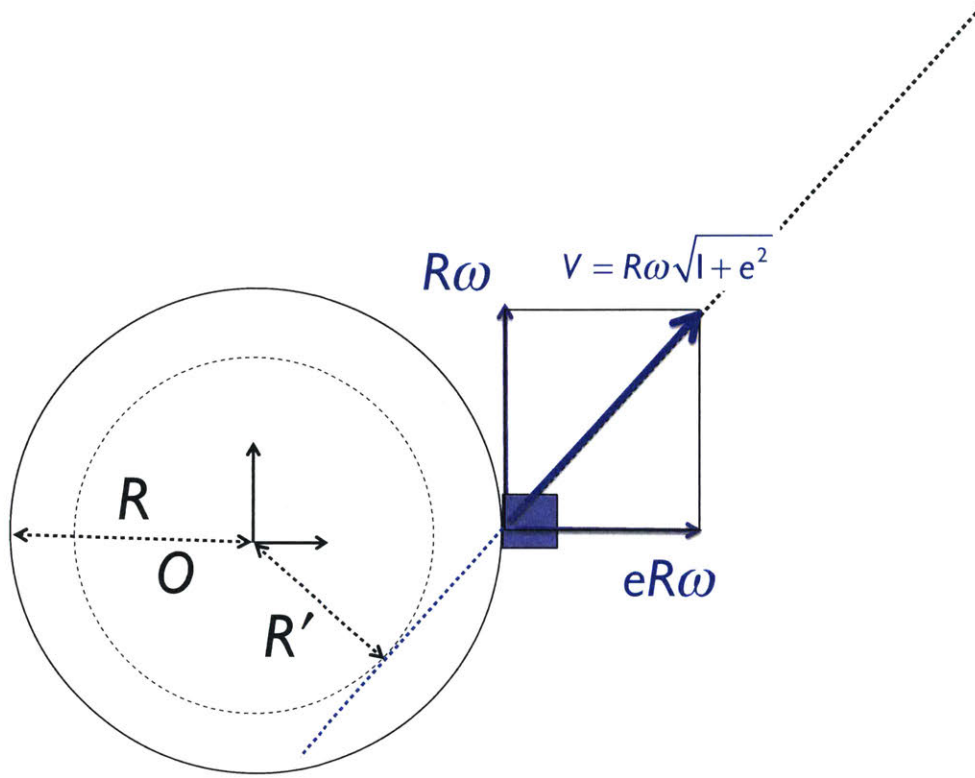


Figure 5-16: (color online). Illustration of the idea of the *virtual cup* (dashed circle). Fluid elements with non-zero radial velocity ($V_r(r = R) = eR\omega$) at the rim of the real cup (a cup with radius R and rotation rate ω), shown by the solid circle, follow a trajectory that is identical to the elements leaving a virtual cup with modified radius $R' = R/\sqrt{1 + e^2}$ and modified rotation rate $\omega' = \omega(1 + e^2)$, shown by the dashed circle.

Using this simple geometrical idea we can find the following equation for the spatial variation of velocity components:

$$\begin{aligned} V_r/R\omega &= \frac{\sqrt{r^2(1 + e^2) - R^2}}{r} \\ V_\theta/R\omega &= \frac{R}{r} \end{aligned} \quad (5.9)$$

and the following expression for the strain rate of the fluid elements:

$$\dot{\epsilon}(r)/\omega = \frac{\omega}{\sqrt{(r/R)^2(1 + e^2) - 1}}. \quad (5.10)$$

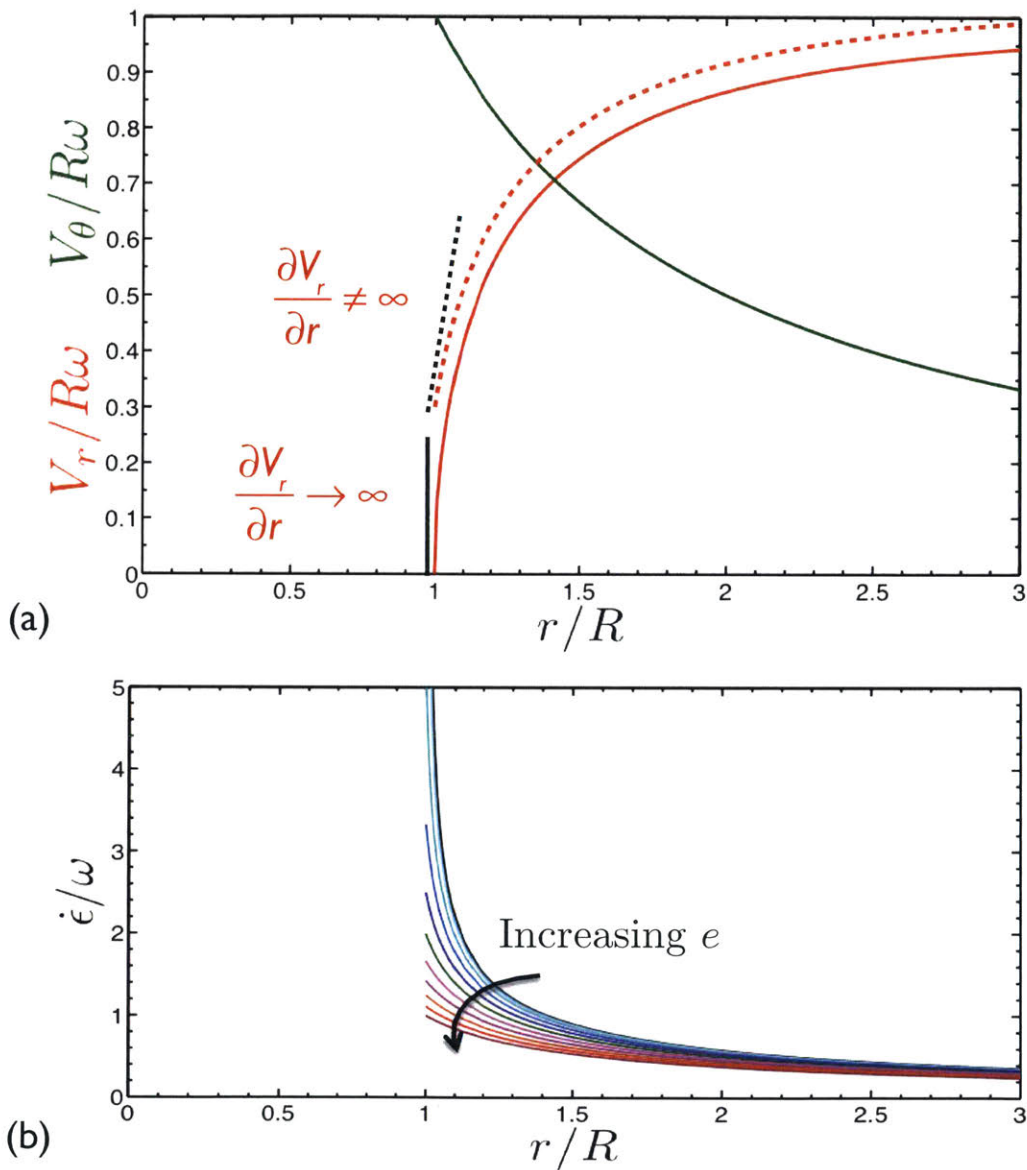


Figure 5-17: (color online). Theoretical predictions of the kinematics of the flow: (a) Dimensionless plot of the velocity components (red for V_r and green for V_θ) in the case of zero (solid lines for $e = V_r(0)/V_\theta(0) = 0$) and non-zero (dashed lines for $e = V_r(0)/V_\theta(0) = 0.3$) initial radial velocity. The profile for the tangential velocity is independent of e but the radial velocity is modified and with $0 < e$ the singularity of $\partial V_r/\partial r \rightarrow \infty$ is avoided. (b) Dimensionless profile of stretch rates for different values of e . The maximum stretch rate $\dot{\epsilon}_{max} = \omega/e$ occurs at the rim of the cup $r/R = 1$.

Figure 5-17 (a) and (b) shows a plot of the derived expression for, respectively, the velocity components in Equation (5.9) and the strain-rate field in Equation (5.10). As it can be seen, the singularity of $\partial V_r / \partial r \rightarrow \infty$ as $r/R \rightarrow 1$ is now resolved with the nonzero radial velocity assumption. The stretch rate profile also shows a finite maximum strain rate at the edge of the cup $\dot{\epsilon}_{max} = \omega/e$.

It is important to notice that the parameter e does not take an arbitrary non-zero value but indeed has a physical meaning and can be connected to certain physical parameters that are involved in this phenomenon. A simple mass balance for a control volume that contains the entire cup shows that the fluid delivered at a volumetric rate $Q_{in} = Q$ is balanced by a outflow at the edge of the cup with a rate of $Q_{out} = N\pi\xi_0^e R\omega$. Thus, this simple conservation of mass leads to a physical value for the parameter $e = (Q/R\omega)/(N\pi\xi_0^2)$ where N is the number of ligaments and ξ_0 is the radius of the ligament at the edge of the cup.

We can also write a differential equation for the spatial evolution of the ligament radius $\xi(r)$. By conserving the volume of the cylindrical element, we can connect the stretch rate of ligament axis to the radial contraction $\dot{\xi}(t')/\xi(t') = (-\dot{L}(t')/2L(t'))$ where $t' = (1/\omega')\sqrt{r^2/R'^2 - 1}$ is the the current lifetime of the fluid element which is measured from the virtual moment that the fluid element has left the imaginary cup (with radius R')². This result, along with the derived kinematics (Equation (5.10)) can be integrated with respect to r and leads to the following expression for the radial evolution of the ligament thickness:

$$\xi(r)/\xi_0 = \left(\frac{e}{\omega t'}\right)^{1/2} = \frac{e^{1/2}}{[(r/R')^2 - 1]^{1/4}}. \quad (5.11)$$

Figure 5-18 shows a plot of the measured ligament thickness at different radial positions. The measured values are compared with the predictions based on Equation (5.11). The agreement suggests that the ligaments follow the predicted kinematics with the resulting axial strain rate leading to a decrease in the ligament thickness.

²In other words $t' = 0$ is a virtual moment that never happened and the minimum value of t' for every fluid element is $t'_{min} = e/\omega$ which correspond to the time at which the element has left the edge of the actual cup $r = R$.

As the ligaments distance from the cup, the local stretch rate and thickness both decrease. The radial evolution of these parameters can help us to find the critical position and thickness at which ligaments become unstable due to the action of capillary forces.

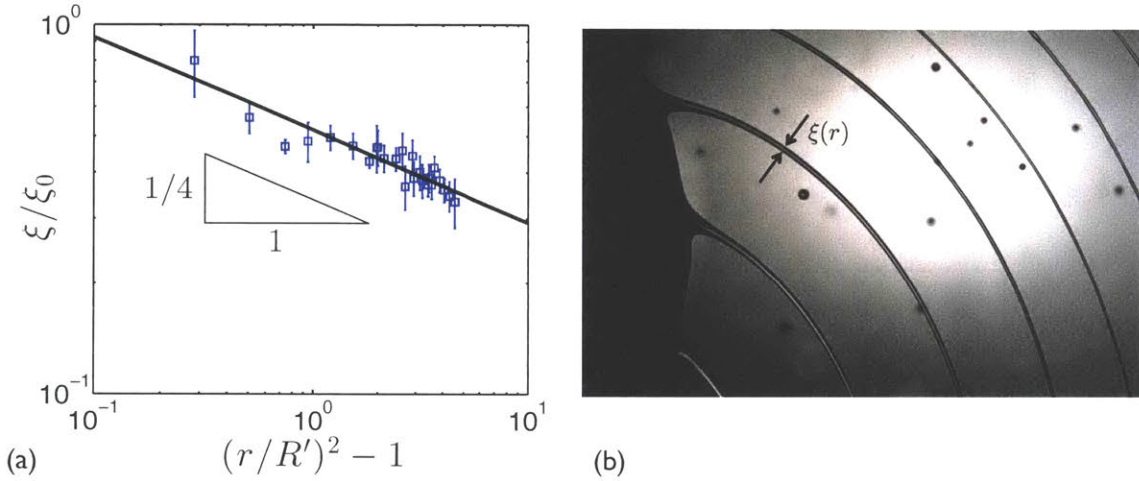


Figure 5-18: (color online). (a) Measured values of the ligament thickness at different radial positions (blue squares). The solid black line shows the prediction of the analytical model (Equation (5.11)). (b) The thickness profile for individual ligaments is measured from the snapshots that are taken by the high-speed camera.

5.6.6 Model for Predicting the Average Droplet Size

It is known that a cylindrical ligament can be stabilized by stretching if the rate of elongation is faster than the rate of capillary thinning [42, 62]. Applying this idea to rotary atomization means that the capillary waves on the ligaments become unstable and grow in amplitude when the local stretch rate $\dot{\epsilon}(r)$ is comparable to the local rate of capillary thinning $1/\sqrt{8\rho\xi^3(r)/\sigma}$. We can rewrite Equation (5.10) into a simple expression for the local stretch rate $\dot{\epsilon}(t') = 1/t'$. Thus, the ligaments become unstable when $t' \simeq \sqrt{8\rho\xi^3(r)/\sigma}$. Inserting this value for t' in Equation (5.11) then give us the following expression for the critical ligament thickness:

$$\xi_c/\xi_0 = \left(\frac{e}{\omega \sqrt{8\rho\xi_c^3(r)/\sigma}} \right)^{1/2}. \quad (5.12)$$

Replacing e with $Q/(N\pi\xi_0^2R\omega)$ and N with $\sqrt{\rho R^3\omega^2/3\sigma}$, we can solve for ξ_c :

$$\xi_c/R = \left[\left(\frac{\sqrt{3}}{\pi\sqrt{8}} \right) \left(\frac{Q/R^2}{R\omega} \right) \left(\frac{\sigma/R}{\rho R^2\omega^2} \right) \right]^{2/7}. \quad (5.13)$$

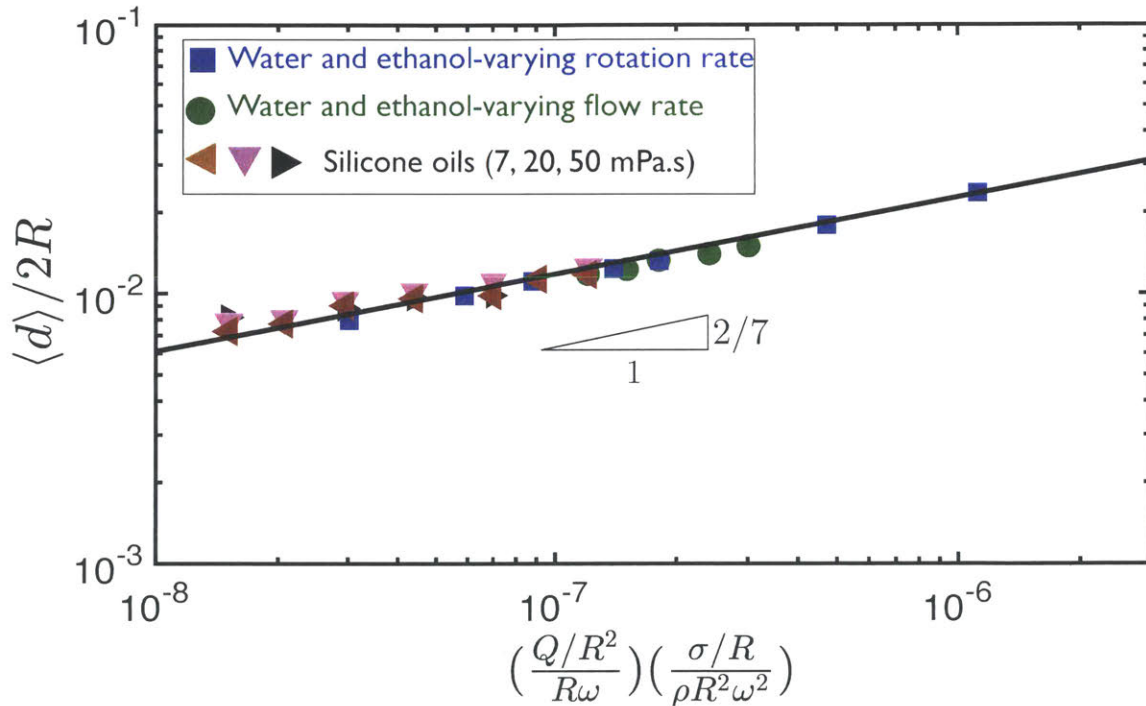


Figure 5-19: (color online). Measured average diameters for all the Newtonian test liquids normalized by the cup diameter $\langle d \rangle / 2R$ is plotted versus the suggested relevant dimensionless group $\Pi = \left(\frac{Q/R^2}{R\omega} \right) \left(\frac{\sigma/R}{\rho R^2\omega^2} \right)$. The solid black line corresponds to the analytical prediction from Equation (5.14).

This expression describes the critical ligament thickness at which capillary waves start to grow. Eggers and Villermaux [140] show that the radius of the generated drops from the capillary breakup of an unstable cylinder with a thickness ξ_c have an average radius $\langle d \rangle / 2 \simeq 1.88\xi_c$. Thus the result derived in Equation (5.13) can be

written in the following form as a prediction for the expected values of average droplet diameter in the rotary fragmentation:

$$\langle d \rangle / 2R = 1.18 \left[\left(\frac{Q/R^2}{R\omega} \right) \left(\frac{\sigma/R}{\rho R^2 \omega^2} \right) \right]^{2/7}. \quad (5.14)$$

Figure 5-19 shows a summary of measured average droplets for different Newtonian test liquids. Results from experiments done with three different silicone oils (7, 20, 50 cSt) and the Newtonian ethanol-water mixture are collected at different rotation and flow rates. It is clear that all the data collapse on a similar trend in this dimensionless plot. Prediction of the theoretical model (Equation (5.14)) is plotted as a black solid line and it shows a remarkable agreement with the measured values.

The suggested prediction is based on a series of simple physical assumptions and shows good agreement with experimental measurements. This theoretical model can explain certain power exponents that are reported in the literature as empirical correlations (see Figure 5-7). Furthermore, it can be a crucial element in new designs of rotary atomization setups.

It is noteworthy to mention that, after reaching the mentioned derivation, we noticed that a similar prediction had been reported in a completely separate and independent work from the Russian fluid mechanics community. Dunsikii and Nikitin [247] derived a final analytical expression in their work that is similar to Equation (5.14). However, this work has remained surprisingly forgotten and up to this date there are no citations of this work to the best of our knowledge. The reader, very much similar to us, may have not been familiar with the work of Dunsikii and Nikitin [247]. It should be emphasized that despite the fact that we independently established the model and checked it with our measurements, we can not claim being the first to derive this analytical prediction.

Aside from the average diameter, the resulting size distribution of the fragmentation process is of great importance in many different industries. In the following section we focus on different aspects of size distributions for Newtonian fluids.

5.7 Droplet Size Distributions for Newtonian Liquids

To study the drop size distribution in rotary atomization, we analyzed the recorded high-speed movies and collected a large population of droplets (~ 10000 droplets). Figure 5-20 shows the measured size distributions for the Newtonian ethanol-water mixture at two different rotational rates. At the higher rotation rate, ligaments were formed and the disintegration into droplets happened in the ligament formation regime (Figure 5-20 (a)). As it is clear from Figure 5-20 (b), for the lower rotation rate, the fragmentation process happened in the drop formation regime. Corresponding size distributions for the ligament and the drop formation regimes are plotted in Figure 5-20 (c) in magenta and gray symbols respectively. It is clear that the ligament formation regime leads to a narrower size distribution. This confirms the general idea that, due to the more organized and highly patterned geometry of ligaments, it is preferred to operate in this regime. A more precise look at the magenta data points in Figure 5-20 (c) can also verify the existence of a double peak in the measured size distributions.

The emergence of a double peak in the distributions was not observed in our measurements of sizes in air-assisted atomization (Chapter 4). However, a direct comparison of the measured size distributions between air-assisted and rotary fragmentation can give us a better sense about the benefits of rotary atomization. Figure 5-21 shows that, despite showing a double peak in the size histogram, rotary fragmentation generates a much narrower size distribution. A larger number of droplets are scattered around the average diameter and a much lower fraction are larger than the average size. In fact, it is 100 times more probable to find a droplet twice the average size in air-assisted fragmentation compared to rotary.

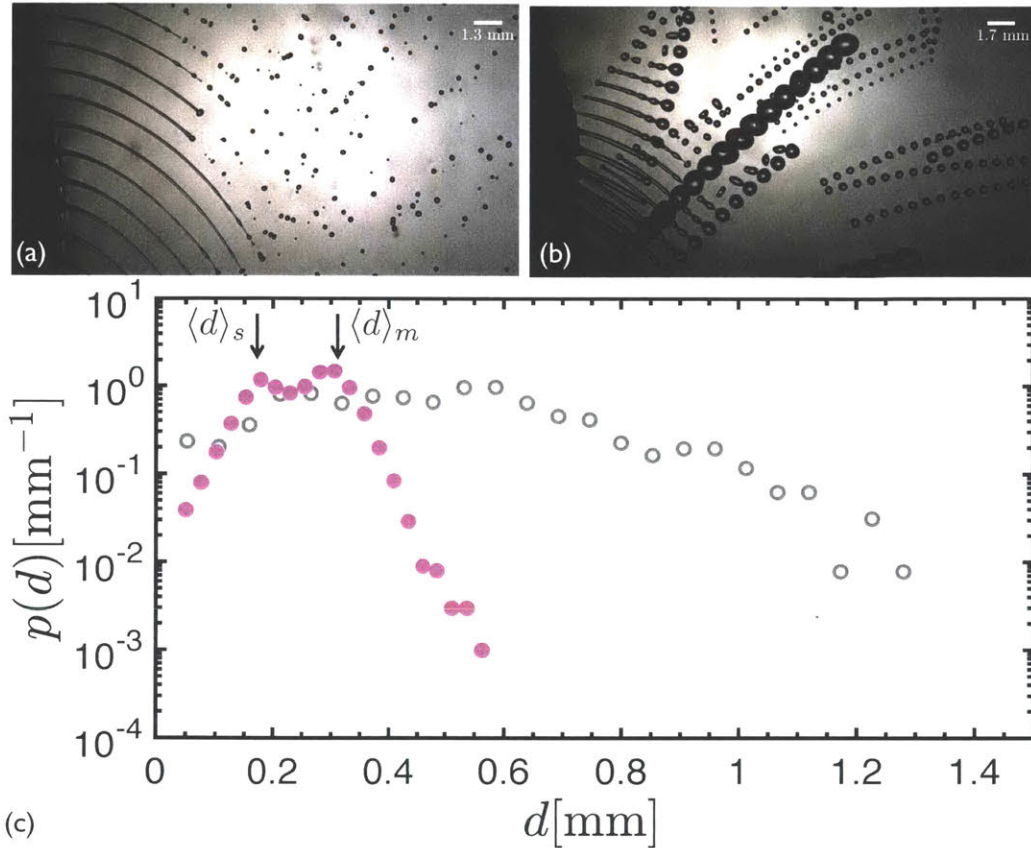


Figure 5-20: (color online). Rotary atomization for the Newtonian solvent (ethanol-water 90%-10% wt. mixture, $\eta = 1$ mPa.s, $Oh_R \equiv \eta/\sqrt{\rho R \sigma} = 1.45 \times 10^{-3}$) with the cup spinning at two different values of rotation rate: (a) Ligament formation regime at $\omega = 219.8$ rad/s, $We \equiv \rho R^3 \omega^2 / \sigma = 6442.8$. The image shows an overlay of two consecutive frames each $\Delta t = 0.4$ ms apart from each other. (b) Drop formation regime at $\omega = 78.5$ rad/s, $We \equiv \rho R^3 \omega^2 / \sigma = 821.8$. The image shows an overlay of sixteen consecutive frames each $\Delta t = 1$ ms apart from each other. (c) Corresponding droplet size distributions are plotted in magenta filled circles (\bullet) for the ligament formation regime (shown in (a)) and in open gray circles (\circ) for the drop formation regime (shown in (b)).

This encouraging result suggest that in rotary atomization there is a higher level of control on the geometry of the formed patterns. It also indicates that the initial corrugations on the ligaments are much smaller in amplitude. Indeed, the ligaments are relatively unperturbed and smooth until they become unstable, and even after that a set of smooth and periodic capillary waves appear on each ligament. This is very different from the violent nature of air-assisted atomization in which random fluctuations of high-speed air flow generates higher level of initial corrugation on the ligaments.

The benefits of rotary atomization highlights the importance of a better physical understanding of the associated fragmentation phenomenon. In particular, the appearance of a bimodal size-distribution has been previously reported in the literature [248, 249, 250, 49, 50], but a physical understanding of this outcome is still incomplete.

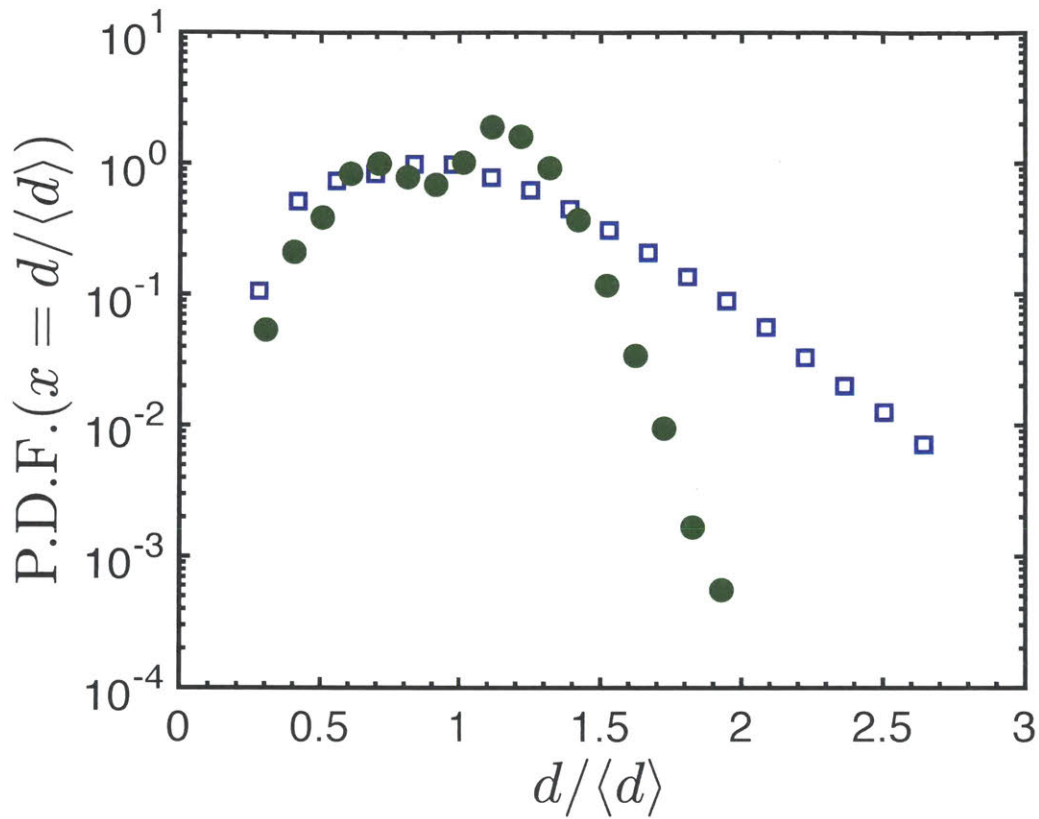


Figure 5-21: (color online). Droplet size distributions for the Newtonian solvents in rotary atomization (green filled circles \bullet) and the corresponding distribution in air-assisted atomization (blue open squared \square). The liquid atomized in the rotary test is the ethanol-water (90%-10% wt.) mixture ($Oh_R = 1.45 \times 10^{-3}$, $We = 13148.6$). The tested liquid in the air-assisted atomization is a water-glycerol (60%-40% wt.) mixture ($Oh_R = 4 \times 10^{-3}$, $We = \rho_{air} V_{air}^2 R / \sigma = 277$).

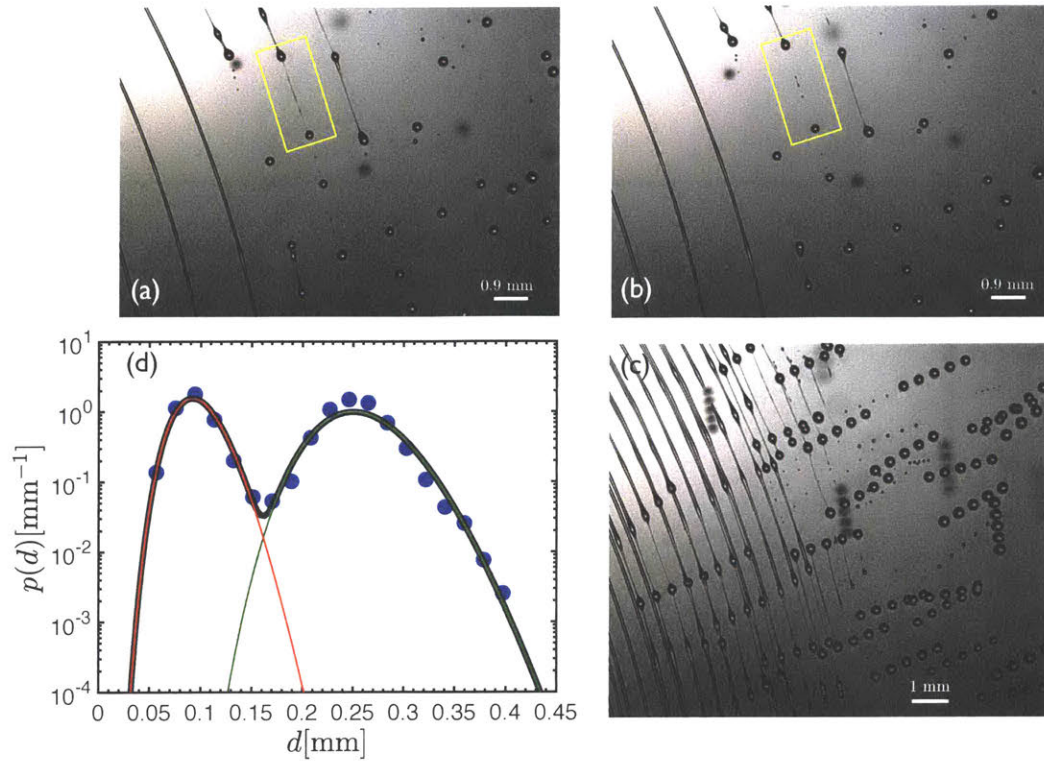


Figure 5-22: (color online). Formation of satellite droplets in the final stage of ligament breakup. The tested liquid is silicone oil ($\nu = 50$ cSt, $Oh_R = 7.3 \times 10^{-2}$) and it is delivered with a rate of $Q = 60$ ml/min into the cup that is rotating at $\omega = 125.6$ rad/s, $We = 2103.7$. (a) and (b): Two consecutive snapshots of the fragmentation with $\Delta t = 0.2$ ms between them. The viscous filament in the yellow box is clearly stretched before final pinch-off (see (a)) and after the pinch-off event the volume of the fluid in the filament retracts and forms one or two satellite droplets (see (b)). (c) An overlay of five consecutive frames, with $\Delta t = 0.2$ ms. It is clear to see that while the fragmentation process leads to a relatively mono-disperse group of *main* droplets, there also exists a considerable group of smaller *satellite* droplets. (d) Measured droplet size distributions for this case (blue bullets \bullet) shows the appearance of two separate peaks which correspond to the size of the main and the satellite droplets in the fragmentation event. The black solid line is the sum of two separate Gamma distributions, Equation (5.15) with $a_s = 0.39$, $\langle d \rangle_s = 0.09$ mm, $n_s \simeq 17$, (the red line) and $a_m = 0.61$, $\langle d \rangle_m = 0.24$ mm, $n_m \simeq 33$ (the green line).

In order to understand the bimodal distribution, we study the final ligament breakup stage in more detail. As it is shown in Figure 5-20(c) and (a), the two apparent peaks are related to the coexistence of both main drops (with average diameter $\langle d \rangle_m$) and satellite drops (with average diameter $\langle d \rangle_s$). Main droplets are the result of fragmentation of the ligaments as a consequence of amplifying capillary wave perturbations. On a ligament, capillary waves grow in amplitude and two neighboring peaks form two main droplets. However, the connecting filament between the two main drops does not entirely empty its volume into them and at the pinch off point it forms an elongated filament that goes through a secondary fragmentation process. Satellite droplets are the consequence of this secondary fragmentation process that happens at a smaller scale.

Figure 5-22 (a), (b) and (c) show a sequence of images for the satellite formation in the case of silicone oil ($\nu = 50$ cSt). We can clearly see that while the primary fragmentation leads to the appearance of the main droplets, the breakup of the connecting filaments between each pair of main droplets sets the secondary fragmentation on a smaller length scale. This can be quantitatively analyzed by studying the measured size distributions and then comparing them to the behavior of Gamma distributions. Gamma distributions are the asymptotic distributions in a coalescence-based fragmentation scenario, suggested by Villermaux and coworkers [13] and validated with experiments in various different studies of liquid fragmentation [251, 42, 54, 66, 11, 8, 62, 69, 252, 253]. In fact, in several works [8, 62], Villermaux and coworkers have observed similar cases in which both a primary and a secondary fragmentation process happen simultaneously giving rise to bimodality in the final size distributions. Villermaux and Bossa [8] suggest that a linear superposition of two separate Gamma distributions is enough to capture the phenomena in detail:

$$p(d) = \frac{a_s}{\langle d \rangle_s} \Gamma(n_s, x = d/\langle d \rangle_s) + \frac{a_m}{\langle d \rangle_m} \Gamma(n_m, x = d/\langle d \rangle_m). \quad (5.15)$$

The first Gamma distribution describes the secondary fragmentation process, which

happens at smaller scales, and the second distribution describes the broadness of main droplets in the primary fragmentation.

Figure 5-22(c) shows a fit of the proposed model (Equation (5.15)) to the measured size distributions. The agreement suggests that rotary atomization is indeed characterized by the superposition of a main and a secondary disintegration event which happens at two different scales.

To further investigate this, we recorded all the sizes for four different Newtonian test liquids, each of them being atomized at different rotation rates. Figure 5-23 shows a summary of the data for the ethanol-water mixture and three different silicone oils (7, 20, 50 cSt). For each liquid the measured sizes at different rotation rates are normalized by the main droplet average diameter ($\langle d \rangle_m$). The self-similarity between the superposed distributions suggests that the rotation rate decreases the average diameter of both main and satellite droplets almost equally. In other words, the nature of the two fragmentation processes does not change with the rotation rate as long as rotary atomization happens in the ligament formation regime. Furthermore, we can clearly see that the fits of the theoretical model (Equation 5.15) can capture the details of the size distributions for all the tested liquids at different rotation rate. We can also see that, as we increase the viscosity of the test liquid, the peak related to the satellite droplet shifts to smaller ratios but the number of sizes around the satellite droplet increases with viscosity. This suggests that for more viscous liquids, longer and thinner filaments form between the main droplets leading to smaller and higher number of satellite droplets. We will quantify this by a simple model in the following sections.

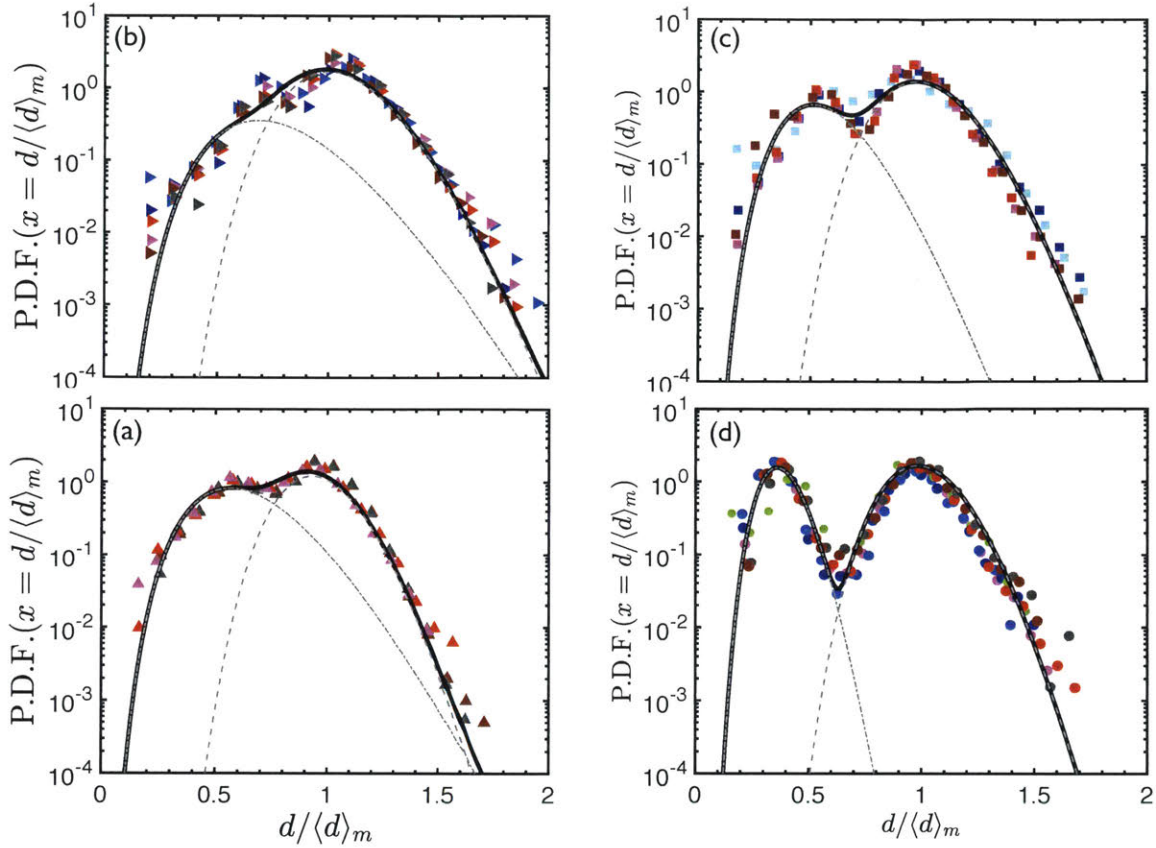


Figure 5-23: (color online). Droplet size distributions for the rotary atomization of Newtonian test liquids: (a) Ethanol-water (90%-10%wt., $Oh_R = 1.45 \times 10^{-3}$) mixture; measured size distributions at four different rotation rates $\{We = 6442.8\}$ (\blacktriangle), $\{We = 8415.1\}$ (\blacktriangle), $\{We = 10650.3\}$ (\blacktriangle) and $\{We = 13148.6\}$ (\blacktriangle). (b) Silicone oil ($\nu = 7$ cSt, $Oh_R = 1.02 \times 10^{-2}$); measured size distributions at six different rotation rates $\{We = 3287.1\}$ (\blacktriangleright), $\{We = 4735.5\}$ (\blacktriangleright), $\{We = 6442.8\}$ (\blacktriangleright), $\{We = 8415.1\}$ (\blacktriangleright), $\{We = 10650.3\}$ (\blacktriangleright) and $\{We = 13148.6\}$ (\blacktriangleright). (c) Silicone oil ($\nu = 20$ cSt, $Oh_R = 2.90 \times 10^{-2}$); measured size distributions at five different rotation rates $\{We = 2103.8\}$ (\blacksquare), $\{We = 4735.5\}$ (\blacksquare), $\{We = 6442.8\}$ (\blacksquare), $\{We = 8415.1\}$ (\blacksquare) and $\{We = 10650.3\}$ (\blacksquare). (d) Silicone oil ($\nu = 50$ cSt, $Oh_R = 7.25 \times 10^{-2}$); measured size distributions at seven different rotation rates $\{We = 1183.4\}$ (\bullet), $\{We = 3287.1\}$ (\bullet), $\{We = 4735.5\}$ (\bullet), $\{We = 6442.8\}$ (\bullet), $\{We = 8415.1\}$ (\bullet), $\{We = 10650.3\}$ (\bullet) and $\{We = 13148.6\}$ (\bullet). For each Newtonian liquid, we can see that normalizing the droplet sizes with the size of the main droplet $\langle d \rangle_m$ shifts all the distributions to a single curve. Black solid lines are the corresponding fits, each of which is a summation of two Gamma distributions. Each distribution is a superposition of a Gamma fit around the satellite droplet size $\langle d \rangle_s$ (-.-) and another fit around the main droplet size $\langle d \rangle_m$ (- -). Fitting Equation (5.15) to the data, the following fit parameters are extracted: $\{\langle d \rangle_s / \langle d \rangle_m, a_s, n_s, a_m, n_m\} =$ (a) $\{0.76, 0.13, 12, 0.87, 18\}$, (b) $\{0.72, 0.06, 7, 0.94, 29\}$, (c) $\{0.58, 0.30, 15, 0.70, 60\}$ and (d) $\{0.38, 0.39, 17, 0.61, 33\}$.

5.8 Rotary Atomization of Viscoelastic Liquids

Knowing that dilute viscoelastic liquids, similar to viscous Newtonian fluids, can form long and thin filaments, we investigated the behavior of viscoelastic fluids. As discussed before, many industrial products have similarities to PEO solutions in their elongational properties. In this section we study the performance of these class of complex fluid in rotary atomization.

As shown in chapter 2 and by Keshavarz *et al.* [238], addition of small amounts of polymer does not affect the shear viscosity in the dilute regime compared to its drastic increases of elongational viscosity. Thus, these dilute polymeric solutions show an almost Newtonian-like behavior in shear but resist strongly against elongational deformations.

Figure 5-24 shows that even adding a minute amount of PEO 1M M_w to the solvent can change substantially the dynamics of fragmentation. While the main droplet average diameter for both the pure solvent and for the PEO solution is almost the same size, appearance of extremely stretched and elongated filaments between main droplets for the viscoelastic fluid is in high contrast with the process undergone by the ethanol-water solvent mixture. In order to quantify our results, we measured both the average droplet diameters and the corresponding droplet size distributions for all three viscoelastic test liquids tabulated in 5.2 .

5.8.1 Average Droplet Size

Figure 5-25 shows a summary of the average droplet diameters for the three PEO solutions. It is clear that the average diameters for all viscoelastic solutions are very close to the corresponding values for the Newtonian solvent. In fact, the data collapse on the same dimensionless plot and agree well with the prediction of the previously proposed model (5.14).

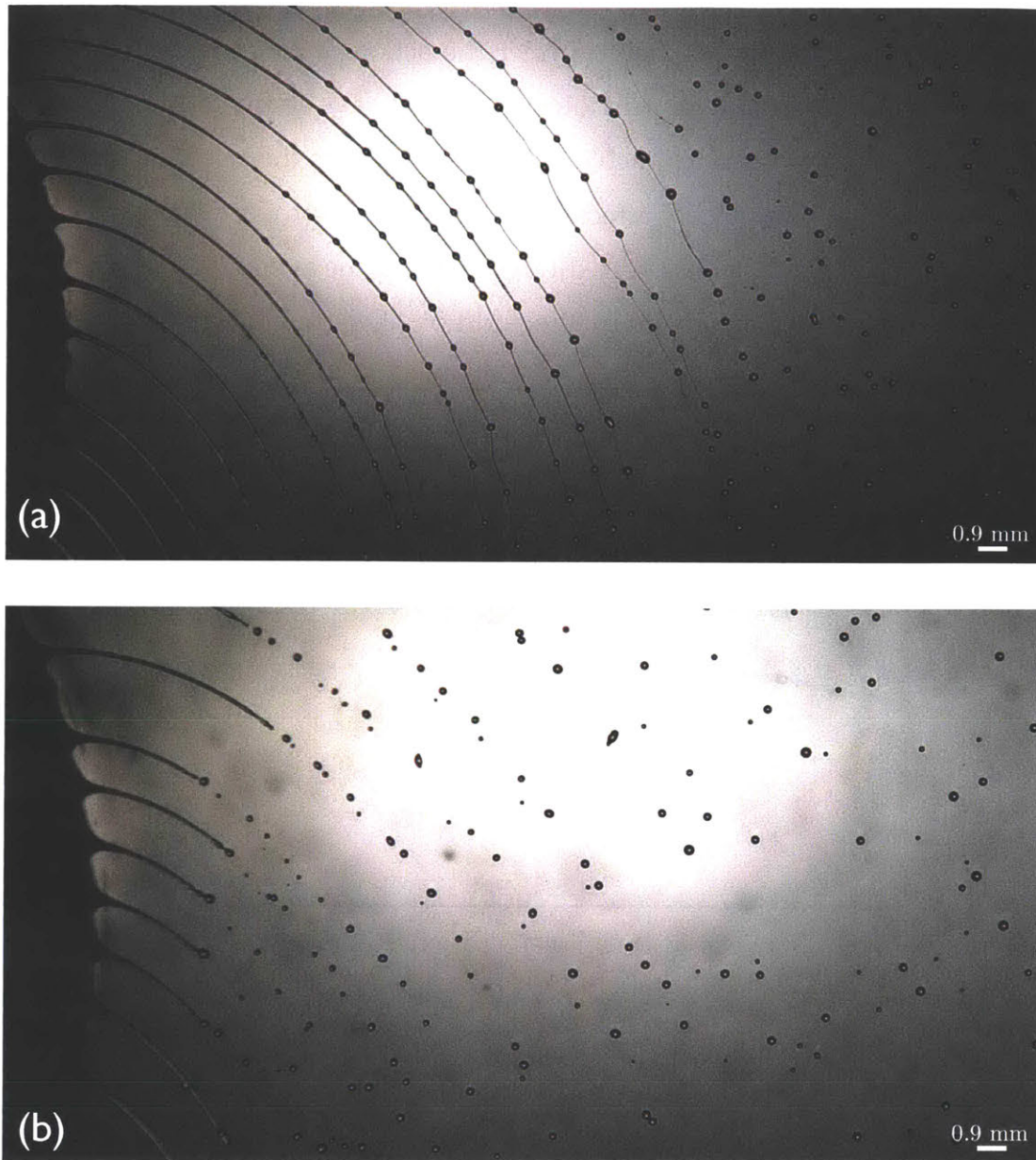


Figure 5-24: (color online). Visualization of the fragmentation process with the cup rotating at $\omega = 251.2$ rad/s and the test liquids delivered at a rate of $Q = 60$ ml/min. Images show the rotary atomization for (a) the viscoelastic fluid (PEO 1M M_w , 0.01% wt. in the ethanol-water solvent) and (b) The ethanol-water solvent (90%-10% wt.). After the drops are formed on the ligaments, the connecting Newtonian filaments between the solvent drops breakup very fast. However, due to the enhanced elongational viscosity, the viscoelastic filaments stretch continuously and resist the pinch-off, leading to the formation of thinner stringy filaments.

This suggests that the critical thickness of the ligaments ξ_c is unaffected by viscoelasticity. The value of ξ_c is set primarily by the linear stability analysis of the ligament ejecting from the cup under the action of centripetal and capillary forces. This is consistent with previous works that have shown that both the critical growth rate and the critical wavelength derived from the stability analysis of a viscoelastic thread are weakly affected by elongational properties [238, 147]. This explains the fact that, for these very dilute solutions, the average measured droplet diameters are almost unchanged by the addition of viscoelasticity.

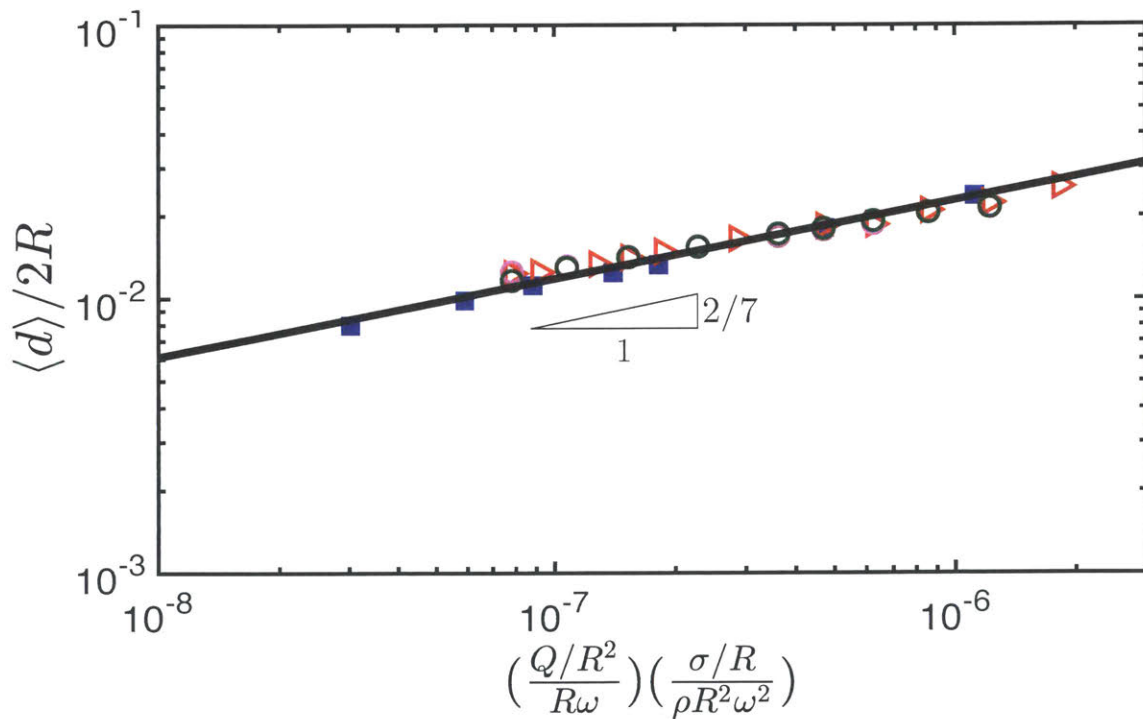


Figure 5-25: (color online). Measured average diameters for the Newtonian solvent (■) and all the viscoelastic test liquids: PEO 300K M_w 0.01% wt. (○), PEO 300K M_w 0.05% wt. (◦) and PEO 1M M_w 0.01% wt. (▷). Results are normalized by the cup diameter $\langle d \rangle / 2R$ and plotted versus the suggested relevant dimensionless group $\Pi = \left(\frac{Q/R^2}{R\omega} \right) \left(\frac{\sigma/R}{\rho R^2 \omega^2} \right)$. The solid black line corresponds to the analytical prediction from Equation (5.14).

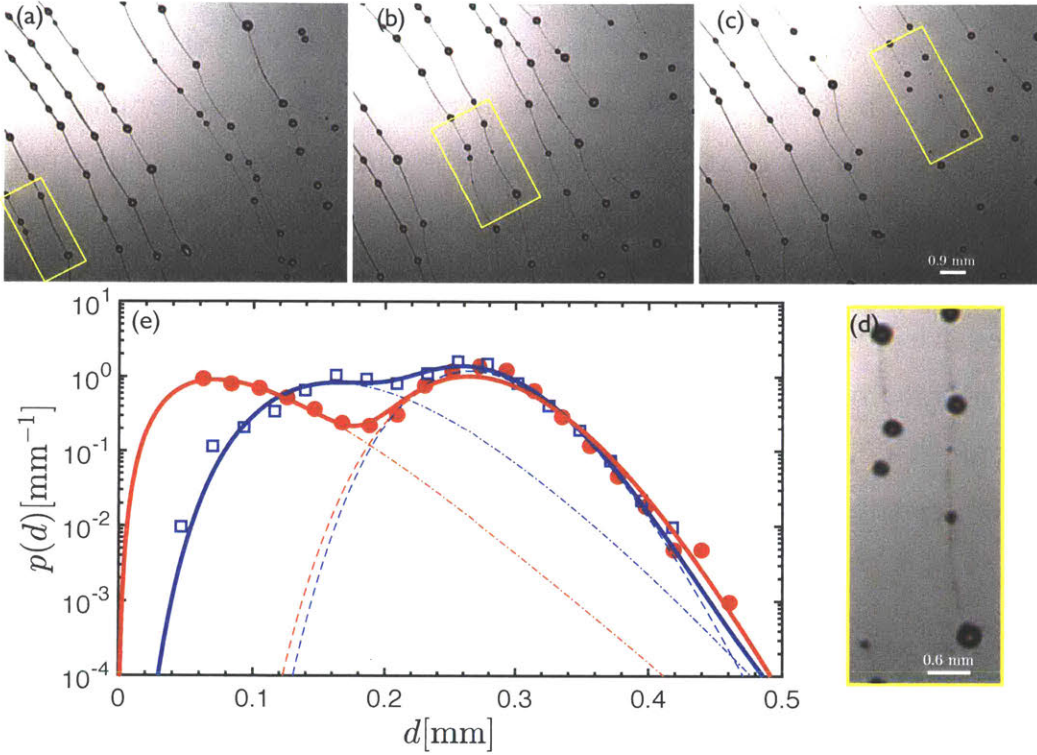


Figure 5-26: (color online). Dynamics of the viscoelastic filaments during the fragmentation process for the PEO 1M M_w 0.01% wt. solution ($Oh_R = 1.45 \times 10^{-3}$, $De_R = 5.0 \times 10^{-3}$). (a), (b) and (c) are taken with $\Delta t = 1$ ms spacing in time. As shown by the yellow box, two typical droplets are connected to each other by an elongated filament that resists the pinch off and finally transforms to a very thin cylindrical volume of fluid. (d) After the filament pinches off from the connecting drops, it forms few very small satellite droplets. (e) The corresponding size distribution are shown by red filled circles (\bullet) and are compared to the corresponding size distributions for the Newtonian solvent (\square). The solid lines are the fits of Gamma distributions. Each fit is a superposition of two Gamma distributions, one for the smaller sizes that are scattered around the satellite diameter $\langle d \rangle_s$ (-.-) and another for the larger sizes around the main droplet diameter $\langle d \rangle_m$ (- -), Equation (5.15). Parameters extracted from the fits are the following: $a_s = 0.13$, $\langle d \rangle_s = 0.21$ mm, $n_s \simeq 12$, $a_m = 0.87$, $\langle d \rangle_m = 0.27$ mm, $n_m \simeq 18$ for the Newtonian solvent and $a_s = 0.49$, $\langle d \rangle_s = 0.09$ mm, $n_s \simeq 4$, $a_m = 0.51$, $\langle d \rangle_m = 0.27$ mm, $n_m \simeq 40$ for the viscoelastic solution.

5.8.2 Droplet Size Distributions for Viscoelastic Solutions

The droplet size distributions for each viscoelastic liquid was measured at different rotation rates. Figure 5-26 shows one of these distributions for the 1M M_w PEO solution. As discussed in the previous section, the average droplet diameter is almost unchanged by the addition of viscoelasticity but the corresponding size distribution shows a clear difference at lower sizes close to the satellite diameter $d \sim \langle d \rangle_s$. Compared to the Newtonian solvent, the viscoelastic solution shows an amplified peak at lower sizes that has shifted to smaller values of $\langle d \rangle_s / \langle d \rangle_m$. It is interesting to note that, despite this clear difference, the behavior of the two size distributions is almost identical at larger sizes $d \sim \langle d \rangle_m$. This again shows that the main droplet size and its corresponding fragmentation dynamics is set by the linear stability of the ligament which is unaffected by viscoelasticity. However, the enhanced non-linear elongational properties of the viscoelastic solutions change the dynamics of the filaments formed between the main droplets and delay their corresponding breakup time. This effect is magnified in the secondary fragmentation and changes the size and the number of the formed satellited droplets. A superposition of two separate Gamma distributions (Equation 5.15) can be again fitted to the data and the resulting fit is plotted with a solid red line.

Figures 5-27(a), (b), and (c) show the distribution for the three different PEO solutions. For each liquid, the normalized droplet distribution at different rotation rates (indicated by different colors on each plot) superpose on a similar trend suggesting that increasing the rotation rate only shifts the average diameter for both the main and satellite droplets to smaller values. Comparing 5-27(a), (b) and (c) it is also clear that, with increasing viscoelasticity, the lower peak in the size distributions shifts to smaller values of $\langle d \rangle_s / \langle d \rangle_m$. Figure 5-27 (d) provides a comparison between the observed viscoelastic size distributions and the corresponding fit for the Newtonian solvent. For the PEO 300K M_w 0.01% solution the droplet size distribution is almost identical to the corresponding histogram for the solvent. The PEO 300K M_w 0.05% and PEO 1M M_w 0.01% solutions show a different behav-

ior which is specifically pronounced around smaller sizes $d \sim \langle d \rangle_s$. Fits of the Gamma distributions to the data for the PEO 1M M_w 0.01% solution gives $n_s = 4$ in the secondary fragmentation. This suggests that the filaments connecting the main droplets have become corrugated due to the nonlinear effect of viscoelasticity which is in agreement with our results in chapter 4 and published literature [253]. The zoomed view of the stretch filament in Figure 5-26(d) shows the appearance of relatively big beads that are connected to each other by tiny strings. This beads-on-a-string structures increase the level of the geometrical corrugations and result in a broader size distribution around $\langle d \rangle_s$.

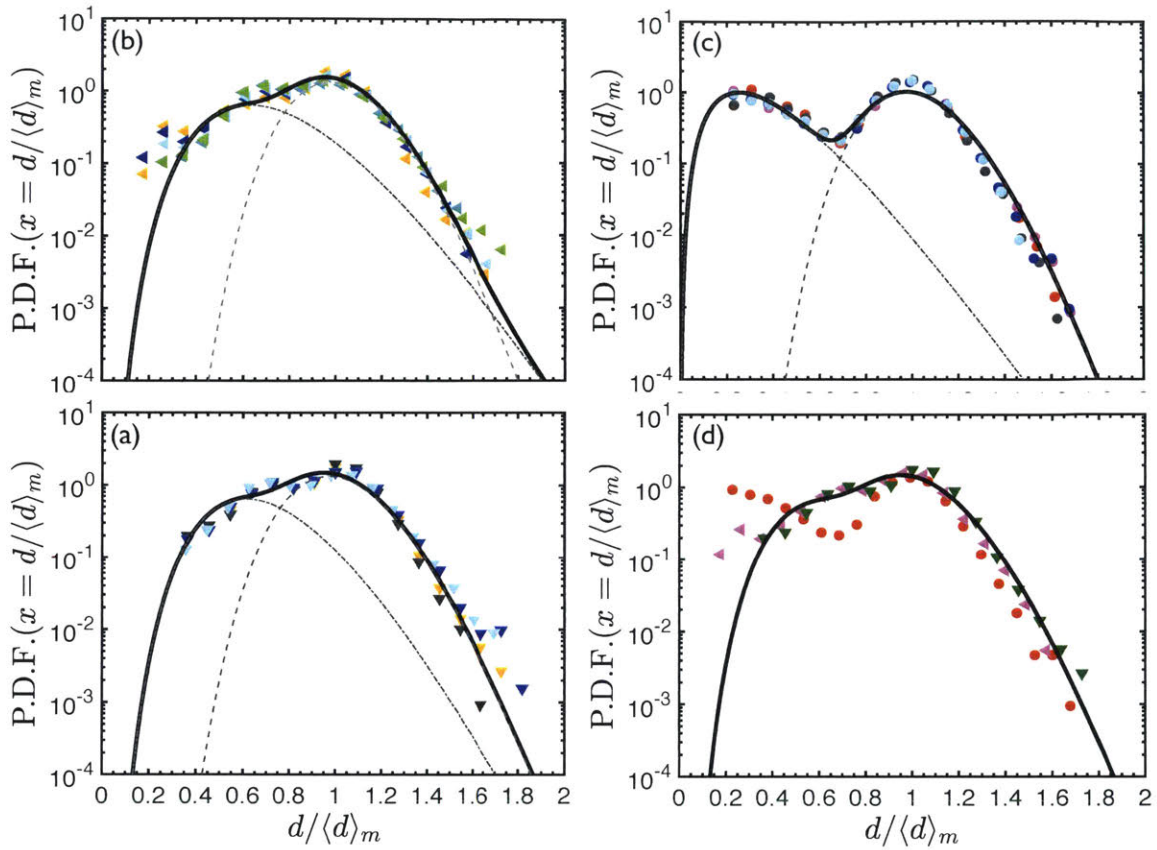


Figure 5-27: (color online). Droplet size distributions for the rotary atomization of viscoelastic liquids: (a) PEO 300K M_w 0.01% wt. solution ($Oh_R = 1.45 \times 10^{-3}$, $De_R = 0.4 \times 10^{-3}$); measured size distributions at four different rotation rates $\{We = 6442.8\}$ (\blacktriangledown), $\{We = 8415.1\}$ (\blacktriangledown), $\{We = 10650.3\}$ (\blacktriangledown) and $\{We = 13148.6\}$ (\blacktriangledown). (b) PEO 300K M_w 0.05% wt. solution ($Oh_R = 1.45 \times 10^{-3}$, $De_R = 0.6 \times 10^{-3}$); measured size distributions at five different rotation rates $\{We = 3977.4\}$ (\blacktriangleleft), $\{We = 4735.5\}$ (\blacktriangleleft), $\{We = 6442.8\}$ (\blacktriangleleft), $\{We = 8415.1\}$ (\blacktriangleleft), and $\{We = 10650.3\}$ (\blacktriangleleft). (c) PEO 1M M_w 0.01% wt. solution ($Oh_R = 1.45 \times 10^{-3}$, $De_R = 5.0 \times 10^{-3}$); measured size distributions at five different rotation rates $\{We = 7396.1\}$ (\bullet), $\{We = 8415.1\}$ (\bullet), $\{We = 9499.9\}$ (\bullet), $\{We = 11866.6\}$ (\bullet) and $\{We = 13148.6\}$ (\bullet). Black solid lines are the corresponding fits, each of which is a summation of two Gamma distributions. Each distribution is a superposition of a Gamma fit around the satellite droplet size $\langle d \rangle_s$ (- -) and another fit around the main droplet size $\langle d \rangle_m$ (- -). Fitting Equation (5.15) to the data, the following fit parameters are extracted: $\{\langle d \rangle_s / \langle d \rangle_m, a_s, n_s, a_m, n_m\} =$ (a) $\{0.70, 0.13, 12, 0.87, 18\}$, (b) $\{0.67, 0.39, 11, 0.61, 42\}$ and (c) $\{0.34, 0.49, 4, 0.51, 40\}$. (d) A comparison between the size distributions of different viscoelastic liquids atomized at a fixed rotation rate $\{We = 8415.1\}$: PEO 300K M_w 0.01% wt. (\blacktriangledown), PEO 300K M_w 0.05% wt. (\blacktriangleleft) and PEO 1M M_w 0.01% wt. (\bullet). The solid black line is the fit for the size distributions of the Newtonian solvent (Figure 5-22(a)).

5.9 Model for Predicting the Size of Satellite Droplets

To understand the dynamics of the secondary fragmentation process, we propose a toy model that enables us to predict the size ratio between the satellite and the main droplet. We assume that, when capillary waves appear on the main ligament, the filament that is connecting two neighboring wave peaks is a cylinder with thickness $2h_0$ and length L_0 . As the waves grow, the two peaks form the main droplets while the connecting filament keeps stretching until at least one of the necks between the filament and the drops pinches off. Assuming that the volume of the filament is constant within this process, we can write the following:

$$l(t)h(t)^2 = l_0h_0^2 \rightarrow \frac{h_0}{h(t)} = \sqrt{\frac{l(t)}{l_0}} = \sqrt{1 + \dot{\epsilon}_c t} \quad (5.16)$$

where $\dot{\epsilon}_c = 1/\sqrt{8\rho\xi_c^3/\sigma}$ is the critical capillary stretch rate at which the capillary waves start to emerge. We also know that the ratio of the main to the satellite droplet diameter $\langle d \rangle_m / \langle d \rangle_s = h_0 / h(t_{pinch-off})$ where $t_{pinch-off}$ is the time at which the connecting necks between the filament and the main drops pinch off. Based on suggested scalings in the literature[140], we assume that the pinch off time is delayed by either viscous or elastic stresses. For viscous Newtonian solutions $t_{pinch-off} = \sqrt{8\rho\xi_c^3/\sigma}(1+6Oh_{\xi_c})$ [140] and for viscoelastic liquids we assume $t_{pinch-off} = \sqrt{8\rho\xi_c^3/\sigma} + (3/2)\tau_E$ [238, 79] where $(3/2)\tau_E$ is the inverse of the elongational rate for a viscoelastic filament undergoing elasto-capillary thinning. Plugging these into Equation (5.16), we derive the following compact expression:

$$\frac{\langle d \rangle_m}{\langle d \rangle_s} = \sqrt{2 + 3x/\sqrt{2}} \quad (5.17)$$

where $x = Oh_{\xi_c} = \eta/\sqrt{\rho\xi_c\sigma}$ for Newtonian liquids and $x = De_{\xi_c} = \tau_E/4\sqrt{\rho\xi_c\sigma}$ for viscoelastic solutions.

Measured values of $\langle d \rangle_m / \langle d \rangle_s$ are plotted for both Newtonian liquids (blue squares) and viscoelastic solutions (red circles) in Figure 5-28. It is evident that both viscous and viscoelastic effects tend to increase the ratio of the main to the satellite droplet

diameter. Predictions of the toy model (Equation (5.17)) are plotted (solid line) and compared with the measurements. The good agreement between model and measurements shows that both viscous delay and the enhanced elongational viscosity have a similar effect on the average size of satellite droplets. Meanwhile, results clearly show that while viscous delay leads to very narrow size distributions for the secondary fragmentation process ($n_s \simeq 17$ for the 50 cSt silicone oil) the corresponding distributions for viscoelastic solutions are much broader ($n_s \simeq 4$ for the PEO 1M M_w 0.01% wt. solution). This broadening can be explained by the increase in the initial geometrical corrugations on the filament due to nonlinear effects of viscoelasticity (see Chapter 4 or related discussion in Keshavarz *et al.*[253]).

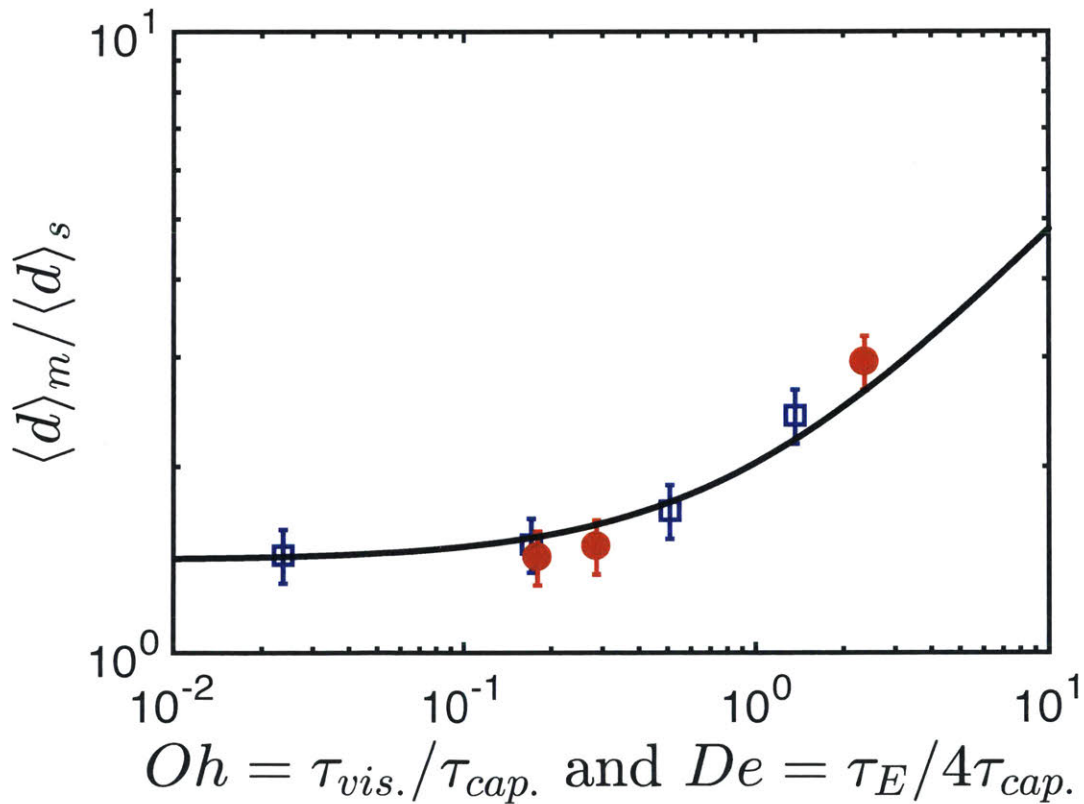


Figure 5-28: (color online). Size ratio of the main droplet to the satellite droplet: the x-axis shows the local Ohnesorge number of the filament $Oh_\xi = \eta / \sqrt{\rho \xi_c \sigma}$ for different Newtonian test liquids (\square) and the local Deborah number $De_\xi = \tau_E / 3\sqrt{\rho \xi_c^3 / \sigma}$ for three viscoelastic fluids (\bullet). The value of ξ is chosen based on the measured values of average droplet diameters ($\xi_c \simeq 66 \mu\text{m}$). The solid black line is the prediction of the model, described in Equation (5.17).

5.10 Conclusions

We have studied the fragmentation process in rotary atomization for both Newtonian and dilute viscoelastic solutions. Our results suggest that operating these atomizers in the ligament formation regime can have certain benefits over other types of atomizers. Organized and evenly-spaced ligaments stretch and break in a repeatable manner. Consequently, the final droplet size distributions are relatively narrow. We provided simple physical analysis for different mechanisms that are involved in this fragmentation process and derived analytical expressions for the number of ligaments projecting out of the rotating cup, the kinematics of the ejecting fluid particles and, most importantly, the final average droplet diameter. All the predictions were compared and validated with results from various experiments done with both Newtonian and viscoelastic solutions.

Droplet size distributions clearly show a bimodal behavior in the ligament formation regime. We show that the nature of this bimodal behavior is due to the existence of a secondary fragmentation process next to the primary process. The main drop diameter and fragmentation is simply set by the linear stability of the continuously stretching ligaments and thus remains unaffected by addition of viscoelasticity. However, the secondary fragmentation which leads to the formation of satellite droplets happens on the filaments that connect the main droplets. Both viscous delay and the enhanced elongational resistance increase the lifetime of the filament and lead to smaller satellite sizes. However, viscoelastic nonlinear effects make the filament more corrugated resulting in lower values of n_s in the Gamma distributions fit (with minimum found to be $n_s \simeq 4$).

Chapter 6

Linear rheology and physical structure of casein gels

A fractal is a mathematical set or concrete object that is irregular or fragmented at all scales.

Benoit Mandelbrot

6.1 Scope

The rheology of gels is key to many industrial and biological applications such as fracture or fragmentation of gel-like solids or liquids. In this chapter we present a rheological study for acid-induced casein gels made of sodium caseinate and acidified by glucono-delta-lactone (GDL) at different concentrations. Linear viscoelasticity measurements, including small amplitude oscillatory shear (SAOS) and stress relaxation in the linear region, show robust power-law behavior holding over a span of four orders of magnitude change in time/frequency. This striking behavior is captured by a simple one-element fractional model similar to the one originally proposed by Scott-Blair [254]. A thorough rheological study of these gels combined with microscopy imaging of the physical network helps us to identify some of the physical origins of the power laws reported in these materials and to interpret the parameters used in the fractional model in terms of the fractal gel microstructure.

6.2 Linear rheology of simple resins

The underlying microstructure of complex fluids such as paints and inks can have different origins and give rise to very different macroscopic behavior. A simple viscoelastic solution can be a good representative model fluid for dilute resins and latex solutions, but it does not display all the rheological features observed in other type of materials such as thick gel-like colloidal resins.

In Figure 6-1 (a) and (b) we show measurements of both shear and elongational properties for an industrial resin named Resin A (provided by Axalta). The oscillatory shear data show power laws for both the loss modulus G'' (shown by blue symbols in 6-1 (a)) and the elastic modulus G' (shown by red symbols in 6-1 (a)) with exponents one and two respectively. Results from CaBER tests, plotted in Figure 6-1 (b), show an elasto-capillary balance in the thinning filament that exhibits an exponential decay for the measured diameters with time. Both these results indicate a single dominant mode of relaxation for the underlying micro-structure in this resin. A simple mechanical model with a single mode of relaxation is shown in Figure 6-1 (c). This rheological model consists of a dash-pot (representing the solvent with $\eta = \eta_s$) parallel to a Maxwell-like element (an elastic spring G_p in series with a dash-pot η_p) that represents the relaxation of the microstructure. This linear model is known as the Oldroyd-B model [255] and its theoretical predictions for a simple oscillatory test are:

$$\begin{aligned} \text{Elastic Modulus: } G'(\omega) &\equiv \Re \left\{ \frac{\bar{\sigma}(\omega)}{\bar{\gamma}(\omega)} \right\} = \frac{G_p \omega^2 \tau^2}{1 + \omega^2 \tau^2} \\ \text{Loss Modulus: } G''(\omega) &\equiv \Im \left\{ \frac{\bar{\sigma}(\omega)}{\bar{\gamma}(\omega)} \right\} = \frac{G_p \omega \tau}{1 + \omega^2 \tau^2} + \eta_s \omega \end{aligned} \quad (6.1)$$

where $\bar{\sigma}$ and $\bar{\gamma}$ are the Fourier transforms of the stress and strain signal respectively. Predictions of this simple model are fitted to the data (solid lines in Figure 6-1(a)) and from the fit we can extract the associated relaxation time of the microstructure $\tau \simeq 0.01$ s.

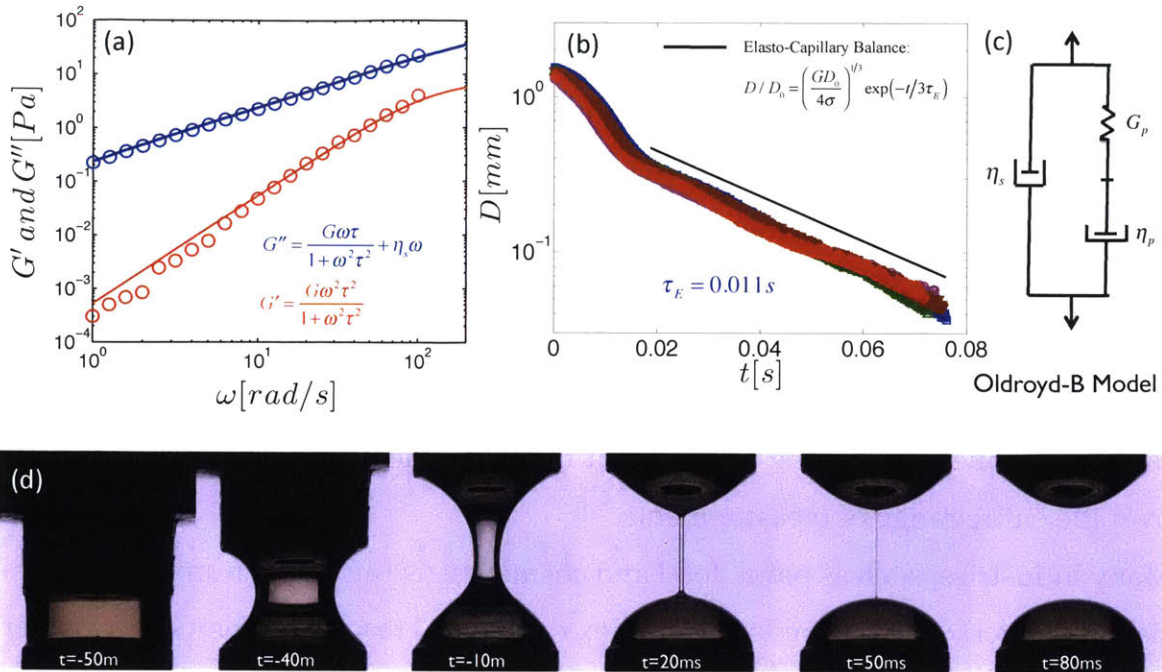


Figure 6-1: (color online). Oscillatory shear and elongational rheology of Resin A. (a) Small amplitude oscillatory shear (SAOS) rheology. Solid lines are fits of the Oldroyd-B model (Equation 6.1). (b) Diameter evolution in time in several CaBER test. (c) A mechanical representation of the Oldroyd-B model. (d) High-speed visualization of the filament breaking up in the CaBER device.

The predictions of the model for a CaBER test is an exponential decay in the filament diameter with a relaxation timescale similar to the one found from the SAOS experiment. Our CaBER measurements in Figure 6-1(b) and (d) give an estimate of $\tau_E \simeq 0.011$ s which is very close to the value found from fits to the SAOS data.

For these type of resins/paints we expect stringy filaments that resist the elongational flows with an intrinsic timescale that is set by the underlying microstructure. Despite having a relatively simple network, the nonlinear response of these materials can still be complex and, as we discussed in previous chapters, it can lead to unexpected performance of these liquids in fragmentation. However, variety of industrial samples have a much more complex rheological behavior and often one single mode of relaxation is not sufficient to model them.

6.3 Linear rheology of gel-like colloidal resins

Resin B, another industrial sample provided by Axalta, is a good example of a complex gel-like liquid resin. The rheological properties of this colloidal resin cannot be modeled with a single mode relaxation model. Figure 6-2(a) shows the mechanical response of this material at different frequencies for a linear oscillatory test. Solid lines show the best attempt to fit a single Oldroyd-B model to the data. It is clear that such an attempt can only capture the mechanical behavior in a small range of frequencies, failing to represent the rheological response of the material over the entire range of measurements.

Many industries, such as paint, food and cosmetics, use an ample number of materials characterized by a similarly complex rheological response. They show power law rheology in certain ranges of frequencies and do not exhibit a single relaxation mode, but often require multiple modes to describe their rheological behavior. The underlying network in these materials is often similar to that of gel-like materials. For Resin B, the cryo-TEM images (Figures 6-2(b) and (c)) clearly show soft squishy viscoelastic gel-like beads floating in the solvent, each of which is a concentrated associated network of low M_w polymer chains aggregated in the background latex due to corresponding hydrophobic-hydrophilic interactions ¹.

These sample spanning microstructure can undergo nonlinear deformation and fracture in any fragmentation/atomization event. To understand this complex phenomenon, we aim to study the linear and non-linear rheology of a class of food gels that have similarities to the gel-like network of complex paints and resins.

¹Personal communications with Michael Koerner, Eric Houze and John Moore from Axalta.

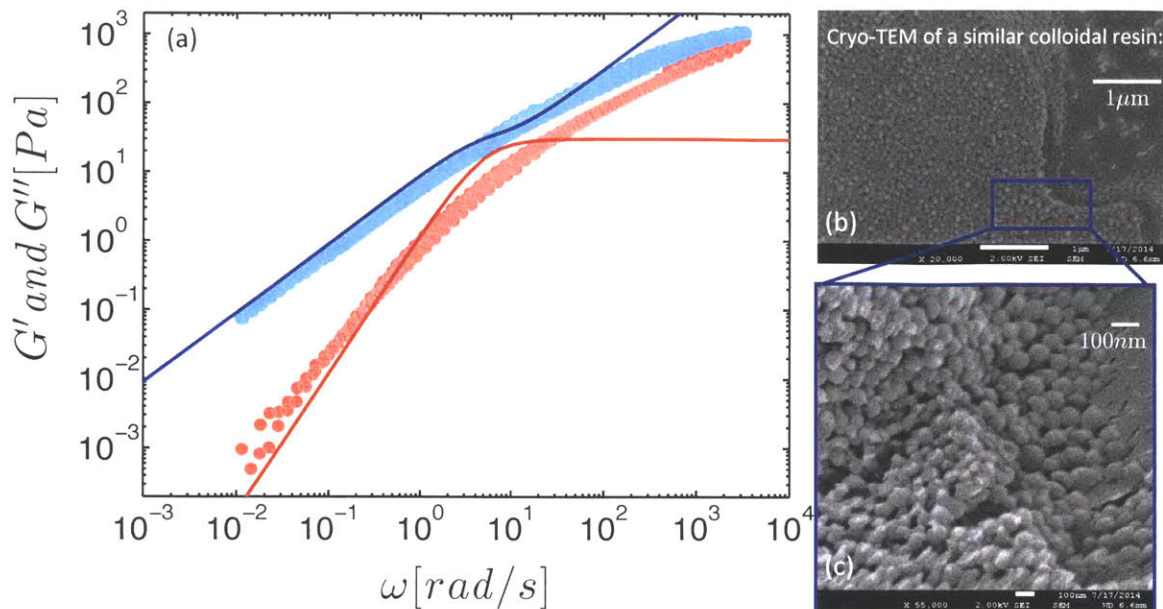


Figure 6-2: (color online). (a) Small amplitude oscillatory shear (SAOS) rheology for Resin B. Solid lines are fits of the single mode Maxwell model. (b) and (c) Cryo-TEM images of Resin B.

6.4 Food gels and soft solids

We chose casein protein gels as a class of gel-like materials for our study which are very close to soft solids. Casein (from Latin caseus, meaning "cheese") is made of a class of phosphoproteins ($\alpha S1, \alpha S2, \beta, \kappa$). Milk is a good source for finding these proteins: about 80% of the proteins in cow's milk are casein proteins.

Normal milk and dairy products such as yogurt are colloidal gels consisting of casein micelles ($\sim 100\text{nm}$ in diameter) that are each an aggregate of much smaller sub-micelles stabilized by calcium phosphate[256, 257, 89, 90]. In our tests, we used purified proteins that does not contain any calcium phosphate. Thus our material, unlike yogurt, forms a protein gel that is closer in nature to a polymer gel and does not have structures similar to casein micelles. We first dissolve the casein in water and pour it into the cell on the rheometer (discussed in chapter 2). After adding an acidifying agent called Glucono delta-lactone (GDL), also known as gluconolactone, the pH of the solution slowly decreases and when it reaches the

isoelectric point at $\text{pH} \sim 4.6$ the casein protein is not soluble anymore and forms a protein network.

6.4.1 Structure

Food gels have often a complex microstructure characterized by length-scales that can span many orders of magnitudes [258]. This usually gives rise to a fractal-like network and, as a direct consequence, the mechanical response of these materials is a superposition of different modes related to different timescales that are associated to all the individual lengthscales involved in the underlying structure.

Casein protein gels are known to have a structure similar to that generated by the aggregation of fractal clusters [89]. This means that below a certain cluster size $R_{cluster}$ they show a power law density profile $M(r) \sim r^{D_f}$ where M is the mass of the gel and D_f is the fractal dimension of the cluster. Our environmental SEM image of the Casein gel (4-1% casein-GDL ratio) is shown in Figure 6-3. One can clearly see that the idea of an aggregation of clusters of mass fractals is relevant and can capture the underlying network in these materials. From first principles, Bremer and coworkers [89, 259] have shown that the elasticity of these networks scales as $G \sim \Phi^{2/(3-D_f)}$, where Φ is the volume fraction of the casein.

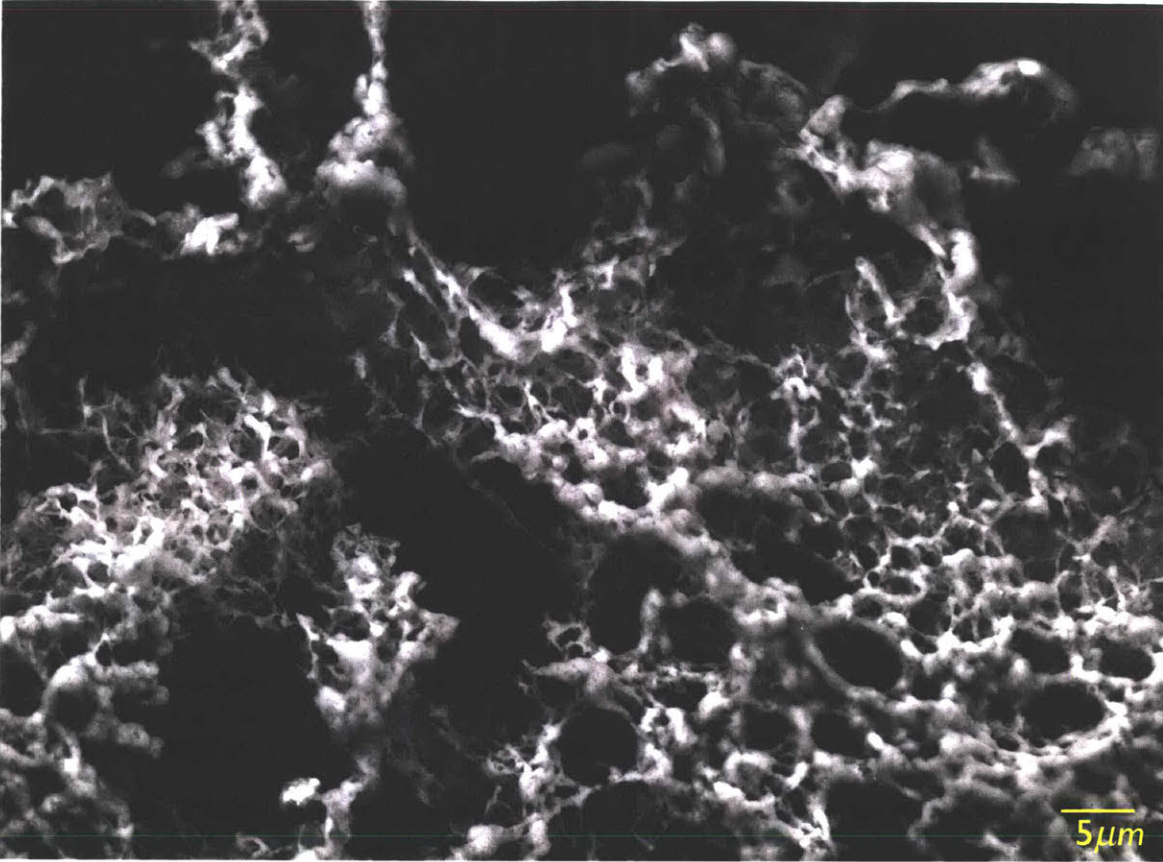


Figure 6-3: (color online). Structure of casein gel. Environmental SEM image of the 4%-1% casein-GDL gel.

6.4.2 Linear rheology

After forming these gels on the rheometer, we performed a series of rheological test to probe their mechanical properties. Oscillatory shear tests and stress relaxation after imposing a step in strain were two of the important tests that were carried out. Figure 6-4(a) shows the results of an oscillatory test. It is clear that both elastic and loss moduli show a power law behavior over a wide range of frequencies. The stress relaxation test (plotted in Figure 6-4(b)) also confirms a slow decay of the modulus that shows a power law behavior over several orders of magnitude in time. Both of these power law trends have an exponent that is close to 0.15.

To mathematically model this behavior, one requires a mechanical model that incorporates many modes of relaxation with different timescales [92]. Scott Blair found a more sophisticated method for mathematically describing these gels which

is based on fractional calculus. Inspired by this idea, which is experimentally observed in many biological materials [93], Jaishankar and McKinley [86] reintroduced the idea of “fractional rheology” as a useful tool for modeling the linear rheology of soft gels. The proposed mechanical element is a *spring-pot* that has a constitutive equation of the form

$$\sigma_{spring-pot} = \mathbb{V} \frac{d^\alpha \gamma}{dt^\alpha} \quad (6.2)$$

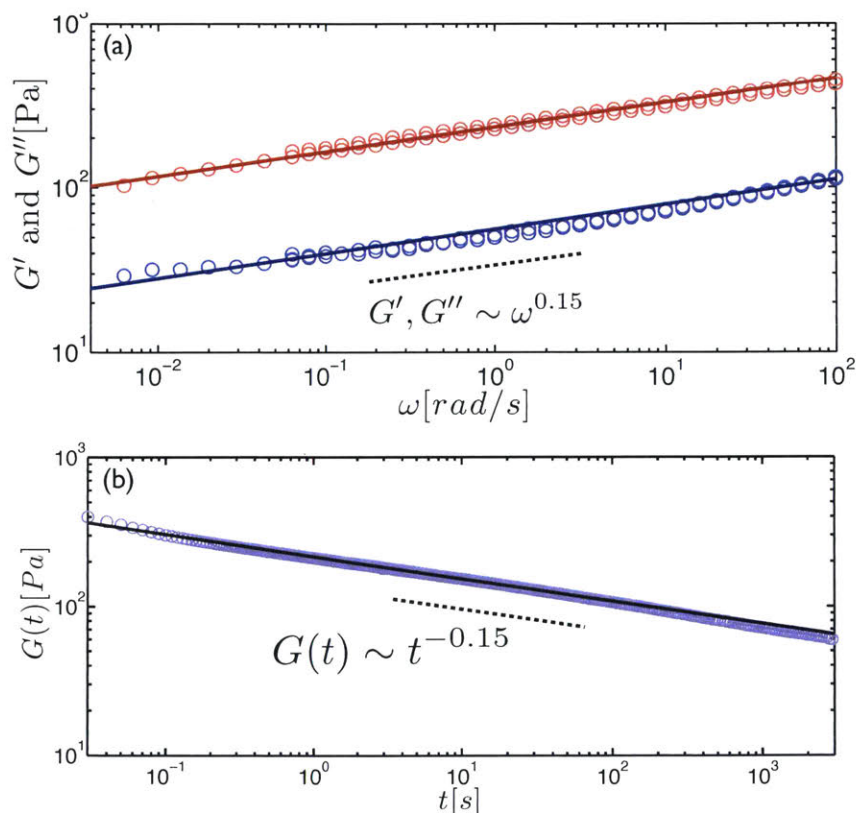


Figure 6-4: (color online). Linear rheology of the 4%-1% casein-GDL gel: (a) Small amplitude oscillatory shear (SAOS) rheology. (b) Stress relaxation after a linear step strain test. Solid lines are fits from the fractional model (Equation (6.4)).

where $\frac{d^\alpha}{dt^\alpha}$ indicates a fractional derivative² of order α defined in the form of a

²Historically the concept of fractional derivatives was first introduced by Leibniz in a letter to L'Hospital [94].

Caputo derivative [95]

$$\frac{d^\alpha}{dt^\alpha} f(t) = \frac{1}{\Gamma(1-\alpha)} \int_0^t (t-t')^{n-\alpha-1} f^{(n)}(t') dt' \quad (6.3)$$

in which n is the nearest integer bigger than or equal to α , i.e. $n = \lceil \alpha \rceil$ and $f^{(n)}$ is the n -th derivative of f .

The fractional model in Equation (6.2) has two parameters: a front factor \mathbb{V} , which has dimensions of $\text{Pa}\cdot\text{s}^\alpha$, and a dimensionless parameter α that can vary from 0 to 1. While \mathbb{V} sets the strength of the gel, α sets the slope of the power law. By varying α from 0 to 1 one can recover a spectrum of rheological responses from a Hookean solid, to gel-like and finally a Newtonian liquid. We will show that the value of α is set by the fractal structure of the gel network while \mathbb{V} is strongly affected by the volume fraction of casein dissolved in water.

The rheological response of this fractional element predicts a power law decay in time for the relaxation modulus after a step strain test such that $G(t) \sim \mathbb{V}t^{-\alpha}$. Similarly, in an oscillatory flow the elastic and loss modulus exhibit power law dependence on frequency $G', G'' \sim \omega^\alpha$. In fact for a simple spring-pot element, using Fourier and Laplace transform the following analytical expressions can be found [86]:

$$\begin{aligned} G(t) &= \frac{\mathbb{V}}{\Gamma(1-\alpha)} t^{-\alpha} \\ G'(\omega) &= \mathbb{V} \cos(\pi\alpha/2) \omega^\alpha \\ G''(\omega) &= \mathbb{V} \sin(\pi\alpha/2) \omega^\alpha \end{aligned} \quad (6.4)$$

where $\Gamma(x)$ is the Euler Gamma function. Using these results we can now fit the rheological data. Solid lines in Figure 6-4 show the predictions of the model with fitted parameters having values of $\mathbb{V} = 301 \text{ Pa}\cdot\text{s}^\alpha$ and $\alpha = 0.15$. The good agreement between the fractional model and the rheological response of the gel once again suggests a broad spectrum of length and timescale for this materials that also resonates well with the idea of a fractal structure.

To understand and find the variables that control the model parameters (\mathbb{V}, α), we prepared a series of gels at constant casein-GDL concentration ratio (4-1) and varied the casein concentration.

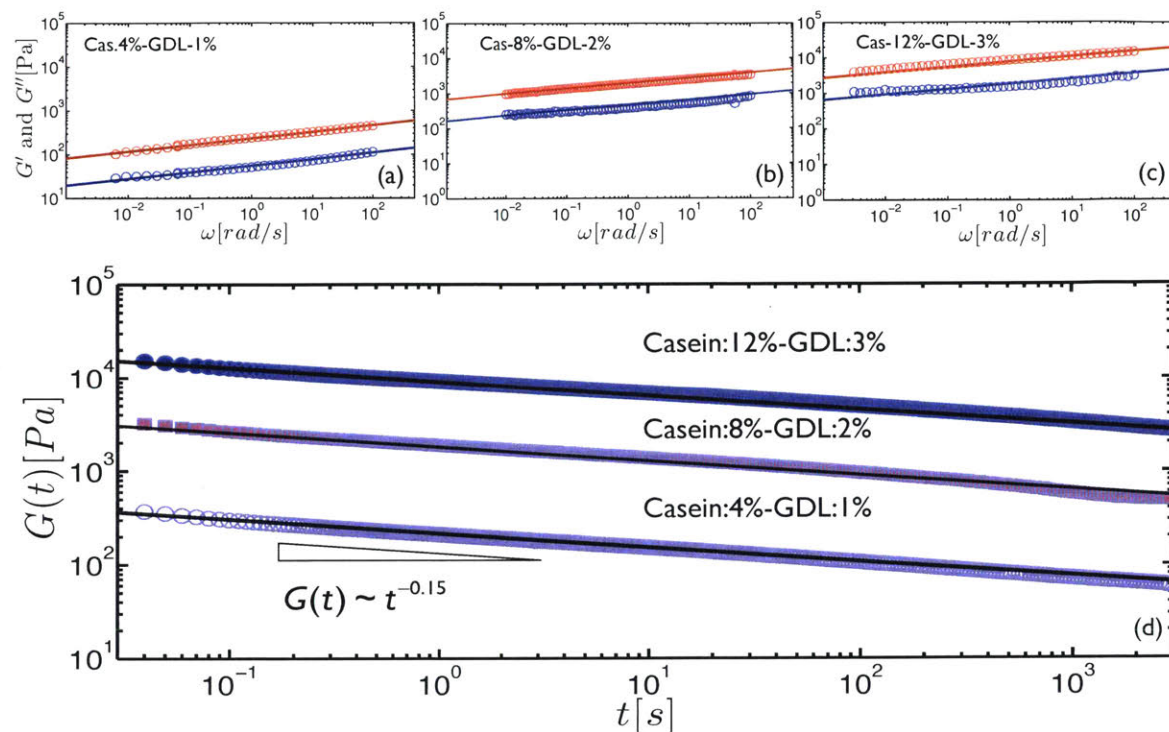


Figure 6-5: (color online). Linear rheology for three different casein gels: SAOS for (a) The 4%-1% casein-GDL gel. (b) The 8%-2% casein-GDL gel. (c) The 12%-3% casein-GDL gel. (d) Stress relaxation for all three gels after applying a linear step in strain.

Figure 6-5 shows a summary of linear test for three different casein gels. All the gels are made at a constant 4-1 casein to GDL ratio. It is clear that by increasing the casein concentration the gel modulus monotonically increases. It is also evident that the observed power laws shows a similar exponent $\alpha \simeq 0.15$ for all these gels. This interesting finding suggests that by fixing the ratio of the protein to GDL concentration, the power law exponent in the rheological response remains unchanged. Meanwhile, the monotonic increase in modulus with increasing casein concentration suggests that the quasi-property \mathbb{V} is strongly affected by the amount of protein per volume. Solid lines show the fractional model pre-

dictions (Equation (6.4)) for a constant value of $\alpha = 0.15$ and increasing values of $\mathbb{V} = 301, 1889, 9831 \text{ Pa}\cdot\text{s}^\alpha$.

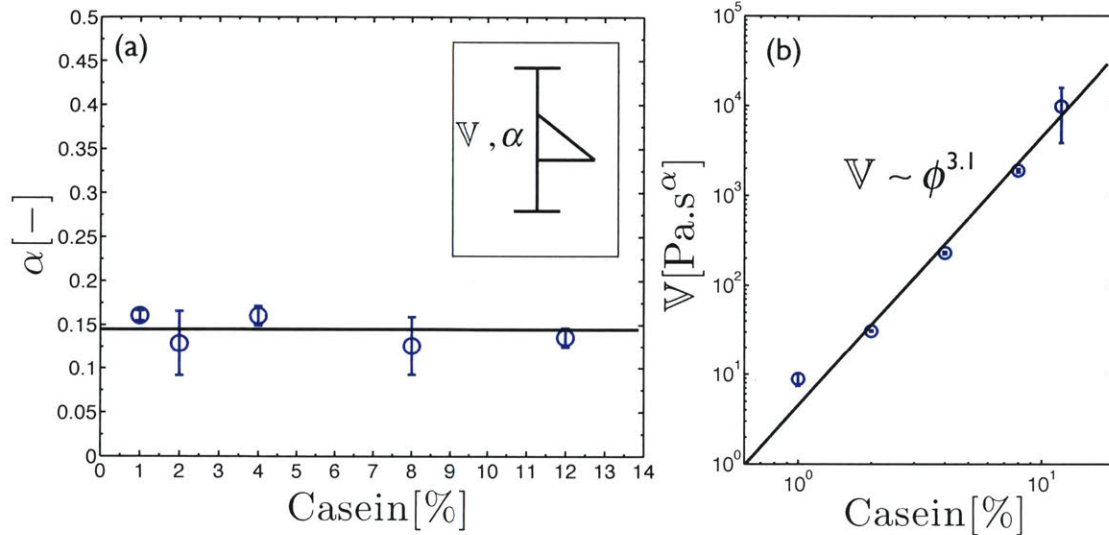


Figure 6-6: (color online). Dependency of (a) the power law exponent α and (b) the quasi-property \mathbb{V} on the weight concentration of casein protein (at a fixed 4-1 casein to GDL concentration ratio).

Although the fits from the fractional model show good agreement with all the rheological measurements, we do not rely on their fitting goodness for determination of quasi properties. Results from 6.4 suggest the following:

$$\alpha_i = \arctan [G''(\omega_i)/G'(\omega_i)]$$

$$\mathbb{V}_i = \sqrt{\left(\frac{G'(\omega_i)}{\omega_i^\alpha}\right)^2 + \left(\frac{G''(\omega_i)}{\omega_i^\alpha}\right)^2} \quad (6.5)$$

where ω_i is the i th frequency in the discrete series of tested frequencies. Equation 6.5 shows a direct way to calculate an estimate pair of α_i, \mathbb{V}_i for every tested frequency. For each SAOS test, we report average values of α_i, \mathbb{V}_i as the quasi-properties derived for that test and standard deviations are selected as the associated error in our estimates. Figure 6-6 shows a plot of quasi-properties versus

the concentration of casein protein. All these gels were made at a fixed 4-1 casein-GDL ratio and, as mentioned before, within measured error-bars all show a similar value of power law exponent $\alpha \simeq 0.15$ but the values of the quasi-property \mathbb{V} increases with the casein concentration in a power law manner $\mathbb{V} \sim \Phi^{3.1}$. This power law trend is very similar to the predictions from Bremer and coworkers [89] which were based on assuming an aggregated fractal cluster network for casein gels. Knowing that $\mathbb{V} \sim \Phi^{2/(3-D_f)}$, we can calculate D_f based on the power law trend observed in Figure 6-6(b) which yields $D_f \simeq 2.4$. This estimate agrees well with the calculated fractal dimensions that were obtained for the same gels by confocal microscopy³, suggesting that the power law exponent α in fractional models is a function of network structural parameters such as the fractal dimension D_f . However, the quasi-properties show also a strong dependence on other factors such as the volumetric concentration.

We further investigated this by preparing a set of gels with a constant amount of protein and an increasing concentration of GDL. By changing the ratio of casein to GDL, we assume that we can change the fractal dimension of the gel network (validation of which is still ongoing with more scattering analysis of these gels). We also performed a set of rheological measurements summarized in Figure 6-7, from which we extracted the corresponding quasi-properties at each GDL concentration following Equation (6.5). Figure 6-8 clearly shows that both the power law exponent α and the quasi-property \mathbb{V} decrease with increasing GDL concentration. It is evident that the increase in GDL concentration has directly affected the structure of the underlying network, modifying its structural properties such as D_f , and consequently changing α . Also, it seems plausible that changes in the geometrical nature of the fractal gel (D_f) combined with the mechanical changes in the strength of building protein strands, can lead to a net decrease in the quasi-property \mathbb{V} .

³Personal communications with Thibaut Divoux and colleagues.

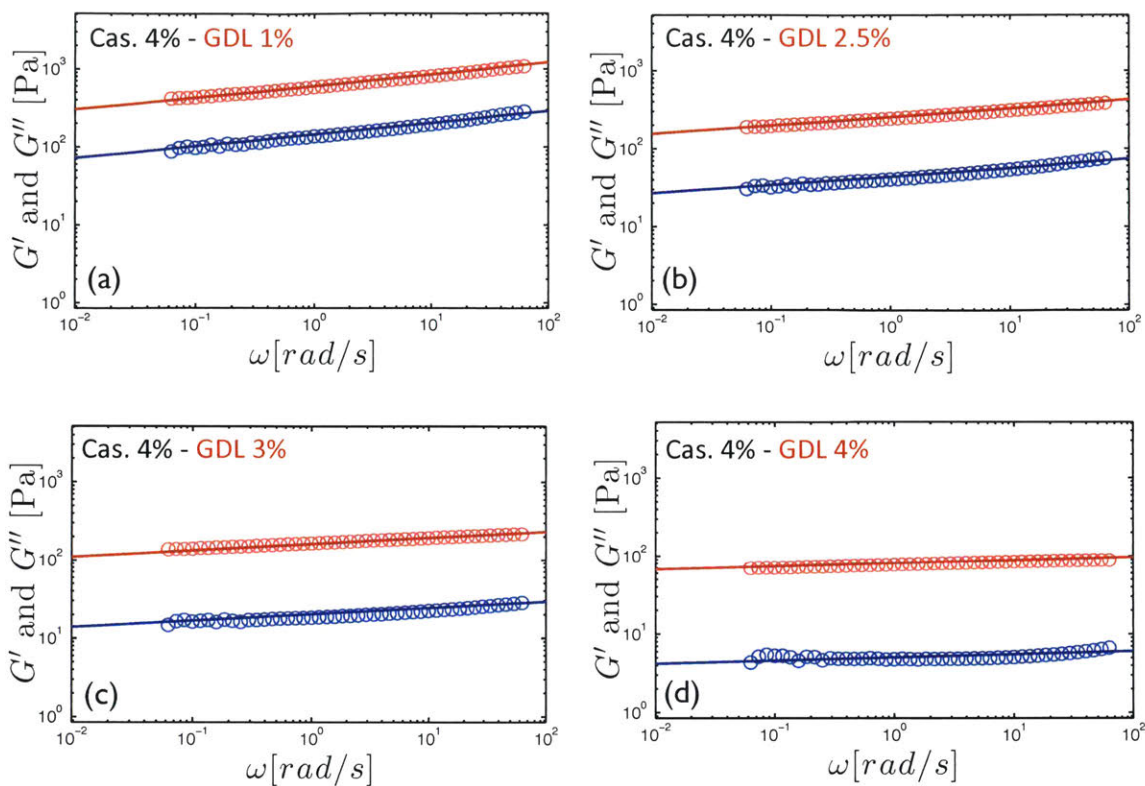


Figure 6-7: (color online). Linear rheology for four different casein gels: SAOS for (a) The 4%-1% casein-GDL gel. (b) The 4%-2.5% casein-GDL gel. (c) The 4%-3% casein-GDL gel. (d) The 4%-4% casein-GDL gel.

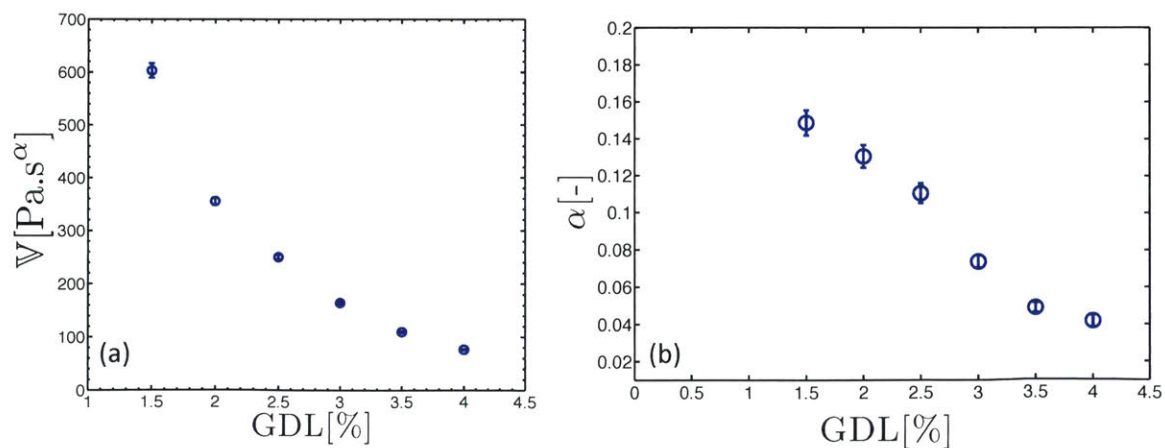


Figure 6-8: (color online). Dependency of (a) the power law exponent α and (b) the quasi-property V on the weight concentration of the acidifying agent GDL (at a fixed 4% wt. casein concentration).

6.5 conclusions

We have explored the linear rheological properties of a class of materials, known as soft gels, which differ substantially from the dilute polymer solutions studied in details in previous Chapters. In this chapter, we show that these materials are characterized by an underlying mass fractal network. We show that the power law rheology can be adequately modeled by fractional models and our results indicate a direct relation between the network structural parameters and the model parameters for the fractional element. The fractal dimension of the underlying gel, measured by confocal microscopy, can be connected to the power law exponent that these materials exhibit in their linear rheology. We show that the elastic modulus of the gels also follows a power law dependence on the volume fraction which can be again understood and explained using the available scalings for the behavior of fractal gels. By studying acid-induced casein gels, we wish to improve our current understanding of the effect of linear and nonlinear rheology on the fracture behavior of solid-like materials. In the next Chapter, we will directly connect the linear and non-linear behavior of acid-induced casein gels to their response before and up to rupture.

Chapter 7

Nonlinear viscoelasticity and generalized failure criterion for biopolymer gels

The problem with linear theory is that it is not nonlinear.

John A. Adam

7.1 scope

In this chapter we will focus on the failure and fracture of two model protein gels. As discussed in the previous chapter, these biopolymer gels display a multiscale microstructure that is responsible for their solid-like properties. Upon external deformation, these soft viscoelastic solids exhibit a generic nonlinear mechanical response characterized by pronounced stress- or strain-stiffening prior to irreversible damage and failure, most often through macroscopic fractures. Here we show on a model acid-induced protein gel that the nonlinear viscoelastic properties of the gel can be described in terms of a 'damping function' which predicts the gel mechanical response quantitatively up to the onset of macroscopic failure. Using a nonlinear integral constitutive equation built upon the experimentally-measured damping function in conjunction with power-law linear viscoelastic response, we

derive the form of the stress growth in the gel following the start up of steady shear. We also couple the shear stress response with Bailey's durability criteria for brittle solids in order to predict the critical values of the stress σ_c and strain γ_c for failure of the gel, and how they scale with the applied shear rate. This provides a generalized failure criterion for biopolymer gels in a range of different deformation histories.

7.2 Introduction

Biopolymer gels find ubiquitous applications in material science, with examples ranging from biological tissues to manufactured goods, among which food stuffs and medical products are the most widespread [260, 261, 262]. These materials commonly feature a porous and fibrillar microstructure filled with water, and exhibit solid-like viscoelastic mechanical properties which can be strongly enhanced by careful control of the viscous dissipation at multiple scales [263, 264]. While biopolymer gels share common features with stiffer and more rigid materials, including delayed failure [265, 266], crack propagation [267, 268] or work-hardening [269], their fibrous microstructure also confers upon them remarkable nonlinear viscoelastic properties. Indeed, such soft solids strongly stiffen upon increasing deformation, which stems from the inherent nonlinear elastic behavior of the polymer chains in the gel network [270, 271, 272]. This enables such materials to endure large strains to failure and dissipate substantial mechanical work, leading to very tough hydrogels and elastomers [264]. However, to date no quantitative link has been made between the nonlinear viscoelasticity of biopolymer gels and the failure that is subsequently observed as the strain-loading is increased beyond the initial stiffening regime.

In the present chapter, we use the concept of a strain damping function, traditionally used for polymeric liquids and rubber-like materials [273], to quantify the nonlinear viscoelastic response of a prototypical protein gel. The form of the damping function is constructed experimentally through a series of independent stress re-

laxation tests that allow us to probe large deformations while injecting very little energy into the gel, hence limiting as much as possible any plastic damage. Following the Boltzmann superposition principle, the damping function is used to construct a time-strain separable K-BKZ (Kaye–Bernstein–Kearsley–Zapas) constitutive equation [71] that predicts the gel mechanical response to steady-shear experiments. This approach enables us to robustly capture the strain-stiffening of the gel during start up of steady shear tests up to the appearance of a stress maximum that is accompanied by the onset of the first macroscopic crack. Finally, in order to link the nonlinear viscoelastic response of the gel to its subsequent brittle-like rupture, we adopt the Bailey criterion, which describes the gel failure as arising from accumulation of irreversible damage [274, 275]. The combination of the stress response predicted by the K-BKZ constitutive formulation with the Bailey criterion allows us to predict the scaling of the critical stress and strain at failure with the magnitude of the applied shear rate, and hence to derive a generalized failure criterion for soft solids such as hydrogels.

7.3 Experiments and gels

Two acid-induced protein gels with substantially different mechanical properties are prepared by dissolving caseinate powder (Firmenich) at 4% wt. (resp. 8% wt.) in deionized water under gentle mixing at 600 rpm and $T = 35^\circ\text{C}$. Homogeneous gelation is induced by dissolving 1% wt. (resp. 8% wt.) glucono- δ -lactone (GDL, Firmenich) in the protein solution [276, 126]. While still liquid, the protein solution is poured into the gap of a cylindrical Couette shear cell connected to a strain-controlled rheometer (ARES, TA Instruments, Delaware). Rheological data were obtained with an ARES-LS strain-controlled rheometer (TA Instrument) using a homemade polished Plexiglas rotating cup of height 20.32 mm and diameter 25 mm with an inner Delrin fixed bob of radius 22.65 mm, yielding a gap of 2.35 mm.

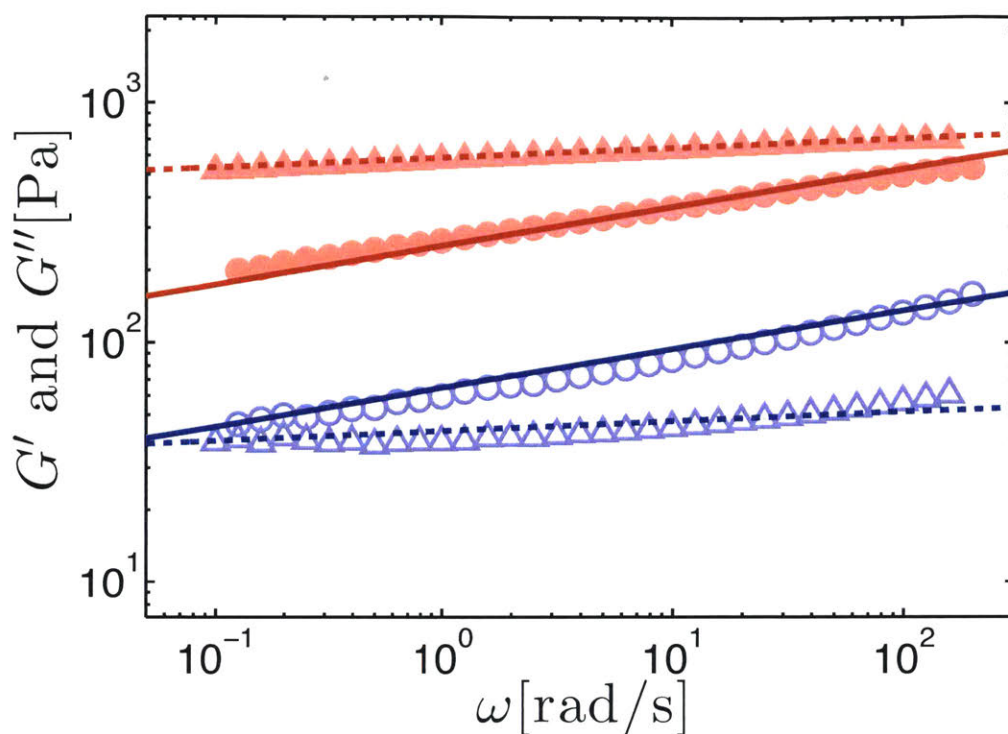


Figure 7-1: (color online) Linear viscoelastic moduli G' (upper, filled symbols) and G'' (lower, hollow symbols) as a function of pulsation ω for a strain amplitude of $\gamma = 0.01$. The symbols \bullet and \blacktriangle respectively correspond to the 4% wt. and 8% wt. casein gels. Dashed and continuous lines correspond to the best fit of the data with the spring-pot model.

We performed tests with two protein gels: 4% casein-1% GDL and the 8% casein-8% GDL gels which we henceforth refer to as 4% and 8% casein gels, respectively. Figure 7-1 shows the frequency dependence of the elastic and viscous moduli of both the 4% wt. and 8% wt. gels. Both gels display a power-law linear rheology that can be modeled by a spring-pot (or fractional) element, as reported in the previous chapter. The elastic and viscous modulus reads respectively $G'(\omega) = \mathbb{V}\omega^\alpha \cos(\pi\alpha/2)$ and $G''(\omega) = \mathbb{V}\omega^\alpha \sin(\pi\alpha/2)$, with $\alpha = 0.18 \pm 0.02$ and $\mathbb{V} = 261 \pm 5$ Pa.s for the 4% gel and $\alpha = 0.04 \pm 0.01$ and $\mathbb{V} = 620 \pm 5$ for the 8% gel.

In situ gelation is achieved within 12 hours after which either a step strain or a constant shear rate is imposed on the sample while the resulting stress response is monitored. In both cases, images of the gel deformation are recorded simultaneously to rheology in order to monitor the nucleation and growth of cracks.

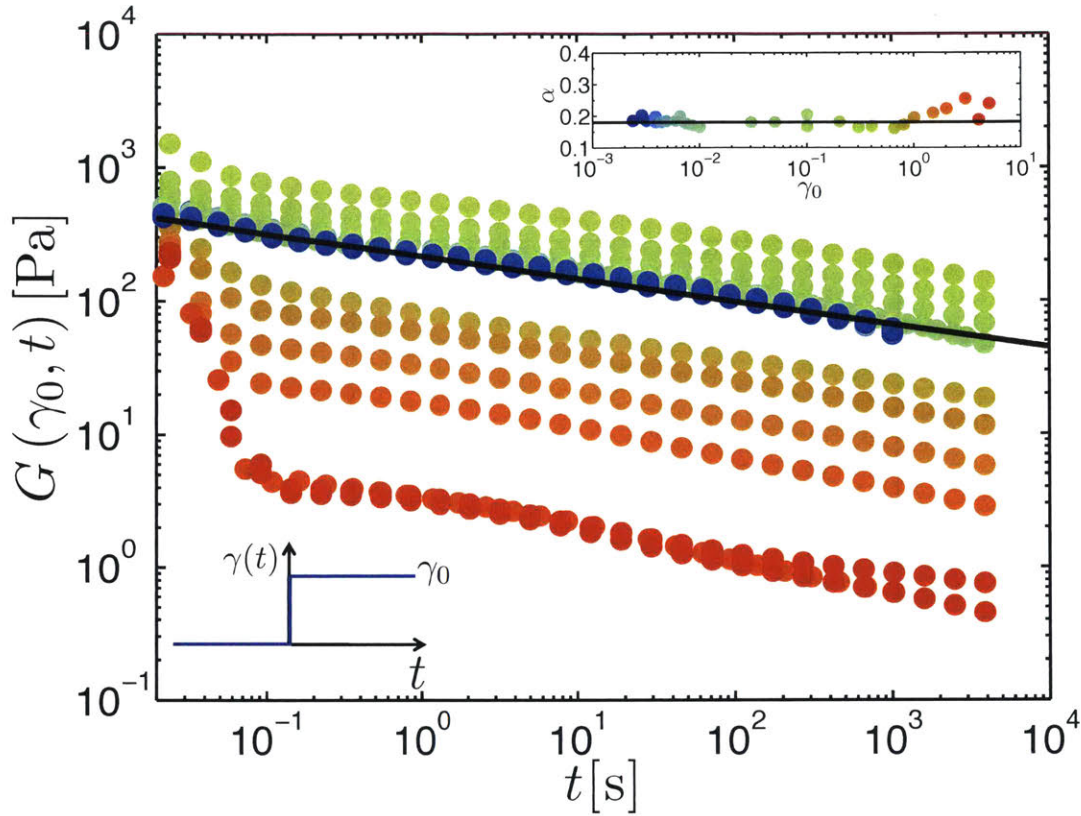


Figure 7-2: (color online) Nonlinear relaxation function $G(\gamma_0, t) = \sigma(t)/\gamma_0$ vs time t determined by step strain tests, each one performed on a freshly prepared 4% wt. casein gel. Colors from blue to red represent strain values ranging from $\gamma_0 = 0.002$ to $\gamma_0 = 5$. The black line is the best power-law fit of the data in the linear region ($\gamma_0 \leq 0.01$). Inset: Stress relaxation exponent α extracted from the power-law fit of the data shown in the main graph with the same color code. The horizontal line is the average exponent $\alpha = 0.18 \pm 0.01$.

7.4 Damping function

To first characterize the viscoelastic properties of the 4% wt. casein gel, we perform a series of step strain tests. Each experiment is performed on a freshly prepared gel and consists of two successive strain steps. The first step is applied within the linear deformation regime and the stress relaxation is followed over the next 4000 s and serves as a reference for the comparison of two independent experiments. This is followed by a second step at a strain amplitude chosen between $10^{-3} \leq \gamma_0 \leq 5$ and the stress is monitored again for 4000 s to measure the gel viscoelastic response. The stress relaxation functions $G(\gamma_0, t) = \sigma(t)/\gamma_0$ associated with the second step of strain are reported in Fig. 7-2. At low applied strains ($\gamma_0 \lesssim 0.01$), the magni-

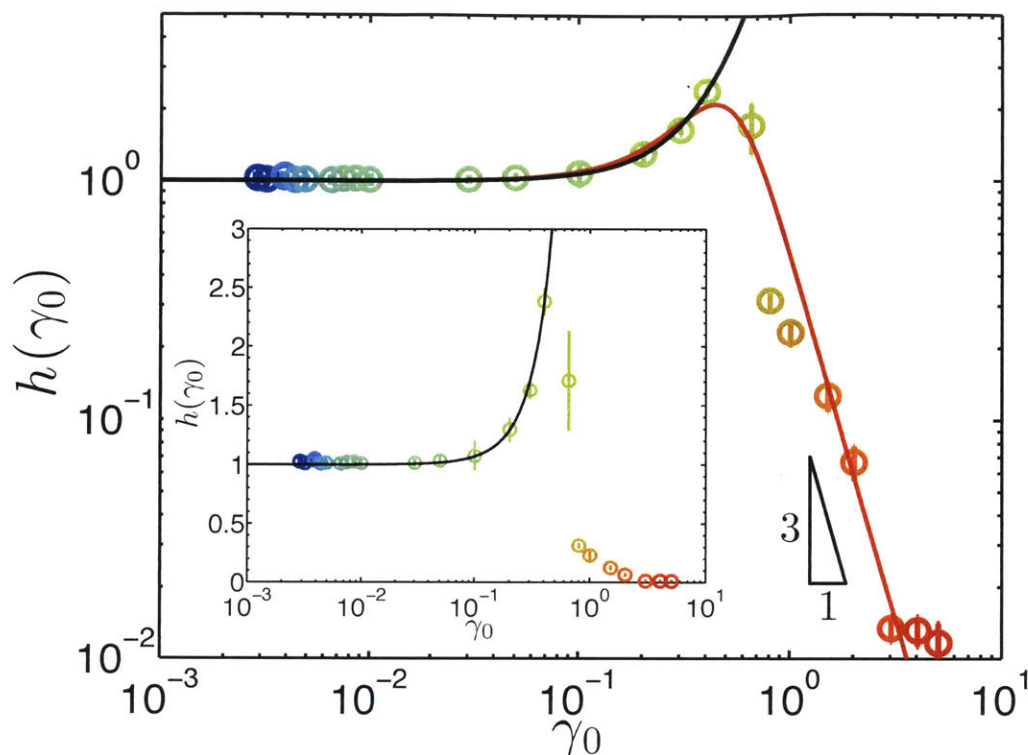


Figure 7-3: (color online) Strain damping function $h(\gamma_0)$ of a 4% wt. casein gel as defined in the text. Same color code as in Fig. 7-2. The solid black line is the best fit function by power series in γ_0^2 as proposed in [52] which captures the stiffening behavior, but does not account for the softening part of the gel response at strains larger than 50%. The red continuous line is the best fit function $\hat{h}(\gamma)$ of the data (see text). Inset: same data plotted in semilogarithmic scales.

tude of the viscoelastic stress scales linearly with the imposed strain and the relaxation modulus exhibits a remarkable power-law decrease over four decades of time which is well modeled by a spring-pot (or fractional viscoelastic element) [277], $G(t) = \mathbb{V}t^{-\alpha}/\Gamma(1-\alpha)$, where \mathbb{V} and α are the only two material properties required to characterize the gel, and Γ denotes the Gamma function. By fitting the data for $\gamma_0 \leq 0.01$ we find that the relaxation exponent $\alpha = 0.18 \pm 0.01$ and the prefactor or “quasiproperty” $\mathbb{V} = 266 \pm 5 \text{ Pa}\cdot\text{s}^\alpha$ [277]. We find similar results for the 8% wt. casein gel. The exponent $\alpha = 0.04 \pm 0.01$ and the prefactor $\mathbb{V} = 640 \pm 5 \text{ Pa}\cdot\text{s}^\alpha$ are determined by a frequency sweep (see Fig. 1 in the Supplemental Material). For $\gamma_0 \gtrsim 0.01$, the stress relaxation still exhibits a power-law decrease in time with the same exponent α , after $t \gtrsim 0.1 \text{ s}$ but the magnitude of the stress at a given time first stiffens and then softens.

Since α is insensitive to the strain amplitude, we can use the concept of strain-time separability [?] to quantify the strain dependence of the stress relaxation response by computing the *damping function* [273], defined as $h(\gamma_0) = \langle G(\gamma_0, t)/G(t) \rangle_t$ where $\langle \dots \rangle_t$ denotes the time average for $1 \leq t \leq 1000$ s for each of the two step-strain experiments. The resulting damping function reported in Fig. 7-3 thus fully characterizes the strain dependence of the viscoelastic response in the material. The gel displays a linear response in the filamentous protein network (i.e. $h = 1$) up to $\gamma_0 = 0.1$, whereas for intermediate strain amplitudes, the gel exhibits a pronounced strain-stiffening, that is characterized by a maximum value $h \simeq 2.2$ reached at $\gamma = 0.5$. Finally, for even larger strains, the material softens due to network rupture and the damping function decreases abruptly as a power law function of the imposed strain with an exponent of ~ -3 . We also emphasize that for all step strain tests, the gel remains visually intact even at strain amplitudes as large as $\gamma_0 \simeq 5$. Therefore independent step strain experiments, instead of traditional strain sweeps which accumulate larger total deformations, allow us to prevent the growth of cracks and to accurately measure the initial stiffening and subsequent softening behavior of such biopolymer gels.

As proposed in [52, 278], the strain hardening portion of the damping function in the fibrous microstructure can be captured in a power series expansion of $h^*(\gamma_0)$, with the fractal dimension d_b of the stress-bearing network backbone as the only fitting parameter. h^* is defined as

$$h^* = 1 + \sum_{j=1}^2 \frac{b_{2j}}{b_0} \gamma^{2j},$$

where $\{b_{2j}\}_{j \in \mathbb{N}}$ are numerical coefficients defined in [278]. Here we find $d_b = 1.3 \pm 0.1$ in good agreement with measurements in the linear regime (see black line in Fig.7-3)[?]. However, fitting the whole damping function also requires us to take into account the gel softening at strains larger than 0.5. Following analogous approaches in the literature for rubbery networks and polymer melts [273] we use the following functional form $\tilde{h}(\gamma_0) = [1 + (\gamma_0/\gamma_m)^2]/[1 + |\gamma_0/\gamma_M|^5]$, where $\gamma_m = 0.34$ and

$\gamma_M = 0.57$ are fitting parameters that respectively mark the departure from linearity and the location of the strain maximum. The quadratic dependence of the numerator is set by symmetry [52] while the exponent in the denominator is purely phenomenological and depends on the strength of the individual network bonds in the gel. This form describes the whole data set remarkably well (Fig. 7-3) and can be used to predict the viscoelastic response of a biopolymer gel to start up of steady shear all the way to sample failure as we now proceed to show.

7.5 K-BKZ description of shear start-up

In Fig. 7-4, we show the evolution of stress and onset of cracking when a 4% wt. casein gel is submitted to a constant shear rate $\dot{\gamma}_0 = 10^{-3} \text{ s}^{-1}$. We see that the stress growth $\sigma(\gamma)$ can be separated into three consecutive regimes: a linear viscoelastic regime, characterized by a power-law growth of $\sigma(t)$ up to $\gamma \simeq 0.2$, followed by a strain-stiffening regime in which σ shows a steeper increase up to a critical strain $\gamma_c \simeq 0.8$ at which the stress goes through a maximum σ_c . Finally, in a third regime, the stress exhibits an abrupt decrease followed by a slower relaxation at larger strains. The gel remains visually intact and homogeneous initially, and the first macroscopic fracture appears at the end of the second regime when $\gamma \simeq \gamma_c$ and $\sigma \simeq \sigma_c$ (see Movie 1 in the Supplemental Material). We predict the viscoelastic stress response using the Boltzmann integral formulation and the principle of time-strain separability shown in Figs. 7-2 and 7-3 such that the stress is given by:

$$\sigma(t) = \int_{-\infty}^t G(t-t')h(\gamma)\dot{\gamma}(t')dt' \quad (7.1)$$

The first regime in Fig. 7-4 is fully accounted for by the linear viscoelastic response based on the power-law behavior of $G(t)$ determined in Fig. 7-2 for $\gamma_0 \leq 1\%$, and since $h(\gamma) = 1$ in this regime the stress can be found analytically [279]:

$$\sigma(t) = \int_{-\infty}^t G(t-t')\dot{\gamma}(t')dt' = \frac{V\dot{\gamma}_0 t^{1-\alpha}}{(1-\alpha)\Gamma(1-\alpha)}. \quad (7.2)$$

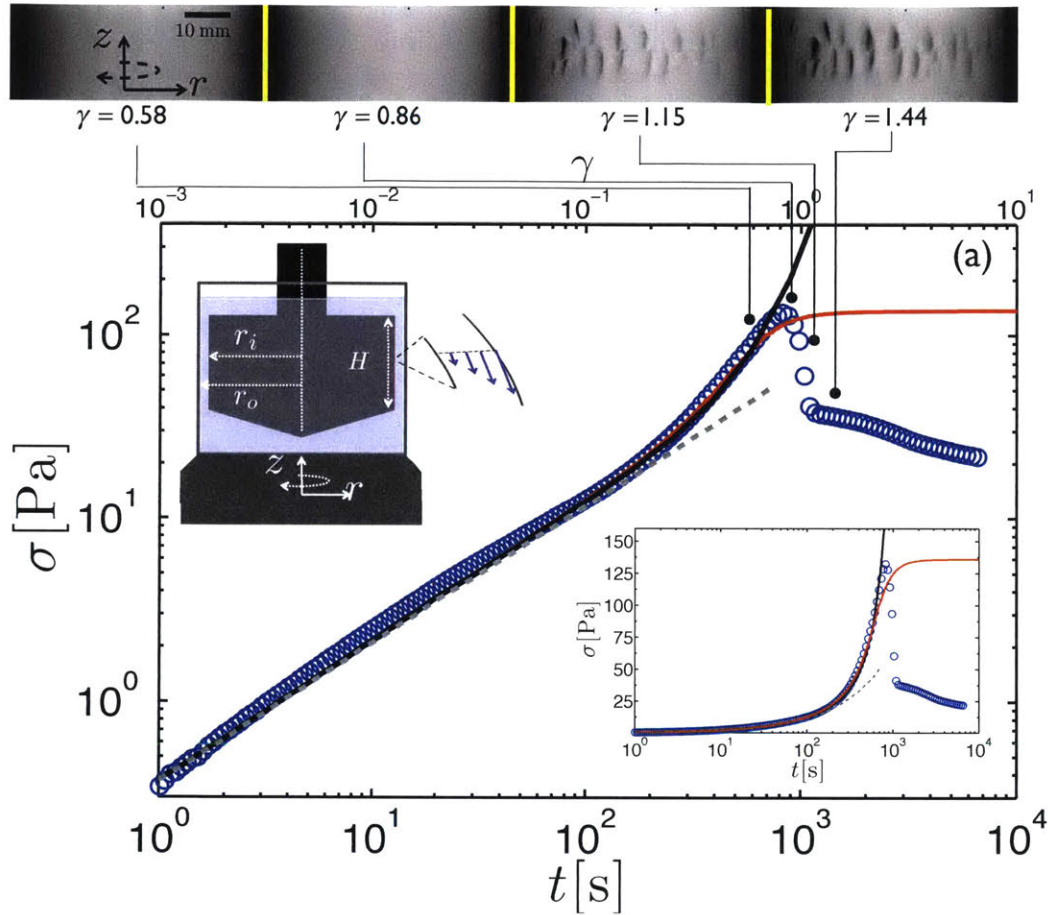


Figure 7-4: (color online) (a) Stress response σ vs time t (lower axis) and vs strain $\gamma = \dot{\gamma}_0 t$ (upper axis) of a 4% wt. casein gel to a constant shear rate $\dot{\gamma}_0 = 10^{-3} \text{ s}^{-1}$ initiated at $t = 0$. The gray dashed line corresponds to linear viscoelastic response [Eq. (7.2)]. The black line corresponds to the K-BKZ equation constructed using only the strain-hardening part of the damping function, $h^*(\gamma_0)$ and reported as the solid black line in Fig. 7-3. The continuous red line corresponds to the K-BKZ equation built upon \tilde{h} , which includes both the hardening and the softening component of the damping function. Lower inset: same data on semilogarithmic scales. Upper inset: sketch and images of the side view of Couette cell at different strains recorded simultaneously to the experiment reported in the main graph.

Equation (7.2) nicely describes the experimental data for $\gamma \lesssim 0.2$ without any additional fitting parameter [see gray line in Fig. 7-4(a) and (c)]. To predict the nonlinear behavior, we substitute the power law form of the relaxation modulus $G(t)$ into Eq. (7.1) [273, 280, 281] and rearrange to give:

$$\sigma(t) = \frac{V\dot{\gamma}_0^\alpha}{\Gamma(1-\alpha)} \int_0^{\dot{\gamma}_0 t} h(\gamma)\gamma^{-\alpha}d\gamma \quad (7.3)$$

where $\gamma = \dot{\gamma}_0 t'$ is the total accumulated strain at time t' .

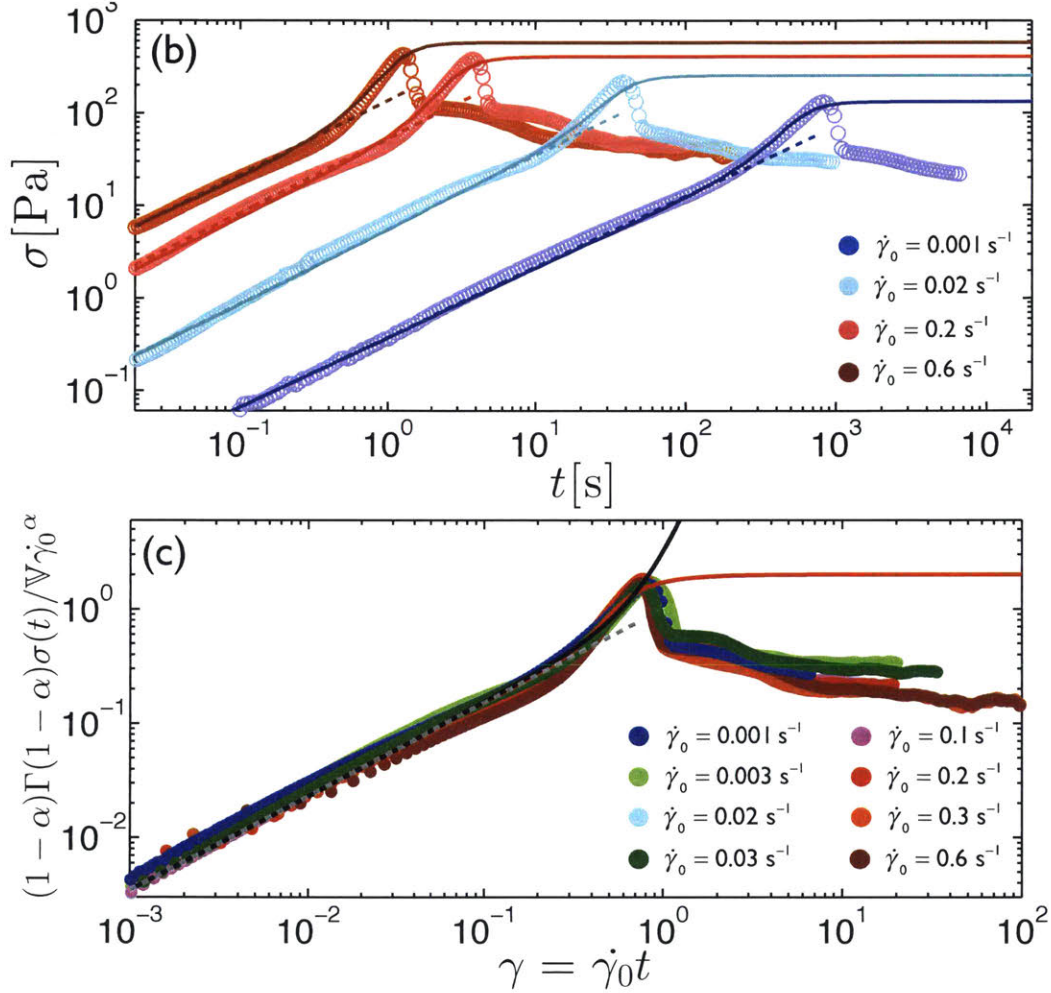


Figure 7-5: (color online) (b) Stress responses to individual constant shear rate experiments ranging from 10^{-3} s^{-1} to 0.6 s^{-1} . Dashed lines indicate the linear response [Eq. (7.2)], and the continuous lines correspond to the K-BKZ predictions using \tilde{h} [Eq. (7.3)]. (c) Normalized stress responses $(1-\alpha)\Gamma(1-\alpha)\sigma(t)/V\dot{\gamma}_0^\alpha$ vs strain γ for all constant shear rate experiments.

To capture the strain-stiffening in the hydrogel we substitute the strain hardening form of the damping function for a protein gel ($h^*(\gamma)$) into Eq. (7.3) to obtain the prediction shown by the solid black line in Fig. 7-4(a) and Fig. 7-5(c). This captures the nonlinear response of the gel at moderate strains, but leads to an ever-increasing rate of stress growth. The softening part of the damping function is

crucial to account for the stress evolution observed experimentally during shear start-up. Substituting \tilde{h} in Eq. (7.3) and integrating numerically we get the red line in Fig. 7-4(a) and Fig. 7-5(c) which accurately predicts the mechanical response of the protein gel up to the stress maximum, without any adjustable parameter. The initial stiffening behavior is described by the numerator of \tilde{h} , while the denominator is responsible for the plateauing of the predicted stress response. The subsequent decrease of the stress observed experimentally in Fig. 7-4 must be associated with the growth of macroscopic fractures that cannot be accounted for by an integral formulation such as the K-BKZ equation, for which the value of the integral always increases monotonically in time. In fact to describe the decrease in the stress we must introduce the idea of an irreversible damage function, commonly used in composites and brittle fracture theories.

Repeating shear start-up experiments for various $\dot{\gamma}_0$ confirms that Eq. (7.3) quantitatively predicts the gel response over almost three decades of shear rate [Fig. 7-4(b)]. The universal nature of the response is evident by the rescaling of the experimental data onto a single master curve [Fig. 7-4(c)] and this rescaling also holds true for 8% wt [see Fig. 2(a) in the Supplemental Material].

Moreover, the steady-state stress value predicted by the K-BKZ formulation coincides closely with the value of the stress maximum observed experimentally [Fig. 7-5(b)], suggesting that there is a deeper connection between the failure point of the gel characterized by σ_c and γ_{cr} , and the nonlinear viscoelastic response of the material preceding macroscopic failure. Figure 7-6 shows the stress responses to shear start-up experiments at different shear rates for the 8% gel, which similar to the 4%, can be rescaled into a single master curve.

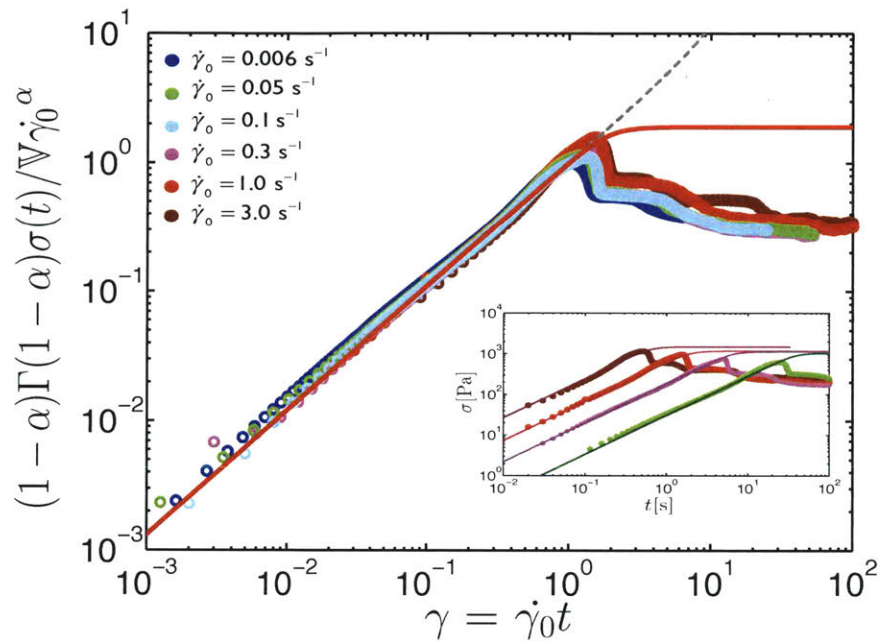


Figure 7-6: (color online) Normalized stress responses $(1 - \alpha)\Gamma(1 - \alpha)\sigma(t)/V\dot{\gamma}_0^\alpha$ vs strain $\gamma = \dot{\gamma}_0 t$ in the start up of steady shear flow experiments for shear rates ranging from 0.006 s^{-1} to 3 s^{-1} for a 8% wt. casein gel. The dashed gray line corresponds to the linear response (Eqn. 2 in the main text) while the red solid line stands for the K-BKZ prediction constructed from the power-law linear viscoelastic response plus the nonlinear damping function \tilde{h} determined independently from step strain experiment (see main text). Inset: non-normalized stress responses for a subset of shear start-up experiments shown in the main graph.

7.6 Failure criteria and discussion

In Figs. 7-7 and 7-8 we show the locus of the stress maximum (σ_c, γ_c) for different imposed shear rates, for both the 4% wt. and 8% wt. casein gels. The critical stress σ_c (above which macroscopic fractures appear) increases as a weak power law of $\dot{\gamma}_0$ with an exponent $\xi = 0.18 \pm 0.01$ for the 4% wt. casein gel and $\xi = 0.13 \pm 0.01$ for the 8% wt. respectively [Fig. 7-7]. However, interestingly, the critical strain γ_c also displays a power-law increase with $\dot{\gamma}_0$ for the 8% casein gel, whereas the 4% casein gel shows a yield strain that is rate independent [Fig. 7-8]. To explain these similarities and differences we need to establish an appropriate failure criterion for viscoelastic biopolymer gels.

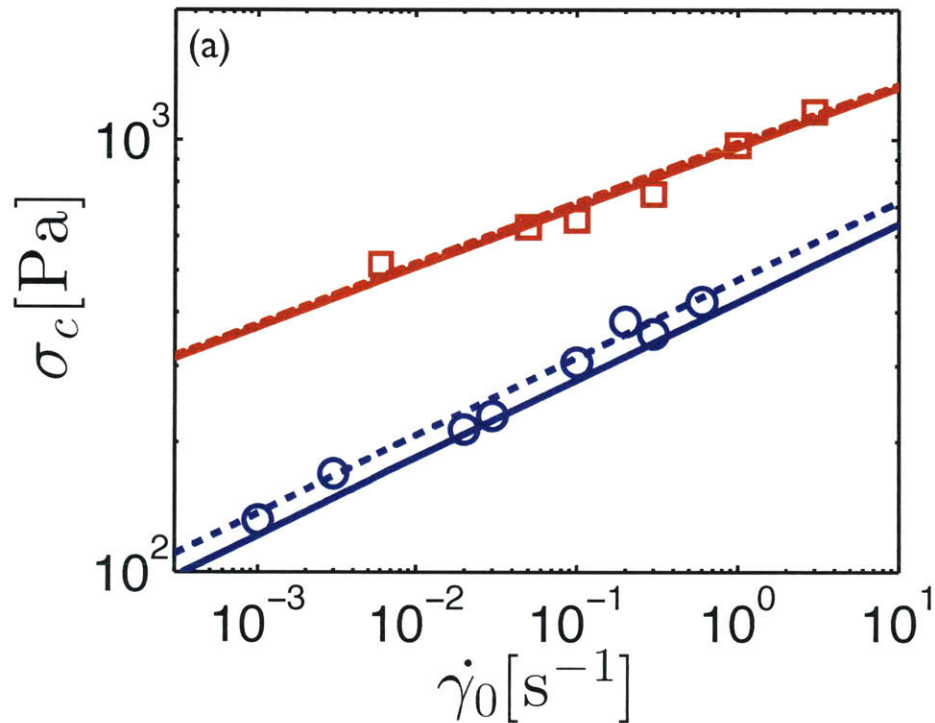


Figure 7-7: (color online) Critical stress σ_c vs applied shear rate $\dot{\gamma}_0$ for both a 4% (\circ) and a 8% (\square) casein gel. In both graphs, the dashed and continuous lines stand for the prediction issued from the combination of the Bailey criterion and the stress response computed either from just the linear response (dashed lines) or the full K-BKZ equation built upon h^* (solid lines).

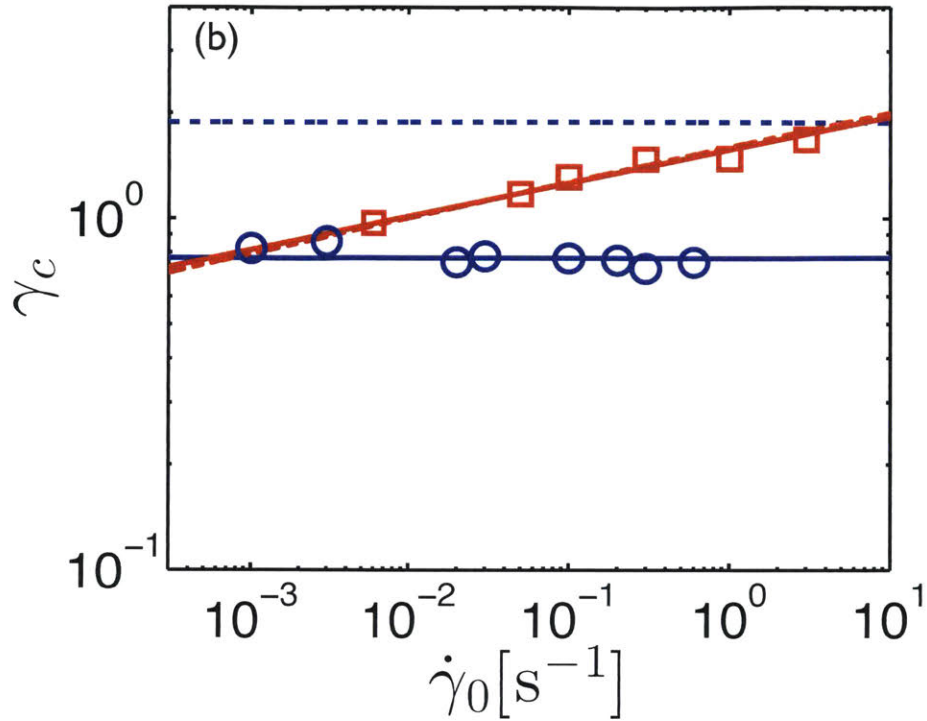


Figure 7-8: (color online) Critical strain γ_c vs applied shear rate $\dot{\gamma}_0$ for both a 4% (\circ) and a 8% (\square) casein gel. In both graphs, the dashed and continuous lines stand for the prediction issued from the combination of the Bailey criterion and the stress response computed either from just the linear response (dashed lines) or the full K-BKZ equation built upon h^* (solid lines).

To account for the different scalings of σ_c and γ_c with $\dot{\gamma}_0$, we build upon an irreversible, brittle-like failure scenario that results from damage accumulation [266, 37]. In this context the failure criterion introduced by J. Bailey, and successfully applied to both glasses [38] and rubbery-like materials [?], provides an implicit expression of the sample lifespan τ_f under an arbitrarily given active loading process $\sigma(t)$. The Bailey criterion reads $\int_0^{\tau_f} dt/F[\sigma(t)] = 1$, where $F(\sigma)$ is the dependence of the time to rupture for creep experiments performed at a series of constant imposed stresses σ [274]. Independent creep tests have been performed on these gels [266] and indicate that $F(\sigma) = A\sigma^{-\beta}$ where A is a scale parameter, with $A = (7.6 \pm 0.1) \times 10^{13} \text{ s.Pa}^\beta$ and $\beta = 5.5 \pm 0.1$ for the 4% wt. gel [266] and $A = (5.0 \pm 0.1) \times 10^{18} \text{ s.Pa}^\beta$ and $\beta = 6.4 \pm 0.1$ for the 8% wt. gel. For this gel, the scaling of the failure time as a function of the applied stress, measured for creep experiments is plotted in Fig. 7-9.

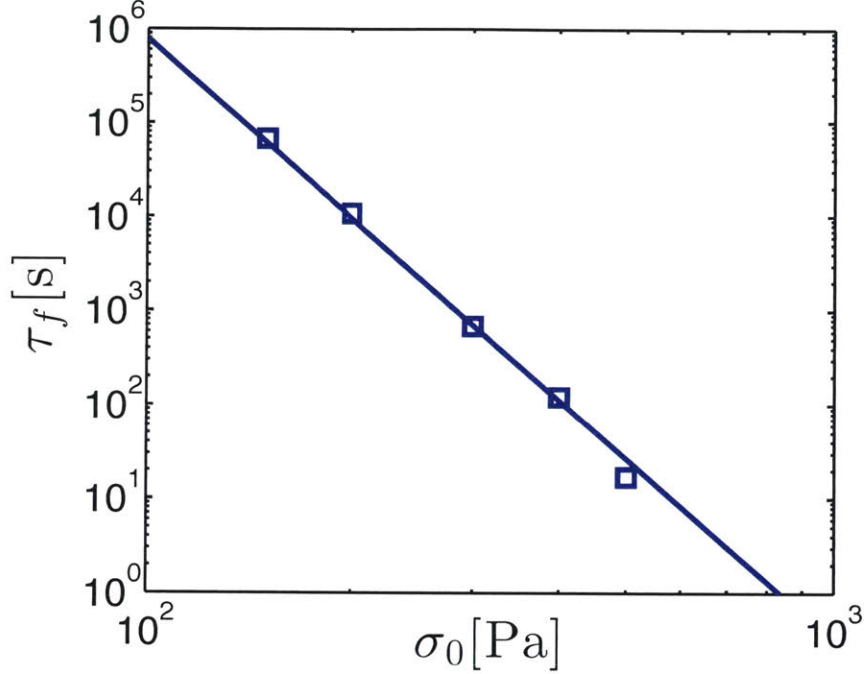


Figure 7-9: (color online) Failure time τ_f as a function of the constant stress σ_0 applied during creep experiments. The solid line is the best power-law fit $\tau_f = A\sigma^{-\beta}$, with $A = (5.0 \pm 0.1) \times 10^{18} \text{ s}\cdot\text{Pa}^\beta$ and $\beta = 6.4 \pm 0.1$ for the 8% wt. gel.

For steady-shear experiments, the Bailey criterion can also be applied to the stress $\sigma(t)$ predicted either by the linear response [Eq. (7.2)] or by the K-BKZ equation constructed with the damping function h^* [Eq. (7.3)]. When combined with Eq. (7.2), the Bailey criterion leads to the following analytic expressions for the critical strain and stress at failure under startup of steady shear:

$$\gamma_c(\dot{\gamma}_0) = S_\gamma \dot{\gamma}_0^{(1-\alpha\beta)/[1+(1-\alpha)\beta]} \quad (7.4)$$

$$\sigma_c(\dot{\gamma}_0) = S_\sigma \dot{\gamma}_0^{1/[1+(1-\alpha)\beta]} \quad (7.5)$$

where S_σ and S_γ are analytic functions of α , \mathbb{V} and β :

$$\begin{aligned} S_\sigma &= \left[\frac{A^{1-\alpha} [1 + \beta(1-\alpha)]^{1-\alpha} \mathbb{V}}{(1-\alpha)\Gamma(1-\alpha)} \right]^{1/[1+\beta(1-\alpha)]} \\ S_\gamma &= \left[A [1 + \beta(1-\alpha)] \left(\frac{(1-\alpha)\Gamma(1-\alpha)}{\mathbb{V}} \right)^\beta \right]^{1/[1+\beta(1-\alpha)]} \end{aligned} \quad (7.6)$$

Whether the critical stress and strain are constant or increase/decrease with $\dot{\gamma}_0$ thus depends on both the parameters in the linear viscoelastic kernel $G(t)$ and on the form of the failure law $F(\sigma)$.

For example, in the 8% wt. casein gel (for which $\alpha = 0.04 \pm 0.01$ and $\beta = 6.4 \pm 0.1$) we find the critical strain increases with $\dot{\gamma}_0$ since the exponent in Eq. (7.4) is $(1 - \alpha\beta)/[1 + (1 - \alpha)\beta] \simeq 0.10 \pm 0.01$. For both the 4% wt. and 8% wt. gels, the agreement between theory (dashed lines in Figs. 7-7 and 7-8) and experiments is excellent for the two power-law exponents, again without any adjustable parameter. However, the prefactor S_γ is clearly overestimated for the 4% wt. casein gels. Indeed, 4% wt. casein gels display a pronounced stiffening responsible for the early rupture of the gel, which is not captured by the linear viscoelastic formulation Eq. (7.2). However, when combined with the Bailey criterion, direct numerical integration of Eq. (7.3) accounting for strain-stiffening leads to the correct value of the prefactor for both 4% and 8% casein gels (solid lines in Figs. 7-7 and 7-8).

7.7 Conclusion

In this chapter, we have shown for a class of model protein gels - which exhibit a clear and pronounced power law viscoelastic relaxation over a wide range of scales - that the combination of the K-BKZ formalism, together with Bailey's failure criterion for brittle solids sets a self-consistent framework to quantitatively predict nonlinear stress evolution in the gel up to yielding as well as the scaling of both the critical stress and strain at failure. The present results are expected to extend beyond protein gels and our formalism is valid for any material which exhibits

a broad spectrum of relaxation times [277] and a brittle-like rupture scenario, including cells [282]. Our results in this chapter provide a unified rheo-mechanical framework to describe the brittle rupture of biopolymer gels that should be helpful in design applications and in developing deeper analogies between soft and hard materials [283].

Chapter 8

Conclusions

A conclusion is the place where you got tired thinking.

Martin H. Fischer

8.1 Conclusions from this study

Almost 2100 years after Roman poet and philosopher Lucretius (99 BC-55 BC) wrote his poem "De rerum natura" [61], in which he presented the principles of atomism, the subject of fragmentation is still an intriguing subject for many scientists. As Villiermaux mentions [13]: "The long history of this subject is certainly not a sign of lack of progress, but rather reflects its ever-renewed fields of application." . As we noticed, in this current study, the fragmentation of viscoelastic liquids and gels are other renewed fields of application. In this chapter we provide a summary of important results and conclusions from our work:

In Chapter 1 we showed that, despite the importance of the subject, there is a paucity of knowledge about different aspects of fragmentation and fracture for viscoelastic liquids and gels. We concluded that challenges in doing proper rheological measurements for these complex fluids have been a major obstacle. Also, many previous researchers in the field did not use the right framework for the fragmentation phenomena and their assumptions were based on old, and now considered to be also unphysical, paradigms.

We showed, in chapter 2, that probing viscoelastic properties of mobile complex liquids can be achieved by a precise recording of their dynamics in the capillary phenomena. Our proposed setup, ROJER, is based on the jet breakup study of a viscoelastic liquid. Our results showed that the dynamic change in diameter enables us to probe the properties of these liquids at very small dimensions (we are, however, limited to the optical resolution). This enabled us to overcome the inertia issues in our measurements. We managed to probe extensional rheology of dilute viscoelastic solutions at very low relaxation times $\tau_E \sim O(10)\mu\text{s}$. Our results showed that this proposed method for extensional rheology can have many advantages for analyzing the elongational rheology of fluids such as paints, resins, inks, saliva, anti-misting fuels, biofluids, and many other examples. We compared our data with linear and non-linear models and showed how models can help understand the experimental results and challenges in a much better way. We also showed that ROJER can have some disadvantages. One particular issue is related to high pressure drops that are required for passing more viscous liquids through a small nozzle (with a diameter of $175\mu\text{m}$). Microfluidic rheometry with hyperbolic channel profiles can be a good alternative device in the viscous regime. We provided a dimensionless nomogram that can guide the researchers for practical measurements of extensional viscosities.

The fragmentation dynamics of a known class of viscoelastic test fluid, namely PEO dissolved in a Newtonian solvent, is studied extensively in Chapters 3 and 4. Our results show that viscoelasticity inhibits the atomization. We provided a model that shows the average droplet diameter monotonically increases with the fluid relaxation time. As predicted from our model, there is a weak dependence of the average droplet diameter on the relaxation time which agrees well with our measurements. For the first time in the literature, results from this model can be used in analyzing the performance of dilute complex fluids in atomization/fragmentation. Our studies of the size distribution for the atomized droplets, presented in Chapter 4, show a universal behavior for the viscoelastic fluids. Four

different dilute viscoelastic liquids, ranging almost two orders of magnitude in their corresponding values of Deborah number, were atomized in three different fragmentation flows and their corresponding droplet size distributions follow a Gamma distribution with $n = 4$. This was also confirmed for a group of industrial paints and resins. We show that this broadening is triggered by the fluid elasticity in elongational flows and the universal limit in size distributions is set by the maximum corrugation level in viscoelastic filament which is set by geometry and of conservation of mass. This new finding can be extremely useful in many natural and biological applications. A chemist formulating paints and resins for coating applications, an inkjet designer concerned about breakup of viscoelastic ligaments, a biologist studying disease transfer during sneeze and cough events or even a material scientist interested in spraying hydrophobic agents on a substrate can all benefit from these results.

For a different class of materials, known as soft gels, we have explored the dynamics of nonlinear deformations preceding rupture and fracture. Chapter 6 shows that these materials have a mass fractal network. By studying acid-induced casein gels, our results help to understand the effect of linear and nonlinear rheology on the fracture behavior. We show that the power law rheology can be adequately modeled by fractional models and our results indicate a direct relation between the network structure parameters and the model parameters for the fractional element. The fractal dimension of the underlying gel, measured by confocal microscopy, can be connected to the power law exponent that these materials exhibit in their linear rheology. We show that the elastic modulus of these gels also follows a power law dependence on the volume fraction which can be again understood and explained using the available scalings for fractal behavior in biopolymer gels. We also show, in chapter 7, that these gels show strain hardening in the nonlinear region of deformation and after a certain strain damage accumulation leads to a fracture/rupture event. Through a systematic study on the nonlinear properties of these gels and using the concept of time-strain separability, we quantify the

nonlinear rheology by introducing a *damping function* that can be experimentally measured. We then provide a rheological framework that predicts the mechanical response of these materials in extreme deformations. We then showed that the well known Basquin's law for fracture of solids apply to these soft gels too and can be used as a proper way for describing the damage accumulation in these gels. We then show that using Bailey's durability criteria, we can combine the linear and nonlinear rheology with the Basquin's description of damage accumulation and provide a rheological framework for predicting the *fracture envelope* for these materials. Our results provide a method for quantitative prediction of fracture properties, such as the fracture stress and strain, under any arbitrary history of deformation or loading. We showed that for two separate gels these framework can quantitatively predict the values of stress and strain at the failure point in a start of shear flow. Predictions of the model agreed with measured values for tests performed over a wide range of applied shear rates (three orders of magnitude change in applied shear rates).

Fracture and rupture of soft materials is a relatively new field with many interesting applications [284]. Soft gels are widely used in many designs for real life applications due to their endurance to large deformations with little irreversible damage. Our results, combines linear and nonlinear properties of these materials with mechanics at large strains and provides a quantitative model for modeling the damage accumulation in these materials. Scientists interested in designing soft material for extreme deformations, engineers studying the fracture of soft solids and biologists looking at the performance of human tissues under cyclic loading can all benefit from certain aspects of our studies on soft gels.

Appendix A

Details of ROJER Analysis

A.1 Deriving the Strobe Factor

If a motion is periodic with a characteristic frequency f then with a suitable choice of initial time to specify the phase the position of the object $x(t)$ can be described by:

$$x(t) = A_0 \sin(2\pi ft) \quad (\text{A.1})$$

where A_0 is the amplitude of oscillation. The velocity of the object at a given time t_0 can be derived by differentiating $x(t)$ with respect to time:

$$V_r(t_0) = 2\pi f A_0 \cos(2\pi f t_0) \quad (\text{A.2})$$

Now when the observer is monitoring the motion with a prescribed frequency close to f (e.g. the frequency of a strobe light pulsed at a frequency close to f) the apparent velocity calculated from observation of the point of two consecutive instants in time to the observer will be different from the real velocity. Lets say that the observer is tracking the object displacement with a frequency $f_{obs} = f - \Delta f$ then the apparent motion from time t_0 to $t_0 + \delta t$ in which $\delta t = 1/f_{obs} = 1/(f - \Delta f)$ will be:

$$x(t_0 + \delta t) - x(t_0) = A_0 [\sin(2\pi f(t_0 + \delta t)) - \sin(2\pi f t_0)] \quad (\text{A.3})$$

which can be expanded to:

$$A_0 [\sin(2\pi f t_0) \cos(2\pi f \delta t) + \cos(2\pi f t_0) \sin(2\pi f \delta t) - \sin(2\pi f t_0)] \quad (\text{A.4})$$

In the limit of $\Delta f/f \ll 1$ it can be shown by Taylor expansion of the trigonometric terms in Eq. A.4 that to first order in $\Delta f/f$:

$$\begin{aligned} \sin(2\pi f \delta t) &\simeq 2\pi(\Delta f/f) \\ \cos(2\pi f \delta t) &\simeq 1 \end{aligned} \quad (\text{A.5})$$

thus the relative apparent motion for the observer can be estimated as:

$$x(t_0 + \delta t) - x(t_0) \simeq 2\pi A_0 (\Delta f/f) \cos(2\pi f t_0) \quad (\text{A.6})$$

from which the apparent velocity can be calculated by:

$$V_{app}(t_0) = \frac{x(t_0 + \delta t) - x(t_0)}{\delta t} \sim 2\pi \Delta f A_0 \cos(2\pi f t_0) \quad (\text{A.7})$$

Comparing the result for apparent velocity from Eq. A.7 with the real velocity from Eq. A.2 shows that the apparent motions seems slower than the real one by a factor equal to $\Delta f/f$.

A.2 Details of the Linear Stability Analysis

Brenn et al. [40] derived the dispersion curve for an axisymmetric viscoelastic jet using corotational Oldroyd eight constant model as the constitutive equation [111]. We retain only the terms that give the Oldroyd-B model. After linearizing the governing equations for conservation of mass and momentum in cylindrical coordinates and applying the right kinematic and dynamic boundary conditions at the liquid/air interface, Brenn et al. [40] show that the following dispersion

relation can be derived for the linear stability of the jet:

$$\begin{aligned}
& \Omega_r^2 \frac{kR_0}{2} \left[\frac{I_0(kR_0)}{I_1(kR_0)} + \frac{\rho_g K_0(kR_0)}{\rho_l K_1(kR_0)} \right] + \Omega_r (kR_0)^2 Oh \frac{1 + (\lambda_2/\lambda_1) De \Omega_r}{1 + De \Omega_r} \times \\
& \left[2kR_0 \frac{I_0(kR_0)}{I_1(kR_0)} \left(1 + (kR_0)^2 \frac{Oh}{\Omega_r} \frac{1 + (\lambda_2/\lambda_1) De \Omega_r}{1 + De \Omega_r} \right) - 1 - 2lR_0 \frac{I_0(lR_0)}{I_1(lR_0)} (kR_0)^2 \frac{Oh}{\Omega_r} \frac{1 + (\lambda_2/\lambda_1) De \Omega_r}{1 + De \Omega_r} \right] \\
& = \frac{(kR_0)^2}{2} (1 - (kR_0)^2) + C \frac{\rho_g}{\rho_l} \frac{k^3}{R_0^3} We \frac{K_0(kR_0)}{K_1(kR_0)}
\end{aligned} \tag{A.8}$$

in which $\Omega_r = \alpha_r \tau_R$ is the dimensionless growth rate (scales with the capillary timescale $\tau_R \equiv \sqrt{\rho_l R_0^3 / \sigma}$), kR_0 is the dimensionless wavenumber, ρ_g and ρ_l are respectively the gas and liquid density, $Oh = \eta_0 / \sqrt{\rho_l \sigma R_0}$ is the Ohnesorge number, $De = \lambda_1 / \sqrt{\rho_l R_0^3 / \sigma}$ is the Deborah number, I_n and K_n are the modified Bessel functions, λ_2 is the retardation time $\lambda_2 = \eta_s \lambda_1 / \eta_0$ and λ_1 is the relaxation time in the Oldroyd-B model. The constant C is an empirical correction factor to incorporate the aerodynamic forces on the jet and has a constant value of $C = 0.175$ according to [40]. Here l is a modified wavenumber defined as:

$$l^2 \equiv k^2 + \frac{\rho(\alpha + ikV_j)}{\eta(\alpha)} \tag{A.9}$$

where $\alpha = \alpha_r + i\alpha_i$ is the (complex) growth rate and:

$$\eta(\alpha) = \eta_0 \frac{1 + \lambda_2(\alpha + ikV_j)}{1 + \lambda_1(\alpha + ikV_j)} \tag{A.10}$$

The dispersion relation shown in Eq. A.8 incorporates the effects of the air/gas flow in the vicinity of the jet and the results converge to the stability analysis carried out by Goldin et al. [159] in the limit of zero air/gas effect, i.e. when ρ_g goes to 0.

Eq. A.8 is a nonlinear dispersion relation and at fixed values of De , Oh , We and for a given value of k the root which is $\Omega_r = \alpha_r \tau_R$ can be found using a simple numerical solver in Matlab. Results at different values of kR_0 are plotted and compared with measurements in Figure 2-7 (black solid line).

Bibliography

- [1] Kristy Wiens. *Design of an optical uroflowmeter and assessing bladder pressure through video analysis of the male urine stream*. Masters thesis, UBC, 2012.
- [2] B. E. Scharfman, A. H. Techet, J. W. M. Bush, and L. Bourouiba. Visualization of sneeze ejecta: steps of fluid fragmentation leading to respiratory droplets. *Experiments in Fluids*, 57(2):24, feb 2016.
- [3] J J Dunkley and D Aderhold. Centrifugal atomization of metal powders. *Advances in Powder Metallurgy and Particulate Materials*, 1:2, 2007.
- [4] Carli Davidson. *Shake*. New York : Harper Design, 2013.
- [5] Duncan C. Blanchard. *The snowflake man : a biography of Wilson A. Bentley*. McDonald & WoodwardPub, 1998.
- [6] J. S. Marshall, W. Mc K. Palmer, J. S. Marshall, and W. Mc K. Palmer. The distribution of raindrops with size. *Journal of Meteorology*, 5(4):165–166, aug 1948.
- [7] Wilson A. Bentley. STUDIES OF RAINDROPS AND RAINDROP PHENOMENA. *Monthly Weather Review*, 32(10):450–456, oct 1904.
- [8] E. Villermaux and B. Bossa. Drop fragmentation on impact. *Journal of Fluid Mechanics*, 668:412–435, jan 2011.
- [9] F Savart. Mémoire sur le choc d’une veine liquide lancée contre un plan circulaire. *Ann. chim*, 54(56):1833, 1833.

- [10] G Magnus. XXIII. Hydraulic researches. *Philosophical Magazine Series 4*, 11(71):178–196, mar 1856.
- [11] E Villermaux and B Bossa. Single-drop fragmentation determines size distribution of raindrops. *Nature Physics*, 5:697–702, 2009.
- [12] N. BREMOND and E. VILLERMAUX. Atomization by jet impact. *Journal of Fluid Mechanics*, 549(-1):273, feb 2006.
- [13] E Villermaux. Fragmentation. *Annual Review of Fluid Mechanics*, 39(1):419–446, jan 2007.
- [14] D. V. Boger and Kenneth. Walters. *Rheological phenomena in focus*. Elsevier, 1993.
- [15] J. W. Hoyt and J. J. Taylor. Turbulence structure in a water jet discharging in air. *Physics of Fluids*, 20(10):S253, oct 1977.
- [16] Greg Mckenna, Gareth H Mckinley, Montgomery T Shaw, and Ralph H Colby. *Rheology Bulletin*. 83(2), 2014.
- [17] Temple C. Patton. *Paint flow and pigment dispersion : a rheological approach to coating and ink technology*. Wiley, 1979.
- [18] Fred. T Trouton. On the coefficient of viscous traction and its relation to that of viscosity. *Proceedings of the Royal Society of London. Series A*, 77(519):426–440, may 1906.
- [19] S. T. J. Peng and R. F. Landel. Preliminary investigation of elongational flow of dilute polymer solutions. *Journal of Applied Physics*, 47(10):4255, 1976.
- [20] C J S Petrie. One hundred years of extensional flow. *Journal of Non-Newtonian Fluid Mechanics*, 137(1-3):1–14, 2006.
- [21] Prasannarao Dontula, Matteo Pasquali, L. E. Scriven, and Christopher W. Macosko. Can extensional viscosity be measured with opposed-nozzle devices? *Rheologica Acta*, 36(4):429–448, jul 1997.

- [22] Laura Campo-Deaño, Francisco J. Galindo-Rosales, Fernando T. Pinho, Manuel A. Alves, and Mónica S.N. Oliveira. Flow of low viscosity Boger fluids through a microfluidic hyperbolic contraction. *Journal of Non-Newtonian Fluid Mechanics*, 166(21-22):1286–1296, nov 2011.
- [23] D F James and K Walters. A Critical Appraisal of Available Methods for the Measurement of Extensional Properties of Mobile Systems. In A A Collyer, editor, *Techniques in Rheological Measurement SE - 2*, pages 33–53. Springer Netherlands, 1993.
- [24] L E Rodd, T P Scott, J J Cooper-White, and G H McKinley. Capillary break-up rheometry of low-viscosity elastic fluids. *Applied Rheology*, 15(1):12–27, 2005.
- [25] P. Schümmer and K H Tebel. Design and operation of the free jet elongational rheometer. *Rheologica Acta*, 21(4-5):514–516, 1982.
- [26] S.T.J. Peng and R.F. Landel. Rheological behavior of FM-9 solutions and correlation with flammability test results and interpretations. *Journal of Non-Newtonian Fluid Mechanics*, 12(1):95–111, jan 1983.
- [27] J Ferguson, N E Hudson, and B C H Warren. The break-up of fluids in an extensional flow field. *Journal of Non-Newtonian Fluid Mechanics*, 44:37–54, sep 1992.
- [28] H E Edgerton, E A Hauser, and W B Tucker. Studies in drop formation as revealed by the high-speed motion camera. *The Journal of Physical Chemistry*, 41(7):1017–1028, jul 1937.
- [29] Samy A. Madbouly, Ying Xia, and Michael R. Kessler. Rheological Behavior of Environmentally Friendly Castor Oil-Based Waterborne Polyurethane Dispersions. *Macromolecules*, 46(11):4606–4616, jun 2013.

- [30] Miloslav Kalab, Paula Allan-Wojtas, and Beverley E Phipps-Todd. Development of microstructure in set-style nonfat yogurt-A review. *Food Structure*, 2(1):7, 1983.
- [31] G W Scott Blair and J Burnett. On the creep, recovery, relaxation and elastic "memory" of some renneted milk gels. *British Journal of Applied Physics*, 10(1):15–20, jan 1959.
- [32] Marie Le Merrer, David Quéré, and Christophe Clanet. Buckling of Viscous Filaments of a Fluid under Compression Stresses. *Physical Review Letters*, 109(6):064502, aug 2012.
- [33] H Tabuteau, S Mora, G Porte, M Abkarian, and C Ligoure. Microscopic mechanisms of the brittleness of viscoelastic fluids. *Phys. Rev. Lett.*, 102:155501, 2009.
- [34] Brian M. Kinney, Lynn L. C. Jeffers, Gregory E. Ratliff, and Dan A. Carlisle. Silicone Gel Breast Implants. *Plastic and Reconstructive Surgery*, 134:47S–56S, jul 2014.
- [35] Qian Huang, Nicolas J. Alvarez, Aamir Shabbir, and Ole Hassager. Multiple Cracks Propagate Simultaneously in Polymer Liquids in Tension. *Physical Review Letters*, 117(8):087801, aug 2016.
- [36] O H Basquin. The exponential law of endurance tests. In *Proc. Astm*, volume 10, pages 625–630, 1910.
- [37] F. Kun, H. A. Carmona, J. S. Andrade, and H. J. Herrmann. Universality behind Basquin's law of fatigue. *Physical Review Letters*, 100(9):1–4, 2008.
- [38] J Bailey. An attempt to correlate some tensile strength measurements on glass: III. *Glass Ind*, 20:95–99, 1939.
- [39] A. D. Freeds and A.I. Leonov. The Bailey criterion: Statistical derivation and applications to interpretations of durability tests and chemical kinetics. *Zeitschrift für angewandte Mathematik und Physik*, 53(1):160–166, jan 2002.

- [40] G Brenn, Z B Liu, and F Durst. Linear analysis of the temporal instability of axisymmetrical non-Newtonian liquid jets. *International Journal of Multiphase Flow*, 26(10):1621–1644, 2000.
- [41] Thomas J. Ober, Simon J. Haward, Christopher J. Pipe, Johannes Soulages, and Gareth H. McKinley. Microfluidic extensional rheometry using a hyperbolic contraction geometry. *Rheologica Acta*, 52(6):529–546, may 2013.
- [42] Philippe Marmottant and Emmanuel Villermaux. Fragmentation of stretched liquid ligaments. *Physics of Fluids*, 16(8):2732, 2004.
- [43] Peter Bär. *Über die physikalischen grundlagen der zerstäubungstrocknung....* H. Schack & co., 1935.
- [44] R P Fraser, N Dombrowski, and J H Routley. The production of uniform liquid sheets from spinning cups. *Chemical Engineering Science*, 18(6):315–321, 1963.
- [45] J O Hinze and H Milborn. Atomization of liquids by means of a rotating cup. *JOURNAL OF APPLIED MECHANICS-TRANSACTIONS OF THE ASME*, 17(2):145–153, 1950.
- [46] R P Fraser, N Dombrowski, and J H Routley. The filming of liquids by spinning cups. *Chemical Engineering Science*, 18(6):323–337, 1963.
- [47] N. Dombrowski and T.L. Lloyd. Atomisation of liquids by spinning cups. *The Chemical Engineering Journal*, 8(1):63–81, jan 1974.
- [48] Hermann Hege. Flüssigkeitsauflösung durch Schleuderscheiben. *Chemie Ingenieur Technik - CIT*, 36(1):52–59, jan 1964.
- [49] Y Oyama, M Eguti, and K Endou. Studies on the Atomization of Water Droplets. *Chemical engineering*, 17(7):269–275, 1953.
- [50] Tamotsu Kamiya and Akira Kayano. On the Ligament Type Disintegration by the Rotating Disk Atomizer. *Chemical engineering*, 34(3):287–292,a1, 1970.

- [51] D J Ryley. Analysis of a polydisperse aqueous spray from a high-speed spinning disk atomizer. *British Journal of Applied Physics*, 10(4):180, 1959.
- [52] T Gisler, R C Ball, and D A Weitz. Strain Hardening of Fractal Colloidal Gels. *Phys. Rev. Lett.*, 82:1064–1067, 1999.
- [53] Norbert Wiener. Nonlinear Problems in Random Theory. *Nonlinear Problems in Random Theory, by Norbert Wiener, pp. 142. ISBN 0-262-73012-X. Cambridge, Massachusetts, USA: The MIT Press, August 1966. (Paper), page 142, 1966.*
- [54] P Marmottant and E Villermaux. On spray formation. *Journal of Fluid Mechanics*, 498:73–111, jan 2004.
- [55] Antoine-Laurent de Lavoisier. *Traité élémentaire de chimie*. Deterville, 1801.
- [56] Max Born, Roger John Blin-Stoyle, and John Michael Radcliffe. *Atomic physics*. Courier Corporation, 1989.
- [57] Arthur Henry Lefebvre. *Atomization and Sprays*. Hemisphere Publishing Corporation, 1989.
- [58] B Derby. Inkjet printing of functional and structural materials: fluid property requirements, feature stability, and resolution. In *Annual Review of Materials Research, Vol 40*, volume 40, pages 395–414. 2010.
- [59] D. A. Soules, R. H. Fernando, and J. E. Glass. Dynamic Uniaxial Extensional Viscosity (DUEV) Effects in Roll Application I. Rib and Web Growth in Commercial Coatings. *Journal of Rheology*, 32(2):181, 1988.
- [60] C J S Petrie. Extensional viscosity: A critical discussion. *Journal of Non-Newtonian Fluid Mechanics*, 137(1-3):15–23, 2006.
- [61] Lucretius. *On the Nature of Things*. W. W. Norton & Company, 2011.
- [62] E Villermaux, V Pistre, and H Lhuissier. The viscous Savart sheet. *Journal of Fluid Mechanics*, 730:607–625, aug 2013.

- [63] Helge M. Gonnermann. Magma Fragmentation. *Annual Review of Earth and Planetary Sciences*, 43(1):431–458, may 2015.
- [64] Duncan C. Blanchard. *From Raindrops to Volcanoes Adventruers with Sea Surface Meteorology*. Doubleday Anchor, 1967.
- [65] A N Kolmogorov. On the log normal distribution of the fragment sizes under breakage. In *Dokl. Akad. Nauk SSSR*, volume 31, pages 99–101, 1941.
- [66] E Villermaux, Ph Marmottant, and J Duplat. Ligament-mediated spray formation. *Physical Review Letters*, 92:74501, 2004.
- [67] Emmanuel Villermaux. Unifying ideas on mixing and atomization. *New Journal of Physics*, 6(1):125–125, sep 2004.
- [68] A. Vledouts, N. Vandenberghe, and E. Villermaux. Fragmentation as an aggregation process. *Proceedings of the Royal Society of London A: Mathematical, Physical and Engineering Sciences*, 471(2184), 2015.
- [69] A. Vledouts, N. Vandenberghe, and E. Villermaux. Fragmentation as an aggregation process: the role of defects. *Proceedings of the Royal Society of London A: Mathematical, Physical and Engineering Sciences*, 472(2185), 2016.
- [70] R G Larson. *Constitutive Equations for Polymer Solutions and Melts*. Butterworth Publishers, Boston, 1988.
- [71] R G Larson. *The Structure and Rheology of Complex Fluids*. Oxford University Press, New York, 1999.
- [72] H A Barnes, J F Hutton, and K Walters. *An Introduction to Rheology*. Elsevier Science Publishers B. V., Amsterdam, 1989.
- [73] C J S Petrie. *Elongational Flows*. Pitman, London, 1979.
- [74] A V Bazilevsky, V M Entov, and A N Rozhkov. Liquid Filament Microrheometer and Some of Its Applications. In D R Oliver, editor, *Third*

European Rheology Conference and Golden Jubilee Meeting of the British Society of Rheology SE - 21, pages 41–43. Springer Netherlands, 1990.

- [75] Gareth H. McKinley and Anubhav Tripathi. How to extract the Newtonian viscosity from capillary breakup measurements in a filament rheometer. *Journal of Rheology*, 44(3):653, may 2000.
- [76] Oliver Arnolds, Hans Buggisch, Dirk Sachsenheimer, and Norbert Willenbacher. Capillary breakup extensional rheometry (CaBER) on semi-dilute and concentrated polyethyleneoxide (PEO) solutions. *Rheologica Acta*, 49(11-12):1207–1217, nov 2010.
- [77] P. G. De Gennes. Coil-stretch transition of dilute flexible polymers under ultrahigh velocity gradients. *The Journal of Chemical Physics*, 60(12):5030, aug 1974.
- [78] V M Entov and E J Hinch. Effect of a spectrum of relaxation times on the capillary thinning of a filament of elastic liquid. *Journal of Non-Newtonian Fluid Mechanics*, 72:31–54, 1997.
- [79] G H McKinley. Visco-elasto-capillary thinning and breakup of complex fluids. *Rheology Reviews*, pages 1–48, 2005.
- [80] Lord Rayleigh. On the instability of jets. *Proceedings of the London Mathematical Society*, 10(1):4–13, 1878.
- [81] Damien C. Vadillo, Wouter Mathues, and Christian Clasen. Microsecond relaxation processes in shear and extensional flows of weakly elastic polymer solutions. *Rheologica Acta*, 51(8):755–769, jul 2012.
- [82] Laura Campo-Deaño and Christian Clasen. The slow retraction method (SRM) for the determination of ultra-short relaxation times in capillary breakup extensional rheometry experiments. *Journal of Non-Newtonian Fluid Mechanics*, 165(23-24):1688–1699, dec 2010.

- [83] Y Christanti and L M Walker. Surface tension driven jet break up of strain-hardening polymer solutions. *Journal of Non-Newtonian Fluid Mechanics*, 100(1-3):9–26, 2001.
- [84] M.-H. Wei, B. Li, R. L. A. David, S. C. Jones, V. Sarohia, J. A. Schmitgal, and J. A. Kornfield. Megasupramolecules for safer, cleaner fuel by end association of long telechelic polymers. *Science*, 350(6256):72–75, oct 2015.
- [85] M. Muthukumar. Dynamics of polymeric fractals. *The Journal of Chemical Physics*, 83(6):3161, sep 1985.
- [86] A Jaishankar and G H McKinley. Power-law rheology in the bulk and at the interface: quasi-properties and fractional constitutive equations. *Proceedings of the Royal Society A: Mathematical, Physical and Engineering Sciences*, 469(2149):20120284, oct 2012.
- [87] Scott C. Grindy, Robert Learsch, Davoud Mozhdehi, Jing Cheng, Devin G. Barrett, Zhibin Guan, Phillip B. Messersmith, and Niels Holten-Andersen. Control of hierarchical polymer mechanics with bioinspired metal-coordination dynamics. *Nature Materials*, 14(12):1210–1216, aug 2015.
- [88] Matthieu Pouzot, Taco Nicolai, Lazhar Benyahia, and Dominique Durand. Strain hardening and fracture of heat-set fractal globular protein gels. *Journal of colloid and interface science*, 293(2):376–83, jan 2006.
- [89] Leon G B Bremer. Theoretical and Experimental Study of the Fractal Nature of the Structure of Casein Gels. pages 3359–3372, 1989.
- [90] J A Lucey. Properties of Acid Casein Gels Made by Rheological Properties. 6946(97):381–388, 1997.
- [91] Mathieu Leocmach, Christophe Perge, Thibaut Divoux, and S??bastien Manneville. Creep and fracture of a protein gel under stress. *Physical Review Letters*, 113(3):1–5, 2014.

- [92] H Schiessel, R Metzler, A Blumen, and T F Nonnenmacher. Generalized viscoelastic models: Their fractional equations with solutions. *Journal of Physics a-Mathematical and General*, 28(23):6567–6584, 1995.
- [93] R Metzler and J Klafter. The random walk’s guide to anomalous diffusion: a fractional dynamics approach. *Physics Reports-Review Section of Physics Letters*, 339(1):1–77, 2000.
- [94] G W Leibniz. Letter from Hanover, Germany, Deptember 30, 1695 to GA L’Hospital. *JLeibnizen Mathematische Schriften*, 2:301–302, 1849.
- [95] I Podlubny. Fractional-order systems and PI-lambda-D-mu-controllers. *Ieee Transactions on Automatic Control*, 44(1):208–214, 1999.
- [96] Christophe Clanet and Emmanuel Villermaux. Life of a smooth liquid sheet. *Journal of Fluid Mechanics*, 462:307–340, 2002.
- [97] Christophe Clanet. Waterbells and Liquid. 2007.
- [98] Hervé Tabuteau, Serge Mora, Matteo Ciccotti, Chung-Yuen Hui, and Christian Ligoure. Propagation of a brittle fracture in a viscoelastic fluid. *Soft Matter*, 7(19):9474, 2011.
- [99] L. Kachanov. *Introduction to continuum damage mechanics*. 1986.
- [100] C W Macosko. *Rheology: Principles, Measurements and Applications*. VCH Publishers Inc, New York, 1994.
- [101] G H McKinley and T Sridhar. Filament-stretching rheometry of complex fluids. *Annual Review of Fluid Mechanics*, 34:375–415, 2002.
- [102] K. Walters. Recent Developments in Rheometry. In P. Moldenaers and R. Keunings, editors, *Theoretical and Applied Rheology*, pages 16–23. Elsevier: Brussels, 1992.
- [103] Pierre-Gilles de Gennes. *Introduction to Polymer Dynamics*. CUP Archive, 1990.

- [104] George William Scott Blair. *An introduction to biorheology*. Elsevier Scientific Publ. Co., 1974.
- [105] SS Davis. The rheological properties of saliva. *Rheologica Acta*, 10:28–35, 1971.
- [106] S J Haward, A Jaishankar, M S N Oliveira, M A Alves, and G H McKinley. Extensional flow of hyaluronic acid solutions in an optimized microfluidic cross-slot device. *Biomicrofluidics*, 7(4):044108, jul 2013.
- [107] Neil F Morrison and Oliver G Harlen. Viscoelasticity in inkjet printing. *Rheologica Acta*, 49(6):619–632, jan 2010.
- [108] Bavand Keshavarz, Vivek Sharma, Eric C. Houze, Michael R. Koerner, John R. Moore, Patricia M. Cotts, Philip Threlfall-Holmes, and Gareth H. McKinley. Studying the Effects of Elongational Properties on Atomization of Weakly Viscoelastic Solutions Using Rayleigh Ohnesorge Jetting Extensional Rheometry (ROJER). *Journal of Non-Newtonian Fluid Mechanics*, feb 2015.
- [109] M.-H. Wei, B. Li, R. L. A. David, S. C. Jones, V. Sarohia, J. A. Schmitgal, and J. A. Kornfield. Megasupramolecules for safer, cleaner fuel by end association of long telechelic polymers. *Science*, 350(6256):72–75, oct 2015.
- [110] Amarin G McDonnell, Naveen N Jason, Leslie Y Yeo, James R Friend, Wenlong Cheng, and Ranganathan Prabhakar. Extensional viscosity of copper nanowire suspensions in an aqueous polymer solution. *Soft matter*, 11(41):8076–82, nov 2015.
- [111] R B Bird, R C Armstrong, and O Hassager. *Dynamics of Polymeric Liquids*, volume 1. John Wiley & Sons, New York, 2nd edition, 1987.
- [112] C J S Petrie. EXTENSIONAL FLOW - A MATHEMATICAL PERSPECTIVE. *Rheologica Acta*, 34(1):12–26, 1995.
- [113] Mahesh Padmanabhan. Measurement of extensional viscosity of viscoelastic liquid foods. *Journal of Food Engineering*, 25(3):311–327, jan 1995.

- [114] David F James. Boger fluids. *Annual Review of Fluid Mechanics*, 41:129–142, 2009.
- [115] D.V. Boger. A highly elastic constant-viscosity fluid. *Journal of Non-Newtonian Fluid Mechanics*, 3(1):87–91, sep 1977.
- [116] Simon J. Haward, Mónica S. N. Oliveira, Manuel A. Alves, and Gareth H. McKinley. Optimized cross-slot flow geometry for microfluidic extensional rheometry. *Physical Review Letters*, 109(12):128301, sep 2012.
- [117] C. Wagner, Y. Amarouchene, Daniel Bonn, and J. Eggers. Droplet Detachment and Satellite Bead Formation in Viscoelastic Fluids. *Physical Review Letters*, 95(16):164504, oct 2005.
- [118] P E Arratia, L A Cramer, J P Gollub, and D J Durian. The effects of polymer molecular weight on filament thinning and drop breakup in microchannels. *New Journal of Physics*, 11, 2009.
- [119] H. Lhuissier, B. Néel, and L. Limat. Viscoelasticity Breaks the Symmetry of Impacting Jets. *Physical Review Letters*, 113(19):194502, nov 2014.
- [120] R Sattler, C Wagner, and J Eggers. Blistering pattern and formation of nanofibers in capillary thinning of polymer solutions. *Physical Review Letters*, 100(16), 2008.
- [121] Y Amarouchene, D Bonn, J Meunier, and H Kellay. Inhibition of the finite-time singularity during droplet fission of a polymeric fluid. *Physical Review Letters*, 86(16):3558–3561, 2001.
- [122] J. E. Matta. Nonlinear viscoelastic breakup in a high-velocity airstream. *Technical Report, May 1979 - Apr. 1980 Army Armament Research and Development Command, Aberdeen Proving Ground, MD. Chemical Systems Lab., 1, mar 1981.*
- [123] J. E. Matta and R. P. Tytus. Viscoelastic breakup in a high velocity airstream. *Journal of Applied Polymer Science*, 27(2):397–405, feb 1982.

- [124] Lynn M. Walker and Yenny Christanti. Quantifying air atomization of viscoelastic fluids through fluid relaxation times. *Atomization and Sprays*, 16(7):777–790, 2006.
- [125] B. R. Elbing, E. S. Winkel, M. J. Solomon, and S. L. Ceccio. Degradation of homogeneous polymer solutions in high shear turbulent pipe flow. *Experiments in Fluids*, 47(6):1033–1044, jun 2009.
- [126] B T O’Kennedy, J S Mounsey, F Murphy, E Duggan, and P M Kelly. Factors affecting the acid gelation of sodium caseinate. *International Dairy Journal*, 16:1132–1141, 2006.
- [127] Shelley L. Anna, Gareth H. McKinley, Duc A. Nguyen, Tam Sridhar, Susan J. Muller, Jin Huang, and David F. James. An interlaboratory comparison of measurements from filament-stretching rheometers using common test fluids. *Journal of Rheology*, 45(1):83, jan 2001.
- [128] Martin L. Sentmanat. Miniature universal testing platform: from extensional melt rheology to solid-state deformation behavior. *Rheologica Acta*, 43(6):657–669, aug 2004.
- [129] M L Sentmanat, B N Wang, and G H McKinley. Measuring the transient extensional rheology of polyethylene melts using the SER universal testing platform. *Journal of Rheology*, 49(3):585–606, 2005.
- [130] G H McKinley and A Tripathi. How to extract the Newtonian viscosity from capillary breakup measurements in a filament rheometer. *Journal of Rheology*, 44(3):653–670, 2000.
- [131] R. Sattler, S. Gier, J. Eggers, and C. Wagner. The final stages of capillary break-up of polymer solutions. *Physics of Fluids*, 24(2):023101, 2012.
- [132] T R Tuladhar and M R Mackley. Filament stretching rheometry and break-up behaviour of low viscosity polymer solutions and inkjet fluids. *Journal of Non-Newtonian Fluid Mechanics*, 148(1-3):97–108, 2008.

- [133] Christian Clasen, Paul M. Phillips, Ljiljana Palangetic, and Jan Vermant. Dispensing of rheologically complex fluids: The map of misery. *AIChE Journal*, 58(10):3242–3255, oct 2012.
- [134] Philipp Erni, Matthieu Varagnat, Christian Clasen, Jérôme Crest, and Gareth H. McKinley. Microrheometry of sub-nanolitre biopolymer samples: non-Newtonian flow phenomena of carnivorous plant mucilage. *Soft Matter*, 7(22):10889, nov 2011.
- [135] C Clasen, J P Plog, W M Kulicke, M Owens, C Macosko, L E Scriven, M Verani, and G H McKinley. How dilute are dilute solutions in extensional flows? *Journal of Rheology*, 50(6):849–881, 2006.
- [136] J C Thompson and J P Rothstein. The atomization of viscoelastic fluids in flat-fan and hollow-cone spray nozzles. *Journal of Non-Newtonian Fluid Mechanics*, 147(1-2):11–22, 2007.
- [137] Pradeep P. Bhat, Santosh Appathurai, Michael T. Harris, Matteo Pasquali, Gareth H. McKinley, and Osman A. Basaran. Formation of beads-on-a-string structures during break-up of viscoelastic filaments. *Nature Physics*, 6(8):625–631, jun 2010.
- [138] M S N Oliveira and G H McKinley. Iterated stretching and multiple beads-on-a-string phenomena in dilute solutions of highly extensible flexible polymers. *Physics of Fluids*, 17(7), 2005.
- [139] J. Plateau. Ueber die Gränze der Stabilität eines flüssigen Cylinders. *Annalen der Physik und Chemie*, 156(8):566–569, 1850.
- [140] J Eggers and E Villermaux. Physics of liquid jets. *Reports on Progress in Physics*, 71(3), 2008.
- [141] J Eggers. Nonlinear dynamics and breakup of free-surface flows. *Reviews of Modern Physics*, 69(3):865–929, 1997.

- [142] Lord Rayleigh. Some applications of photography. *Nature*, 44(249):441, 1891.
- [143] E A Hauser, H E Edgerton, B M Holt, and J T Cox. The application of the high-speed motion picture camera to research on the surface tension of liquids. *The Journal of Physical Chemistry*, 40(8):973–988, jan 1935.
- [144] Roland Eötvös. Ueber den Zusammenhang der Oberflächenspannung der Flüssigkeiten mit ihrem Molecularvolumen. *Annalen der Physik*, 263(3):448–459, 1886.
- [145] Niels Bohr. Determination of the surface-tension of water by the method of jet vibration. *Philosophical Transactions of the Royal Society of London. Series A, Containing Papers of a Mathematical or Physical Character*, pages 281–317, 1909.
- [146] F W Kroesser and S Middleman. Viscoelastic jet stability. *AICHE Journal*, 15(3):383–&, 1969.
- [147] S Middleman. Stability of a viscoelastic jet. *Chemical Engineering Science*, 20(12):1037–&, 1965.
- [148] S Middleman. *Modeling axisymmetric flows: Dynamics of films, jets and drops*. Academic Press, San Diego, 1995.
- [149] D W Bousfield, R Keunings, G Marrucci, and M M Denn. Nonlinear analysis of the surface tension driven breakup of viscoelastic filaments. *Journal of Non-Newtonian Fluid Mechanics*, 21(1):79–97, 1986.
- [150] P. Schümmer and K H Tebel. The use of controlled jet instability for elongational rheometry. *Journal of Rheology*, 26(1):77–78, 1982.
- [151] P Schümmer and K H Tebel. A new elongational rheometer for polymer solutions. *Journal of Non-Newtonian Fluid Mechanics*, 12(3):331–347, 1983.
- [152] A V Bazilevsky, V M Entov, A N Rozhkov, and A L Yarin. Polymeric Jets Beads-on-String Breakup and Related Phenomena. In D R Oliver, editor,

Third European Rheology Conference and Golden Jubilee Meeting of the British Society of Rheology SE - 22, pages 44–46. Springer Netherlands, 1990.

- [153] V. M. Entov and A. L. Yarin. Influence of elastic stresses on the capillary breakup of jets of dilute polymer solutions. *Fluid Dynamics*, 19(1):21–29, 1984.
- [154] Y Christanti and L M Walker. Effect of fluid relaxation time of dilute polymer solutions on jet breakup due to a forced disturbance. *Journal of Rheology*, 46(3):733–748, 2002.
- [155] Vivek Sharma, Arezoo M Ardekani, and Gareth H McKinley. ‘Beads on a String’ Structures and Extensional Rheometry using Jet Break-up. In *5th Pacific Rim Conference on Rheology (PRCR-5)*, 2010.
- [156] Harold E. Edgerton. *Electronic Flash, Strobe*. Massachusetts Institute of Technology(MIT), 1987.
- [157] S. P. Lin. *Breakup of Liquid Sheets and Jets*. Cambridge University Press, 2010.
- [158] Subrahmanyam Chandrasekhar. *Hydrodynamic and Hydromagnetic Stability*. Dover Publications, 1961.
- [159] Michael Goldin, Joseph Yerushalmi, Robert Pfeffer, and Reuel Shinnar. Breakup of a laminar capillary jet of a viscoelastic fluid. *Journal of Fluid Mechanics*, 38(04):689–711, 1969.
- [160] A. M. Ardekani, V. Sharma, and G. H. McKinley. Dynamics of bead formation, filament thinning and breakup in weakly viscoelastic jets. *Journal of Fluid Mechanics*, 665:46–56, dec 2010.
- [161] Nagi N. Mansour and Thomas S. Lundgren. Satellite formation in capillary jet breakup. *Physics of Fluids A: Fluid Dynamics*, 2(7):1141, jul 1990.
- [162] R P Mun, J A Byars, and D V Boger. The effects of polymer concentration and molecular weight on the breakup of laminar capillary jets. *Journal of Non-Newtonian Fluid Mechanics*, 74(1-3):285–297, 1998.

- [163] Lord Rayleigh. On the capillary phenomenon of jets. *Proceedings of the Royal Society of London*, 29:71–97, 1879.
- [164] C Clasen, J Bico, V M Entov, and G H McKinley. ‘Gobbling drops’: the jetting-dripping transition in flows of polymer solutions. *Journal of Fluid Mechanics*, 636:5–40, 2009.
- [165] S. P. Lin and R. D. Reitz. DROP and spray formation from a liquid jet. *Annual Review of Fluid Mechanics*, 30(1):85–105, jan 1998.
- [166] M Doi and S F Edwards. *The Theory of Polymer Dynamics*. Oxford University Press, New York, 1988.
- [167] V Tirtaatmadja, G H McKinley, and J J Cooper-White. Drop formation and breakup of low viscosity elastic fluids: Effects of molecular weight and concentration. *Physics of Fluids*, 18(4), 2006.
- [168] R. Byron Bird, Charles F. Curtiss, Robert C. Armstrong, and Ole Hassager. *Dynamics of Polymeric Liquids, Kinetic Theory (Dynamics of Polymer Liquids Vol. 2) (Volume 2)*. Wiley-Interscience, 1987.
- [169] A. Peterlin. Hydrodynamics of macromolecules in a velocity field with longitudinal gradient. *Journal of Polymer Science Part B: Polymer Letters*, 4(4):287–291, apr 1966.
- [170] C J Pipe and G H McKinley. Microfluidic rheometry. *Mechanics Research Communications*, 36(1):110–120, 2009.
- [171] F. J. Galindo-Rosales, M. A. Alves, and M. S. N. Oliveira. Microdevices for extensional rheometry of low viscosity elastic liquids: a review. *Microfluidics and Nanofluidics*, 14(1-2):1–19, jul 2013.
- [172] S. J. Haward. Microfluidic extensional rheometry using stagnation point flow. *Biomicrofluidics*, 10(4):043401, jul 2016.

- [173] E. B. Adams, J. C. Whitehead, and D. C. Bogue. Stresses in a viscoelastic fluid in converging and diverging flow. *AIChE Journal*, 11(6):1026–1032, nov 1965.
- [174] F N Cogswell. Converging flow of polymer melts in extrusion dies. *Polymer Engineering and Science*, 12(1):64–73, jan 1972.
- [175] F.N. Cogswell. Converging flow and stretching flow: A compilation. *Journal of Non-Newtonian Fluid Mechanics*, 4(1-2):23–38, jan 1978.
- [176] A. E. Everage and R. L. Ballman. The extensional flow capillary as a new method for extensional viscosity measurement. *Nature*, 273(5659):213–215, may 1978.
- [177] D.M. Binding and K. Walters. On the use of flow through a contraction in estimating the extensional viscosity of mobile polymer solutions. *Journal of Non-Newtonian Fluid Mechanics*, 30(2-3):233–250, jan 1988.
- [178] D F James and J H Saringer. FLOW OF DILUTE POLYMER-SOLUTIONS THROUGH CONVERGING CHANNELS. *Journal of Non-Newtonian Fluid Mechanics*, 11(3-4):317–339, 1982.
- [179] G H McKinley, W P Raiford, R A Brown, and R C Armstrong. NONLINEAR DYNAMICS OF VISCOELASTIC FLOW IN AXISYMMETRICAL ABRUPT CONTRACTIONS. *Journal of Fluid Mechanics*, 223:411–456, 1991.
- [180] Mónica S. Neves Oliveira, Manuel A. Alves, Fernando T. Pinho, and Gareth H. McKinley. Viscous flow through microfabricated hyperbolic contractions. *Experiments in Fluids*, 43(2-3):437–451, may 2007.
- [181] M. Nyström, H. R. Tamaddon Jahromi, M. Stading, and M. F. Webster. Numerical simulations of Boger fluids through different contraction configurations for the development of a measuring system for extensional viscosity. *Rheologica Acta*, 51(8):713–727, may 2012.

- [182] P C Sousa, F T Pinho, M S N Oliveira, and M A Alves. Extensional flow of blood analog solutions in microfluidic devices. *Biomicrofluidics*, 5(1):14108, jan 2011.
- [183] Gareth H McKinley, Lucy E Rodd, Mónica S N Oliverira, and Justin Cooper-White. Extensional flows of polymer solutions in microfluidic converging/diverging geometries. *Journal of Central South University of Technology*, 14(S1):6–9, feb 2007.
- [184] Eugene J Lim, Thomas J Ober, Jon F Edd, Salil P Desai, Douglas Neal, Ki Wan Bong, Patrick S Doyle, Gareth H McKinley, and Mehmet Toner. Inertio-elastic focusing of bioparticles in microchannels at high throughput. *Nature Communications*, 5:4120, jan 2014.
- [185] Gaetano D'Avino, Giovanni Romeo, Massimiliano M Villone, Francesco Greco, Paolo A Netti, and Pier Luca Maffettone. Single line particle focusing induced by viscoelasticity of the suspending liquid: theory, experiments and simulations to design a micropipe flow-focuser. *Lab on a chip*, 12(9):1638–45, may 2012.
- [186] A M Leshansky, A Bransky, N Korin, and U Dinnar. Tunable nonlinear viscoelastic "focusing" in a microfluidic device. *Physical Review Letters*, 98(23):234501, jun 2007.
- [187] Seungyoung Yang, Jae Young Kim, Seong Jae Lee, Sung Sik Lee, and Ju Min Kim. Sheathless elasto-inertial particle focusing and continuous separation in a straight rectangular microchannel. *Lab Chip*, 11(2):266–273, jan 2011.
- [188] Kyowon Kang, Sung Sik Lee, Kyu Hyun, Seong Jae Lee, and Ju Min Kim. DNA-based highly tunable particle focuser. *Nature Communications*, 4:2567, jan 2013.
- [189] C J Pipe, T S Majmudar, and G H McKinley. High shear rate viscometry. *Rheologica Acta*, 47(5-6):621–642, 2008.

- [190] L E Rodd, T P Scott, D V Boger, J J Cooper-White, and G H McKinley. The inertio-elastic planar entry flow of low-viscosity elastic fluids in micro-fabricated geometries. *Journal of Non-Newtonian Fluid Mechanics*, 129(1):1–22, 2005.
- [191] L E Rodd, J J Cooper-White, D V Boger, and G H McKinley. Role of the elasticity number in the entry flow of dilute polymer solutions in micro-fabricated contraction geometries. *Journal of Non-Newtonian Fluid Mechanics*, 143(2-3):170–191, 2007.
- [192] John R. Collier, Ovidiu Romanoschi, and Simioan Petrovan. Elongational rheology of polymer melts and solutions. *Journal of Applied Polymer Science*, 69(12):2357–2367, sep 1998.
- [193] No Title.
- [194] Lewis E. Wedgewood, Daniel N. Ostrov, and R. Byron Bird. A finitely extensible bead-spring chain model for dilute polymer solutions. *Journal of Non-Newtonian Fluid Mechanics*, 40(1):119–139, jul 1991.
- [195] G H McKinley. Visco-elasto-capillary thinning and break-up of complex fluids. *Rheology Reviews*, pages 1–48, 2005.
- [196] Danielle J Mai, Christopher Brockman, and Charles M Schroeder. Microfluidic systems for single DNA dynamics. *Soft matter*, 8(41):10560–10572, jan 2012.
- [197] D C Vadillo. Evaluation of the inkjet fluid's performance using the "Cambridge Trimaster" filament stretch and break-up device. *Journal of rheology*, 54(2):261–282, 2010.
- [198] Sir Horace Lamb. *Hydrodynamics*. Courier Corporation, 1945.
- [199] Gareth H. McKinley and Michael Renardy. Wolfgang von Ohnesorge. *Physics of Fluids*, 23(12):127101, dec 2011.

- [200] Gareth H. McKinley. Dimensionless Groups For Understanding Free Surface Flows of Complex Fluids. *SOR Bull.*, 74 (2)(6):6, 2005.
- [201] Adel Mansour and Norman Chigier. Air-blast atomization of non-Newtonian liquids. *Journal of Non-Newtonian Fluid Mechanics*, 58(2-3):161–194, jul 1995.
- [202] J. W. Hoyt. Recent progress in polymer drag reduction. *Research and Development Report, Jan. - Apr. 1974 Naval Undersea Center, San Diego, CA.*, -1, oct 1974.
- [203] K. K. Chao, C. A. Child, E. A. Grens, and M. C. Williams. Antimisting action of polymeric additives in jet fuels. *AIChE Journal*, 30(1):111–120, jan 1984.
- [204] J. W. Hoyt. Drag reduction-jet breakup correlation with kerosene-based additives. *Journal of Rheology*, 24(5):685, oct 1980.
- [205] Michael S. Owens, Madhu Vinjamur, L.E. Scriven, and C.W. Macosko. Mist-ing of non-Newtonian liquids in forward roll coating. *Journal of Non-Newtonian Fluid Mechanics*, 166(19-20):1123–1128, oct 2011.
- [206] B J de Gans, P C Duineveld, and U S Schubert. Inkjet printing of polymers: State of the art and future developments. *Advanced Materials*, 16(3):203–213, 2004.
- [207] Nicole Arockiam. The future of aerospace propulsion: viscoelastic non-Newtonian liquids. *Journal of Purdue Undergraduate Research*, 1(1):2–9, aug 2011.
- [208] Jennifer A Mallory, Sarah Jo DeFini, and Paul E Sojka. Formulation of gelled propellant simulants. In *46th AIAA/ASME/SAE/ASEE Joint Propulsion Conference & Exhibit*, 2010.
- [209] Joseph E. Matta, Raymond P. Tytus, and Jeffrey L. Harris. Aerodynamic atomization of polymeric solutions. *Chemical Engineering Communications*, 19(4-6):191–204, jan 1983.

- [210] Y Christanti and L M Walker. Quantifying air atomization of viscoelastic fluids through fluid relaxation times. *Atomization and Sprays*, 16(7):777–790, 2006.
- [211] S C Geckler and P E Sojka. Effervescent atomization of viscoelastic liquids : experiment and modeling. *Journal of Fluids Engineering*, 130(6):1–11, 2008.
- [212] A. Aliseda, E.J. Hopfinger, J.C. Lasheras, D.M. Kremer, A. Berchielli, and E.K. Connolly. Atomization of viscous and non-Newtonian liquids by a coaxial, high-speed gas jet. Experiments and droplet size modeling. *International Journal of Multiphase Flow*, 34(2):161–175, feb 2008.
- [213] Emmanuel Villermaux. The formation of filamentary structures from molten silicates: Pele’s hair, angel hair, and blown clinker. *Comptes Rendus Mécanique*, 340(8):555–564, aug 2012.
- [214] D T Papageorgiou. On the breakup of viscous liquid threads. *Physics of Fluids*, 7:1529–1544, 1995.
- [215] Jens Eggers. Universal pinching of 3D axisymmetric free-surface flow. *Physical Review Letters*, 71(21):3458–3460, nov 1993.
- [216] Michael P. Brenner, John R. Lister, and Howard A. Stone. Pinching threads, singularities and the number 0.0304... *Physics of Fluids*, 8(11):2827, nov 1996.
- [217] Michael Jaffe and Sahitya Allam. POLYMER CHEMISTRY. Safer fuels by integrating polymer theory into design. *Science (New York, N.Y.)*, 350(6256):32, oct 2015.
- [218] A Déchelette, E Babinsky, and P E Sojka. Drop Size Distributions. In Nasser Ashgriz, editor, *Handbook of Atomization and Sprays SE - 23*, pages 479–495. Springer US, 2011.
- [219] E Villermaux and J Duplat. Mixing as an aggregation process. *Physical Review Letters*, 91:184501, 2003.

- [220] M. A. Gorokhovski and V. L. Saveliev. Analyses of Kolmogorov's model of breakup and its application into Lagrangian computation of liquid sprays under air-blast atomization. *Physics of Fluids*, 15(1):184, dec 2003.
- [221] R. D. Cohen. Shattering of a Liquid Drop due to Impact. *Proceedings of the Royal Society A: Mathematical, Physical and Engineering Sciences*, 435(1895):483–503, dec 1991.
- [222] Marian Von Smoluchowski. Versuch einer mathematischen Theorie der Koagulationskinetik kolloidaler L{ö}sungen. *Zeitschrift für physikalische Chemie*, 92(2):129–168, 1917.
- [223] C. Wagner, Y. Amarouchene, Daniel Bonn, and J. Eggers. Droplet Detachment and Satellite Bead Formation in Viscoelastic Fluids. *Physical Review Letters*, 95(16):164504, oct 2005.
- [224] Zeynep Ergungor, Charles W. Manke, and Esin Gulari. Atomization and elongational viscosity of associating triblock copolymer solutions. *Journal of Non-Newtonian Fluid Mechanics*, 97(2-3):159–167, feb 2001.
- [225] A. A. Avdienko. Experimental evaluation of the distribution function of droplets in a viscoelastic liquid spray. *Journal of Engineering Physics and Thermophysics*, 66(2):149–152, feb 1994.
- [226] E. Babinsky and Paul E. Sojka. PREDICTING DROP SIZE DISTRIBUTIONS FROM FIRST PRINCIPLES FOR NON-NEWTONIAN FLUIDS. *Atomization and Sprays*, 11(6), 2001.
- [227] R B Bird, R C Armstrong, and O Hassager. Dynamics of Polymeric Liquids. 1, 1977.
- [228] Patrick S. Doyle, Eric S.G. Shaqfeh, Gareth H. McKinley, and Stephen H. Spiegelberg. Relaxation of dilute polymer solutions following extensional flow1Dedicated to the memory of Professor Gianni Astarita.1. *Journal of Non-Newtonian Fluid Mechanics*, 76(1-3):79–110, apr 1998.

- [229] Thomas T Perkins, Douglas E Smith, Ronald G Larson, and Steven Chu. Stretching of a single tethered polymer in a uniform flow. *Science*, page 83, 1995.
- [230] Lord Rayleigh. XII. On the resultant of a large number of vibrations of the same pitch and of arbitrary phase. *The London, Edinburgh, and Dublin Philosophical Magazine and Journal of Science*, 10(60):73–78, 1880.
- [231] Michael S Longuet-Higgins. On the statistical distributions of sea waves. *J. Mar. Res.*, 11(3):245–265, 1952.
- [232] Tom M. Apostol and Mamikon A. Mnatsakanian. A Fresh Look at the Method of Archimedes. *The American Mathematical Monthly*, 111(6):496, jun 2004.
- [233] Audun Holme. *Geometry: Our Cultural Heritage*. Springer Science & Business Media, 2013.
- [234] G. Magnus. Hydraulische Untersuchungen. *Annalen der Physik und Chemie*, 171(5):1–59, 1855.
- [235] N. Bremond and E. Villermaux. Atomization by jet impact. *Journal of Fluid Mechanics*, 549(-1):273, feb 2006.
- [236] E Villermaux and B Bossa. Drop fragmentation on impact. *Journal of Fluid Mechanics*, 668:412–435, 2011.
- [237] Lydia Bourouiba, Eline Dehandschoewercker, and John W. M. Bush. Violent expiratory events: on coughing and sneezing. *Journal of Fluid Mechanics*, 745:537–563, apr 2014.
- [238] Bavand Keshavarz, Vivek Sharma, Eric C. Houze, Michael R. Koerner, John R. Moore, Patricia M. Cotts, Threlfall-Holmes Philip, and Gareth H. McKinley. Studying the Effects of Elongational Properties on Atomization of

- Weakly Viscoelastic Solutions Using Rayleigh Ohnesorge Jetting Extensional Rheometry (ROJER). *Journal of Non-Newtonian Fluid Mechanics*, 2015.
- [239] Rayleigh. Investigation of the Character of the Equilibrium of an Incompressible Heavy Fluid of Variable Density. *Proceedings of the London Mathematical Society*, s1-14(1):170–177, nov 1882.
- [240] Geoffrey Taylor. The instability of liquid surfaces when accelerated in a direction perpendicular to their planes. I. In *Proceedings of the Royal Society of London A: Mathematical, Physical and Engineering Sciences*, volume 201, pages 192–196. The Royal Society, 1950.
- [241] NCFMF. *Illustrated experiments in fluid mechanics: the NCFMF book of film notes*. MIT Press, 1972.
- [242] Milton S Plesset and Christopher G Whipple. Viscous effects in Rayleigh-Taylor instability. *The Physics of Fluids*, 17(1):1–7, 1974.
- [243] P. Eisenklam. On ligament formation from spinning discs and cups. *Chemical Engineering Science*, 19(9):693–694, sep 1964.
- [244] Chr Huygens. 1673 Horologium oscillatorium sive de motu pendulorum ad horologia aptato demonstrationes geometricae, Paris 1673. *The complete Works of Christiaan Huygens*, 17, 1673.
- [245] Joella G Yoder. Christiaan huygens, book on the pendulum clock (1673). *Landmark Writings in Western Mathematics 1640–1940*, page 33, 2005.
- [246] Francis C Moon. *The Machines of Leonardo Da Vinci and Franz Reuleaux: kinematics of machines from the Renaissance to the 20th Century*, volume 2. Springer Science & Business Media, 2007.
- [247] V F Dunsikii and N V Nikitin. The size of “secondary” droplets when a liquid is atomized by a rotating disc. *Journal of engineering physics*, 17(1):791–795, 1969.

- [248] James C Ogbonna, Masatoshi Matsumura, Toshihito Yamagata, Hideo Sakuma, and Hiroshi Kataoka. Production of micro-gel beads by a rotating disk atomizer. *Journal of fermentation and bioengineering*, 68(1):40–48, 1989.
- [249] Linda M. Boize and N. Dombrowski. The atomization characteristics of a spinning disc ultra-low volume applicator. *Journal of Agricultural Engineering Research*, 21(1):87–99, mar 1976.
- [250] TAMOTSU KAMIYA and AKIRA KAYANO. DISINTEGRATION OF VISCOUS FLUID IN THE LIGAMENT STATE PURGED FROM A ROTATING DISK. *Journal of Chemical Engineering of Japan*, 4(4):364–369, 1971.
- [251] H. Lhuissier and E. Villermaux. Bursting bubble aerosols. *Journal of Fluid Mechanics*, 696:5–44, nov 2011.
- [252] A Vledouts, J Quinard, N Vandenberghe, and E Villermaux. Explosive fragmentation of liquid shells. *Journal of Fluid Mechanics*, 788:246–273, 2016.
- [253] Bavand Keshavarz, Eric C Houze, John R Moore, Michael R Koerner, and Gareth H McKinley. Ligament mediated fragmentation of viscoelastic liquids. *Physical review letters*, 117(15):154502, 2016.
- [254] G W Scott Blair and B C Veinoglou. A Study of the Firmness of Soft Materials Based on Nutting’s Equation. *Journal of Scientific Instruments*, 21(9):149–154, sep 1944.
- [255] R G Larson. CONSTITUTIVE RELATIONSHIPS FOR POLYMERIC MATERIALS WITH POWER-LAW DISTRIBUTIONS OF RELAXATION-TIMES. *Rheologica Acta*, 24(4):327–334, 1985.
- [256] Pieter Walstra. On the stability of casein micelles1. *Journal of Dairy Science*, 73(8):1965–1979, 1990.
- [257] Pieter Walstra. Casein sub-micelles: do they exist? *International Dairy Journal*, 9(3):189–192, 1999.

- [258] Ann H Barrett and Micha Peleg. Applications of fractal analysis to food structure. *LWT-Food Science and Technology*, 28(6):553–563, 1995.
- [259] L G B Bremer and T van Vliet. The modulus of particle networks with stretched strands. *Rheologica acta*, 30(1):98–101, 1991.
- [260] R Mezzenga, P Schurtenberger, A Burbidge, and M Michel. Understanding foods as soft materials. *Nature Materials*, 4:729–740, 2005.
- [261] J Thiele, Y Ma, S M C Bruekers, S Ma, and W T S Huck. 25th Anniversary Article: DeDesign Hydrogels for Cell Cultures: A Materials Selection Guide. *Advanced Materials*, 26:125–148, 2014.
- [262] M J Webber, E A Appel, E W Meijer, and R Langer. Supramolecular biomaterials. *Nature Materials*, 15:13–26, 2016.
- [263] J.-Y. Sun, X Zhao, W R K Illeperuma, O Chaudhuri, K H Oh, D J Mooney, J J Vlassak, and Z Suo. Highly stretchable and tough hydrogels. *Nature*, 489:133–136, 2012.
- [264] X Zhao. Multi-scale multi-mechanism design of tough hydrogels: building dissipation into stretchy networks. *Soft Matter*, 10:672–687, 2014.
- [265] D Bonn, H Kellay, M Prochnow, K Ben-Djemaa, and J Meunier. Delayed fracture of an inhomogeneous soft solid. *Science*, 280:265–267, 1998.
- [266] M Leocmach, C Perge, T Divoux, and S Manneville. Creep and Fracture of a Protein Gel under Stress. *Phys. Rev. Lett.*, 113:38303, 2014.
- [267] K E Daniels, S Mukhopadhyay, P J Houseworth, and R.P.Behringer. Instabilities in Droplets Spreading on Gels. *Phys. Rev. Lett.*, 99:124501, 2007.
- [268] T Baumberger, C Caroli, and D Martina. Solvent control of crack dynamics in a reversible hydrogel. *Nature Materials*, 5:552–555, 2006.
- [269] K M Schmoller, P Fern'andez, R C Arevalo, D L Blair, and A R Bausch. Cyclic hardening in bundle actin networks. *Nature Communications*, 134:1–7, 2010.

- [270] C Storm, J J Pastore, F C MacKintosh, T C Lubensky, and P A Janmey. Non-linear elasticity in biological gels. *Nature*, 435:191–194, 2005.
- [271] Izabela K Piechocka, Rommel G Bacabac, Max Potters, Fred C MacKintosh, and Gijsje H Koenderink. Structural hierarchy governs fibrin gel mechanics. *Biophysical journal*, 98(10):2281–2289, 2010.
- [272] J.-M.Y. Carrillo, F C MacKintosh, and A V Dobrynin. Nonlinear Elasticity: From Single Chain to Networks and Gels. *Macromolecules*, 46:3679–3692, 2013.
- [273] V H Rolón and M H Wagner. The damping function in rheology. *Rheol Acta*, 48:245–284, 2009.
- [274] G M Bartenev and Y S Zuyev. Strength and Failure of visco-elastic materials. chapter Chapter 7, pages 193–211. Pergamon Press, 1968.
- [275] Alan D Freed and Arkady I Leonov. The Bailey criterion : Statistical derivation and applications to interpretations of durability tests and chemical kinetics. 53:160–166, 2002.
- [276] J A Lucey, T van Vliet, K Grolle, T Geurts, and P Walstra. Properties of Acid Casein Gels Made by Acidification with Glucono- δ -lactone. 1. Rheological Properties. *Int. Dairy Journal*, 7:381–388, 1997.
- [277] A Jaishankar and G H McKinley. Power-law rheology in the bulk and at the interface: quasi-properties and fractional constitutive equations. *Proc. R. Soc. A*, 469:20120284, 2013.
- [278] M Pouzot, T Nicolai, L Benyahia, and D Durand. Strain hardening and fracture of heat-set fractal globular protein gels. *Journal of Colloid and Interface Science*, 293:376–383, 2006.
- [279] R I Tanner. From A to (BK)Z in Constitutive Relations. *J. Rheol.*, 32:673–702, 1988.

- [280] E Mitsoulis. 50 years of the K-BKZ constitutive relation for Polymers. *ISRN Polymer Science*, 2013:1–22, 2013.
- [281] Aditya Jaishankar and Gareth H. McKinley. A fractional K-BKZ constitutive formulation for describing the nonlinear rheology of multiscale complex fluids. *Journal of Rheology*, 58(6):1751–1788, nov 2014.
- [282] Philip Kollmannsberger and Ben Fabry. Linear and nonlinear rheology of living cells. *Annual review of materials research*, 41:75–97, 2011.
- [283] K M Schmoller and A R Bausch. Similar nonlinear mechanical response in hard and soft materials. *Nature Materials*, 12:278–281, 2013.
- [284] Costantino Creton and Matteo Ciccotti. Fracture and adhesion of soft materials: a review. *Reports on Progress in Physics*, 79(4):046601, apr 2016.